The Pennsylvania State University

The Graduate School

Department of Chemistry

STRUCTURAL INVESTIGATIONS OF STRONTIUM IN INORGANIC CRYSTALS, ORGANIC CRYSTALS, AND PHYLLOSILICATE MINERALS WITH ^{87}Sr NMR

A Thesis in

Chemistry

by

Geoffrey M. Bowers

Submitted in Partial Fulfillment
of the Requirements
for the Degree of

Doctor of Philosophy

August 2006

The thesis of Geoffrey M. Bowers was reviewed and approved* by the following:

Karl T. Mueller
Associate Professor of Chemistry
Thesis Advisor
Chair of Committee

Thomas E. Mallouk
DuPont Professor of Materials Chemistry and Physics

Alan J. Benesi
Lecturer in Chemistry

Brian A. Dempsey
Professor of Environmental Engineering

Ayusman Sen
Professor of Chemistry
Head of the Department of Chemistry

*Signatures are on file in the Graduate School

ABSTRACT

At numerous United States Department of Energy (US DOE) facilities such as Hanford near Richland, Washington, an enormous volume of high-level nuclear waste has been released from leaking storage tanks. This waste is contaminated primarily with the intermediate half-life (20 to 30 years) radioisotopes ^{137}Cs and ^{90}Sr and possesses a number of harsh chemical properties, such as a high alkalinity, a high ionic strength, and a high level of aqueous aluminum. The immobilization and remediation of strontium from the environment and the remaining stored waste are issues of great importance to the US DOE and populations surrounding the storage facilities: a portion of any ^{90}Sr ingested from contaminated food or drinking water will be incorporated into bone mass, leading to bone defects in minors and cancer in adults. In order to design appropriate waste remediation strategies and predict the mobility of strontium in the environment, it is necessary to understand the interactions of strontium with soil minerals and remediation materials on the molecular level. This dissertation seeks to enhance our grasp of strontium-mineral interactions through solid-state ^{87}Sr nuclear magnetic resonance (NMR).

Strontium-87 is a particularly challenging isotope to study with solid-state NMR due to severe sensitivity limitations brought about by intrinsic properties of the ^{87}Sr nucleus (the only stable NMR-active strontium isotope). As a direct result of these limitations, only three publications containing solid-state ^{87}Sr NMR spectra were available at the beginning of this research project. In order to achieve the overall goal of characterizing the strontium binding environment in minerals, it is thus necessary to (i)

examine known sensitivity enhancing NMR methods to determine the most appropriate approach for strontium-bearing minerals, (ii) apply this technique to identify NMR parameter/structure relationships in systems with known structure, and (iii) apply the knowledge gained from (i) and (ii) to analyze the strontium binding site(s) in strontium-saturated minerals using ^{87}Sr NMR.

The initial chapter of this thesis motivates the project by examining the political and chemical history of the main US plutonium production facility at Hanford, providing insight into the nature of the high-level waste and how it was generated. A brief introduction to soil mineralogy is also presented in this chapter, concluding with some comments on how the waste chemistry affects the natural soil minerals. The second chapter covers the theoretical basis of NMR, beginning with a framework for understanding the SIMPSON simulations used to extract NMR parameters in the remainder of the dissertation. It also presents the major internal interactions relevant to ^{87}Sr NMR and the theory behind the experimental methods that will be used in subsequent chapters.

Chapter 3 details research into the effectiveness of magic angle spinning (MAS) at improving the sensitivity and resolution of ^{87}Sr NMR spectra. In cases where the electric field gradient at the strontium site is small, i.e. when the coordination sphere is symmetric, MAS provides sufficient enhancement to observe the strontium resonance in periods of six to twelve hours. MAS is used to examine the distribution of electric field gradients due to crystal defects in the simple systems SrO (octahedrally coordinated Sr), SrF_2 (cubic Sr coordination), and $SrCl_2$ (cubic Sr coordination). In situations where a moderate to large electric field gradient is present, experimental and theoretical results

show that MAS is not effective at improving sensitivity or the interpretability of the resonances with quadrupolar couplings larger than 10 MHz.

Because MAS offers limited benefits with respect to ^{87}Sr NMR, alternative methods of sensitivity enhancement are explored in Chapter 4. The first section summarizes ^{87}Sr NMR studies of strontium-rich crystalline minerals with the quadrupolar Carr-Purcell-Meiboom-Gill (QCPMG) pulse sequence at a 21.14 T static field. The increase in field provides greater than an order of magnitude enhancement to the signal-to-noise ratio at 11.74 T in the case of $SrCO_3$, while QCPMG contributes an additional order of magnitude enhancement. QCPMG studies demonstrate that the strontium quadrupolar parameters are highly sensitive to variations in the strontium coordination sphere and that the quadrupolar asymmetry parameter, in particular, is closely associated with the spatial symmetry of the coordination environment. Despite the benefits of QCPMG at 21.14 T, this technique proved incapable of efficiently detecting strontium in a saturated phyllosilicate mineral. The second section of Chapter 4 explores the additional enhancement produced by double-frequency sweep (DFS) preparation prior to QCPMG at 21.14 T. The use of DFS reduces the necessary spectral acquisition time for a $SrCO_3$ sample by an additional factor of 10 to 40, permitting studies of strontium in systems that were not possible with QCPMG alone at 21.14 T. DFS-QCPMG studies show that the trends identified earlier in the chapter are followed by a number of additional inorganic and organic crystal systems. Evidence is also be presented that coordinating water has a profound effect on the strontium quadrupolar parameters and the limit of detection for ^{87}Sr DFS-QCPMG at 21.14 T is calculated based on strontium acetylacetonate data.

In Chapter 5, DFS-QCPMG at 21.14 T is used to study the strontium environments in a number of strontium-saturated phyllosilicate minerals, including three synthetic micas designed as strontium remediation materials and two natural montmorillonites. The results of ^{87}Sr NMR investigations are combined with ^{19}F MAS NMR and X-ray diffraction (XRD) analyses to characterize the interlayer strontium binding environment in heated forms of the micas that are known to sequester strontium. These results show that the presence of a layer offset induces a steric hindrance, forcing strontium to bind deep in the di-trigonal cavities following dehydration. Experimental evidence is also presented that strontium with (i) water in the coordination sphere and (ii) restricted cation mobility is invisible to direct room temperature ^{87}Sr NMR methods in simple crystals, phyllosilicate minerals, and tectosilicate minerals. This fact along with XRD results helps assign the interlayer strontium binding environment in both montmorillonites as a six-coordinate outer-sphere complex regardless of heat treatment at 500°C, in agreement with available extended X-ray absorption fine structure (EXAFS) literature. Preliminary investigations into indirect detection methods, such as ^{1}H-^{87}Sr TRAPDOR NMR, will also be presented. A few successful TRAPDOR experiments support the earlier assignments, but failures in some of the micas and montmorillonites draw attention to the difficulty of indirect ^{87}Sr NMR methods.

Having successfully completed the objectives of the research project in Chapter 5, Chapter 6 reviews the key results and contains three preliminary studies that highlight the remaining challenges in ^{87}Sr NMR. The first study applies ^{87}Sr NMR to a pair of titanate strontium sorbants that are currently a part of the DOE waste remediation strategy at the Savannah River facility. The second study examines the precipitated material formed

after a thirty-day incubation period in a strontium-rich simulated tank waste (Sr-STWL) solution seeded with colloidal silica. Both of these studies demonstrate that ^{87}Sr NMR is highly sensitive to the formation of strontium carbonate that may be invisible to X-ray techniques. The final section recounts an attempt to study the strontium environment in apatite minerals with ^{87}Sr NMR. Plans for future studies are then formulated based on these preliminary results.

TABLE OF CONTENTS

LIST OF FIGURES

LIST OF TABLES

ACKNOWLEDGEMENTS

I would like to begin by thanking my advisor, Prof. Karl T. Mueller, for relating numerous lessons about NMR, the practice of science, life as an academic, and for providing an environment that helped me to succeed. Karl's approach to graduate student development matched with my work style very well and catalyzed my advancement. I've learned a lot, but have a lot more to learn, and I hope that we continue to interact though positive collaboration in the future. The assistance of Dr. Andrew S. Lipton was also indispensable, as Andy provided me with a foundation for the SIMPSON simulations presented in this dissertation and a large dose of experience with low-γ quadrupolar nuclei and the QCPMG sequence. I would also like to thank our collaborators at the University of Arizona, Prof. Jon Chorover and Dr. Sunkyung Choi, for synthesizing and providing the homogeneous nucleation samples that I worked with before immersing myself in ^{87}Sr NMR. I am deeply grateful to the United States Department of Energy for financially supporting this research through grant numbers DE-FG07-99ER15012 and DE-FG02-06ER64191 and also the Penn State Center for Environmental Chemistry and Geochemistry (CECG) for supporting me in the summers of 2005 and 2006. Some of the computational work involving the LionXO cluster at Penn State was supported by the Penn State Center for Environmental Kinetics Analysis, National Science Foundation grant number CHE-0431328.

I would like to send special thanks to Dr. Garry Crosson, my predecessor on the DOE project, who worked on the original clay mineral weathering objectives. Garry in many ways served as a second mentor throughout the early years of my involvement in

the Mueller group. His accumulated knowledge about clay mineralogy, nuclear magnetic resonance spectroscopy, courses at Penn State, University politics, and life in general were extremely beneficial. I am sure that Garry's contributions through general conversation and direct scientific challenges enhanced the quality and applicability of this dissertation work significantly.

Many thanks to my other fellow group members during my time at Penn State: Rod Fry, Nancy Washton, Rebecca Golombeck, Mike Davis, Kim Earnhart, Caleb Strepka, Dr. Bill Brouwer, and Dr. S. Prabakar. Everyone has contributed something positive to my graduate educational experience. My thanks also to the Penn State NMR facility staff, Dr. Alan Benesi, Bernie O'Hare, and John Lintner. Your expertise with probe electronics, spectrometer consoles, pulse programming, and experimental NMR was indispensable in the course of preparing this research. Thank you for taking the time to share some of your experiences and skills with me. I also thank my dissertation committee (Karl, Alan, Prof. Tom Mallouk, and Prof. Brian Dempsey) for challenging me to become a better student every step along the way.

I would be remiss if I did not thank the undergraduate teaching faculty, specifically Dr. Joe Keiser and Rich Desmond, and the general chemistry support technicians, Ken Brown and John Bloom, for support during my early years at Penn State. I am grateful for your confidence, friendship, and the experience of being a supervising teaching assistant. I hope that some of my involvement has had a positive impact on the development of the courses, material, and the future chemistry teachers and chemists I worked with during my tenure.

I also thank the staff at the High Field Magnetic Resonance User Facility (HFMRF) at Pacific Northwest National Laboratory: part of the research described in this dissertation was performed in the Environmental and Molecular Sciences Laboratory, a national scientific user facility sponsored by the Department of Energy's Office of Biological and Environmental Research and located at Pacific Northwest National Laboratory. Completion of this work in four years is due in large part to HFMRF instrumentation and the assistance of my friends in Richland: Dr. Andrew Lipton, Dr. Joseph Ford, Dr. David Hoyt, Dr. Nancy Isern, Jesse Sears, and Mike Frolicke.

Despite the indispensable support of the individuals mentioned here already, the most instrumental people in developing the skills I needed at Penn State and as a person are my family, Prof. Larry D. Bowers, Janet M. Bowers, and my sister, Kimberly A. Bowers. Thanks Mom, Dad, and Kim for all of the contributions over the years. Thank you for never making me feel in need, developing in me an appreciation for this country and for the gifts I have been given, helping me form the character that I pride myself on, helping me develop a strong relationship with God that was integral in this effort, and making countless other contributions and sacrifices along the way. The completion of this dissertation is a testament to the quality people you are and is a culmination of everything you taught me over the years. I'll never be able to thank you enough.

Finally, but certainly not least, I thank my wife, Ruth A. Bowers. Your love and support was a necessary piece of this puzzle, and I could not have accomplished this in four years without you. Thanks for your laughter, your tears, working on the car, fishing, the trips to Bald Eagle, expanding my horizons, and putting up with me being me. This work is dedicated to us and our future. I can't wait to see where we go from here!

Chapter 1

History and Chemistry of the Hanford Site

1.1 Brief Historical Overview of Hanford

The legacy of the Hanford Works in Richland, Washington is one of environmental challenges for physicists, chemists, and geologists that persist today. To fully understand the complexity of the difficulties facing scientists working on site remediation and to prevent such contamination in the future, it is necessary to develop an appreciation for the history of the facility, both scientific and political. This section will present a brief summary of important historical events that are relevant to the origin, chemical history, and current mission of the United State Department of Energy facility at Hanford. While a complete account of the history of the Hanford Works is not relevant to this dissertation nor capable of being recounted in such a brief space, the interested party is referred to an excellent document prepared by the Hanford Historical and Cultural Resources Program.[1] This document is the source of a majority of the information included in this section as well as many of the figures.

1.1.1 Inception: Historical Events Leading to Nuclear Weapons

Two years after the discovery of the neutron by James Chadwick in 1932, Szilard authored a patent application describing how collisions of neutrons in chain reactions could release enormous amounts of energy and be harnessed to create powerful

explosives.[2,3] Years later (1938), the German scientists Otto Hahn and Fritz Strassman were studying neutron bombardment of uranium and found that uranium nuclei could split into radioactive barium and other fragments accompanied by a significant release of energy.[4] Their results were confirmed by Otto Frisch and Lise Meitner in January of 1939, who took the research a step further and calculated the energy released when uranium splits.[5] Based on their results, they proposed the fission process as the source of the uranium transformation and energy release. In March of 1939, scientists at Columbia University (including Szilard and Enrico Fermi) determined that a greater number of neutrons per uranium atom ae released during the neutron-induced fission of uranium-238 than are absorbed, suggesting that a sustainable and potentially explosive chain reaction was possible.[6,7] This finding fueled a growing interest and concern that Szilard's idea for a nuclear weapon was feasible. Later that year, theoretical calculations would show that uranium-235 was more fissile than uranium-238 and predicted that an as yet unknown trans-uranic element (with an atomic number of 94 and mass of 239 amu) would be even more fissile under certain conditions.[8]

In September of 1939, Germany invaded Poland and initiated World War II. That same year, the well-known letter from Szilard and Einstein was sent to U.S. president Franklin Roosevelt warning of the dangers of a German nuclear weapons program and encouraging the development of such a weapon by the United States to keep the Germans "in check".[1] Roosevelt responded by forming the Advisory Committee on Uranium, who provided funding for academic research related to nuclear weapons in the United States. In 1941, Glenn Seaborg complicated the situation for the Advisory Committee by proving the existence of the trans-uranic element 94, which he named plutonium.[9,10]

Faced with a difficult choice between pursuing a uranium-235 or plutonium-239 based explosive device, the Advisory Committee recommended the simultaneous development of both weapons. In August of 1942, Seaborg concluded research demonstrating that a series of oxidation and reduction reactions could be used to separate plutonium-239 from uranium-238, the final piece of chemical technology necessary to design a full-scale plutonium production facility.[11] That same month, the U.S. Army Corps of Engineers was assigned the task of building facilities for the mass production of both isotopes (Note: this is *prior* to the design of a functional nuclear reactor), resulting in the creation of the Clinton Engineer Works (now Oak Ridge National Laboratory) to pursue uranium-235 production and the Hanford Engineer Works (now Pacific Northwest National Laboratory) to pursue plutonium-239 production. Fermi and Allison successfully started the first self-sustained, uranium-based and graphite-moderated nuclear reactor at the University of Chicago one month after the decision to build a plutonium production facility at Hanford (December 2, 1942).[12,13] Nineteen days later, DuPont was awarded the contract for the Hanford works and construction began on the production scale facilities that would generate the plutonium used in the Trinity test and the nuclear weapon dropped on Nagasaki.

1.1.2 Manhattan Project

The Hanford Works involvement in the Manhattan Project was clearly substantial. As nuclear technology remained in the developmental stage, the Hanford Works facilities, designers, and engineers were always working just ahead of or concurrently

with the development of laboratory scale operations. The difficulty of constructing full-scale production equipment and processes concurrent to or even ahead of laboratory development is worth spending a moment to consider. The most amazing aspects of these facilities are the almost total success of untested production equipment and relatively low occurrence of safety incidents.[1]

By March 1943, construction had begun at the Hanford Engineering Works, barely three months after Fermi's reactor came online at Chicago.[1] Initial plans called for the construction of three reactors, to be known as the B, D, and F reactors, located just off the Columbia river north of present-day Richland (Figure **1-1**). The reactors built at Hanford were of a similar graphite-moderated and uranium-fueled design as Fermi's pilot reactor but with four times the fuel capacity and a cooling system fed by liquid water (something no one had done before in a laboratory setting). To run the reactors, it was also necessary to construct the support facilities on site (cooling water treatment, fuel element and waste storage, separations, fuel manufacturing, etc.), as well as create the infrastructure to house the workers, scientists, and technicians who would operate the facility. Fuel manufacturing operations went on-line in December of 1943. The world's first production-scale plutonium production reactor, designated the B reactor, began operating on September 26, 1944 and was soon followed by the startup of D reactor. The original bismuth-phosphate based plutonium separations plant, the T plant, came on-line December 26, 1944. The startup of the T plant necessitated the installation of the first 64 single-shelled waste storage tanks buried underground in the vadose zone (region of the soils between the surface and groundwater table). These tanks were designed to hold either 500,000 or 54,500 gallons of high-level liquid nuclear waste. By late January of

1945, plutonium finishing operations were being performed adjacent to the separations facilities. Three months later, construction of the Hanford Engineer Works was completed, roughly one month before Germany surrendered. The first successful atomic weapon (Trinity) was powered by Hanford plutonium and detonated in New Mexico on July 16, 1945. The secrecy and mission of the Hanford Works culminated in the dropping of the second atomic bomb, a plutonium-based implosion-type weapon known as Fat Man, on Nagasaki, Japan, August 9, 1945. Japan surrendered five days later.

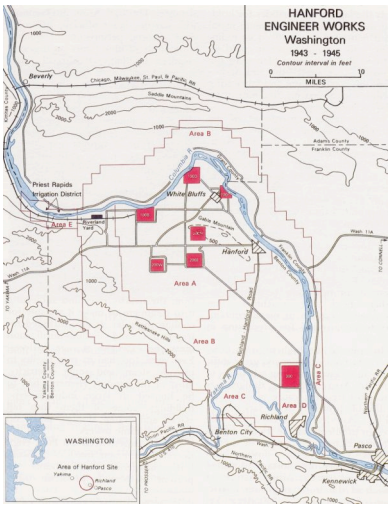

Figure **1-1**: Map of the original Hanford complex near Richland, WA.[14]

1.1.3 Cold War Years and Current Mission

The remaining events at the Hanford site were closely related to the Cold War and spanned the next 40 years, with the final plutonium production reactor shutting down in January of 1987.[1] The Hanford Works went through a number of periods of intense expansion soon after the end of the Manhattan project until the facility slowly ceased

plutonium operations through the 1970s and 80s. At times, the Hanford reactors concentrated on producing radioisotopes other than plutonium-239 for the weapons program, such as tritium used in the more modern hydrogen bomb. By the time plutonium production halted, nine different reactors had operated on the Hanford reservation, producing a yield of 54.5 metric tons of weapons-grade plutonium.[15] In addition, three different separation facilities were utilized during the 40 years of operation. The development of more efficient separations processes necessitated the expansion of the underground storage facilities to 167 waste storage tanks, many of which are single-shelled.[16,17] Despite the huge storage capacity of these tanks, the site operated under a chronic shortage of storage space. Evaporator facilities were eventually built to concentrate the nuclear waste and conserve space in the tanks. The underground tanks and the waste they store are the primary source of the contamination and clean-up problems facing scientists today.

By the 1980's, public perception of nuclear reactors and nuclear waste had deteriorated considerably.[1] Between the intense public pressure and the end of the Cold War, the need and political support for a facility such as Hanford was negligible. Faced with the vast amount of waste stored at the Hanford facility, the mission of the United State Department of Energy (created and accepting responsibility for the site in 1977) turned to one of cleanup and research. Today, the cite houses the Pacific Northwest National Laboratory, where scientists perform environmental and biological research using the latest analytical instrumentation. One reactor continues to operate on the grounds, producing power for the Pacific Northwest rather than plutonium for weapons.

1.2 Plutonium Production and Fission By-products

The reactors at Hanford produced plutonium-239 from uranium-238 via the capture of neutrons generated by the fission of uranium-235.[1] While uranium-235 itself is a suitable fuel for a weapon, two factors make the pursuit of plutonium-239 worthwhile: (a) the separation of uranium-235 from uranium-238 consumes both significant time and significant energy and (b) plutonium-239 is more fissile (under certain conditions) and can therefore produce a more powerful weapon. Uranium-238, by far the most naturally abundant isotope of uranium, is less fissile than uranium-235 or plutonium-239 and unsuitable for use in a weapon. However, the absorption of a neutron by the uranium-238 nucleus produces plutonium-239 through two subsequent decay processes. The fission of U-235 generates a number of dangerous fission by-products that represent the greatest present-day threat to the environment. It is the fission by-products that are the primary contributor to the radioactivity of the Hanford tank waste. The following sub-sections discuss the genesis of plutonium in a nuclear reactor and the chemistry of the most problematic by-products at Hanford today.

1.2.1 Neutron Absorption[18]

The first step in plutonium-239 production is the absorption of a neutron by a uranium-238 nucleus. As stated in the introductory comments to this section, the neutron source is the less abundant but more readily fissile uranium-235. What makes U-235 useful as a fuel in a nuclear reactor is that U-235 is highly efficient at absorbing low-energy neutrons, forming the very short-lived U-236 isotope. The U-236 nucleus is

spontaneously fissile, producing two fission fragments and an on-average yield of 2.5 neutrons per fission event. Some of these neutrons are absorbed by the highly abundant U-238 isotope, forming highly unstable uranium-239 (${}^{239}_{92}U$). This species has a very short half-life of roughly 20 minutes, after which a β-particle (${}^{0}_{-1}e$) is emitted from the nucleus, resulting in the formation of neptunium-239 (${}^{239}_{93}Np$). Note that the emission of a particle increases the atomic number of the nucleus: a side effect of electron ejection from the nucleus is the conversion of a neutron to a proton. Neptunium-239 has a half-life of roughly 2.3 days and decays to plutonium-239 by emitting a β-particle. This isotope of plutonium is highly fissile provided certain conditions are met, but is also very stable compared to the other radio-isotopes in this decay series: plutonium-239 has a half-life of approximately 24,000 years.

Plutonium can undergo further neutron adsorptions to become plutonium-240 or plutonium-241. Plutonium-240 decays into americium (a highly toxic and undesirable isotope) and plutonium-241 is spontaneously fissile. Therefore, the timing of fuel element insertion and removal are critical to maximize production of plutonium-239.

$$
\begin{aligned}
{}^{235}_{92}U + {}^{1}_{0}n &\rightarrow {}^{236}_{92}U \\
{}^{236}_{92}U &\rightarrow X + y\,{}^{1}_{0}n + \gamma \\
{}^{238}_{92}U + {}^{1}_{0}n &\rightarrow {}^{239}_{92}U \\
{}^{239}_{92}U &\rightarrow {}^{239}_{93}Np + {}^{0}_{-1}e + \gamma \\
{}^{239}_{93}Np &\rightarrow {}^{239}_{94}Pu + {}^{0}_{-1}e
\end{aligned}
$$

1.2.2 Fission By-products

During the fission of U-235, a distribution of daughter nuclei is produced (Figure **1-2**). The daughter fragments may be separated into three categories based on their half-lives: short, intermediate, and long-lived isotopes.[1,18,19] The short-lived fission by-products are not a cause of concern today. They have half-lives ranging from seconds or fractions of seconds to a few days or weeks. A majority of the radiation produced by these isotopes was either emitted in the cooling ponds or within a month or so of residence in the storage tanks. The long-lived isotopes are also not a major contributor to the radiation yield of modern waste, based on their low abundance and long half-lives on the order of thousands to billions of years. These isotopes are persistent, but produce little radiation on a day to day basis. The isotopes with intermediate half-lives, on the order of tens of years, are a very different matter. These isotopes do produce radiation on a day-to-day basis and are persistent enough to be a threat for hundreds of years. Two of the isotopes that fall into this category, ^{137}Cs and ^{90}Sr, are generally considered the most dangerous fission products in the tank waste today. They are the radioactive contaminants present in the largest quantities and are responsible for 99% of the radioactivity in the high-level Hanford tank waste.[1,17,20]

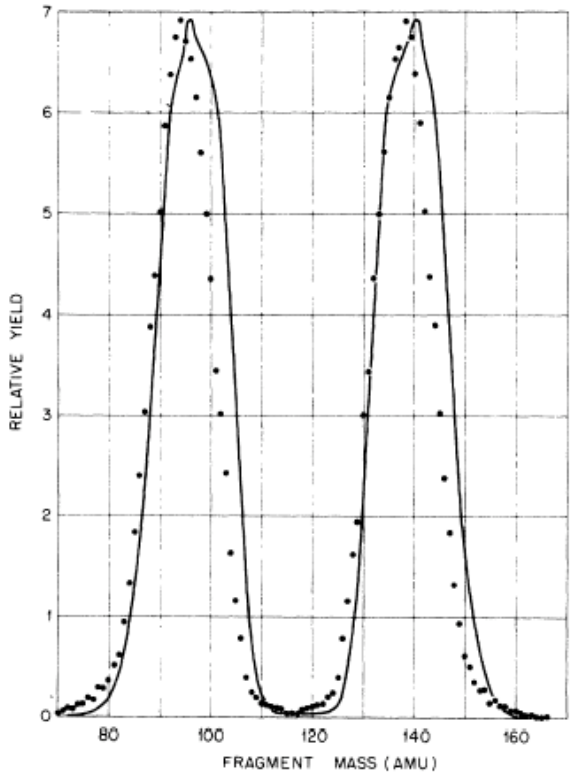

Figure **1-2**: Distribution of daughter nuclei produced during the fission of U-235 induced by thermal neutrons. The dots represent experimental data and the solid lines the theoretical maxima.[21]

Cesium-137 has a half life of 30.1 years and produces β-particle radiation with a yield of 88 Curies per gram (1 Curie = 3.7×10^{10} disintegrations per second).[18] After emitting a β-particle, an unstable barium-137 nucleus is produced with a half life of roughly two days. The unstable barium nucleus emits a gamma ray, transforming it into

$$^{137}_{55}Cs \rightarrow {}^{137}_{56}Ba^{*} + {}^{0}_{-1}e \rightarrow {}^{137}_{56}Ba + \gamma$$

stable Ba-137. Two aspects of Cs-137 make it particularly problematic in Hanford high-level waste. First, one of the probability maxima in the U-235 fission product

distribution under thermal neutron bombardment is at mass number 137. Roughly six out of every hundred fission events produces a Cs-137 fragment, making it the most abundant radioactive isotope in the waste. The second factor that makes Cs-137 harmful is that it has similar chemical properties to potassium, a nutrient required by living creatures.[22] The body will readily absorb Cs-137 into the bloodstream and tends to concentrate it in the muscular system. However, both potassium and cesium are easily excreted from the body, a fact which helps minimize the negative impact of internal exposure to Cs-137.

Strontium-90 has a half-life of 28.6 years and is also a β-emitter with a radiation yield of 136.5 Curies per gram.[18] Strontium-90 decays to Yttrium-90 (half-life of 64.4 hours) which then decays via another β-emission to stable Zirconium-90. Strontium-90

$$^{90}_{38}Sr \rightarrow {}^{90}_{39}Y + {}^{0}_{-1}e \rightarrow {}^{90}_{40}Zr + {}^{0}_{-1}e$$

is also a frequent by-product of the U-235 fission process, particularly in fission processes not induced by thermal neutrons, with roughly five out of every hundred fission events yielding a Sr-90 nucleus. The biological danger posed by Sr-90 is more substantial than that of Cs-137 because strontium is treated by the body as a substitute for calcium.[23-25] Less ingested strontium is absorbed by the body on a per gram basis, but roughly 15% of the strontium that is present in the bloodstream is deposited in bone mass.[23-25] Organisms that incorporate large quantities of radioactive strontium are known to develop bone defects as well as certain forms of cancer.[22,26,27] The remainder of metabolized strontium tends to collect in the kidneys and extra-cellular fluids where it is readily excreted.

1.3 Plutonium Isolation and Purification Chemistry

In order to use the plutonium generated in the reactors for weapons, it is necessary to isolate and purify the appropriate isotope from the spent fuel elements. Plutonium recovery is a complex chemical process involving harsh chemical conditions that produce a significant amount of radioactive liquid waste. Over the life of the Hanford operations, roughly 245,000,000 gallons of high-level liquid waste were generated, primarily originating from the 200 area separations facilities.[1] A discussion of the purification methods and their associated chemistry is therefore necessary to understand the chemical composition of Hanford tank waste.

Three different isolation and purification methods were employed at the Hanford site over its operating lifetime, with each new process providing greater separation efficiency and decreased waste production. The original separation process made use of a series of reversible oxidation-reduction reactions developed by Glenn Seaborg.[9,11,18] By alternating the oxidation state of plutonium between states with markedly different chemical properties, it may be separated from the other fuel element materials. The second process, known as the REDOX process, involved the use of liquid-liquid extraction columns to achieve a more efficient separation. This method, while more efficient, had more demanding space requirements due to the large extraction columns and used a volatile organic solvent. The final process, known as the PUREX process, involved pulsed-columns to achieve an even higher degree of separation in a more compact space and used a safer organic phase. A brief discussion of fuel element

manufacture, dissolution, and the chemistry of each separation process is provided in the following subsections.

1.3.1 Fuel Elements

Plutonium production began with the manufacture of fuel elements.[1] Uranium metal was delivered to the Hanford site in billet form by railcar. The uranium billets measured 4.5 inches in diameter and were 12-20 inches in length – giving each billet a minimum weight of 125 pounds. The first processing step was to extrude the uranium billets into a rod shape, which was then cut into cylindrical segments called cores. Uranium metal was found to be highly reactive with water, forming uranium oxides that would deform the cores. To protect the metal from the cooling water in the reactor process tubes, the uranium cores were cleaned and sealed within an aluminum cladding (in the later years of operation, uranium was canned in zirconium cladding). The aluminum-clad uranium was sealed by welding an aluminum end-cap to the open end of the can, which was then machined and faced. The result of this process was a uranium-containing aluminum cylinder of roughly 8 inches in length and 1.5 inches in diameter (Figure **1-3**). After stringent testing to ensure the quality of the fuel element and its imperviousness to water, approved fuel elements were loaded into the process tubes of a reactor. Spent fuel elements were pushed out the back of the reactor into a large water-filled storage tank to "cool" (allow for the decay of radioisotopes with short half-lives). The cooled elements would then be prepared for shipment by rail car to the separations facilities in the 200 area.

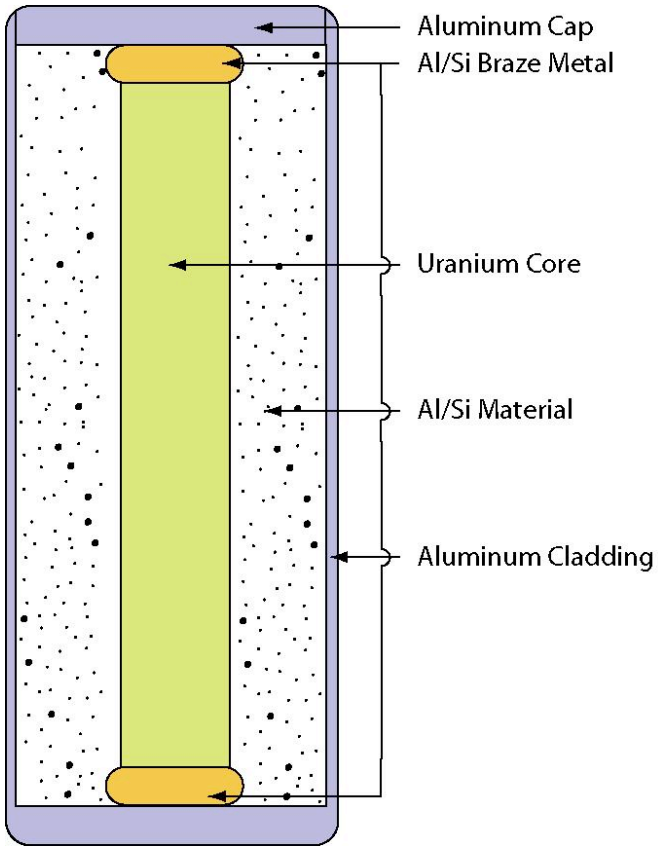

Figure **1-3**: Cross sectional diagram of a finished fuel element (adapted from Marceau).[1]

Before beginning the separations processes, it was necessary to gain access to the plutonium within the core through a series of dissolution processes. First, a highly caustic solution of sodium hydroxide was used to dissolve the aluminum metal casing, since aluminum is soluble in aqueous solutions of pH greater than 9.0. Once the casing was removed, the caustic solution containing the dissolved aluminum was ejected from the dissolver tank directly into waste storage. The uranium metal was un-affected by the NaOH solution and required further washes (usually three) with a solution of nitric acid to dissolve the core. The resulting core-bearing slurry would be passed on to the

chemical separation operations. The same fuel element dissolution procedure was used in the bismuth-phosphate, REDOX, and PUREX processes.

1.3.2 Bismuth-Phosphate Process

The original two separations facilities, the T and B plants, were based on Seaborg's bismuth-phosphate process and operated between 1944 and 1956.[1,9,11,18] In this procedure, selective oxidation/reduction reactions were performed on the plutonium bearing solution, alternating the plutonium valence between a plus six and a plus four state. In the lower oxidation state, plutonium would be carried out of solution by a bismuth phosphate precipitate. When in the higher oxidation state, plutonium would remain in solution and the contaminants would co-precipitate with the bismuth phosphate. A schematic of the bismuth-phosphate batch process is contained in Figure **1-4**.[28]

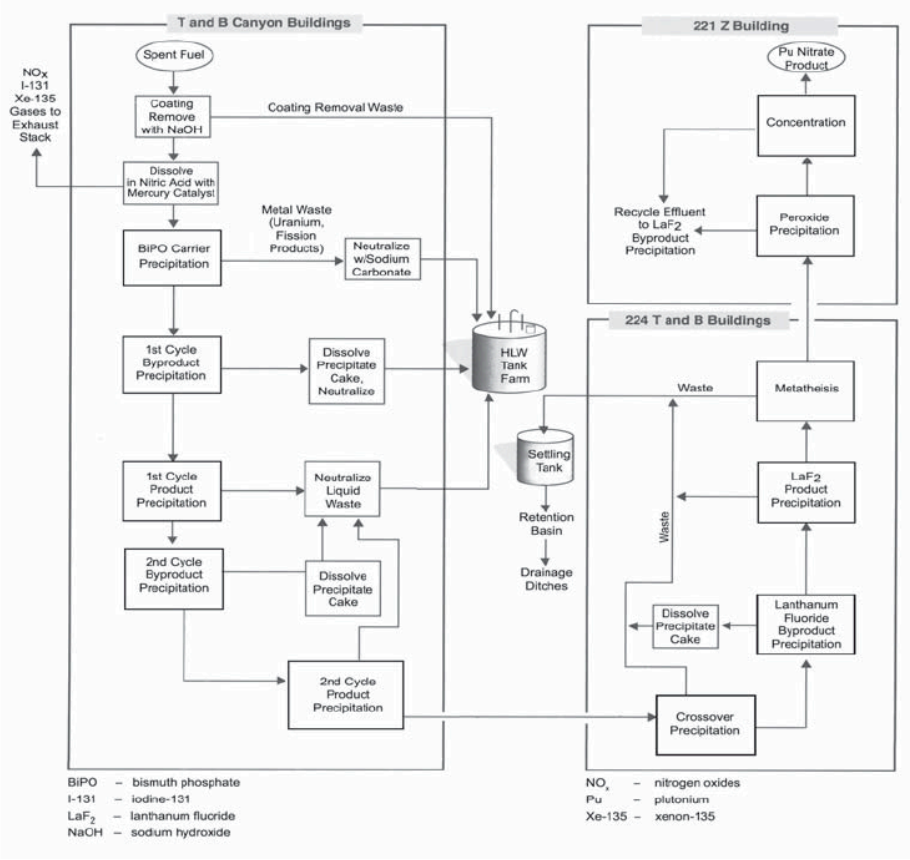

Figure **1-4**: Process flow schematic of the bismuth-phosphate purification procedure.[1]

After ejection from the dissolver, the core solution contained plutonium in a plus-4 valence state. Bismuth nitrate and phosphoric acid were added to this solution, forming a plutonium carrying bismuth phosphate ($Bi(III)PO_4$) precipitate and nitric acid. The resulting slurry was centrifuged to separate the semi-solid precipitate and the liquid was jettisoned to the waste tanks. The plutonium-bearing precipitate was dissolved with nitric acid and passed to the next tank in the separation train. In tank #2, sodium bismuthate ($NaBi(V)O_3$) or potassium permanganate ($KMnO_4$) was added to oxidize the plutonium into the plus-6 valence state ($Pu(VI)O_2^{2+}$). Sodium dichromate ($Na_2Cr_2O_7$) was added to

lock the plutonium in the plus-6 state, causing the subsequent bismuth phosphate carrier to precipitate from solution along with any remaining contaminants. After centrifugation, the plutonium-bearing solution went to a third tank and the contaminant-rich precipitate phase was dissolved with nitric acid, neutralized with sodium hydroxide, and then sent to the waste tanks. In process tank #3, the plutonium was reduced by reacting it with ferrous sulfate ($Fe(II)SO_4$). The addition of bismuth nitrate and phosphoric acid once again caused a plutonium-bearing bismuth phosphate precipitate to form and the oxidation process was repeated in a fourth process tank. These four steps resulted in an overall reduction in gamma activity of 100,000-fold over the original dissolved core solution.[28]

The concentration cycle of the bismuth-phosphate process was a bulk reduction procedure that converted a 330 gallon batch of aqueous plutonium solution into 8 gallons of plutonium nitrate solution. The first step in the concentration cycle was to oxidize the plutonium in solution to the plus-6 state with sodium bismuthate. Phosphoric acid was then added, forming a bismuth phosphate precipitate that was separated from solution by centrifugation, re-dissolved, and discarded. The plutonium solution was locked in the plus-6 state with potassium permanganate and sodium dichromate in a second tank, which then had lanthanum salts and hydrogen fluoride added to the solution. A lanthanum fluoride precipitate formed, carrying away the strontium and lanthanides that bismuth phosphate could not remove from solution. The plutonium-bearing solution was then centrifuged to remove the precipitate and sent to a third processing tank. The lanthanum fluoride precipitate from tank #2 was dissolved with nitric acid, neutralized with sodium hydroxide, and sent to the waste tanks. The plutonium in solution was then

reduced to the plus-4 state in tank #3 by the addition of oxalic acid. Subsequent addition of lanthanum salts and hydrogen fluoride formed a lanthanum fluoride precipitate that carried the plutonium out of solution. After removing the liquid phase, potassium hydroxide was added to the precipitate, inducing a metathesis reaction that converted the lanthanum/plutonium fluoride into plutonium lanthanum oxide. Any remaining liquid was removed by centrifugation after which the plutonium lanthanum oxide was dissolved with nitric acid and sent to the plutonium isolation process.

In the isolation cycle, the plutonium-bearing solution from the concentration cycle was converted into a plutonium nitrate paste suitable for shipping to the Los Alamos weapons production site. Hydrogen peroxide, sulfates, and ammonium nitrate were added to the plutonium nitrate solution, oxidizing the plutonium to the plus-6 state accompanied by the formation of a plutonium peroxide precipitate. After centrifugation, the plutonium peroxide was dissolved in nitric acid and boiled by subjection to hot air until it reached a paste-like consistency. The paste was stored in nearby Gable Mountain until it could be shipped to Los Alamos.

The bismuth-phosphate process was effective, but had a number of drawbacks. An enormous amount of liquid waste was generated in this process as a consequence of the number of separation steps and the batch nature of the procedure. This put strain on the liquid waste storage facilities, prompting expansion of the tank farms and motivating the development of a process that produced less liquid waste. Additionally, batch processes are inherently inefficient, and the bismuth-phosphate process struggled to keep up with the production demands for weapons-grade plutonium. The bismuth-phosphate process had the additional limitation that it could only produce plutonium as a final

product, meaning that valuable uranium was being ejected to the waste storage tanks rather than being recovered for re-use. Because of these limitations, the Hanford Works quickly moved into continuous plutonium extraction methods for plutonium isolation and purification.

1.3.3 REDOX

The REDOX facility was the first of the two continuous purification processes and operated from 1952 to 1967.[1] In a continuous process, a constantly flowing process stream is used rather than a series of batch reactors charged with fresh solutions. There are numerous advantages to using a continuous operation over a batch operation. Continuous processes frequently recycle streams, leading to reduced waste production. REDOX also allowed both plutonium and uranium to be recovered from the dissolved fuel elements, which was not possible in the original batch process. REDOX was based on liquid-liquid extraction columns in which an aqueous phase and an immiscible organic phase are caused to flow in a counter-current direction. Proper design of the extraction columns allows the phases to be well mixed, resulting in an efficient separation of the product into the appropriate process stream.[29] Components of the product-bearing process stream are forced to partition selectively into the aqueous or organic phase depending on their oxidation state in the column. The oxidation state of components can be changed by adding salts to the column, analogous to the oxidation state changes in the bismuth-phosphate process. By repeatedly passing the aqueous and organic streams through extraction columns while selectively varying product partitioning, the desired

material may be separated from the waste stream in a highly efficient manner with less total waste production.

The REDOX process train may be divided into four sections: (i) a pre-cycle, (ii) a partition cycle, then the (iii) uranium and (iv) plutonium recovery cycles. During the pre-cycle, the uranium and plutonium were converted to a plus-6 oxidation state by adding aluminum nitrate nonahydrate to the aqueous stream. This caused the plutonium and uranium to partition into the organic phase (for the REDOX process, hexone (methylisobutylketone) was the organic process stream) while the fission products remained in the aqueous stream and were ejected into waste storage. The Pu/U was then stripped into an aqueous stream in a second column and the hexone was passed to organic phase recovery operations. The aqueous Pu/U stream was concentrated in a separate tank before continuing through the process train.

In the partition cycle, the uranium and plutonium are separated from one another and passed to separate purification cycles. Ferrous sulfamate was added to the aqueous stream, selectively converting the plutonium to a plus-3 oxidation state while leaving the uranium in the plus-6 state. This caused the uranium to partition into the organic phase while the plutonium remained in the aqueous phase. The aqueous plutonium phase was then directed to pre-processing tanks and the plutonium recovery cycle. The uranium was stripped from the hexone into an aqueous stream in a different column, concentrated, and sent to the uranium recovery cycle.

The uranium recovery cycle began by partitioning the uranium selectively into the organic phase, leaving any remaining fission products and plutonium in the aqueous phase. This aqueous phase was ejected to the concentrator tank serving as the input to

the partition cycle rather than being sent to the waste tanks. Returning this stream to the partition cycle increased the yield of plutonium from the REDOX process. The uranium in the organic phase was then stripped into an aqueous phase in a second column, passed to a concentrator, and transferred to the uranium concentration plant.

The plutonium recovery cycle purified the plutonium by removing any remaining fission by-products. Sodium dichromate and nitric acid were added to the aqueous feed stream, selectively converting the plutonium into the plus-6 oxidation state. The hexa-valent plutonium was stripped into the organic phase while the nitrate-bearing aqueous stream containing the remaining fission products was sent to the waste storage facility. The plutonium was reacted with a ferrous reducing agent and then transferred from the organic phase to the aqueous phase in another column before being transferred to the concentration facility. The organic phase was sent to the hexone recovery column and re-used in the process.

The REDOX process also had a number of negative aspects. Hexone is a solvent with a low flash point, making it an explosion hazard that had to be accounted for in the design of the process equipment. Hexone was also difficult to recycle as it is moderately soluble in water and unstable in the presence of nitric acid. The waste streams that are removed from continuous processes may also be problematic as they are significantly more concentrated than the waste streams generated by batch processes. The REDOX process also lacked long-term versatility, as it was only capable of recovering uranium and plutonium. As time progressed, it became desirable to recover other radionuclides from the process streams. The drawbacks of the hexone-based process and drive for the recovery of other isotopes necessitated the design of a third separation process.

1.3.4 PUREX

PUREX proved to be the most efficient operation and was the workhorse process over a majority of Hanford's operating life (1956-1988).[1] The basic process is similar to the REDOX design with a few key changes (Figure **1-5**). The PUREX organic stream was a much more "friendly" solvent, tri-butyl phosphate. Additionally, to further reduce waste production and space requirements, the PUREX facility made use of pulsed extraction columns rather than conventional extraction columns. In a pulsed extraction column, the aqueous and organic streams are forced to flow in one direction and then the other a number of times in the same column.[29] This reduces the size of the column, as the same degree of separation may be achieved in a smaller unit. It also inherently requires less organic and aqueous solvent to operate the smaller pulsed columns. The final difference between REDOX and PUREX was that PUREX was designed to recover additional isotopes. PUREX could generate weapons- and fuel-grade plutonium, depleted and enriched uranium, neptunium, and thorium.[1] In some cases, the isolation and purification of these additional isotopes required the use of ion exchange columns rather than extraction units. In an ion exchange column, a resin extracts a desired ion from the process stream by selectively exchanging the original surface cation with the desired product cation. A wash with a second stream containing a high concentration of the original surface cation removes the desired component from the resin and re-generates the resin sorption capacity. Many of the details of the PUREX process are still protected and the discussion of the operating chemistry will thus be abridged.

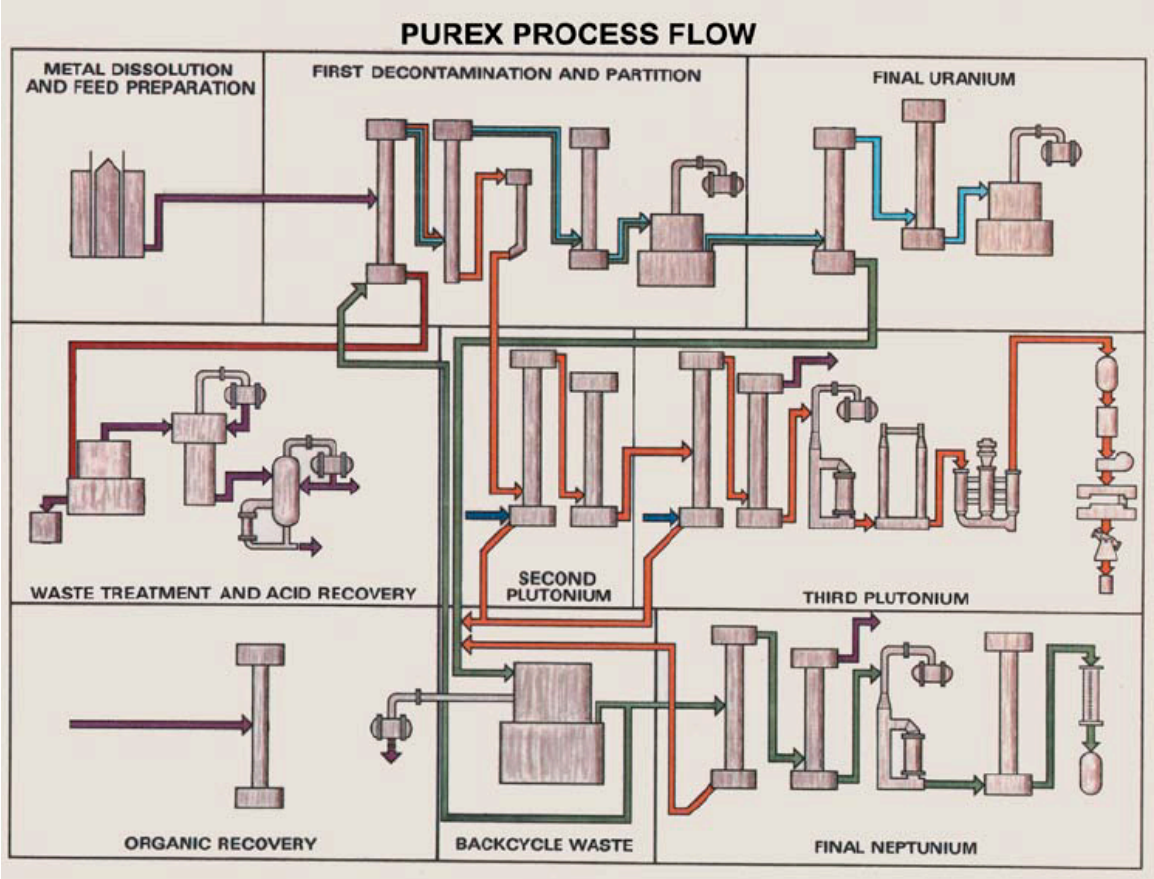

Figure **1-5**: Process flow schematic of the PUREX purification procedure.[1]

The PUREX process may be divided into six separate processing units: (i) the co-decontamination cycle, (ii) the partition cycle, (iii) the uranium cycle, (iv) the plutonium cycle, (v) the neptunium cycle, and (vi) the N cell cycle. During the co-decontamination cycle, the uranium, plutonium, and neptunium were extracted into the organic stream such that 99% of the fission products were contained in the aqueous stream. The partition cycle isolated the plutonium from the uranium and neptunium by stripping the plutonium into the aqueous stream while retaining the uranium and neptunium in the

organic phase. The uranium and neptunium were removed from the organic phase in a subsequent column and passed as the aqueous stream to the uranium cycle unit. In the uranium cycle, any remaining fission products and the neptunium were removed from the uranium stream by extracting the uranium into the organic phase. A second column returned the uranium to the aqueous phase, which was then concentrated and sent to the uranium tri-oxide facility. The plutonium aqueous stream from the partition cycle was further purified by two additional extraction/stripping cycles before undergoing the final processing and concentration steps. The neptunium cycle used many of the waste streams from earlier processes as feeds. Extraction and stripping steps were used to isolate and concentrate the neptunium. Once the neptunium concentration was high enough in the process stream, it was passed through an ion exchange column to isolate the desired neptunium isotope.

1.4 Waste Disposal

The previous two sections presented the mechanisms by which the high-level liquid waste and fission by-products were generated, providing insight into the nature of the dangerous contaminants and chemical composition of typical Hanford tank waste. Other types of radioactive waste were also generated in the course of plutonium production, including solid materials and low-level liquid waste. As nuclear technology was emerging concurrent to the full-scale production operations at Hanford, there was limited knowledge of many dangers associated with handling and disposing of nuclear waste. As new dangers were recognized, changes to waste handling and disposal

procedures were implemented. The problems facing the United States Department of Energy today are closely related to the methods used to dispose of the various waste forms. We will briefly review the disposal methods for each type of waste in this section (the interested reader is again referred to the Hanford Cultural Resources Project work by Marceau *et al* for a more detailed discussion.).[1]

1.4.1 Solid and Low-level Liquid Waste

Low-level waste is considered by the Department of Energy to be any solid or liquid waste contaminated with radioactive isotopes that are not "high-level waste, trans-uranic waste, spent nuclear fuel, or by-product material".[1] This encompasses many different forms, from the reactor cooling water to clothing worn by individuals working closely with radioactive material and even the process equipment itself. Over the lifetime of the Hanford operations, vast quantities of low-level liquid and solid waste were generated that required disposal such that their biological impact would be minimized. This was achieved primarily through dilution or radionuclide sequestration in the natural soils.

The vast majority of the low-level liquid waste was generated in the form of reactor cooling water. The cooling water passed through the same reactor process tubes that contained the fuel elements, meaning that (a) the cooling water was exposed to the high neutron flux levels within the reactor and (b) in the case of a fuel element rupture, the cooling water would carry uranium, plutonium, and fission products out of the reactor. Numerous radioisotopes were incorporated in the cooling water from both

sources and jettisoned into the Columbia at mid-river through underground pipelines. Over the production lifetime of the Hanford reactors, the number of curies released to the Columbia per year ranged between 200,000 in 1944-45 and 2,000,000 in 1960. While these numbers seem staggering, the volume of fresh water flowing through the Columbia each year implies that even these levels of radiation were highly diluted and not a major danger to plant and animal life.

Other low-level liquid waste was created by a variety of processes at each of the major Hanford production areas. The most common solution for disposing of these low-level liquids was to bring them into contact with the native soils. It was hoped that ion exchange processes would sequester harmful cationic species in the soils (see section 1.5.2), thereby preventing their migration into groundwater or the Columbia. The original mechanism to facilitate these interactions involved collecting low-level liquid waste in man-made trenches or open ponds (Figure **1-6**). Open disposal methods had the drawback of providing the local animal populations easy access to the contaminated water. Also, the winds passing over these pools could spread volatile contaminants off-site, leading to the mandate that only low-activity waste be disposed of in exposed pools following 1946. Low-level wastes with higher activities were disposed of through reverse wells, French drains, and cribs. Reverse wells pumped the waste liquids below ground, permitting them to migrate out of the well bore radially into the sub-surface soils. These also received limited use as they placed radionuclides in close proximity to the groundwater plume. French drains are three- to six-foot diameter pipes buried in the ground and filled to a depth of roughly three feet with rock or gravel. The waste entered the drain at the top of the pipe and was forced to percolate through the gravel before

entering the natural soils. Cribs were large chambers located a few feet below the surface that were constructed of loosely interlocked timbers. Larger volumes of low-level waste were disposed of in cribs, where the waste percolated through the piled timbers before coming into contact with the vadose zone minerals. These methods all proved effective at minimizing radionuclide interactions with humans in the case of low-level liquid wastes. All low-level solid wastes were disposed of through burial.

Figure **1-6**: Low-level open waste pool with overflow protection.[1]

1.4.2 High-level Liquid Waste

High-level liquid waste, as defined by the United States Department of Energy, is "Solid and liquid waste from the reprocessing of spent reactor fuel to extract plutonium and containing some elements that decay slowly and remain radioactive for thousands of

years, requiring permanent isolation."[1] All of the liquid waste from the purification and recovery routines is considered high-level liquid waste. Most high-level waste streams were jettisoned through underground transfer lines to the storage tanks and allowed to mix. The chemical makeup of the waste is therefore highly complex and varies from tank to tank. In general, the waste is characterized by a high ionic strength (high sodium and nitrate levels), relatively high levels of soluble aluminum from the dissolved fuel element casings, and a high pH both from the sodium hydroxide used to dissolve the casing and additional sodium hydroxide added to neutralize the nitric acid in acidic waste streams.[17,30,31] Additional variables, such as temperature, exposure to air, radioactive decay, and chemical treatment produced even larger variability between the waste tanks. Despite the variability, the primary sources of radiation in the waste tanks are ^{137}Cs (38% of radioactivity) and ^{90}Sr (60% of radioactivity).[1,18]

In general, a high-level waste storage tank is a large concrete container with either one or two inner carbon steel liner(s) (Figure **1-7**). Numerous monitoring devices are incorporated through access ports at the top of the tanks. Additional monitoring is performed through sampling wells placed around the tanks to detect leaks and monitor radionuclide transport in the event of a leak. The tanks were buried so that the earth surrounding the tanks functions as a barrier to the high levels of radiation emitted by the waste. Two types of high-level liquid waste storage tanks may be found on the Hanford site, the so-called "double shell" and "single shell" varieties alluded to earlier. Double shell tanks have an outer concrete structure that contains two inner steel liners separated by an open space. In the event of a leak in the first liner, the waste is trapped in this space and monitoring stations alert personnel that an inner-shell failure has occurred.

None of the double shell tanks are known to have released material into the environment to date, though these are the youngest of the storage facilities. By far, a majority of the tanks are an older single shell design (149 of 177 total tanks) that contains only one steel liner directly mated to the concrete.[1] When a failure occurs in the liner of a single shelled tank, the waste easily migrates through the porous concrete and into the surrounding vadose zone soils. Unfortunately, many single-shell tank failures are known to have occurred (67 out of the 149 tanks to date), releasing radioactive material into the soils.[17,20,30]

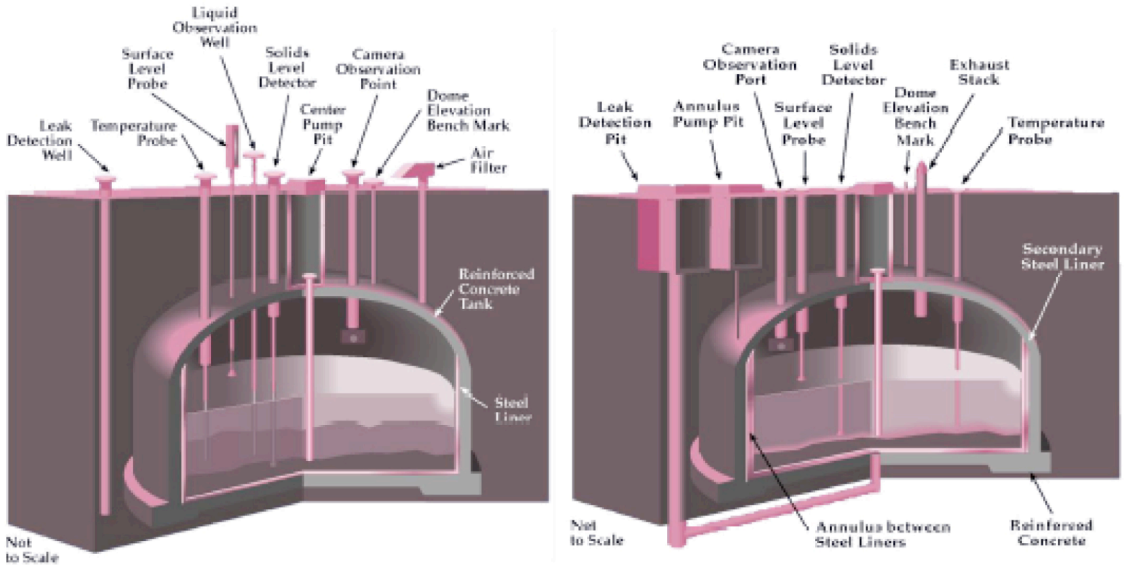

Figure **1-7**: Schematic of the (a) single shell and (b) double shell waste tanks.[1]

The precise mechanisms responsible for tank failures are not well understood. The materials in the tank are exposed to harsh and varying chemical conditions which may wear away at the carbon steel over time. Wide variations in temperature have also

occurred within the tanks: some have reached temperatures of 110°C due to heat released during radioactive decay.[32-34] Changes in temperature and pressure within the tanks stress the walls and potentially contribute to mechanical failure of the liners. Regardless of the mechanism responsible for an integrity breach, the tanks at the Hanford site were designed with a 20-year lifetime, meaning that the oldest tanks are 40 years beyond their original expected life today.[1,28] With the current target date for tank waste cleanup of 2018, it is reasonable to assume that future leak events will occur as these storage tanks continue to age. For this reason, it is important to develop a more complete understanding of radionuclide interactions with the natural soil minerals and how these interactions affect the migration of cesium and strontium in the environment.

1.5 Phyllosilicate Soil Minerals

By the early days of Hanford operations, it was already known that many soil minerals are capable of exchanging their charge-balancing cations with cations in the soil solution. When ion exchange reactions occur, the rate at which exchangeable radiocations travel through the environment is retarded based on the affinity of a mineral for a particular cation. Knowledge of the mineral species present in the Hanford soils and their associated cation exchange properties is therefore a prerequisite to modeling the reactive transport properties of radionuclides. In the Hanford system, accurate modeling is even more complicated because mineral transformation reactions are known to occur when soils are exposed to caustic solutions with high ionic strength (such as the Hanford waste solutions).[17,31] At Hanford, the transformation kinetics as well as the identity of

any precipitated phases must also be known to design effective transport models and/or soil-based remediation methods. In this section, we will examine the structure of layered soil minerals, the ability of these minerals to adsorb and exchange cations, and the most important features of mineral weathering in the vadose zone. Our goals are to (i) introduce the types of cation/mineral interactions and (ii) form a foundation for discussions of strontium binding by minerals in subsequent chapters. Much of the information conveyed in the following section may be found in the text compiled by Dixon and Weed.[35]

1.5.1 Structure and Classification of Phyllosilicates

Layered soil minerals are by definition naturally occurring materials with a definite (but not fixed) composition and a unique atomic arrangement (crystal structure).[35] Layered silicate minerals (phyllosilicates) are a major component of soils and are generally daughter materials produced through the weathering of igneous, sedimentary, or metamorphic rocks. All layered silicates belong to a much larger category of abundant minerals, the silicates, in which the silicate tetrahedron is a key component of the mineral structure. The phyllosilicate family of minerals all possess silicate tetrahedra that share three vertices with other silicate tetrahedra, forming large 2-dimensional sheets of silicate groups (Figure **1-8**).[35] The sheets of tetrahedrally-coordinated silicon atoms are always linked via shared oxygen atoms with a sheet of octahedrally coordinated cationic species, primarily aluminum or magnesium. The covalently bonded tetrahedral and octahedral sheets form what is known as a layer in the

mineral, and these layers stack to produce a three dimensional structure (thus the term layered silicates). Adjacent layers are held together by either electrostatic or hydrogen bonding interactions, but never through covalent bonding. This lack of covalent bonding between layers allows a space to form between adjacent layers known as the interlayer. We will return to the concept of the interlayer in section 1.5.2.

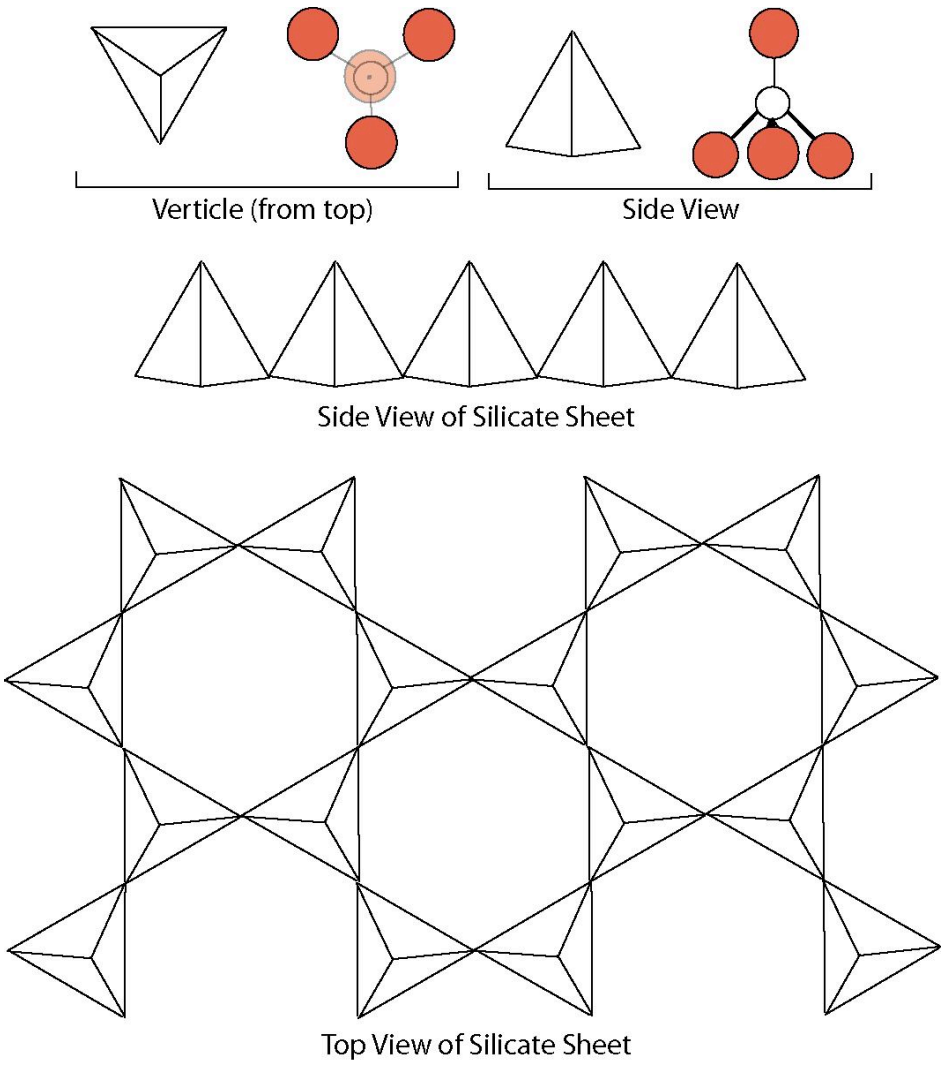

Figure **1-8**: The ideal structure of the silicate sheet.

Phyllosilicate species are readily classified according to a four-step hierarchy. Phyllosilicates are initially divided into two broad categories based on the general structure of each layer. When a layer of the phyllosilicate is made up of a single tetrahedral sheet and a single octahedral sheet, it is known as a 1:1 mineral (Figure **1-9**). In phyllosilicates where the octahedral sheet is bonded to tetrahedral silicate sheets on both surfaces, the minerals are classified as 2:1 phyllosilicates. The next level in the classification hierarchy groups minerals by the permanent degree of charge per *formula unit* (most basic chemical formula describing the overall composition of the mineral). It is possible to form layered phyllosilicates with no permanent charge per formula unit (cpfu) or with a permanent charge imbalance due to isomorphic substitutions within the sheets. For example, aluminum can substitute relatively easily for silicon in the tetrahedral sheet and cations such as iron, magnesium, and aluminum can be incorporated in the octahedral sheet. Phyllosilicates with no charge imbalance are included in the serpentine-kaolin group if they are 1:1 phyllosilicates or the talc-pyrophyllite group if they are 2:1 phyllosilicates. The layers in these balanced structures are held together through hydrogen bonding interactions. When the cpfu ranges between 0.2 and 0.6, the mineral is classified in the smectite group, and when it ranges from 0.6 to 0.9, the minerals are included in the vermiculite group. A cpfu of 1.0 falls in the mica group and minerals with a cpfu of 2.0 are known as brittle micas. Variably charged minerals also exist and are classified as either chlorites or in the sepiolite-palygorskite group depending on the conformation of the sheets (planar or inverted ribbon). The layers of partially charged 2:1 minerals are held together by electrostatic interactions with charge-balancing cations in the interlayer space. The third level of the classification hierarchy divides the

aforementioned groups into categories based on the type of octahedral sheet. When the octahedral sheet is composed of magnesia octahedra, each available cation position in the sheet contains an octahedrally coordinated magnesium atom, and the sheet is known as a tri-octahedral sheet (Figure **1-10**). When the octahedral sheet contains alumina octahedra, one out of every three possible positions for an aluminum atom is vacant, and the sheet is known as a di-octahedral sheet. The final level of classification distinguishes mineral species based on overall composition usually obtained via inductively coupled plasma atomic emission spectroscopy and the atomic arrangement determined from x-ray diffraction analysis.

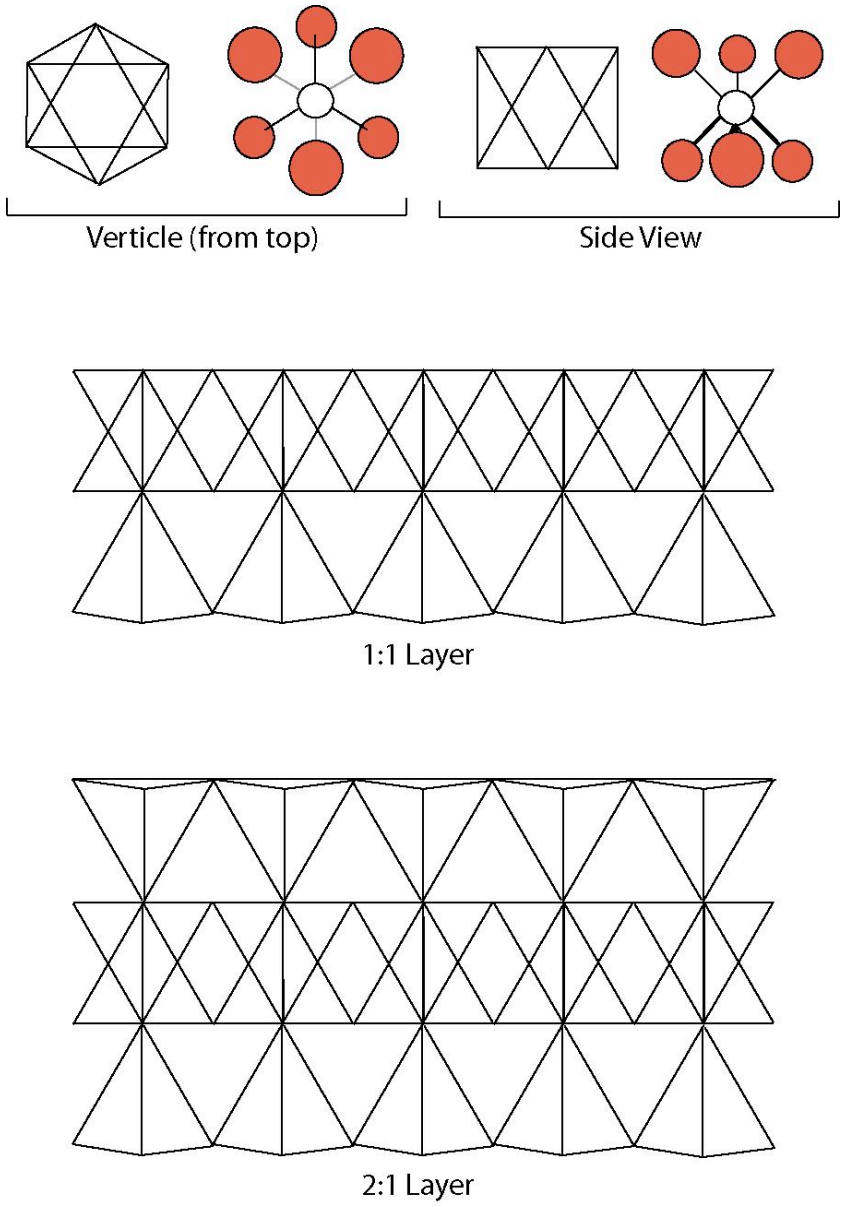

Figure **1-9**: Structures of 1:1 layered and 2:1 layered phyllosilicates.

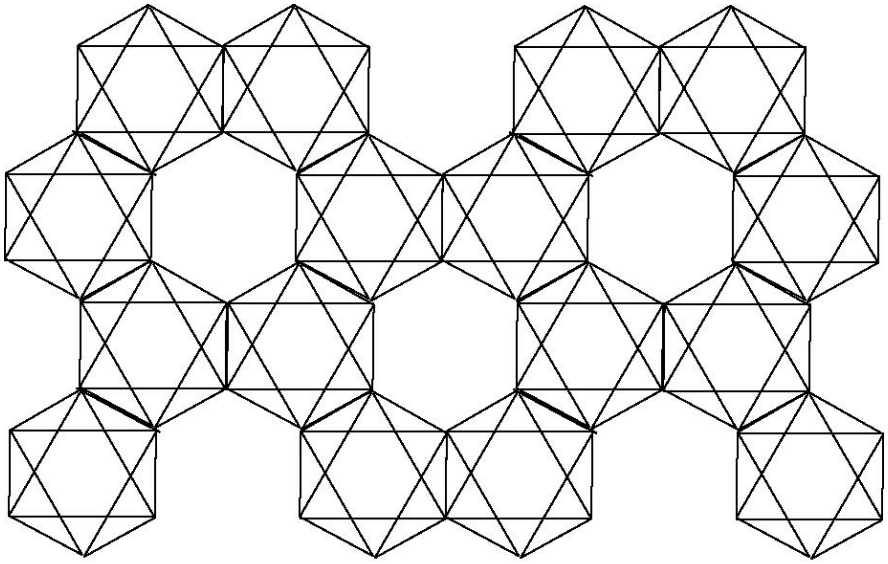

Top View of Di-octahedral Sheet

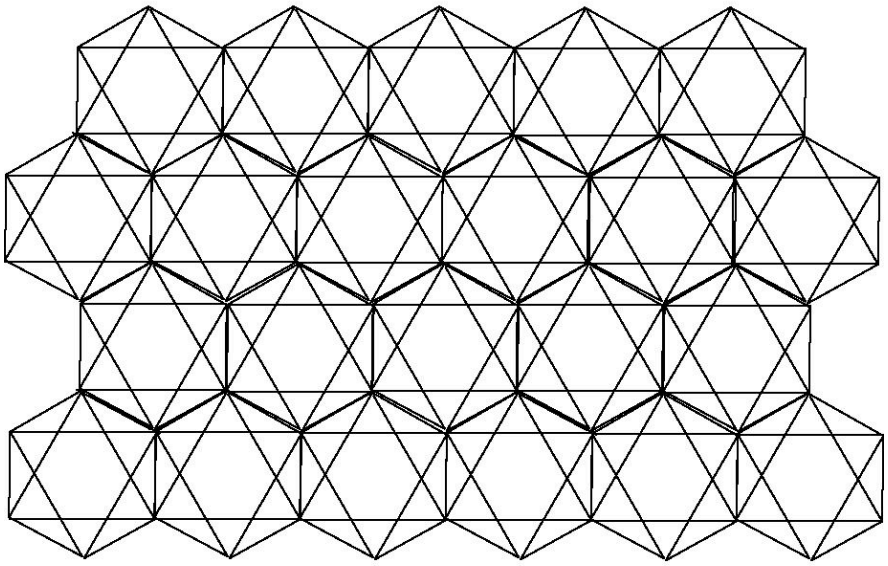

Top View of Tri-octahedral Sheet

Figure **1-10**: The two forms of the octahedral sheet.

1.5.2 Cation Exchange and Selectivity

As discussed briefly in section 1.5.1, when the phyllosilicate layers have a non-zero cpfu, charge-balancing cations stabilize the repulsive forces between layers through electrostatic interactions. These cations typically reside in the interlayer space but can also be found in vacant octahedral positions within dioctahedral sheets or in pockets formed by the oxygens on the interlayer surface (di-trigonal cavities). Charge-balancing cations that coordinate to the interlayer surface do so through one of three sorption mechanisms. In the general case of a dioctahedral mineral, the first sorption mechanism corresponds to a ligand exchange at the interlayer surface where the cationic species displaces a proton from a surface hydroxyl group and forms a direct covalent Si-O-M bond. This is known as chemisorption or inner-sphere complexation. The cation can either be completely dehydrated or retain a partial sphere of coordinating waters in this sorption mechanism. The second general sorption mechanism involves the adsorption of hydrated cations by the mineral surface through hydrogen bonding between the surface and waters coordinating the cation. Because binding in this case occurs through weaker hydrogen bonds, this type of sorption is known as physisorption or outer-sphere complexation. The final type of binding occurs through electrostatic interactions where no covalent bonds are formed between the cation and sorption site.

Charge balancing cations are in many cases exchangeable, with physisorbed species more readily exchanged than chemisorbed or electrostatically-sorbed species. Some charge-balancing cations may be non-exchangeable under typical soil pH and

moisture content; for example, cations that are contained in voids within the layer itself rather than the interlayer space. The ability of a soil mineral to exchange cations is therefore mineral dependent and must be determined experimentally. The cation exchange capacity (CEC) of a mineral is determined by measuring the number of reversibly exchangeable cations during a standardized cation exchange experiment, where the mineral is exposed to a high-ionic strength solution. CECs are usually expressed in units of milli-equivalents (meq) per 100 g of mineral, where one equivalent is defined to be the weight of a particular cation divided by its charge ($\frac{\text{cation weight}}{\text{charge}} = 1 \text{ eq}$). Micas are an example of a layered aluminosilicate with a high CEC (typically 250 meq per 100 g) while kaolinite is an example of a very low CEC aluminosilicate (typical CEC < 4 meq per 100 g). Many factors affect the CEC of phyllosilicates, such as particle size, temperature, interlayer spacing, ability to swell, degree of hydration, identity of the cations, etc.

Implicit in our discussion of CEC is that each mineral species possess an inherent selectivity for certain cations over others. In fact, there are five factors that affect the affinity of a layered mineral for a particular cation. The first is the structural properties of the mineral, which relate directly to the second factor, the size and charge of the cation. A stacking offset can produce steric restrictions, as can the structure of the binding site itself. Within each mineral, there are pH-dependent binding sites at the edges of layers, in frayed edges of weathering minerals, and at the external surfaces. Additionally, there are permanent charge deficiencies that can be de-localized over external surfaces or more commonly in the interlayer space. In some cases, larger

cationic species are favored, such as in minerals with larger interlayer spacings or large charges per formula unit. The degree of hydration of the cation also plays a role, as frayed edge sorption sites generally exhibit preferential sorption of hydrated species.

The location of the charge in the mineral structure is the third important factor. Sorption of small cations into octahedral voids is favored when the charge is located in the octahedral sheets as opposed to a charge imbalance resulting from isomorphic substitution in the tetrahedral sheet. The selectivity of a mineral also can vary with temperature, the fourth factor, since this affects the hydration state of cationic species. The ionic strength and pH of the exchange solution serve as the fifth important factor. A high ionic strength provides a strong driving force for diffusion leading to cation exchange. Also, if the solution pH is acidic, proton sorption may compete with the sorption of cationic species and decrease the observed pickup of the exchange cation.

A quantitative measure of the cation selectivity can be expressed as the Gapon selectivity coefficient (k_G), defined to be:

$$k_G = \left(\frac{\alpha_{B,\mathrm{soln}}}{\alpha_{A,\mathrm{soln}}} \right) \frac{[A_{exch}]}{[B_{exch}]} \tag{1.1}$$

in the case of monovalent cations, where $[A_{exch}]$ and $[B_{exch}]$ are the concentrations of species A and B in the mineral (respectively) and $\alpha_{A,\mathrm{soln}}$ and $\alpha_{B,\mathrm{soln}}$ are the activities of species A and B in solution (in mol/L). If monovalent cations are being exchanged with divalent cations, the form of the Gapon selectivity coefficient is:

$$k_G = \left(\frac{\left(\alpha_{B,\mathrm{soln}}\right)^{1/2}}{\alpha_{A,\mathrm{soln}}} \right) \frac{[A^{+}_{exch}]}{\left[B^{2+}_{exch}\right]}. \tag{1.2}$$

A high value of k_G implies that replacement of cation A in the mineral with cation B from solution is favored.

1.5.3 Mineral Weathering

All soils are exposed to environmental conditions that are conducive to weathering. The process of weathering involves the transformation of one mineral phase into another with a more thermodynamically stable structure. For example, highly charged phyllosilicates, such as micas, generally weather to minerals with lower cpfu, such as vermiculites, in the presence of water and charge-balancing cations that exchange for potassium. Fully weathered soils generally contain highly stable quartz and inorganic metal oxides. Weathering can take place through physical processes, such as mechanical fracture, and/or chemical processes, such as dissolution reactions. Chemical weathering is generally considered to be the more important process.

A number of factors affect the rate of mineral weathering and the extent to which mineral species transform. These factors are attributed to the nature of the mineral, the particle size of the mineral, and the environmental conditions. For example, the chemical nature of the mineral affects the ease with which charge balancing cations can be extracted from the interlayer. Minerals that contain a significant amount of fluorine exhibit a greater cation affinity (in general) than those with no substituent fluorine, meaning that stronger driving forces are necessary to exchange cations in fluorinated minerals. Also, dioctahedral phyllosilicates tend to bind larger cations more strongly than trioctahedral phyllosilicates due to steric hindrances on the position of hydroxyl

protons in the di-trigonal cavity. The type and degree of ionic substitution also has profound effects on the dimensions of the unit cell, distance between layers, and charge density on each layer, all of which are important factors in mineral weathering. The location of interlayer charges and the structural defects produced by stacking sequences, structural distortions, and site vacancies also affect interlayer bond strength and the number of sites susceptible to weathering reactions.

The influence of particle size on weathering rates is quite straightforward: smaller particles offer a greater surface area than large particles and thus weather faster. This is a consequence of the strong dependence of the weathering rate on the diffusion of chemical species to and from the mineral.

Finally, the chemical nature of the soil environment significantly affects the extent of weathering and the weathering rate. The type and activity of ions in the soil solution plays a role. High concentrations of potassium in the soil solution inhibit the release of potassium by micas whereas low potassium and high levels of calcium or sodium promote the release of potassium from micas. When the activity of cations in the soil solution is high, the driving force for diffusion is high, and weathering is more rapid. The pH of the soil solution also affects weathering, as some components of phyllosilicates are soluble only in certain pH regions and because hydrogen can compete for binding sites when the concentration of hydrogen ions is high. The presence of organic material in the soil solution also affects weathering, as cationic species may complex with these materials and become unavailable for cation exchange. The temperature and oxidation-reduction potential of the soil solution also affect dissolution

rates, with higher temperatures generally leading to more rapid weathering. Finally, the quantity of water external and internal to the mineral can influence the reaction rate.

Accompanying the physical and chemical processes discussed above, mechanisms must exist through which the charge on each layer can be decreased for weathering to occur. A basic understanding of potential charge decrease mechanisms for a general phyllosilicate mineral may be achieved by examining the possible mechanisms for charge decrease in micas. The first mechanism involves the oxidation of iron from the ferrous to ferric state, causing an electron to be produced that may (i) induce the removal of an interlayer cation, (ii) release a proton from a hydroxyl group, (iii) eject a cation from an adjacent octahedral sheet, or (iv) eject a hydroxyl group. A second mechanism occurs when a proton is incorporated into the mineral structure without any associated electronic changes. Two theories have been proposed to explain this mechanism; (i) proton sorption at de-protonated hydroxyl sites in structurally deficient micas and (ii) proton attachment to apical oxygens. The apical oxygens are the oxygen atoms on the tetrahedral sheet that are shared with the octahedral sheet within a layer. The second mechanism would require the proton to access and then break the bond between sheets, making this theory the less likely explanation for proton-induced charge reduction. Finally, silicon can substitute for tetrahedrally coordinated aluminum and iron under basic conditions, reducing the charge on the layer.

1.5.4 Weathering in the Hanford Vadose Zone

The waste tanks at Hanford are buried in the vadose zone sediments of the 200 East and West areas. The Hanford vadose zone may be divided into three unique sedimentary layers.[36-38] The surface layer contains coarse sand and gravel composed of quartz, potassium-feldspars, plagioclase, and mica with a clay fraction that contains vermiculite, smectite, illite, and chlorite. The next layer is composed of medium and fine-grained sand with the same mineralogy. These two layers compose 85% of the vadose zone and range from 26 - 35 m total depth from the surface. The remaining 15% of the vadose zone is the Ringold Silt formation, consisting of fine sand and silt composed of quartz, K-feldspar, plagioclase, and mica.

The composition of the vadose zone is therefore quite complex, and as such, the weathering of model 1:1 and 2:1 phyllosilicates has been used to estimate the weathering behavior of Hanford sediments. Researchers have explored the weathering of phyllosilicate minerals under low ionic strength and highly alkaline conditions without free aluminum.[39-44] In almost all cases, the transformation of high-charge minerals to lower-charge minerals was observed, accompanied by dissolution and precipitation of fully-tetrahedral secondary phases (zeolites and feldspathoids). Bauer and Velde, Komarneni and White, and Bauer *et al*. also examined the weathering of clay minerals as a function of temperature and found that the weathering rate is reduced at lower temperatures.[39,42,44] In only a few cases have layered aluminosilicate minerals been exposed to alkaline conditions with a composition that mimics the waste solutions at Hanford.[31,45,46] In these cases, dissolution of the parent minerals was found to

accompany the formation of feldspathoid and zeolitic materials over time with rates that were dependent on the initial concentrations of Cs^{+} and Sr^{2+} in the reaction mixture. Additionally, these experiments showed that both strontium and cesium were taken up by the complex mixture of parent clays and neo-formed tetrahedral minerals. It is therefore necessary to learn about cesium/strontium interactions with both phyllosilicate and tectosilicate minerals if accurate reactive transport models and appropriate waste remediation methods are to be synthesized. When it comes to performing such analyses on the molecular level, the primary analytical tools include extended x-ray absorption fine structure (EXAFS) and solid-state nuclear magnetic resonance (NMR). Unfortunately, it is difficult to apply both of these techniques to strontium nuclei bound in minerals; strontium binding in these materials make up one current research frontier in the field of EXAFS. The aim of this dissertation research is to examine strontium/mineral interactions in these systems with solid-state nuclear magnetic resonance spectroscopy.

Chapter 2

Solid-State Nuclear Magnetic Resonance

Solid-state nuclear magnetic resonance (NMR) is a powerful and continually evolving technique used to probe the structure of complex materials on the molecular level. Parameters extracted from NMR spectra provide information about the local electromagnetic environment of a nucleus, which is dependent on the coordination number, bond lengths and angles, and the identity of neighboring atoms. NMR studies frequently complement synchrotron X-ray techniques, such as extended X-ray absorption fine structure (EXAFS) analyses. While the information provided by EXAFS and NMR is similar, NMR provides two primary advantages: (i) it can distinguish between nuclei in multiple unique chemical environments in a model free manner and (ii) it may be applied to homo- or hetero-geneous crystalline and amorphous materials. Therefore, solid-state NMR presents a unique opportunity to learn about the binding environment(s) of strontium in complex Hanford-relevant mineral systems.

Extracting the relevant NMR parameters from experimental spectra requires either (a) iterative fitting of theoretical line shapes to the data or (b) true simulation of an NMR experiment under the influence of the valid NMR interactions. The first option offers the advantage of simplicity, but generally cannot account for such factors as pulse power effects, pulse imperfections, or the contributions of multiple interactions on a complicated line shape. The second option is more computationally intensive, but allows the user to account for many of these limitations and improve the accuracy of the results.

In the subsequent chapters, strontium NMR parameters will be extracted from calculations performed with SIMPSON, a true solid-state NMR simulation package developed by Bak and Nielsen[47]. SIMPSON calculates an NMR spectrum by evolving the state of a specified spin system through time under the influence of the interaction Hamiltonians and pulse sequence dictated in the input file. To understand how the simulation calculations proceed and how the NMR parameters relate to the interaction Hamiltonians and the local structure, it is necessary to discuss the theoretical basis of NMR. The goal of the first two sections of this chapter is to present a brief framework regarding the fundamentals of solid-state NMR that are relevant to SIMPSON and the interpretation of spectral data (a more practical discussion of SIMPSON as well as a number of sample input files may be found in Appendix A). The final section of this chapter will describe the operation of an NMR spectrometer and discuss the utility of the NMR experiments applied in chapters 3 – 6.

2.1 Fundamentals of Modern Fourier Transform Solid-State NMR

Most discussions of NMR begin with a classical mechanical description of the NMR experiment, which adequately describes the most basic NMR experiments, but fails when applied to multiple-pulse and more complicated situations. NMR is a quantum-mechanical phenomenon and has no complete and readily visualized classical analogue. In fact, various aspects of NMR are usually explained in classical, thermodynamic, or quantum/statistical mechanical terms depending on the complexity of the feature under discussion. This presentation will forgo the classical approach and present nuclear

magnetic resonance in terms of only quantum/statistical mechanics and a few points regarding thermodynamics. Most of the information in this section was compiled from a few key sources, especially the texts written by Slichter[48]; Ernst, Bodenhausen, and Wokaun[49]; Mehring[50]; Mehring and Weberuss[51]; and Levitt.[52] Excellent discussions of NMR from the classical perspective may be found in many books such as those of Levitt or Slichter.[48,52]

2.1.1 Spin Angular Momentum

An atomic nucleus is composed of protons and neutrons, particles with nearly identical mass but different charges. To a rough approximation, the total mass of the nucleus is equal to the sum of the masses of the protons and neutrons and the total charge is the sum of their charges. The additive nature and existence of properties such as mass and charge are intuitive since these properties can be observed in the macroscopic world. There are other intrinsic properties of particles such as magnetism and spin angular momentum that are less intuitive. For example, unlike macroscopic angular momentum, the spin angular momentum of a fundamental particle does not vary…the spin angular momentum of an electron or quark is the same at absolute zero and infinite temperature.[52] Spin angular momentum is not directly additive like mass or charge and there are no simple rules for predicting the spin angular momentum of a nucleus. Despite the difficulty in predicting net nuclear spin, it has been shown that most of the nuclei in the periodic table possess a net spin angular momentum. This property is characterized by

the quantum number I, which may be a half-integer or integer ranging from $I = 0$ (no net spin, e.g. ^{12}C) up to $I = 7$ (e.g., ^{176}Lu).

When a nucleus has a net spin angular momentum, it also has a net magnetic moment, $\vec{\mu}$. The nuclear spin angular momentum is related to the magnetic moment of the nucleus through the following equation:

$$\vec{\mu} = \gamma \hbar \vec{I} \tag{2.1}$$

where γ is a scalar quantity known as the gyromagnetic ratio (also an intrinsic property of a nucleus) and $\vec{I}$ is the spin angular momentum.[48] It is important to note that the net magnetic moment and net spin angular momentum of a nucleus are tensors. In equation 2.1, they are viewed as vectors (tensors of rank one), meaning that they have both a magnitude and a direction. There is no particular directional preference in real space for either of these vector quantities, implying that it is not possible to predict the orientation of the net magnetic moment of an isolated nuclear spin.

2.1.2 Ensemble of Spins in a Magnetic Field[48]

In practice, one rarely studies a single isolated spin. A real sample is composed of an ensemble of many nuclear spins, the magnetic moments of which are randomly oriented and of equal spin energy in the absence of a magnetic field. When the ensemble of spins is placed within a magnetic field, the directionality of the field causes an energy splitting that is directly related to the spatial orientation of the nuclear magnetic moments: it now requires less energy to orient a magnetic moment with the magnetic

field than it does to have a magnetic moment oriented against the field. We can describe this energy splitting using quantum mechanics. From the time-dependent Schroedinger equation (equation 2.2), we know that each state of a system is described by a ket, $|\Psi\rangle$, and that to find the energy of an isolated spin in state $|\Psi\rangle$ due to an arbitrary interaction *a* requires the Hamiltonian operator for that interaction, $\widehat{H_a}$ (operators will be denoted in this dissertation with a hat):

$$\frac{d}{dt}|\Psi(t)\rangle = -\frac{i}{\hbar}\widehat{H}_a|\Psi(t)\rangle \tag{2.2}$$

The interaction Hamiltonian that describes the response of the spins to the external (static) magnetic field is called the Zeeman Hamiltonian.[52] If we define the positive *z* direction of a *laboratory axis system* to coincide with the direction of the applied magnetic field $\vec{B}$, the form of the Zeeman Hamiltonian is:

$$\widehat{H_z} = -\vec{\mu}\bullet\vec{B} = -\gamma\hbar B_0\widehat{I_z} \tag{2.3}$$

where $\widehat{I_z}$ is a spin angular momentum operator, B_0 is the strength of the applied magnetic field, and $\hbar$ is Plank's constant divided by 2π (note that the Zeeman Hamiltonian is independent of time). Alternatively, the quantity γB_0 may be replaced with a single frequency term, ν_0, known as the Larmor frequency. The importance of this substitution will be apparent shortly. As we know from quantum mechanics, the allowed energy values of the system correspond to the eigenvalues of the Hamiltonian operator, and in this case they are just multiples of the eigenvalues of $\widehat{I_z}$:

$$E = -\gamma\hbar B_0 m \tag{2.4}$$

where m is an index that can range from I to $-I$ in steps of 1. The net effect of the Zeeman interaction is that the energetic degeneracy of the nuclear spin states is split into $2I + 1$ equally-spaced discrete energy levels due to the presence of a static magnetic field (Figure 2-1). The spacing between adjacent energy levels is uniform under the influence of the Zeeman Hamiltonian and equal to $|-\gamma\hbar B_0|$.

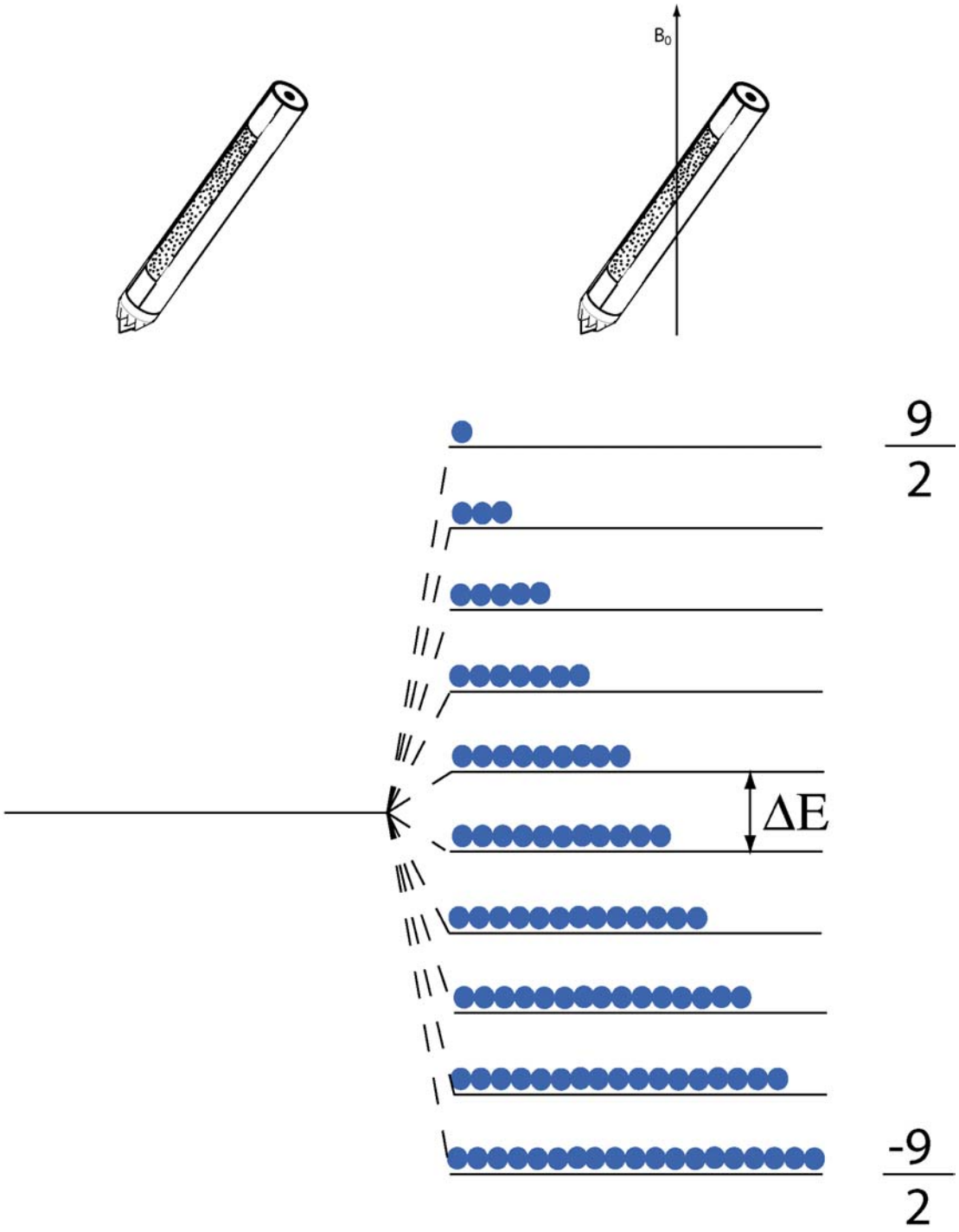

Figure **2-1**: The degeneracy of the nuclear spin substates in the absence of a magnetic field (left) is lost upon application of a magnetic field (right), as described by the Zeeman interaction.

It is important to note that placing the spin ensemble within a magnetic field does not force the nuclei into one of these discrete energy levels. In fact, well known theoretical and experimental studies by Stern and Gerlach in the 1920s have shown that it is impossible to predict the orientation of the magnetic moment of an isolated nuclear spin in the ensemble.[52] As in the field-free situation, the magnetic moment of each individual nucleus is constantly changing orientation due to thermal motion. When placed within a magnetic field, this implies that an isolated nucleus is constantly changing its energetic state as well and is not restricted to the energy levels created by the Zeeman Hamiltonian. It is the act of making a measurement that forces the nuclei in the spin ensemble into one of the quantized energy states. It is impossible to predict with absolute certainty the number of nuclei present in each energy level at an arbitrary point in time. We may only calculate a statistical probability of finding a spin from the ensemble in a particular energy state following a measurement. However, it can be shown that in the presence of a magnetic field after some time *t*, there is a slightly higher statistical probability of finding a spin in a low-energy state than a high-energy state following a measurement. This small population difference in the bulk spin system is what gives rise to the observable NMR signal.

A second phenomenon occurs when the ensemble of spins is placed in a magnetic field. If we return to the Schroedinger equation, we can examine the time-dependent behavior of the spin ensemble under the influence of only the Zeeman Hamiltonian. If we do so, we find that the Schroedinger equation takes the form of a simple first order differential equation that has solutions of the type:

$$\left|\Psi(t_2)\right\rangle = \exp\left(-i\hbar\gamma B_0(t_2 - t_1)\hat{I}_z\right)\left|\Psi(t_1)\right\rangle = \exp\left(-i\hbar\omega_0\tau\hat{I}_z\right)\left|\Psi(t_1)\right\rangle \qquad (2.5)$$

where τ is defined to be the time interval $t_2 - t_1$.[48] An exponential function of the type found on the right hand side of this equation is known as a *time evolution operator*. This particular time evolution operator has a similar form to a *rotation operator*, which is used to move objects in space (we will discuss rotation operators in more detail in a later section). If we examine the form of equation 2.5 that contains the Larmor frequency ω_0, the time evolution operator $\exp(-i\hbar\omega_0\tau\hat{I}_z)$ describes the rotation of a spin about the magnetic field (z axis) at a rate ω_0. The rotation of the magnetic moments about the applied magnetic field is known as *precession* and every spin whose magnetic moment is not aligned exactly with the laboratory z axis will precess about the field at the Larmor frequency. We also see that the rate of precession is unique for each NMR-active nucleus in the periodic table: the Larmor frequency is a function of the gyromagnetic ratio, which we know to be an intrinsic property of a nucleus.

2.1.3 Describing the Spin System – The Density Matrix[48,49]

In order to adequately describe an NMR experiment, it is convenient to define a quantum/statistical mechanical representation for the states of the entire spin ensemble in tensor form. This tensor representation is known as the density matrix (or the density operator). The mathematical definition of the density operator results from expanding the state $\left|\Psi\right\rangle$ from the Schroedinger equation in an orthonormal basis set $\left|i\right\rangle$:

$$\left|\Psi(t)\right\rangle = \sum_{i=1}^{n} c_i(t)\left|i\right\rangle \tag{2.6}$$

where the time dependence is contained in the coefficients of the basis vectors c_i and the basis space has dimensionality n.[49] An isolated spin in the ensemble may be found in any number of $2I + 1$ spin states following a measurement and therefore $\left|\Psi\right\rangle$ represents a mixed state. As mentioned earlier, it is not possible to predict the number of spins in each energy level with certainty in this mixed state. However, we can identify the probability p^k of finding a spin in the state $\left|\Psi^k\right\rangle$ following a measurement. The density operator $\hat{\rho}(t)$ is then defined as follows and corresponds to an ensemble average representation of the state of the system:

$$\hat{\rho}(t) = \sum_k p^k \left|\Psi^k(t)\right\rangle\left\langle\Psi^k(t)\right| \tag{2.7}$$

$$\hat{\rho}(t) = \sum_k p^k \sum_i \sum_j c_k^i(t) c_k^j(t)\left|i\right\rangle\left\langle j\right| = \sum_i \sum_j \overline{c_i(t) c_j^*(t)}\left|i\right\rangle\left\langle j\right| \tag{2.8}$$

where the sum of p^k is one and the bar over the coefficients indicates that it is an ensemble average.[49] The matrix elements of the density operator representing a mixed state can be expressed as:

$$\left\langle i\right|\hat{\rho}(t)\left|j\right\rangle = \sum_k p^k c_i^k(t) c_j^{k*}(t) = \overline{c_i(t) c_j^*(t)} \tag{2.9}$$

meaning that the matrix elements are ensemble averages of the products of the expansion coefficients appearing in equation 2.6.

The density operator is a Hermitian operator, implying that the eigenvalues of the density operator are real and that the eigenstates of the density operator are orthogonal to one another (and normalizable). These properties hold true for any Hermitian operator

and, in fact, all of the operators we are interested in for NMR will be Hermitian. Mathematically speaking, an operator is Hermitian if the operator and its complex conjugate transpose are equal. In Dirac notation, this property makes the following equation valid if $\widehat{Op}$ is Hermitian:

$$\langle i|\widehat{Op}|j\rangle = \langle j|\widehat{Op}|i\rangle^{*}. \tag{2.10}$$

One other useful property of the density matrix is that the diagonal matrix elements ρ_{ii} represent the fractional probability of finding a spin in the state $|i\rangle$. Thus, if the diagonal matrix elements are added together, they equal one (this operation is termed taking the trace of the matrix). The off-diagonal elements of the density matrix represent coherent superpositions of state (generally known as coherences in the NMR community) that represent detectable transverse components of magnetization.

The observable due to a generic Hamiltonian $\left[\widehat{H}\right]$ acting on the spin system can be calculated by taking the trace of the product of the Hamiltonian operator and the density matrix:

$$\left[\widehat{H}\right] = Tr\left(\widehat{H}\widehat{\rho}(t)\right). \tag{2.11}$$

Equation 2.11 contains a subtle point about the Hamiltonian operators we will use frequently in this chapter. We already know that the density operator is a tensor. To make the evaluation of equation 2.11 straightforward, it would be best to express the Hamiltonian in tensor form as well. Conveniently, the Hamiltonian operators applicable to solid-state NMR can all be written in tensor form. We will return to this idea in section 2.2.

In the case of NMR, the internal Hamiltonians of interest only affect the nuclear spins and perhaps some electronic spins. Therefore, it is more convenient to work with a reduced form of the density matrix when calculating NMR spectra. The reduced form can be derived by breaking the basis states $|i\rangle$ into a product of two components; one dealing with the relevant spin components ($|s\rangle$) and the other involving all other aspects of the system ($|l\rangle$). It is common to refer to the non-spin related components $|l\rangle$ of the density matrix as the *lattice* components. A Hamiltonian operator that acts only on the ensemble of spins will be diagonal with respect to the lattice components and allows us to define the reduced density matrix $\hat{\sigma}(t)$:

$$\langle s'|\hat{\sigma}(t)|s\rangle = \sum_{l} \langle s'l|\hat{\rho}(t)|ls\rangle .^{49} \tag{2.12}$$

In the reduced density matrix, the effects of the Zeeman Hamiltonian have been lumped into the $|l\rangle$ states. This is because the Zeeman Hamiltonian is a constant multiplied by a diagonal matrix and has a much greater magnitude than the internal interactions of an NMR experiment (in general).[49] While the Zeeman interaction will not explicitly be expressed in the reduced density matrix, it is involved in the dissipation of energy from the ensemble of spins. The expectation value (denoted by triangular brackets) of a spin Hamiltonian $\widehat{H_S}$ can be found simply by taking the trace of the product of the Hamiltonian and the reduced form of the density matrix:

$$\left\langle \widehat{H_S} \right\rangle = Tr\left(\widehat{H_S}\hat{\sigma}(t) \right). \tag{2.13}$$

SIMPSON uses the reduced density operator in NMR calculations.

2.1.4 Evolving the Spin System in Time

Now that we have a complete description of the spin ensemble in the density operator, it is necessary to discuss how to describe the behavior of the system through time. The Schroedinger equation will not be useful, since it describes the evolution of only a particular state through time. However, through some manipulation of the Schroedinger equation, we arrive at a master equation for the time evolution of the mixed state system described by the density matrix[51]:

$$\frac{d}{dt}\hat{\rho}(t) = -\frac{i}{\hbar}\left[\hat{H}(t), \hat{\rho}(t)\right]. \tag{2.14}$$

This equation is the Liouville-von Neumann equation. The derivation of the Liouville-von Neumann equation and its solutions may be found in numerous texts such as Ernst and Slichter.[48,49] The formal solution to this equation for the density operator takes the form of a unitary transformation:

$$\hat{\rho}(t) = \hat{U}(t)\hat{\rho}(0)\hat{U}(t)^{\dagger} \tag{2.15}$$

where $\hat{\rho}(0)$ is the density matrix prior to the time interval *t* and $\hat{U}(t)$ is called a time-evolution operator. The formal definition of the time-evolution operator is:

$$\hat{U}(t) = \exp\left(-i\int_0^t \hat{H}(t')dt'\right). \tag{2.16}$$

The true usefulness of this expression is found when an appropriate set of assumptions is made so that the Hamiltonian is made to be time independent over discrete time intervals (see section 2.1.6). When the Hamiltonians are time-independent, the density operator can be propagated through time by applying a series of transformations of the type described in 2.15 with:

$$\hat{U}(t) = \exp(-i\hat{H}t)\,. \tag{2.17}$$

Note the similarity of the time-evolution operator in equation 2.17 to the rotation operator described in section 2.1.2. Indeed, applying the time evolution operator is equivalent to moving an object or operator through time.

While the previous exercise was performed with the full density matrix rather than the reduced form, a similar result is obtained for the reduced density matrix. Remember that in the reduced form, the components related to the ensemble of nuclear spins were separated from the other quantum mechanical aspects of the full density matrix. Because of this distinction, the form of the Liouville-von Neumann equation is slightly different for the evolution of the reduced density matrix:

$$\frac{d}{dt}\hat{\sigma}(t) = -\frac{i}{\hbar}\left[\widehat{H_S}, \hat{\sigma}(t)\right] - \hat{\hat{\Gamma}}\left(\hat{\sigma}(t) - \widehat{\sigma_0}\right) \tag{2.18}$$

where $\hat{\hat{\Gamma}}$ is known as the relaxation superoperator and σ_0 is the equilibrium reduced density matrix. The relaxation superoperator contains terms representing the interactions between the spin ensemble and the lattice components (including the Zeeman interaction). These interactions provide a mechanism for the ensemble of spins to dissipate energy and return to thermal equilibrium after it has been perturbed. Relaxation back to equilibrium is a major factor driving the decay of the oscillatory NMR signal over time. Equation 2.18 is the master equation SIMPSON uses to evolve the density matrix through time; however, the relaxation component of equation 2.18 is not explicitly calculated in a SIMPSON simulation.

2.1.5 Rotations

Operators that contain exponential functions are clearly important to a thorough description of NMR. The precessional behavior of spins in the presence of a magnetic field is described by a complex exponential function. The evolution of the density matrix through time requires the use of complex exponential functions that incorporate interaction Hamiltonians. Though not discussed in detail, the decay of the NMR signal and the return of z magnetization to thermal equilibrium may also be described with exponential functions. The first two examples fall into the general category of rotation operations, or rotations. Rotation operators are always complex exponential functions. They are also both linear and unitary in nature. In general, rotation operations do not commute, meaning that the order in which they are applied is important. This section is devoted to a brief discussion of the types of rotations used in NMR in more detail.

2.1.5.1 Rotations of Spatial Components[48,50,51]

As stated, both the density matrix and interaction Hamiltonians may be written in tensor form. The tensor form of the interaction Hamiltonians can be further separated into two components, one containing information about the spins (T_{kq}) and the other relating to elements of the spatial (or coupling) tensor (A_{kq}). It is convenient to express the NMR interactions in tensor form since that makes them (i) amenable to rotation with the methods we will discuss and (ii) puts them in a convenient form for evolving the density operator through time. Rotations of the spatial tensor component are used to transform between relevant reference frames during the calculation of NMR spectra.

Spatial rotations are also used to understand the effects of mechanical re-orientation of samples. We will look at two methods of rotating objects in space, Euler rotations and Wigner rotations.

Formally, a rotation is defined as a one-to-one transformation of three dimensional space that conserves a point in space, the angles and distances, and the left or right handedness of the reference frame.[53] Full transformation of a three dimensional axis system in space requires the axis system be rotated through three angles (α, β, γ) called Euler angles (Figure **2-2**). The most straightforward way to accomplish such a rotation is to use Euler's rotation rules. In an Euler rotation, the first step is to rotate about the *z* axis by an angle α, followed by a rotation about the new *y* axis (*y*' axis) by the angle β, followed by a rotation about the new *z* axis (*z*' axis) by the angle γ. Mathematically, the rotation of a generic tensor $\widehat{Op}$ through space to produce $\widehat{Op}'$ via this sequence of operations is expressed as:

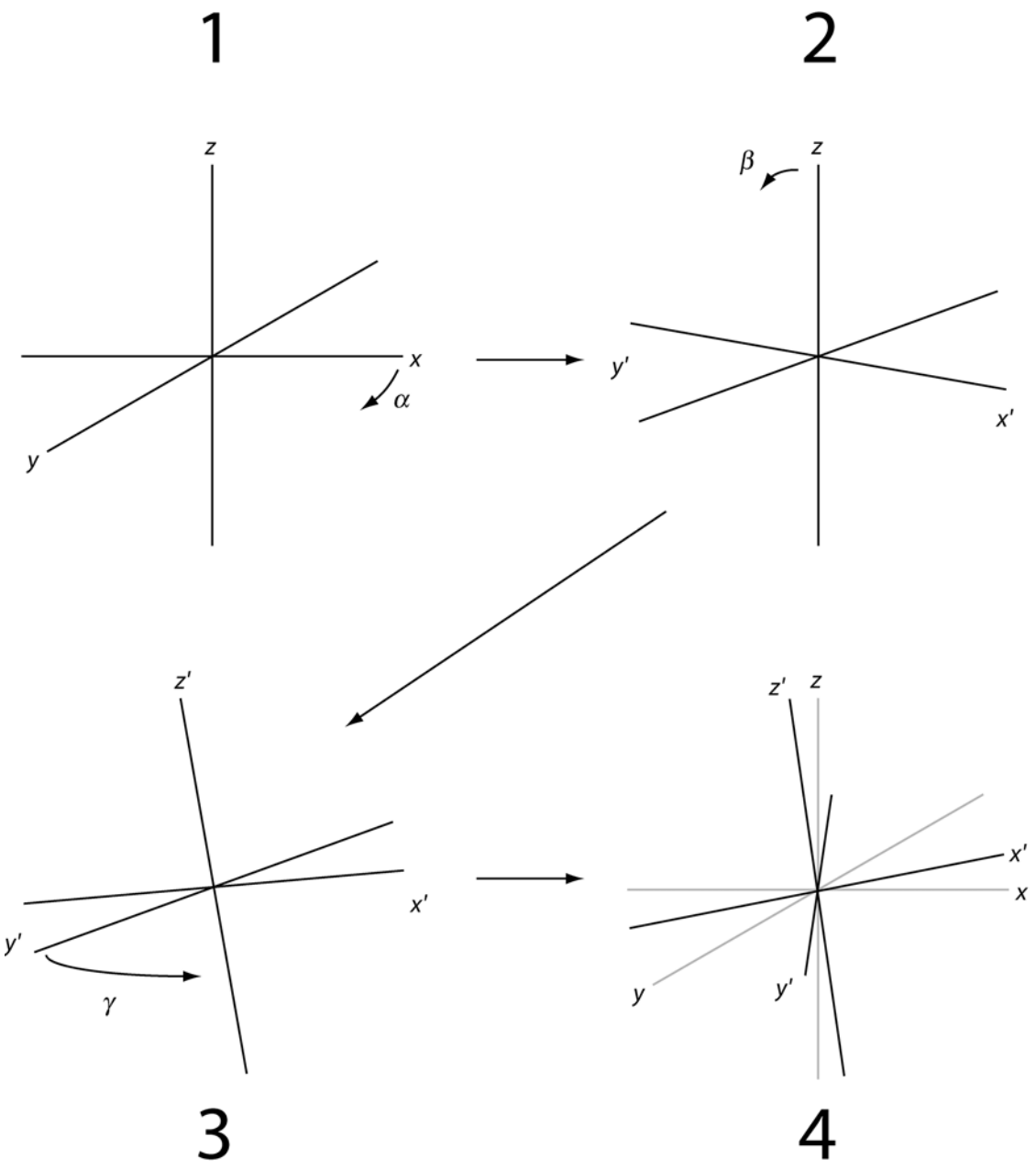

Figure **2-2**: Transformation of an axis system through rotation of the Euler angle α about the original z axis (1), rotation through the angle β about the new y axis (2), and finally rotation about the new z axis by the angle γ (3) to produce the new coordinate system, shown relative to the original system in (4).

$$\widehat{Op}' = \hat{R}_{z'}(\gamma)\hat{R}_{y'}(\beta)\hat{R}_{z}(\alpha)\widehat{Op}\hat{R}_{z}^{-1}(\alpha)\hat{R}_{y'}^{-1}(\beta)\hat{R}_{z'}^{-1}(\gamma) \tag{2.19}$$

where $\hat{R}_n(\theta)$ represents a rotation of angle θ about the *n* axis. Alternatively, these three rotation operators could be written in matrix form:

$$\widehat{Op}' = \hat{R}(\alpha,\beta,\gamma)\widehat{Op}\hat{R}^{-1}(\alpha,\beta,\gamma). \tag{2.20}$$

While any operator may be rotated in space with the Euler method, the rotation matrix can be quite complicated and cumbersome to use in computations.

Mathematically, a rotation may be accomplished more easily using Wigner rotations. In NMR, the coupling tensor components of interaction Hamiltonians are frequently expressed as irreducible spherical tensor operators, $\hat{A}_{kq}$. Irreducible spherical tensor operators may be rotated with Wigner rotation matrices, which are related to Euler rotations as follows:

$$\hat{A}'_{kq} = \hat{R}(\alpha,\beta,\gamma)\hat{A}_{kq}\hat{R}^{-1}(\alpha,\beta,\gamma) = \sum_{p=-k}^{k} \hat{A}_{kp} D^{k}_{pq}(\alpha,\beta,\gamma) \tag{2.21}$$

where the Wigner rotation matrix $D^{k}_{pq}(\alpha,\beta,\gamma)$ can be expressed in terms of a reduced Wigner rotation matrix $d^{k}_{pq}(\beta)$:

$$D^{k}_{pq}(\alpha,\beta,\gamma) = \exp(-i\alpha p)\, d^{k}_{pq}(\beta) \exp(-i\gamma q). \tag{2.22}$$

The reduced Wigner rotation matrices are real and may be found in numerous tables such as pg. 294 of Appendix B in the classic monograph of Mehring.[50] Through the use of equations 2.21 and 2.22 any NMR tensor may be rotated in space to coincide with any useful reference frame.

2.1.5.2 Rotations of Spin Components

The spin components of the interaction Hamiltonians can also be rotated with similar methods. The example where the Zeeman Hamiltonian was shown to induce precessional motion when the spin ensemble is placed in a magnetic field is one such case. This motion was expressed as an exponential operator that contained time and a Hamiltonian composed of a frequency and the spin angular momentum operator $\hat{I}_z$. The time evolution operator $\widehat{U}(t)$ described in equations 2.16 and 2.17 is also a rotation operator. Note that it has the same components as the exponential operator from section 2.1.2: an exponential function involving time and an interaction Hamiltonian. The density operator is "rotated" through time under the effect of various spin angular momentum operators by the time evolution operator. SIMPSON simulations use rotations to simulate the effects of various interaction Hamiltonians and pulses on the spin system of interest. In section 2.2, we will look at form of the various interaction Hamiltonians that are relevant to evolve a system of ^{87}Sr spins through time during an NMR experiment.

2.1.6 Average Hamiltonians and the Rotating Frame[49]

Before discussing the internal NMR interactions, we must introduce two additional concepts, one of which is average Hamiltonian theory. We saw in the Liouville-von Neumann equation that the time evolution of the density operator may easily be calculated if the applicable Hamiltonians can be made time independent.

However, the relevant perturbing interaction Hamiltonians for NMR are time dependent in the laboratory reference frame. As we will see, one elegant solution to remove the time dependence of the internal interaction Hamiltonians is to calculate an average Hamiltonian valid over a fixed time interval *t*. Average Hamiltonian theory was initially developed by Haeberlen and Waugh[54,55] to explain multiple-pulse NMR experiments and is thoroughly reviewed in the books of Ernst and Mehring.[49,50] It can also be used to calculate the form of certain internal interaction Hamiltonians for NMR. A brief review of the key results will be presented here.

A Hamiltonian that is periodic with period τ_p and subject to stroboscopic sampling in tune with the period of the interaction meets the criterion for average Hamiltonian theory. This condition can be achieved for the internal NMR interactions by defining an appropriate rotating reference frame with a period $\tau_p = 2\pi/\omega_0 = 1/\nu_0$.[49] The density operator can be transformed from the laboratory frame into the rotating frame ($\hat{\rho}_r(t)$) with a rotation:

$$\hat{\rho}_r(t) = \exp\left(-ih\nu_0 t\hat{I}_z\right)\hat{\rho}(t)\exp\left(ih\nu_0 t\hat{I}_z\right) \tag{2.23}$$

where the new reference frame is rotating about the laboratory *z* axis at the Larmor frequency of the nucleus of interest in units of Hz (ν_0) (Figure **2-3**). In this new reference frame, over some time t_c, the density operator $\hat{\rho}_r(t)$ is propagated through time with equation 2.14 where the propagator is expressed by:

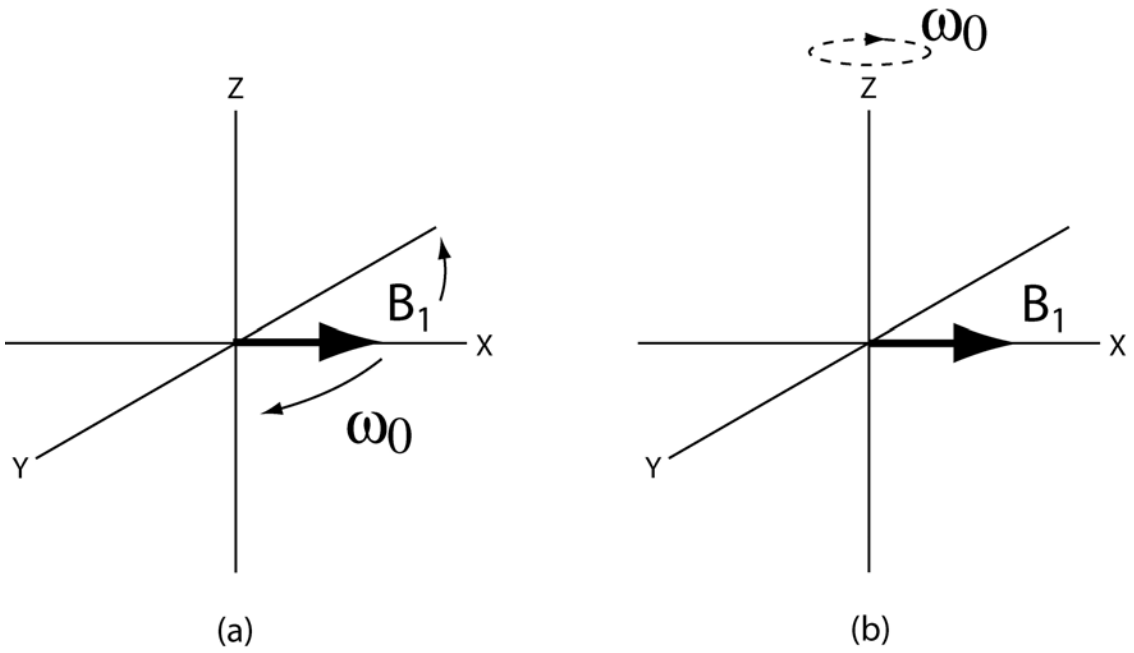

Figure **2-3**: In the laboratory frame (a), the magnetic field induced by the RF pulse oscillates along an axis in the transverse plane, effectively generating two counter-rotating components at the Larmor frequency. In the rotating frame (b), the entire coordinate system rotates at the Larmor frequency, causing the magnetization induced by the RF pulse to appear stationary.

$$\widehat{U}(t_c = n\tau) = \exp\left(i\widehat{H}_n\tau_n\right)\cdots\exp\left(i\widehat{H}_1\tau_1\right). \tag{2.24}$$

Equation 2.24 shows that the propagator $\widehat{U}(t_c = n\tau)$ is really a series of unitary transformations over the discrete sampling intervals τ. Since the product of two unitary transformations is still a unitary transformation, we may write an equivalent expression to equation 2.24 using a single exponential function containing an average Hamiltonian $\overline{H}$ over the interval t_c:

$$U(t_c = n\tau) = \exp\left(-i\overline{H}(t_c)t_c\right). \tag{2.25}$$

The appropriate form of this average Hamiltonian can be found by expanding the exponential products of equation 2.24 with the Baker-Campbell-Hausdorff relation.[49] The key result of this exercise is that the average Hamiltonian can be approximated well as a sum of contributions of various order:

$$\overline{H} = \overline{H}^{0} + \overline{H}^{1} + \overline{H}^{2} + \cdots . \tag{2.26}$$

A similar idea may be used to express the average Hamiltonians as a sum of terms of varying order with the Magnus expansion[56,57], yielding the following for the terms of the propagator $\widehat{U}(t_c = n\tau)$:

$$\overline{H}^{0} = \frac{1}{t_c}\int_{0}^{t_c} \widehat{H}(t_1)dt_1 \tag{2.27}$$

$$\overline{H}^{1} = \frac{1}{t_c}\int_{0}^{t_c}\int_{0}^{t_2}\left[\widehat{H}(t_2),\widehat{H}(t_1)\right]dt_1 dt_2 \tag{2.28}$$

.

It is important to note that if the time interval $t_c = t_p$, the average Hamiltonian describes the motion of the system through extended time periods, according to the criteria defined at the beginning of this paragraph. Equations 2.27 and 2.28 correspond directly to the first two orders of perturbation theory and will be used in our discussion of the internal interaction Hamiltonians in section 2.2.

The advantages average Hamiltonian theory offers for NMR calculations can be identified by examining a situation in the rotating frame where the Zeeman interaction is present and perturbed by an internal NMR interaction.[49] Again, this perturbation view is valid because the strength of the Zeeman interaction is typically much larger than the

internal NMR interactions. In the rotating frame, both of these Hamiltonians will be time-independent and the total Hamiltonian will be expressed as follows:

$$\widehat{H_T} = \widehat{H}_z + \widehat{H}_p \tag{2.29}$$

where $\widehat{H}_T$ is the total Hamiltonian and $\widehat{H}_p$ is the perturbation to the Zeeman Hamiltonian. The propagator $\widehat{U}(t)$ under the influence of the total Hamiltonian will contain a term for the Zeeman Hamiltonian and the perturbing Hamiltonian. Since the propagator is a unitary operator, it is valid to split the overall propagator $\widehat{U}(t)$ into a component corresponding to the Zeeman Hamiltonian and a component corresponding to the perturbing Hamiltonian:

$$\widehat{U}(t) = \widehat{U}_z(t)\widehat{U}_p(t) \tag{2.30}$$

where:

$$\widehat{U}_z(t) = \exp(-i\widehat{H}_z t)\,. \tag{2.31}$$

The proper form of $\widehat{U}_p(t)$ can be found by rotating the perturbing Hamiltonian into a time *dependent* reference frame defined by the Zeeman interaction using equation 2.15 where the propagator is given by equation 2.31. However, because the Zeeman Hamiltonian is cyclic in nature with period $t_c = \tau_p$, $\widehat{U_z}(t_c) = 1$ and the perturbing Hamiltonian is thus periodic with period $t_c = \tau_p$. In this time dependent "toggling" reference frame, the perturbing Hamiltonian inherits a time-dependence which we may eliminate by applying average Hamiltonian theory:

$$H_p^0 = \frac{1}{t_c}\int_0^{t_c} \widetilde{H_p}(t_1)dt_1 \tag{2.32}$$

where the tilde indicates that $\widehat{H}_p$ is in the toggling frame, producing the following form of $\widehat{U}_p(t)$:

$$U_p(t=t_c) = \exp\left(-i\overline{H}_p t_c\right). \tag{2.33}$$

The implication of this exercise is that some terms of the original perturbing Hamiltonian will be averaged away and do not need to be considered further. This implies that all oscillating terms of the perturbing Hamiltonians will vanish during the integration of equation 2.32. The only terms that survive to be components of $\overline{H}_p^0$ are the secular terms of $\widehat{H}_p$ that do not vary with rotation about the *z* axis. In this way, $\widehat{H}_p$ has been *truncated* to include only terms that commute with the Zeeman Hamiltonian, simplifying the calculation. The term $\overline{H}_p^0$ is equivalent to a first-order perturbation of the Zeeman Hamiltonian.

2.1.7 Efficient Powder Averaging

Thus far, we have discussed the quantum mechanical description of the spin ensemble and the mathematical methods for evolving the system through time. This is precisely the mechanism with which SIMPSON calculates an NMR spectrum. The one remaining aspect of solid-state NMR simulations that must be introduced is the concept of efficient powder averaging. Efficient powder averaging is a method for approximating the nearly infinite number of unique crystallite orientations in a powdered sample, permitting an accurate re-production of an anisotropic line shape while maximizing

calculation efficiency. A number of useful papers discussing efficient powder averaging are available in the literature and thus a detailed treatment will not be covered here.[58-63] Instead, we will summarize the concept of powder averaging and introduce the methods commonly employed to generate efficient powder averaging crystal files.

In liquid-state NMR, the molecules of interest are solvated and rapidly tumble under the influence of Brownian motion. The molecular re-orientation rate is fast enough (for most molecules) that the anisotropic interactions do not affect the resulting NMR spectrum. In solid-state NMR, samples are typically powders and motion is restricted. In this situation, the orientation-dependent interactions do affect the NMR spectrum. If each grain of the powdered sample is considered to be a "crystallite", the sample contains crystallites in a nearly infinite number of orientations with respect to the laboratory axis system. Anisotropic interactions cause each of the crystallites to experience a slightly different effective field, meaning that each crystallite resonates at a slightly different frequency. Since nature provides a powder average over all possible crystallite orientations in a powdered solid, it is necessary to integrate over all orientations to calculate the NMR spectrum of a polycrystalline solid exactly. The total NMR signal as a function of time, *s(t),* can be calculated with[58]:

$$s(t) = \frac{1}{8\pi^2}\int_0^{2\pi} d\alpha \int_0^{\pi} d\beta \sin\beta \int_0^{2\pi} d\gamma s(t,\alpha,\beta,\gamma) \qquad (2.34)$$

where $s(t,\alpha,\beta,\gamma)$ is the time evolution of a single crystallite and the Euler angles relate the crystal frame and the laboratory frame. The integrals of equation 2.34 are difficult to evaluate numerically, even if the γ angles are treated separately. However, we may approximate equation 2.34 with a summation term:

$$s(t) = \sum_{a=1}^{N} \sum_{b=1}^{M} s(t, \alpha_{ab}, \beta_{ab}) w_{ab} \tag{2.35}$$

where w_{ab} is the crystalline weighting factor and a and b are indices upon which the Euler angles depend.[58] The application of equation 2.35 to simplify the calculation of a time-domain solid-state NMR signal is known as efficient powder averaging.

Efficient powder averaging is usually accomplished by creating a *crystal file* that contains a large number of Euler angles α, β and weighting factors w_{ab} that describe the orientation of the crystallites with respect to the magnetic field. A variety of methods have been developed to generate crystal files[58-63], the most straightforward of which is the REPULSION method.[58] In this algorithm, a computer distributes a specified number of point charges about the surface of a sphere and adjusts their position to minimize the repulsive interactions between the points. While it is not possible to accurately account for an infinite number of crystallite orientations in this way, most spectra can be reproduced adequately with a fixed number of orientations. Use of the smallest number of crystallite orientations required to accurately re-produce the line shape yields the most time-efficient calculation. SIMPSON calculates the frequency contribution from each individual crystallite orientation in a crystal file and then combines the contributions to produce the full time domain NMR signal.

2.2 Select Interactions of Solid-State NMR

Now that we have a theoretical framework for understanding SIMPSON calculations, it is necessary to discuss the interactions relevant to a ^{87}Sr NMR experiment.

As alluded to in section 2.1, each NMR interaction can be described with a Hamiltonian operator that may be written in tensor form. Two of these interactions may be classified as external to the spin system: the Zeeman interaction that was already presented, which describes the effect of a strong external (or static) magnetic field on the spin system, and the RF Hamiltonian that describes the effects of a radio-frequency pulse on the spin ensemble. The rest of the NMR interactions that apply to ^{87}Sr are internal and include the chemical shift Hamiltonian, the dipolar Hamiltonian, and the quadrupolar Hamiltonian. This section will describe each of these interactions, how they related to an NMR spectrum, and how they apply to solid-state ^{87}Sr NMR.

2.2.1 RF Interaction[52]

In modern FT NMR, the ensemble of spins is perturbed by applying a pulse of radio-frequency (RF) radiation to a coil of wire surrounding the sample. The frequency of the pulse is selected such that it is identical (or very close) to the Larmor frequency of the nucleus of interest. When (and only when) the pulse is being applied, a new oscillating magnetic field (which we will denote as $\vec{B_1}$) is induced in the *x*-*y* plane of the laboratory axis system. More precisely, this $\vec{B_1}$ field is composed of two different components, one that rotates clockwise and one that rotates counter-clockwise in the plane. We know from earlier discussions that the spins in our ensemble precess about the $\vec{B_0}$ field in only one direction (the direction of free precession is determined by the sign of the gyromagnetic ratio). This means that only one rotating component of the $\vec{B_1}$ field

is rotating in the same direction as the spins and it can be shown that only this component affects the spin system.[52] If we define the time-dependent RF Hamiltonian using equation 2.3:

$$\widehat{H}_{RF}(t) = -\vec{\mu} \bullet \vec{B}_1, \tag{2.36}$$

then after some manipulation according to the properties of the RF Hamiltonian that were just presented, we find the equivalent expression:

$$\widehat{H}_{RF}(t) = -\frac{1}{2}\gamma B_1 \left(\cos\left(\omega_{spec} t + \phi\right) \hat{I}_x + \sin\left(\omega_{spec} t + \phi\right) \hat{I}_y \right) \tag{2.37}$$

where ω_{spec} is the irradiation frequency, ϕ is the phase of the RF radiation, B_1 is the magnitude of the induced $\vec{B}_1$ field, and $\hat{I}_x$ and $\hat{I}_y$ are spin angular momentum operators. The factor of ½ in equation 2.37 accounts for the $\vec{B}_1$ component that does not rotate with the direction of precessional motion.

The RF Hamiltonian described by equation 2.37 has a clear time dependence. As mentioned in sections 2.1.4 and 2.1.6, the choice of an appropriate rotating reference frame will render the RF Hamiltonian time-independent, allowing us to propagate the density matrix under the influence of any pulse with the Liouville-von Nuemann equation. In the rotating frame, the $\vec{B}_1$ field induced by the RF Hamiltonian is fixed along either the *x*, *-x*, *y*, or *–y* axis depending on the phases of the irradiation and the receiver. Since the position of the $\vec{B}_1$ field does not vary with time in this frame, we may express the RF Hamiltonian as follows:

$$\widehat{H}_{RF} = -\frac{1}{2}\gamma B_1 \left(\hat{I}_x \cos\phi + \hat{I}_y \sin\phi \right). \tag{2.38}$$

The effect of the RF Hamiltonian on the ensemble of spins can be determined by applying the Liouville-von Neumann equation:

$$\widehat{\rho_r}(t) = e^{-i\widehat{H}_{RF}t}\widehat{\rho_r}(0)e^{i\widehat{H}_{RF}t} = e^{-\frac{i}{2}\gamma B_1 \hat{I}_\phi t}\widehat{\rho}_r(0)e^{\frac{i}{2}\gamma B_1 \hat{I}_\phi t} \tag{2.39}$$

where $\hat{I}_\phi = \hat{I}_x \cos\phi + \hat{I}_y \sin\phi$. This expression shows that the RF Hamiltonian rotates the density matrix about the axis defined by $\hat{I}_\phi$ through the angle defined by $\gamma B_1 t$.

2.2.2 Chemical Shift Interaction[51]

The chemical shift and Knight shift Hamiltonians together comprise the general shielding Hamiltonian. The Knight shift is typically only important for metallic solids and therefore is not a significant interaction for the materials studied in this dissertation. However, the chemical shift does play an important role in low electric-field gradient materials and a smaller but still significant role in the case of broad ^{87}Sr resonances. Phenomenologically, the chemical shift interaction arises from two sources. The magnetic moments of the nuclei can couple with the magnetic field generated by the motion of local electrons due to the interaction of these electrons and the external magnetic field. This causes a local variation in the field strength experienced by the nucleus via a diamagnetic effect. A paramagnetic contribution to the chemical shift arises from nuclei that have partially filled electron shells. The electronegativity of neighboring atoms and the type of bonding strongly influences the behavior of electrons and thus the chemical shift. Since the chemical shift interaction depends highly on the

structure of the sample, all chemical shifts are reported with respect to a reference compound with a known, stable structure.

A frame of reference exists where the coupling tensors for the internal Hamiltonians are diagonal; we will denote this axis system the principle axis system (PAS) of the particular interaction. In spherical tensor notation, the chemical shift can be expressed in its principle axis system as:

$$\widehat{H}_{CS} = \gamma \sum_{l=0,2} \sum_{m=-l}^{l} (-1)^m T_{l,m}^{CS} A_{l,-m}^{CS} \tag{2.40}$$

where $T_{l,m}$ and $A_{l,-m}$ are the spin and coupling tensor components, respectively. The coupling tensor components include terms from the chemical shift (CSA) tensor ($\overline{\overline{\sigma}}$). The trace of the CSA tensor is non-zero and is directly related to the isotropic chemical shift σ_{iso}:

$$\sigma_{iso} = \frac{1}{3} Tr\left(\overline{\overline{\sigma}}_{PAS}\right). \tag{2.41}$$

The isotropic chemical shift is the frequency shift that would be observed in a liquid-state NMR experiment. In solid-state NMR, the anisotropic components of the chemical shift tensor may become important as well (i.e., ^{31}P NMR). The anisotropy of the CSA tensor is characterized with a parameter known as the chemical shift anisotropy ($\Delta\sigma$) and an asymmetry parameter (η_{cs}):

$$\Delta\sigma = \sigma_{zz} - \frac{1}{2}(\sigma_{xx} + \sigma_{yy}) \tag{2.42}$$

$$\eta_{CS} = \frac{3}{2} \frac{\left(\sigma_{xx} - \sigma_{yy}\right)}{\Delta\sigma} \tag{2.43}$$

where σ_{ii} is one of the diagonal components of the CSA tensor.

The important spin tensors for the chemical shift Hamiltonian may be expressed in terms of Cartesian spin operators as follows (as calculated by Mehring):

$$T_{0,0}^{CS} = \hat{I}_z B_0 \tag{2.44}$$

$$T_{2,0}^{CS} = \sqrt{\frac{2}{3}} \hat{I}_z B_0 \tag{2.45}$$

$$T_{2,\pm 1}^{CS} = \mp \frac{1}{2} \hat{I}_{\pm} B_0 \tag{2.46}$$

where $\hat{I}_{\pm}$ are the ladder operators defined as:

$$I_{+} = I_x + iI_y \tag{2.47}$$

$$I_{-} = I_x - iI_y .^{50} \tag{2.48}$$

The non-zero coupling tensor components in the PAS of the CSA tensor are:

$$A_{0,0}^{CS} = \sigma_{iso} \tag{2.49}$$

$$A_{2,0}^{CS} = \sqrt{\frac{2}{3}} \Delta\sigma \tag{2.50}$$

$$A_{2,\pm 2}^{CS} = \frac{\Delta\sigma}{3} \eta_{cs} . \tag{2.51}$$

In order to propagate the density operator with the chemical shift Hamiltonian (or any internal interaction Hamiltonian), we need to transform from the PAS of the chemical shift tensor into the rotating reference frame. We will perform this transformation with the help of Wigner rotations and average Hamiltonian theory. Recall from section 2.1.6 that transforming to the rotating frame imparts a time-dependence to the perturbing Hamiltonian (in this case, the chemical shift Hamiltonian). Also remember that

transformation to the rotating frame truncates the perturbing Hamiltonian so that only terms that commute with the Zeeman Hamiltonian survive the transformation. The only parts of the spherical tensor representation that meet this criterion are the terms where *m* = 0. Thus, the average chemical shift Hamiltonian in the rotating frame only contains two components to first order:

$$\overline{H_{cs}^{rot}} = T_{0,0}^{cs}\overline{A_{0,0}^{cs,rot}} + T_{2,0}^{cs}\overline{A_{2,0}^{cs,rot}} \tag{2.52}$$

We have already evaluated the $T_{l,0}$ components in equations 2.44 – 2.46. When we rotate the $A_{l,0}$ terms into the rotating frame, we find the following expressions:

$$\overline{A_{0,0}^{cs,rot}} = \frac{1}{3}Tr\left(\overline{\overline{\sigma}}\right) = \sigma_{iso} \tag{2.53}$$

$$\overline{A_{2,0}^{cs,rot}} = \frac{1}{3}\Delta\sigma\left(\left(3\cos^2\beta - 1\right) - \eta_{cs}\cos 2\alpha \sin^2\beta\right) \tag{2.54}$$

where α and β are the Euler angles relating the PAS of the chemical shift tensor and the axis system of the rotating reference frame. A similar procedure may be used to transform any internal interaction Hamiltonian from its PAS to the rotating frame. We will express the remaining interactions important for ^{87}Sr solid-state NMR in a similar form.

In general, under the sole influence of the chemical shift Hamiltonian with negligible anisotropy, a narrow resonance will appear in the NMR spectrum centered at the isotropic chemical shift with respect to the reference compound. As the value of the chemical shift anisotropy increases, the resonance develops a characteristic shape (Figure **2-4**) and increases in width. As the asymmetry parameter varies, the position of the singularity will change (and the width, to some extent). The effects of the chemical

shift anisotropy and asymmetry on a spectrum of ^{31}P are represented pictorially in Figure 2-4. These spectra were simulated with SIMPSON according to the code located in Appendix A.

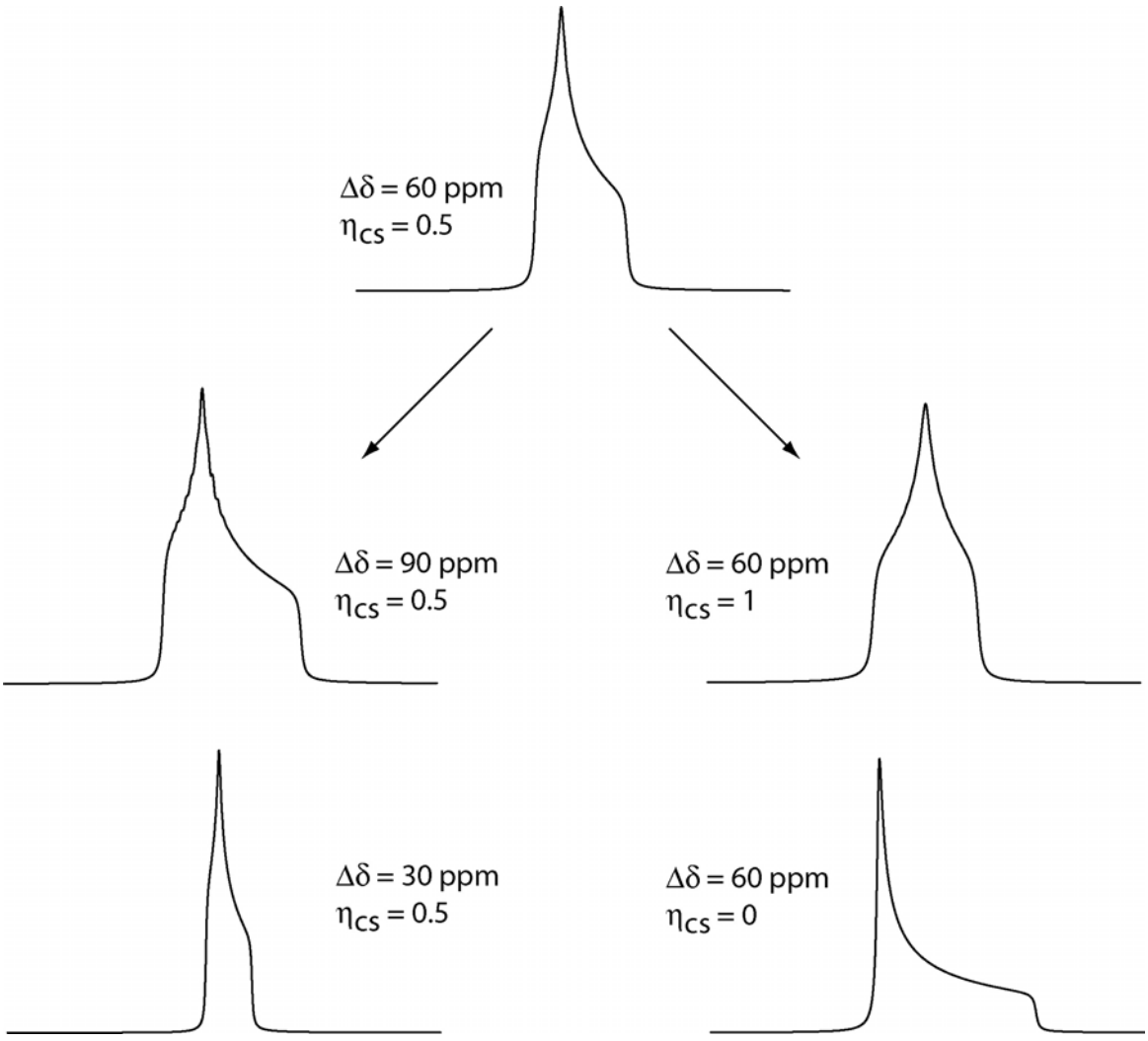

Figure **2-4**: The effects of chemical shift anisotropy on the static powder pattern. In the left column, the chemical shift anisotropy is varied, and on the right the chemical shift asymmetry parameter is varied.

2.2.3 Dipolar Interaction

In some cases, heteronuclear dipolar couplings will occur between ^{87}Sr and other nuclei. In this interaction, the magnetic moments of nuclei that are proximal in space interact, producing small variations in the magnetic field experienced by each coupled nucleus. This interaction always involves two nuclei and the strength of the coupling is directly dependent on the distance between the coupled nuclei. Dipolar couplings play a fundamental role in a number of multiple-resonance NMR experiments such as cross polarization (CP)[64], rotational echo double resonance (REDOR)[65], and transfer of populations by double resonance (TRAPDOR)[66].

In spherical tensor notation, the form of the dipolar Hamiltonian is:

$$\widehat{H}_D = -2\sum_{m=-2}^{2}(-1)^m T_{2,m}^D A_{2,-m}^D \tag{2.55}$$

The relevant coupling tensor for this interaction is the dipolar tensor. Unlike the CSA tensor, the dipolar tensor is traceless and does not have a meaningful asymmetry parameter. For this reason, the only non-zero term of the spatial coupling tensor $A_{2,-m}^D$ in the PAS is $A_{2,0}^D$:

$$A_{2,0}^D = \sqrt{\frac{3}{2}}\frac{\hbar\gamma_I\gamma_S}{d_{IS}^3} \tag{2.56}$$

where γ_I and γ_S are the gyromagnetic ratio of the I and S nuclei and d_{IS} is the distance between the I nucleus and the S nucleus. If we apply average Hamiltonian theory to first order and use Wigner rotations to transform equation 2.56 from the PAS of the dipolar tensor into the rotating frame, we find:

$$\overline{A_{2,0}^{D,rot}} = \sqrt{\frac{3}{2}}\frac{\hbar\gamma_I\gamma_S}{d_{IS}^3}\left(1-3\cos^2(\beta)\right) \tag{2.57}$$

Because of the truncation associated with this set of operations and the fact that all the other $A_{2,-m}^{D}$ are zero, there is only one term of the spin tensor we need to consider:

$$T_{2,0}^{D} = \sqrt{\frac{1}{6}}\left(3I_zS_z - \vec{I}\bullet\vec{S}\right). \tag{2.58}$$

The exact form of $T_{2,0}^{D}$ depends on whether the dipolar coupling is homonuclear or heteronuclear in nature. Since this is a two-spin interaction, magnetization can be transferred between nuclei via the dipolar interaction. The interested reader is referred to Mehring for a more complete discussion of the dipolar Hamiltonian.[50]

2.2.4 Quadrupolar Interaction

Greater than 70% of the NMR active nuclei in the periodic table are known to be quadrupolar. A quadrupolar nucleus is a nucleus with a non-spherically symmetric charge distribution, producing a non-zero nuclear electric quadrupole moment, *Q*. Quadrupolar couplings occur between the nucleus and the electric field gradient at the position of the nucleus and are generally of a greater magnitude than dipolar couplings. Typically, if a nucleus is a low-γ quadrupolar nucleus (such as ^{87}Sr), the quadrupolar interaction dominates the solid-state NMR spectrum, leading to extremely broad resonances. For this reason, we will examine the quadrupolar interaction in more detail.

The physical basis of the quadrupolar interaction is most easily understood by examining the classical mechanical equation for the electrostatic interaction energy of a

particle. In classical mechanics, the electrostatic interaction energy of a nucleus with a charge density ρ(r) in a potential V(r) can be expressed by a Taylor series expanded about the center of mass of the nucleus:

$$E = ZeV(0) + \sum_{i=1}^{3} P_i \left(\frac{\partial V}{\partial x_i} \right)_{r=0} + \sum_{i=1}^{3} \sum_{j=1}^{3} Q'_{ij} \left(\frac{\partial^2 V}{\partial x_i \partial x_j} \right)_{r=0} + \ldots \tag{2.59}$$

where Ze represents the total charge on the nucleus, P_i is the ith component of the electric dipole moment $\vec{P}$, and Q'_{ij} is the ijth term of the electric quadrupole moment $\overline{\overline{Q}}'$.[67] The third term of the series expansion is a mathematic expression of the energy due to a nucleus with an electric quadrupole moment interacting with an electric field gradient at the position of the nucleus, the quadrupolar interaction. It is made up of two tensor components. The first is the electric quadrupole moment $\overline{\overline{Q}}'$, a symmetric but not traceless second rank tensor. A more convenient, traceless form of the quadrupole moment $\overline{\overline{Q}}$ can be defined as follows:

$$Q_{ij} = 3Q'_{ij} - \delta_{ij} \sum_{k=1}^{3} Q'_{kk} \tag{2.60}$$

where δ_{ij} is the Kronecker delta and i, j, and k are the indices of individual components of the quadrupole moment tensor. Further discussion of the quadrupole moment tensor will be postponed until the quantum mechanical quadrupolar Hamiltonian is derived. The second important tensor component of the quadrupolar interaction is the electric field gradient tensor $\overline{\overline{V}}$ with the components:

$$V_{ij} = \left(\frac{\partial^2 V}{\partial x_i \partial x_j} \right)_{r=0} . \tag{2.61}$$

The electric field gradient (EFG) tensor is symmetric and traceless in any general coordinate system. The electric field gradient also has a PAS system in which it is diagonal. The PAS is generally defined so that the largest component of the EFG is oriented along the z-axis and the smallest component along the x-axis. Because the EFG tensor is symmetric, traceless, and diagonal in the PAS, it can be fully described by two components: the magnitude of the EFG tensor *eq* and the quadrupolar asymmetry parameter η. In the PAS, the diagonal elements of the EFG tensor can be expressed as:

$$V_{zz} = eq \tag{2.62}$$

$$V_{yy} = -\frac{eq}{2}\left(1+\eta_q\right) \tag{2.63}$$

$$V_{xx} = -\frac{eq}{2}\left(1-\eta_q\right). \tag{2.64}$$

The quadrupolar asymmetry parameter is restricted to values between 0 and 1 while there are no limitations *per se* on the magnitude of the EFG tensor. As with other second-rank tensors that describe NMR interaction Hamiltonians, the EFG tensor may be rotated with Euler angles into any relevant reference frame.

Cook and De Lucia first derived the quantum mechanical form of the quadrupolar Hamiltonian in spherical tensor notation:

$$\widehat{H}_Q = \frac{eQ}{2I(2I-1)h}\sum_{m=-2}^{2}(-1)^m T^Q_{2m} A^Q_{2,-m} \tag{2.65}$$

where *e* is the fundamental unit of charge and *Q* is the nuclear electric quadrupole moment (we will return to *Q* momentarily).[68] The relevant terms of the coupling tensor components are related to the electric field gradient tensor and can be shown to be:

$$A_{20}^{Q} = \sqrt{\frac{3}{8}} V_{zz} \tag{2.66}$$

$$A_{2\pm1}^{Q} = \mp\left(V_{xz} \pm iV_{yz}\right) \tag{2.67}$$

$$A_{2\pm2}^{Q} = \frac{1}{2}\left(V_{xx} - V_{yy} \pm 2iV_{xy}\right) \tag{2.68}$$

in a general coordinate system or:

$$a_{20}^{Q} = \sqrt{\frac{3}{8}} eq \tag{2.69}$$

$$a_{2\pm1}^{Q} = 0 \tag{2.70}$$

$$a_{2\pm2}^{Q} = \frac{1}{2} eq\eta \tag{2.71}$$

in the PAS of the EFG tensor. In the quantum mechanical form of the quadrupolar interaction, the traceless quadrupole moment tensor of equation 2.60 is expressed as a second-rank operator known as the quadrupole operator.[67] The quadrupole operator can be related to the spin tensor components involved in equation 2.65 through the Wigner–Eckart theorem.[69] This theorem states that all irreducible tensor operators of rank L are proportional to one another, meaning that the second-rank quadrupole operator is proportional to the second-rank spherical harmonics. It can be shown that the constant of proportionality for this relation is $\frac{eQ}{2I(2I-1)h}$, where eQ is known as the electric quadrupole moment and I is the spin quantum number of the nucleus. Due to symmetry considerations and our use of the traceless form of $\overline{\overline{Q}}$, eQ is the only component necessary to fully express the quadrupole operator. With the constant of proportionality

known, the applicable spin tensor components for equation 2.65 as calculated by Mehring are[50]:

$$T_{20}^{Q} = \frac{1}{\sqrt{6}}\left(3I_z^2 - I(I+1)\right) \tag{2.72}$$

$$T_{2\pm1}^{Q} = \mp\frac{1}{2}\left(I_z I_\pm + I_\pm I_z\right) \tag{2.73}$$

$$T_{2\pm2}^{Q} = \frac{1}{2} I_\pm I_\pm . \tag{2.74}$$

In order to calculate the NMR spectrum, we must transform from the PAS of the quadrupolar Hamiltonian to the rotating reference frame. As we have already observed, this is accomplished by rotating the spin tensor components about the *z* axis of the laboratory reference frame at the Larmor frequency. Mathematically, the quadrupolar Hamiltonian in the rotating frame can be expressed as[50]:

$$\widetilde{H_Q^{rot}}(t) = e^{i\omega_0 I_z t} H_Q e^{-i\omega_0 I_z t} = \frac{eQ}{2I(2I-1)h}\sum_{m=-2}^{2}(-1)^m e^{i\omega_0 m t} T_{2m}^{Q} A_{2-m}^{Q} . \tag{2.75}$$

2.2.4.1 First Order Effects

To find the form of the first-order average quadrupolar Hamiltonian in the rotating frame, we again apply average Hamiltonian theory (equation 2.27) and find:

$$\overline{H_Q^{rot}} = \frac{1}{2}\left(\frac{e^2 qQ}{4I(2I-1)h}\right)\left(\left(3\cos^2\beta - 1\right) + \eta\cos 2\alpha \sin^2\beta\right)\left(3\hat{I}_z^2 - \hat{I}^2\right) \tag{2.76}$$

where $\frac{e^2qQ}{h} = C_q$ (the quadrupolar coupling constant) and all other terms are as defined in previous sections. We may also calculate the frequency perturbation to the Zeeman energy levels brought about by the first order quadrupolar interaction:

$$\omega_{m+1,m}^{1Q} = \frac{1}{\hbar}\left(\langle m+1|\overline{H_Q^{rot}}|m+1\rangle - \langle m|\overline{H_Q^{rot}}|m\rangle\right) \tag{2.77}$$

$$\omega_{m+1,m}^{1Q} = (2m+1)\frac{3e^2qQ}{8I(2I-1)\hbar}\left[\left(3\cos^2\beta - 1\right) + \eta\cos 2\alpha \sin^2\beta\right] \tag{2.78}$$

A quick calculation of the frequency perturbation for the central transition (in which case m = -1/2), shows that the central transition is not perturbed by the quadrupolar interaction to first order. All other transitions will be affected in an anisotropic fashion. Equation 2.78 shows that the frequency perturbation is dependent on the angles α and β, which relate the PAS of the quadrupolar interaction to the rotating frame. In a polycrystalline sample, each crystallite orientation will provide a unique frequency contribution to the resulting NMR resonance, leading to a broad powder pattern.

2.2.4.2 Second Order Effects

The first order quadrupolar powder patterns of the satellite transitions are typically too broad to be observed in a conventional solid-state NMR experiment, but the central transition typically can be observed. Since the central transition is not affected to first order by the quadrupolar interaction, we must examine the second order frequency perturbation to determine if second order affects are large enough to influence the central transition.

Samoson, Kundla, and Lippmaa showed that the second order average quadrupolar Hamiltonian takes the form:

$$\overline{H_Q^{rot(1)}} = -\frac{i\omega_0}{4\pi}\left(\frac{eQ}{2I(2I-1)}\right)^2 \int_0^{2\pi/\omega_0} dt_2 \int_0^{t_2} dt_1 \sum_{m=-2}^{2}(-1)^m \sum_{m'=-2}^{2}(-1)^{m'} \times \left[T_{2m}^Q, T_{2m'}^Q\right] \overline{A_{2-m}^{Q,rot} A_{2-m'}^{Q,rot}} e^{im\omega_0 t_1} e^{im\omega_0 t_2} \tag{2.79}$$

which, upon substitution of spin commutators and integration over both time variables, yields the second order average quadrupolar Hamiltonian in terms of spatial tensor components[70]:

$$\overline{H_Q^{rot,1}} = \frac{1}{\omega_0}\left(\frac{eQ}{4I(2I-1)}\right)^2 \begin{pmatrix} 2\overline{A_{21}^{Q,rot} A_{2-1}^{Q,rot}}\left(4I^2-8I_z^2-1\right)I_z + \\ 2\overline{A_{22}^{Q,rot} A_{2-2}^{Q,rot}}\left(2I^2-2I_z^2-1\right)I_z - \\ \sqrt{12}\,\overline{A_{20}^{Q,rot} A_{2-1}^{Q,rot}}\left(4I^2-4I_z^2-1\right)\left(-\frac{1}{\sqrt{2}}(I_x+iI_y)\right) - \\ \sqrt{12}\,\overline{A_{20}^{Q,rot} A_{21}^{Q,rot}}\left(4I^2-4I_z^2-1\right)\left(\frac{1}{\sqrt{2}}(I_x-iI_y)\right) + \\ 4\sqrt{6}\,\overline{A_{20}^{Q,rot} A_{2-2}^{Q,rot}}\left(I_z-1\right)\left(-\frac{1}{\sqrt{2}}(I_x+iI_y)\right)^2 + \\ 4\sqrt{6}\,\overline{A_{20}^{Q,rot} A_{22}^{Q,rot}}\left(I_z+1\right)\left(\frac{1}{\sqrt{2}}(I_x-iI_y)\right)^2 \end{pmatrix}. \tag{2.80}$$

It is thus possible to compute the second order frequency perturbation for the central transition in terms of spatial tensor components:

$$\omega_{\frac{1}{2},-\frac{1}{2}}^{2Q} = \left(\frac{e^2qQ}{4I(2I-1)\hbar}\right)^2 \left(\frac{4I(I+1)-3}{\omega_0}\right)\left(2\overline{A_{21}^{Q,rot} A_{2-1}^{Q,rot}} + \overline{A_{22}^{Q,rot} A_{2-2}^{Q,rot}}\right). \tag{2.81}$$

Equation 2.81 shows that the central transition has an anisotropic frequency component described by the second order average quadrupolar Hamiltonian. The second order average quadrupolar Hamiltonian also contains an isotropic component, typically denoted

as the quadrupolar shift. The isotropic frequency shift associated with the quadrupolar interaction can be calculated by evaluating equation 2.81 and integrating over the surface of a sphere, producing the following expression for the second order isotropic quadrupolar shift:

$$\omega_{\frac{1}{2},-\frac{1}{2}}^{2Q,iso} = -\frac{3}{10}\left(\frac{e^2qQ}{4I(2I-1)\hbar}\right)^2\left(1+\frac{\eta^2}{3}\right)\frac{4I(I+1)-3}{\omega_0}. \qquad (2.82)$$

Close inspection of the frequency perturbations due to the first and second order average quadrupolar Hamiltonians reveals that only two unknown parameters are present in each equation. These are the quadrupolar coupling constant defined earlier (C_q) and the quadrupolar asymmetry parameter (η). The width of a quadrupolar powder pattern is directly related to C_q, as is readily apparent in Figure **2-5**. The asymmetry parameter describes the shape of the powder pattern, just as for the chemical shift interaction. These parameters characterize the electric field gradient at the nucleus, which has a direct dependence on the local electronic environment about the nucleus of interest. The magnitude of these parameters is related to the local coordination sphere and the types of interactions between members of the sphere and the nucleus (direct covalent bonding, electrostatic interactions, hydrogen bonding, etc.). In theory, the quadrupolar parameters will be quite sensitive to the strontium binding environment in materials such as phyllosilicate and titanosilicate minerals. We will rely heavily on this interaction to characterize the strontium coordination sphere in subsequent chapters.

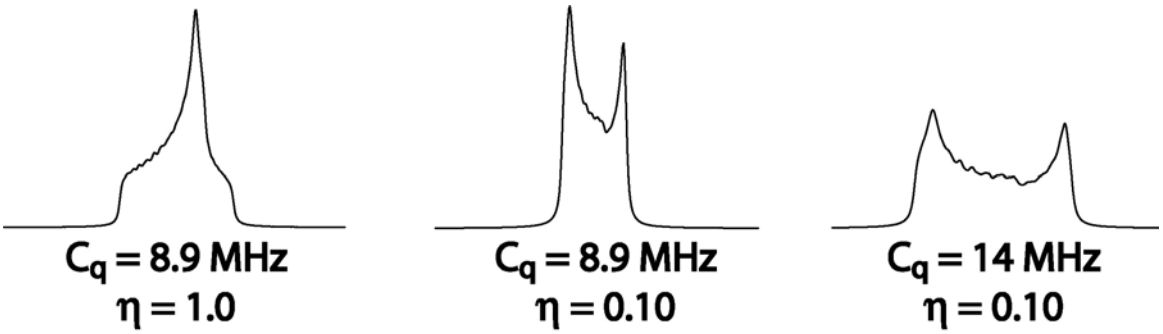

Figure **2-5**: Variations in the quadrupolar powder pattern as a function of quadrupolar coupling constant and quadrupolar asymmetry parameter.

2.3 NMR Experiments

The only remaining aspect of NMR theory pertinent to this dissertation is a discussion of the NMR experiments performed in subsequent chapters. Since the theoretical basis of the experimental methods used in this dissertation are established, we will not delve deeply into theoretical treatments of each technique. This section aims to impart a qualitative feel for the usefulness of each experiment as well as the pros and cons of each method. We will begin with a basic discussion of the modern Fourier transform (FT) NMR spectrometer and how it is used to perturb the system of spins in the context of a Bloch-decay experiment. We will then move on to discussions of specific experiments relevant to the solid-state NMR analyses presented in the subsequent chapters, such as the spin echo experiment and methods for enhancing the sensitivity of ^{87}Sr NMR (Figure **2-6**). Finally, we will discuss the ^{1}H-^{87}Sr TRAPDOR experiment for probing strontium environments that are strongly coupled to protons indirectly with NMR.

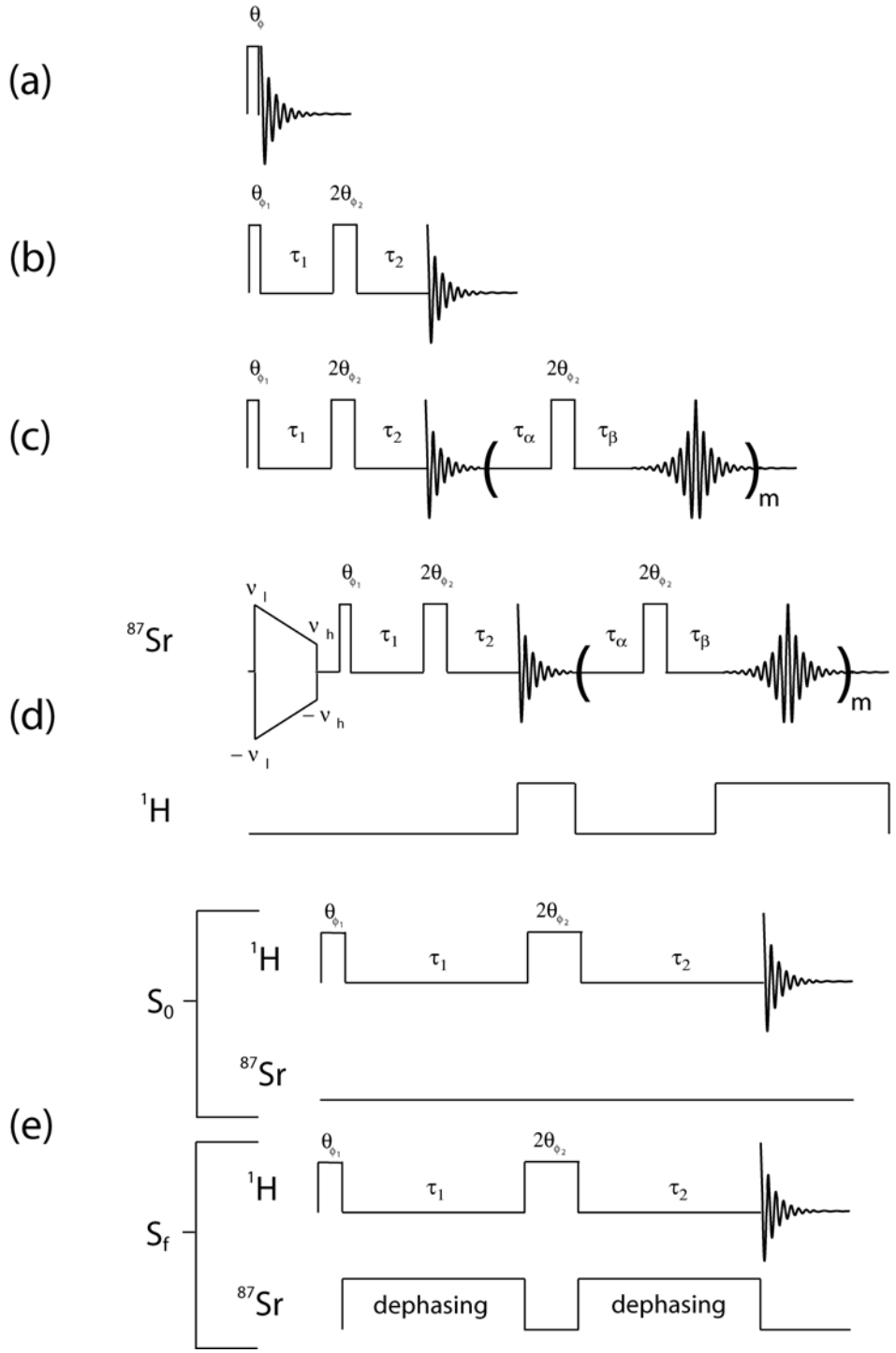

Figure **2-6**: Pulse sequence schematics of the techniques used in this dissertation: (a) Bloch-decay, (b) Oldfield echo, (c) QCPMG, (d) proton-decoupled DFS-QCPMG, and (e) TRAPDOR.

2.3.1 The FT NMR Spectrometer

The FT NMR spectrometer may be thought of as a combination of a radio source and receiver. It is responsible for producing a pulse of radiation at the appropriate frequency at the desired power and also serves as the detection system for acquiring the NMR signal. We will explore the components of the spectrometer in terms of the most basic NMR experiment, the Bloch-decay technique.[71,72]

The first task of an NMR spectrometer in a Bloch-decay experiment is to produce a pulse of radiation at the appropriate excitation frequency, also called the carrier frequency or transmitter frequency, with the appropriate phase and duration. These operations involve proper implementation and control of the frequency synthesizer, mixers, pulse programmer, and high-power amplifiers. Typically, the spectrometer has a very stable, low-power fixed frequency source that produces the internal or intermediate frequency (IF). The IF is used to set the pulse phase in a hardware element known as a quadrature phase shifter, although many (if not all) newer spectrometers implement a combination of direct digital synthesis and digital phase shifting. Additional, tunable frequency sources are used to produce local oscillator (LO) frequencies that are mixed with the IF frequency to produce the desired excitation frequency at the proper phase. Once the excitation frequency is attained, the pulse programmer opens a gate for a specified duration, permitting a pulse at the excitation frequency to travel down transmission lines to the high-power amplifiers and on to the probe.

The NMR probe is the hardware element that is placed within the magnet and contains tunable LC circuity, the RF coil, and the sample. The sample is centered within

the RF coil and is positioned in the most homogeneous region of the static magnetic field. The coil is attached to anywhere from one to four LC or transmission-line based circuits that can be tuned to resonate at the appropriate frequency by adjusting a variable capacitor or length of transmission line. The probe circuits usually contain a second variable capacitor that is used to match the impedance of the tuned circuit with the rest of the spectrometer. Once appropriately tuned and matched, the high-power excitation frequency passes through the probe circuit and into the coil. The electromotive force (EMF) passing through the coil produces an oscillating magnetic field within the coil according to the principles of electromagnetic induction (Faraday's Law):

$$\varepsilon = -N\frac{d\Phi_B}{dt} \tag{2.83}$$

where ε is the EMF in the coil of wire, N is the number of turns in the coil, and Φ_B is the magnetic flux through a single loop of the coil. In the rotating reference frame, the pulse effectively produces a static local magnetic field $\overrightarrow{B_1}$, as discussed for the RF Hamiltonian. The power of the pulse governs the strength of B_1 and the duration of the pulse determines the angle through which the bulk magnetization travels about $\overrightarrow{B_1}$. The power of the pulse is typically selected so that the RF interaction is much stronger than the internal interactions. The duration of the pulse is usually selected such that the bulk magnetization lies fully in the transverse plane following the pulse, meaning that the flip angle is 90° from thermal equilibrium.

At the conclusion of the pulse, the bulk magnetization is coherent in the transverse plane and precesses about the static magnetic field. The magnetization evolves under the influence of the internal NMR interactions present in the system,

resulting in slight frequency offsets from the excitation frequency (on the order of kHz). At the same time, the system returns to equilibrium at a characteristic rate by dissipating energy through the various interactions. The motion of the bulk magnetization induces a small EMF in the coil at the carrier frequency according to 2.83; the NMR signal. This signal travels from the probe circuit through transmission lines to the detection side of the spectrometer.

The low-power NMR signal is passed through a pre-amplifier and on to the receiver, where the signal is mixed again with the LO frequency and the component oscillating near the IF is passed on to a phase-sensitive detector. In the phase sensitive detector, the IF is split into two equal components that are mixed with the signal such that the two components become 90° out of phase with respect to one another. The components containing the NMR signal in the kHz frequency range are retained from the mixers. After a suitable delay for electronic ring-down in the system, the pulse programmer opens gates so that the two signal components are passed to a set of audio filters and then to the analogue-to-digital converters (ADCs). Each signal component is converted to a digital form by the ADC and stored in a computer, one as the "real" signal and the other the "imaginary" signal, corresponding to oscillations along orthogonal axes defined by the receiver phase, respectively. A complex Fourier analysis of these two components produces the frequency spectrum that is most commonly reported.

2.3.2 Spin-Echo Experiment

The Bloch-decay experiment has the advantage of being quantitative, provided that an appropriate flip angle is selected (for quantitative NMR of quadrupolar nuclei, the flip angle must be small). However, low-γ nuclei such as ^{87}Sr are plagued by dead-time issues such as acoustic ringing. Ringing is a consequence of the pulse, which causes a spatial movement of the coil such that it crosses field lines within the magnet. As it does so, a false signal is induced in the coil that can again be described by equation 2.83. This particular source of dead-time becomes increasingly problematic as the resonance frequency decreases and may be hundreds of microseconds for low-γ quadrupolar nuclei. Since the integral of the NMR signal is proportional to the intensity of the first data point, waiting for ring-down in the Bloch decay experiment results in significant loss of sensitivity or, in the most extreme case, total loss of the NMR signal. Thus, the Bloch-decay experiment is not an appropriate technique for observing strontium.

One tactic for overcoming this limitation is to use a two-pulse sequence known as an echo sequence (Figure 2.6) and the appropriate phase cycling (such as that developed by Oldfield[73,74]). In the case of half-integer quadrupolar nuclei, the first pulse is usually a central transition selective $\pi/2$ pulse that maximizes the central transition magnetization in the transverse plane. The second pulse is always twice the length of the first pulse, for reasons we will examine shortly. The second pulse is preceded and followed by a time delay τ such that ring-down and other artifacts have decayed away. Following the τ delay after the second pulse, the NMR signal forms an "echo" of the Bloch-decay signal and is acquired free of dead-time effects with a higher intensity. As the sequence is

repeated, the pulse phases are cycled to cancel the effects of "stimulated" echos and the effects of the second pulse on the satellite transitions (in the case of half-integer quadrupolar nuclei).

The first pulse of the echo experiment forms coherent superpositions of states in the density matrix. As the bulk magnetization evolves in the transverse plane, different contributions to the bulk magnetization precess at slightly different rates, partly due to magnetic field inhomogeneities over the volume of the sample and partly due to the NMR interactions. The variability in the precession rate causes the once coherent components to fan out, like the opening of a traditional oriental fan, reducing the observed in-plane magnitude of the bulk magnetization. When the second longer pulse is applied after time τ, the components are rotated 180° around the axis they started on, analogous to flipping the open fan upside down by rotating one's forearm with a locked wrist. As the individual components begin to precess at their characteristic rates following the pulse, instead of continuing to fan out, they sweep towards their initial position and build coherent magnetization, analogous to the oriental fan closing. After time τ following the pulse, the components are fully coherent and oriented along their original position in the transverse plane; our oriental fan is now closed and in the original position. Acquisition at this point produces an "echo" of the signal we would obtain in the Bloch-decay experiment without the effects of ringing. Despite the advantages of the echo, it will be shown that additional sensitivity enhancement is necessary to observe strontium nuclei in complex materials.

While the effects of ringing are eliminated and sensitivity is gained over a traditional Bloch-decay experiment when dead-time is long, there are disadvantages to

the echo approach. First, improper phase cycling will permit stimulated echos and partially affected satellite components that will convolute the echo spectrum. In addition, some relaxation processes do occur during the two delay periods and the second pulse, meaning that the echo intensity is slightly reduced compared to a Bloch-decay experiment if dead-time effects are not significant.

2.3.3 Sensitivity Enhancement

Since a vast majority of the NMR-active nuclei in the periodic table are quadrupolar, a significant number of methods have been developed for enhancing the sensitivity of low-γ quadrupolar nuclei. Low-γ quadrupoles have benefited recently from advances in magnet technology as well as innovations in multiple-pulse NMR. Magic angle spinning (MAS) is a routinely applied technique to enhance the sensitivity and resolution of solid-state NMR experiments and has some applications for low-γ quadrupoles.[75-79] Significant sensitivity enhancement can be achieved by decreasing the temperature of the electronics and the sample to cryogenic conditions, but with the drawback of significant reductions in longitudinal relaxation rates.[80,81] Pulse techniques such as the quadrupolar Carr-Purcell-Meiboom-Gill (QCPMG) sequence and preparatory schemes that saturate or invert the satellite transitions also have been shown to provide significant sensitivity enhancement.[82-87] These pulse sequences are also the most readily implemented sensitivity enhancing methods for existing NMR spectrometers. In this section, we will examine the sensitivity enhancing properties of increasing the static field strength, MAS, and pulse sequences used in the remainder of this dissertation.

2.3.3.1 Increased Applied Magnetic Field

An increase in the strength of the static magnetic field provides three main advantages for low-γ quadrupolar nuclei: an increased population difference across the central transition, a narrowing of the second-order quadrupolar line width, and an increase in the EMF produced in the coil at higher resonance frequencies.[88]

The first benefit of high static fields is described by the Curie magnetization law, which can be derived as follows. Recall that any particular quantum mechanical observable for the system can be evaluated by taking the trace of the commutator between the relevant operator and the density matrix. To calculate the average bulk magnetization along the *z* axis, we may use the following equation:

$$\overline{M_z} = Tr\left[\widehat{M_z}\widehat{\rho_0}\right] \tag{2.84}$$

where M_z is traceless and ρ_0 is the density operator at thermal equilibrium. We can define a thermal equilibrium density operator by passing the time dependence of equation 2.11 to the Hamiltonian operator.[48] The equilibrium density operator is then defined from thermodynamics as:

$$\widehat{\rho}_0 = \frac{\exp\left(-\widehat{H}\hbar / k_b T\right)}{Tr\left\{\exp\left(-\widehat{H}\hbar / k_b T\right)\right\}}. \tag{2.85}$$

From equation 2.85, one finds that the diagonal matrix elements of ρ_0 (probability of finding a spin in some particular state) are described by a Boltzmann distribution.[48,49] If we substitute equation 2.85 for the density operator in 2.84 and consider the system to be in the high temperature limit (valid for temperatures above a few Kelvin), we find that:

$$\overline{M_z} = \frac{Tr\left[\widehat{M_z}\exp\left(-\widehat{H}\hbar/k_BT\right)\right]}{2I+1}. \tag{2.86}$$

By performing a series expansion on the exponential term and neglecting the significance of all but the early terms in the series, we find that the bulk average *z* magnetization is roughly equivalent to the following expression:

$$M_z \approx \frac{\gamma^2\hbar^2 B_0}{k_BT(2I+1)}Tr\left[\widehat{I_z^2}\right] = \frac{N\gamma^2\hbar^2 B_0 I(I+1)}{3k_BT} \tag{2.87}$$

for a system with *N* spins. The right hand side of equation 2.87 is the Curie magnetization law, which shows us that the average bulk *z* magnetization is directly proportional to the static magnetic field strength, B_0. Therefore, the population difference of the central transition can be enhanced by increasing the magnetic field strength.

In the special case where the quadrupolar interaction dominates, increasing the applied magnetic field also improves sensitivity by narrowing the line-width of the central transition. In equations 2.81 and 2.82, the frequency shift of the central transition due to the second-order quadrupolar interaction was shown to be inversely related to the Larmor frequency. Based on our definition of the Larmor frequency in section 2.1.2, we may re-write equation 2.81 as follows:

$$\omega^{2Q}_{\frac{1}{2},\frac{-1}{2}} = \left(\frac{e^2qQ}{4I(2I-1)\hbar}\right)^2\left(\frac{4I(I+1)-3}{\gamma B_0}\right)\left(2\overline{A^{Q,rot}_{21}}\,\overline{A^{Q,rot}_{2-1}} + \overline{A^{Q,rot}_{22}}\,\overline{A^{Q,rot}_{2-1}}\right) \tag{2.88}$$

where we clearly see the inverse relationship between applied field and the orientation-dependent second-order frequency perturbation. Since the total integral under the line shape is preserved in NMR, narrowing the width of a resonance increases the intensity of the resonance with respect to the random noise.

Finally, as the applied magnetic field increases, the signal EMF produced in the coil increases. If we return to Faraday's law of electromagnetic induction, we know that a voltage is produced that is proportional to the time rate of change of the magnetic flux through the coil. Following the derivation of Hoult[89], we find that the induced voltage in the coil can be calculated from the following:

$$\varepsilon = \frac{NV_c\gamma^3 B_0^2\hbar^2 I(I+1)}{3k_B T} \tag{2.89}$$

where V_c is the volume of sample within the coil and all other symbols are as defined earlier. Though the field strength is clearly not as critical in equation 2.89 as the gyromagnetic ratio, the increase in EMF can be an important factor for low-γ quadrupolar nuclei.

2.3.3.2 Magic Angle Spinning

As mentioned in section 2.1.7, one of the major differences between liquid and solid-state NMR is the lack of rapid molecular re-orientation in the latter case. In many applications of NMR, it is desirable to obtain liquid-like resolution for solid samples, which may only be achieved by suppressing contributions from anisotropic interactions on the NMR time scale. One routine NMR method that achieves this objective is magic angle spinning (MAS) introduced by Andrew *et al*. and Lowe.[90-92] Both authors recognized from the work of Gutowsky and Pake[93,94] that by mechanically rotating the sample about an angle θ_m such that:

$$1 - 3\cos^2\theta_m = 0\,, \tag{2.90}$$

the time-averaged dipolar coupling will vanish. In fact, any part of an anisotropic interaction that depends on the 2nd Legendre polynomial (ie. contains the left side of equation 2.90) will produce a net zero contribution to the NMR lineshape under rapid rotation about the angle θ_m ($\approx 54.74°$). Looking back at section 2, we find this functional form present in the anisotropic portion of the chemical shift Hamiltonian (equation 2.54), the two spin dipolar Hamiltonian (equation 2.57), and the first order quadrupolar Hamiltonian (equation 2.78). Since the contribution of all of these interactions is averaged away over time by rotation about the angle θ_m, it is known as the "magic" angle.

To facilitate mechanical rotation, NMR samples are typically packed in ceramic cylinders known as rotors (Figure **2-7**). The tip of a rotor contains precisely machined fins and pressurized gas is used to levitate and rotate the sample. The effects of rotational averaging on the NMR spectrum are that (i) the resolution of the spectrum is improved since the lines narrow and (ii) the sensitivity is improved since the integral of the resonance is conserved. In the limiting case of infinite spinning speed and only a chemical shift interaction, each resonance in the NMR spectrum collapses to a single narrow line whose center of gravity is centered at the isotropic chemical shift. The chances of two different resonance lines overlapping under MAS are much lower than in static spectra, leading to improved resolution, and the sensitivity is enhanced since the number of spins contributing to the integral intensity has not changed. In practice, mechanical considerations and sample volume limit the available spinning speeds and therefore the benefits of MAS for extremely broad resonances. If the sample cannot be spun at a rate fast enough to produce a single line, one peak appears centered at the isotropic chemical shift surrounded by a series of "spinning sidebands" (Figure **2-8**). The

sidebands appear at integer multiples of the spin rate and thus are readily identified. Here, sensitivity and resolution are still improved, but not as much as in the very fast spinning case. Despite slightly reduced sensitivity compared to higher spin rates, the appearance of spinning sidebands can be advantageous: in some situations, resolution is actually better for one or more of the spinning sidebands than the isotropic peaks. For reasons that will be discussed in a subsequent chapter, MAS only benefits ^{87}Sr NMR in certain cases, and thus we must consider additional means to enhance the sensitivity of low-γ quadrupolar nuclei.

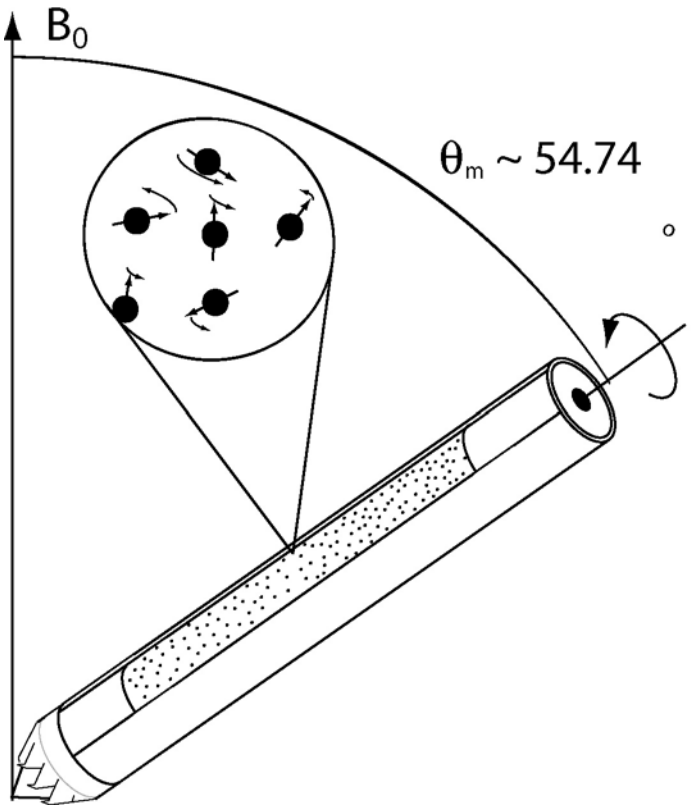

Figure **2-7**: Cross-sectional schematic of an NMR rotor oriented at the magic angle with respect to the static magnetic field.

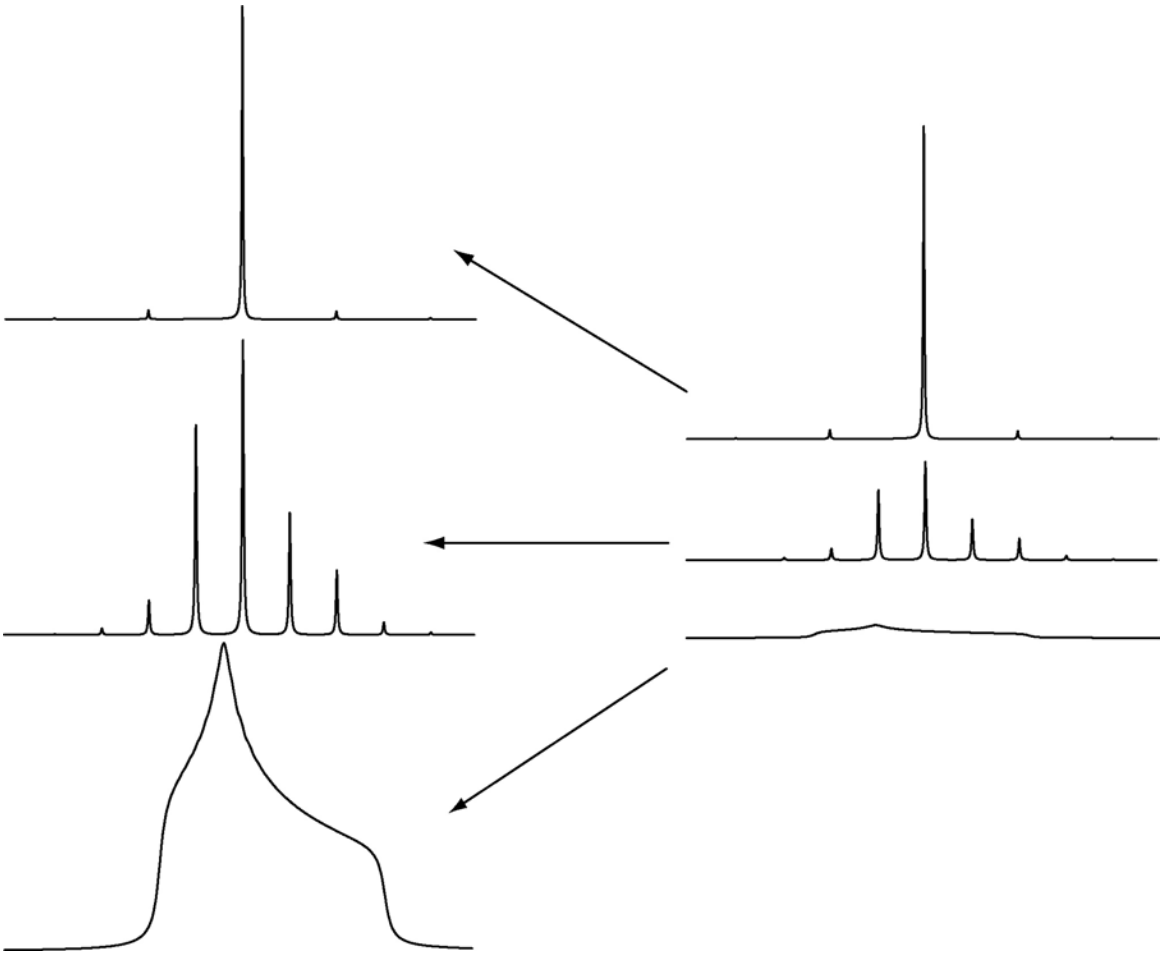

Figure **2-8**: Static vs. magic angle spinning spectra of ^{31}P with a $\Delta\delta$ of 60 ppm and an η_{cs} of 0.50. The spectra in the right column are plotted on the same intensity scale while the left column contains normalized versions of the spectra. The middle spectrum was simulated with 5 kHz MAS conditions, producing a sideband pattern that is similar to the static spectrum. The top spectrum was simulated with 20 kHz MAS and collapses to nearly a single peak.

2.3.3.3 Quadrupolar Carr-Purcell-Meiboom-Gill (QCPMG) Sequence

The Carr-Purcell-Meiboom-Gill pulse sequence[95] has long been used in NMR to measure the true transverse relaxation time of spins within a sample (T_2). The method is a modification of Hahn's echo experiment, where rather than a single inversion pulse and

acquisition of a half-echo, a train of inversion pulses is applied and a full echo is acquired after each pulse in the train (Figure 2.6). The inversion pulses refocus the true NMR interactions, permitting the detection of pure T_2 without the complication of magnetic field inhomogeneity. Garroway was the first to propose an alternate use of the method to reduce the line width of ^{13}C spectra in 1977.[84] The major advance for low-γ quadrupolar nuclei came in 1989, when Cheng and Ellis applied the sequence to improve the sensitivity of solid-state ^{87}Rb NMR.[85] This study prompted the low-γ work of Larsen *et al*. in the late nineties, where the method was dubbed QCPMG.[78,96-98] Larsen *et al*. and Cheng and Ellis both demonstrated that the Fourier transform of the QCPMG NMR signal breaks a static powder pattern into a series of narrow "spikelets" that map out the static pattern exactly. The spacing between these spikelets, ν_{QCPMG}, is directly related to the time interval between echo maxima in the NMR signal, meaning it may be readily controlled. All of the information stored in the static powder pattern can be retrieved from this spikelet spectrum, but sensitivity is dramatically improved as the integrated intensity of the pattern is forced into the narrow peaks. QCPMG provides the additional advantage of separating the effects of the homogeneous and inhomogeneous interactions: homogeneous interactions affect the shape of the individual spikelets while inhomogeneous interactions affect the shape of the spikelet manifold.[84,96] A number of research publications have reported improvements to the signal-to-noise (S/N) ratio of low-γ quadrupolar nuclei of roughly an order of magnitude when QCPMG is used.[78,81,83,97,99-104]

Leforte *et al*. performed a detailed theoretical analysis of the QCPMG pulse sequence in 2002 that allows us to characterize the improvement in signal and S/N ratio based on some simple parameters.[105] When the spikelet spacing is selected so as to minimize truncation effects (ie. each half echo is allowed to decay away fully before the next echo is formed), they found that the signal gain *S* is proportional to:

$$S \propto 2T_2\nu_{QCPMG} \tag{2.91}$$

where T_2 is the true transverse relaxation time in seconds and ν_{QCPMG} is the frequency separation of the spikelets in the transformed QCPMG signal. Likewise, Leforte *et al*. show that the theoretical gain in S/N ratio ($G_{S/N}$) achieved through QCPMG rather than a standard echo experiment can be calculated with the following expression:

$$G_{S/N} = 2\nu_{QCPMG}\sqrt{T_2 T_{off}} \tag{2.92}$$

where T_{off} is the time required for the NMR signal to approach the noise level in a standard echo experiment. As both of these equations show, the sensitivity enhancement is directly related to the spikelet spacing and the length of data acquisition (within the limits of T_2).

Leforte *et al*. also analyzed a few data processing methods for QCPMG spectra, one of which is the so-called "comb" filter originally proposed by Lipton, Sears, and Ellis.[81] The comb filter is an apodization scheme where each individual half echo is apodized with an exponential function whose decay rate is similar to T_{off}. A pictorial representation of this apodization scheme (Figure **2-9**) resembles the teeth of a comb, preserving the intensities of the echo maxima while minimizing the noise between each echo maximum. This type of apodization will increase the width of the spikelet manifold

in the spectrum while significantly reducing the noise level, providing additional gains in sensitivity. The width of the individual spikelets in the transformed spectrum can be adjusted by apodizing the entire QCPMG NMR signal by a single exponentially-decaying function, analogous to the apodization of a normal NMR signal.

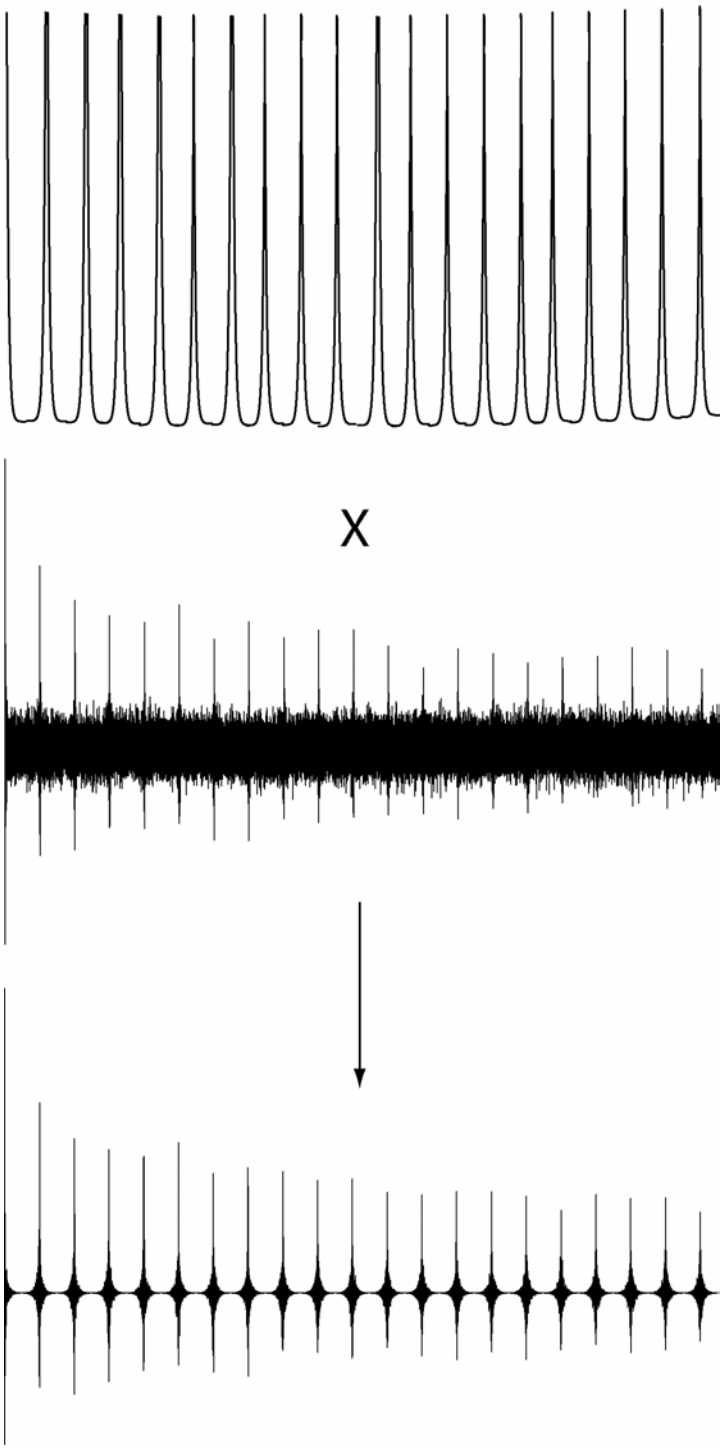

Figure **2-9**: Pictorial representation of the "comb" filter apodization scheme (top) and the effect that it has on a QCPMG NMR signal. The signal as acquired (middle) has a much higher noise level between echo maxima than following the comb filter (bottom).

QCPMG is a robust method and requires no special hardware requirements to implement. The technique may be applied to both spin ½ and quadrupolar nuclei to improve sensitivity when the resonances are fairly broad. QCPMG will be used to acquire a vast majority of the data presented in the remainder of this dissertation.

2.3.3.4 Double Frequency Sweep (DFS)

Research from the Kentgens and Conradi labs in the 1990's demonstrated that the sensitivity of half-integer quadrupolar nulcei in polycrystalline solids is enhanced when the transmitter frequency is swept adiabatically through the satellite transitions (analogous to continuous wave NMR) prior to the start of a pulse sequence.[106-109] Frequency sweeping belongs to a general series of methods (rotor assisted population transfer[86], hyperbolic secant pulses[110], fast amplitude modulation[111,112]) that increase the sensitivity of quadrupolar nuclei by either saturating or inverting the populations of the satellite transitions. By sweeping the frequency adiabatically through the satellite transitions but fast enough that double-quantum transitions are in the sudden passage regime, the populations of $\Delta m = 1$ transitions are caused to invert (Figure **2-10**) while multiple-quantum transitions remain in the sudden passage regime where they do not affect the spin system. Full inversion of each satellite transition provides a theoretical sensitivity enhancement of $2I$ for half-integer quadrupolar nuclei, making it a very efficient method for sensitivity enhancement.

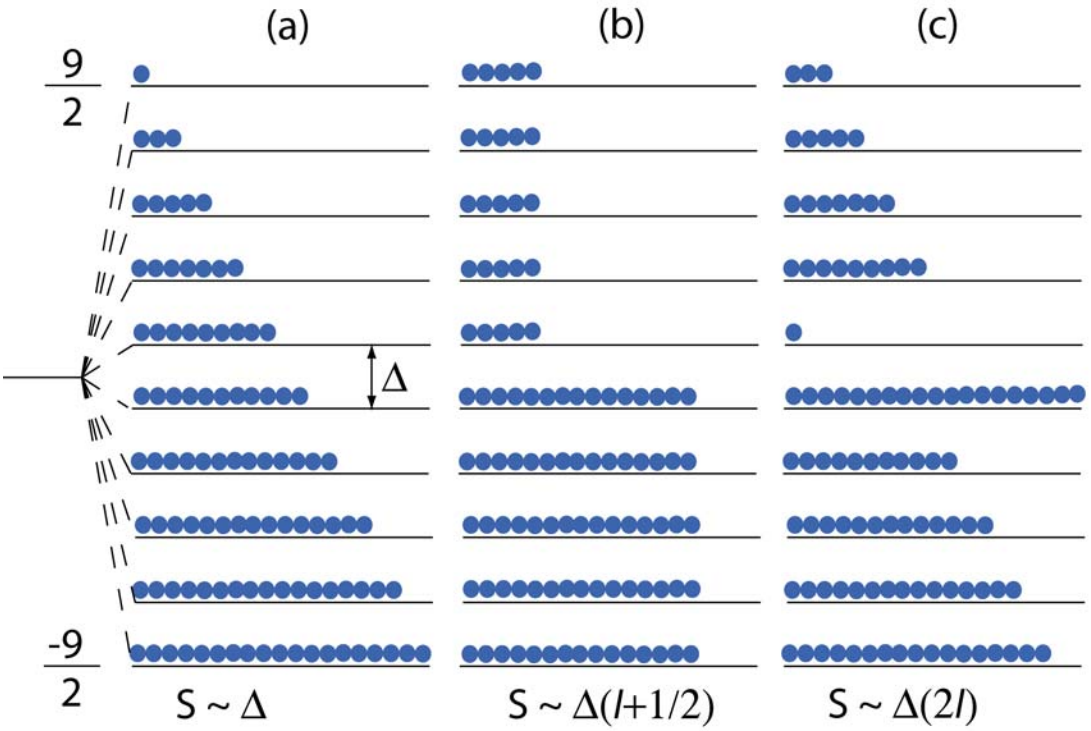

Figure **2-10**: The affect on the ^{87}Sr spin populations of (b) full saturation of the satellites and (c) full inversion through DFS. The theoretical maximum sensitivity enhancements are expressed below the energy level diagram each case.

Early frequency sweep experiments used single sweep pulses or multiple frequency-swept pulses, the latter producing greater enhancement due to the inversion of the upfield and downfield transitions consecutively. Detailed theoretical insight into CW-sweep methods may be found in the paper of van Veenendaal *et al.*[107] and will not be reviewed further here. Despite the enhancements achieved using CW swept pulses, Kentgens and Verhagen realized that the sensitivity enhancement would best approach the 2*I* limit for full inversion by sweeping the frequency through the upfield and downfield satellite transitions simultaneously rather than through multiple pulse CW methods.[82] To achieve this goal, Kentgens and Verhagen turned to amplitude-modulated pulses originally pioneered in FT-NMR by Vega and Naor in 1981.[113] Vega and Naor

demonstrated that efficient excitation of triple-quantum coherence in single crystals and subsequent conversion of this coherence back to single-quantum coherence can be achieved with amplitude modulated radiofrequency pulses where the modulation frequency ω_f matches the quadrupolar frequency ω_q. Kentgens and Verhagen found that by applying a similar amplitude modulated pulse under adiabatic conditions, simultaneous inversion of upfield and downfield satellite transitions can be realized.[82] They deemed their method the double-frequency sweep (DFS) technique, which will be a key component of many ^{87}Sr NMR studies discussed in the remained of this dissertation. The theoretical details of DFS are worked out in a series of papers from the Kentgens lab.[114-116] DFS has been shown to provide significant sensitivity enhancements for ^{87}Rb and ^{39}K when combined with the QCPMG sequence previously discussed.[83,110,117] Sensitivity enhancements due to DFS-QCPMG of up to two orders of magnitude have been reported in the literature.[83] Clearly, DFS-QCPMG represents a promising method for low-γ nuclei.

2.3.4 Transfer of Populations by Double Resonance (TRAPDOR)

Spin-spin interactions, such as dipolar coupling in solids and scalar coupling in liquids, may interfere with an NMR experiment by broadening and/or splitting the resonances. At the same time, dipolar coupling interactions also provide a mechanism to transfer magnetization between coupled spins, which may be advantageous to the NMR spectroscopist. By transferring magnetization between nuclei, one can in principle enhance the sensitivity of less abundant spins and/or determine connectivity and inter-

nuclear distances. When magnetization is transferred from an abundant spin population to a sparse spin population for sensitivity enhancement, the technique is called cross polarization (CP)[64,118]. Cross polarization can also be useful if coupled nuclei have dramatically different longitudinal relaxation rates, as is the case for ^{1}H-^{29}Si couplings. Likewise, a number of double resonance solid-state NMR techniques that determine connectivity and/or inter-nuclear distance rely on magnetization transfer via heteronuclear dipolar couplings.

The transfer of populations by double resonance (TRAPDOR) technique pioneered by van Eck and colleagues in 1990[66,119] is one example of such a method. A TRAPDOR experiment is part of a sub-class of double resonance methods known as difference experiments and thus has two parts (Figure 2-6). In the first step, a rotor-synchronized echo experiment is performed on the detect nucleus (A) and the initial signal, S_o, is acquired. In the second step, the echo experiment is repeated on the detect nucleus, but this time a spin lock pulse is applied on the second channel (B) during either the first echo delay or during both echo delays. This "dephasing" pulse prevents any A nuclei that are strongly coupled (i.e. close in space) to B nuclei from re-focusing following the inversion pulse on the A channel. Therefore, the echo signal from step two (S_f) is slightly attenuated and if one subtracts S_f from S_o, the peaks that appear in the difference spectrum correspond only to A spins that are coupled to B spins. TRAPDOR therefore provides a mechanism to indirectly detect ^{87}Sr nuclei through interactions with more abundant spins, such as protons in waters of hydration. TRAPDOR is generally considered to be a qualitative experiment: the efficiency of the dephasing process must be known in order to obtain any quantitative information from the difference spectrum. A

detailed discussion of the theory and limitations of TRAPDOR may be found in the papers of Grey, Veeman, and Vega[120] and Grey and Vega[66].

TRAPDOR has become an increasingly popular method in recent years and as such, a complete review of the TRAPDOR literature is beyond the scope of this dissertation. Typically, TRAPDOR is used when there is a spin ½ nucleus coupled with a quadrupolar nucleus, as is the case in many phyllosilicate and tectosilicate minerals. TRAPDOR has been used by numerous authors to examine ^{1}H-^{27}Al and ^{29}Si-^{27}Al connectivity in zeolites and glasses.[66,121-123] TRAPDOR studies of ^{31}P-^{27}Al connectivities in AlPO, SAPO, phosphate glasses, and lamellar materials have also been explored.[124-126] In chapter 5, ^{1}H-^{87}Sr TRAPDOR will be used to detect strontium nuclei sorbed to the exterior surfaces of minerals and hydrated interlayer species.[127]

Chapter 3

^{87}Sr Magic Angle Spinning NMR

As mentioned in chapter 2, one of the most common methods for improving sensitivity in solid-state NMR is to mechanically rotate the sample about the "magic" angle (MAS NMR). In many cases, MAS NMR also improves resolution, though the extent of this effect depends on the spinning rate, width of the resonances, and their frequency separation. Because of these factors and the potential for multiple unique strontium environments in complex materials, MAS is an attractive approach for strontium NMR studies. However, in the case of very broad resonances that one typically observes with strong quadrupolar couplings, MAS may have little effect on the sensitivity and decrease rather than improve resolution. The initial ^{87}Sr NMR investigations of this thesis will therefore focus on exploring the utility and limitations of ^{87}Sr MAS NMR in simple, well-characterized samples where strontium is abundant.

The first section of this chapter will highlight the subset of systems where MAS NMR is useful, specifically those with low or no electric field gradient (EFG) at the strontium site(s). Three inorganic strontium compounds where strontium nuclei have a symmetric coordination sphere were studied at conventional field strengths and spinning speeds. When the coordination sphere is symmetric, MAS is shown to provide sufficient sensitivity and resolution enhancement for observing the strontium NMR spectrum at moderate field strengths. One useful application of ^{87}Sr MAS NMR in low EFG

materials is also presented, where the distribution of electric field gradients due to defects in the crystal structure is calculated from the MAS NMR results.

The second section of the chapter presents ^{87}Sr MAS NMR studies of samples where a moderate to large electric field gradient exists at the strontium lattice sites. Experimental spectra collected at static fields of 11.74 T and 21.14 T demonstrate that MAS can be useful for quadrupolar coupling constants below 10 MHz. Beyond quadrupolar couplings of 10 MHz, the benefits of MAS degrade significantly with increasing quadrupolar coupling. Theoretical simulations that support these conclusions and identify the limiting conditions of quadrupolar coupling and spin rate at 11.74 T and 21.14 T are also offered. The ineffectiveness of MAS NMR in some of these samples provides the motivation for pursuing the static quadrupolar Carr-Purcell-Meiboom-Gill (QCPMG) methods discussed in the remainder of the chapters.

3.1 MAS of Low Electric Field Gradient Materials (This section contains excerpts of reference 75, copyright the American Physics Society)

In this section, strontium oxide (SrO), anhydrous strontium chloride ($SrCl_2$), and strontium fluoride (SrF_2) are examined with MAS NMR. Strontium oxide has a rock salt structure where strontium is coordinated to six oxygen atoms in an octahedral arrangement. Strontium chloride and strontium fluoride are both structural analogues of fluorite, CaF_2, where the strontium atoms sit at the center of a cube of anions, producing a symmetric, eight-coordinate strontium site. The ideal symmetry of these coordination environments theoretically eliminates the possibility of a strong strontium quadrupolar interaction, as no electric field gradient is produced at the strontium site. In theory, ^{87}Sr

MAS NMR will yield a single narrow peak appearing at the isotropic chemical shift regardless of the applied field. MAS NMR experiments were performed at two field strengths in order to (i) confirm that little to no quadrupolar interaction was present in the samples and (ii) demonstrate that MAS NMR is a highly effective technique for observing strontium nuclei in symmetric environments.

3.1.1 Experimental

3.1.1.1 Samples and Sample Preparation

Strontium oxide (99.9% metals basis) and anhydrous strontium chloride (99.99+ %) were obtained from Sigma-Aldrich. Strontium fluoride (99% metals basis) was obtained in its anhydrous form from Alpha Aesar. As these chemicals are moisture sensitive, they were stored under vacuum in a desiccator at room temperature. Samples were packed and sealed in 5 mm outer diameter, pencil-type MAS rotors in an argon filled glove bag before performing NMR experiments, thereby minimizing exposure to atmospheric moisture.

3.1.1.2 MAS NMR

MAS echo experiments were performed on both a Varian/Chemagnetics wide-bore Infinity 11.74 T NMR spectrometer (^{1}H resonance frequency of 500 MHz) using a 5 mm triple resonance MAS probe, and a home-built Tecmag Libra 9.4 T instrument (^{1}H resonance frequency of 400 MHz) using a second 5 mm triple resonance MAS probe.

The low channels of each probe were tuned to the strontium resonance frequencies of 21.662 MHz and 17.333 MHz at 11.74 and 9.4 T, respectively. Echo experiments of the θ - τ_1 - 2θ - τ_2 - *acquire* variety (Figure 2.6) were implemented to eliminate the effects of acoustic probe ringing on the spectra while maximizing signal intensity.[128] All spectra are referenced to the ^{87}Sr resonance from a 1 M aqueous solution of $SrCl_2$ prepared from $SrCl_2 \cdot 6H_2O$. In each MAS experiment, the delays (τ_1 and τ_2) were adjusted so as to synchronize the experiment with the rotor period and to ensure the collection of the echo maximum.

At 11.74 T, spectra were collected at a spin rate of 8 kHz with corresponding delays of τ_1 = 116 μs and τ_2 = 106 μs. A central-transition selective π/2 pulse width of 4.4 μs was found for the solid samples from the liquid π/2 pulse width by assuming a scaling of nutation frequency by I + ½. Either 4,096 or 8,192 data points were collected in each acquisition while sampling every 5 μs. The spectrum for SrO is an average of 10,240 scans while 40,960 scans were acquired for SrF_2 and $SrCl_2$.

MAS experiments at two spin rates were performed at 9.4 T; 8 kHz to confirm the absence of second order quadrupolar effects (see following paragraph) and at 5 kHz (τ_1 = 196 μs, τ_2 = 186 μs) to generate a greater number of spinning sidebands for use in the application presented in section 3.1.3. Experiments at 9.4 T were acquired with a central transition selective π/2 pulse width of 4 μs and a 600 kHz sweep width. The oxide and chloride spectra at both spin rates are an average of 61,440 acquisitions with 16,384 points collected during each acquisition cycle. Because the signal to noise ratio of the strontium fluoride was so poor compared to the other samples at 11.74 T, 153,600

acquisitions were collected for this sample at 9.4 T, again with 16,384 data points per acquisition. A Bloch-decay experiment at 5 kHz employing sufficient acquisition/receiver delays to remove ringing effects was also performed on the $SrCl_2$ sample to test the quantitative accuracy of peak integrals calculated from the echo experiments.

All spectra were processed by phasing the free induction decay (FID) and left shifting the data until the first data point in the "real" quadrature channel corresponded to the echo maximum. Exponential apodizations in the time domain equivalent to 50 Hz of Lorentzian broadening were applied to each data set prior to Fourier transformation. The resonance lines for the 8 kHz data at both field strengths were also analyzed in DMfit[129] to extract the peak position. From the peak shifts at two fields, one can in principle calculate the isotropic chemical shift and quadrupolar product ($P_q = C_q\sqrt{1+\frac{\eta^2}{3}}$) and confirm the absence of second-order quadrupolar effects.

3.1.2 Spectra of SrO, SrF_2, and $SrCl_2$

Strontium oxide has a simple cubic crystal structure in its anhydrous form and, therefore, an ideal crystal will contain strontium in a symmetric six-coordinate environment with $C_q \approx 0$.[130] Figure **3-1** displays the 8 kHz MAS NMR results from both field strengths for SrO. The resulting spectra have a very high signal-to-noise ratio, illustrating that MAS NMR provides suitable sensitivity enhancement to observe naturally abundant ^{87}Sr in SrO. Also, a well defined sideband manifold at an 8 kHz spin

rate can clearly be seen at both fields. The sidebands most likely originate from the 1st order quadrupolar interaction affecting the satellite transitions, indicating that some small degree of quadrupolar coupling is present in the system. This hypothesis is supported by the observed reduction in the width of the sideband manifold at 11.74 T (4500 ppm at 9.4 T reduces to roughly 3000 ppm at 11.74 T): the 1st order quadrupolar linewidth is independent of applied magnetic field, meaning that the sideband manifold will reduce on a ppm scale with increasing field strength. It is also apparent by observation that there is little shift in the position of the isotropic resonance line due to a second order quadrupolar shift (340.4 ± 1.2 ppm at 11.74 T vs. 339.8 ± 0.6 ppm at 9.4 T), implying that the overall quadrupolar coupling constant for the strontium nuclei in our SrO sample is small and that the central resonance is an isotropic peak. In fact, when P_q is calculated for SrO based on the observed difference in chemical shift between the two fields, a value of 0.6 MHz is obtained. This is below the uncertainty in the P_q value, rendering the experimental P_q statistically insignificant.

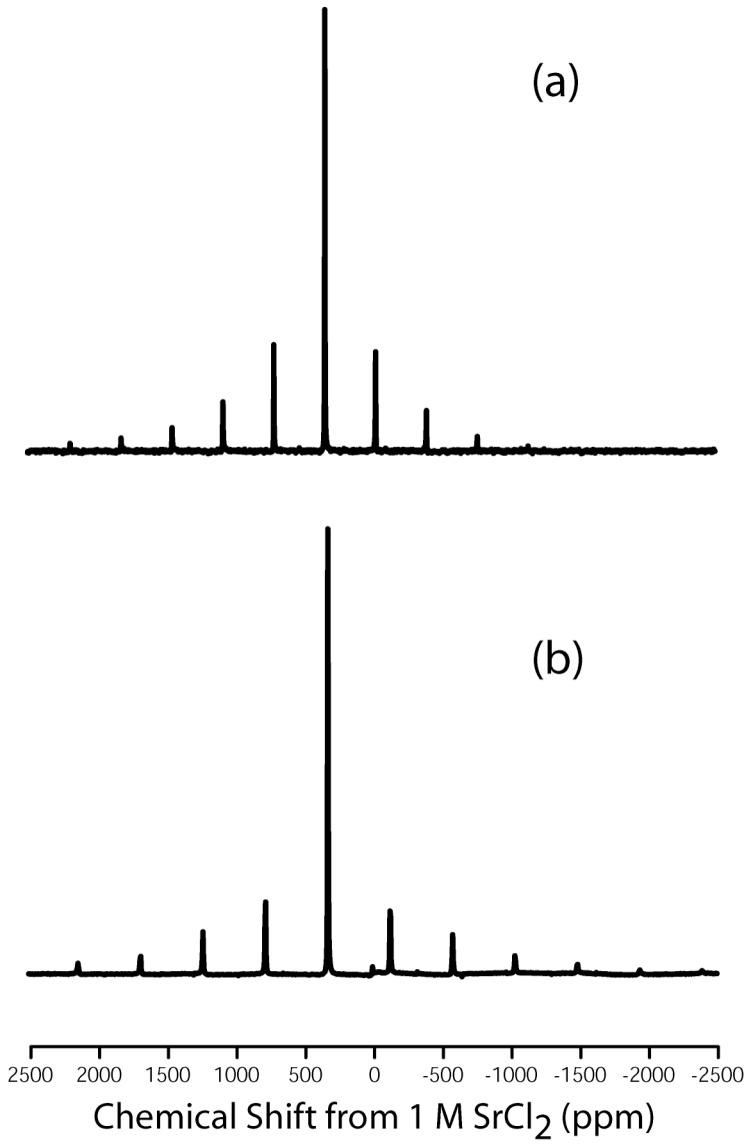

Figure **3-1**: Eight kHz ^{87}Sr MAS NMR spectra of SrO at (a) 11.74 T and (b) 9.4 T.

Just as in the case of SrO, we see that an excellent signal to noise ratio is obtained for $SrCl_2$ under 8 kHz MAS, again demonstrating that the sensitivity enhancement due to MAS is sufficient to observe the ^{87}Sr resonance low EFG samples. Strontium chloride has

the fluorite (CaF_2) structure, so that in the ideal case the strontium atoms sit in the center of a cube made up of eight chlorine atoms in a uniformly symmetric arrangement.[131] In a perfect crystal, this arrangement will also produce an EFG of zero at the strontium nuclei, producing a resonance free of second-order quadrupolar effects. Indeed, the resonance line shifts very little between the two field strengths (46.2 ± 1.2 ppm at 11.74 T vs. 45.4 ± 0.6 ppm at 9.4 T), resulting in a negligible P_q (Figure **3-2**). However, a sideband manifold similar in appearance to the manifold observed for the SrO is present, suggesting that a small 1st order quadrupolar interaction that affects the satellite transitions is present in anhydrous $SrCl_2$ as well.

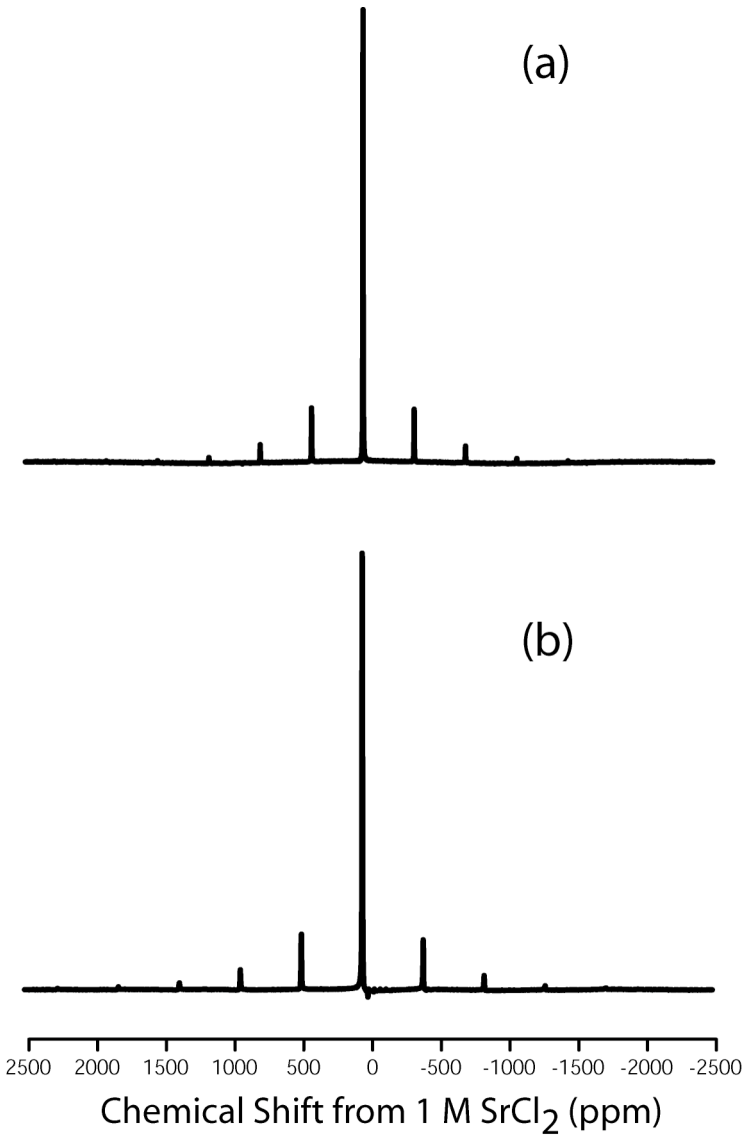

Figure **3-2**: Eight kHz ^{87}Sr MAS NMR spectrum of $SrCl_2$ at (a) 11.74 T and (b) 9.4 T.

The signal to noise (S/N) ratio obtained from similar experiments performed on a strontium fluoride sample, which also possesses the fluorite structure[132], is much lower than that of either the oxide or chloride samples (Figure **3-3**). The precise reason for this

discrepancy is unknown; however, ^{19}F MAS NMR and XRD suggest that impurity phases that affect the ^{87}Sr NMR results may be present. Another potential factor affecting the signal to noise ratio is the pulse width: without strong second order quadrupolar effects, the "selective" pulse applied in these experiments is effectively a $\pi/10$ pulse for a pseudo-spin ½ system. Despite the observed reduction in S/N ratio, we see that an easily detectable isotropic peak is produced accompanied by the same type of sideband manifold as in the strontium oxide and chloride samples. Again, the resonance line does not shift appreciably between the two field strengths (-12.3 ± 1.2 ppm at 11.74 T vs. -13.6 ± 0.6 ppm at 9.4 T), indicating that any quadrupolar interaction must be small in magnitude.

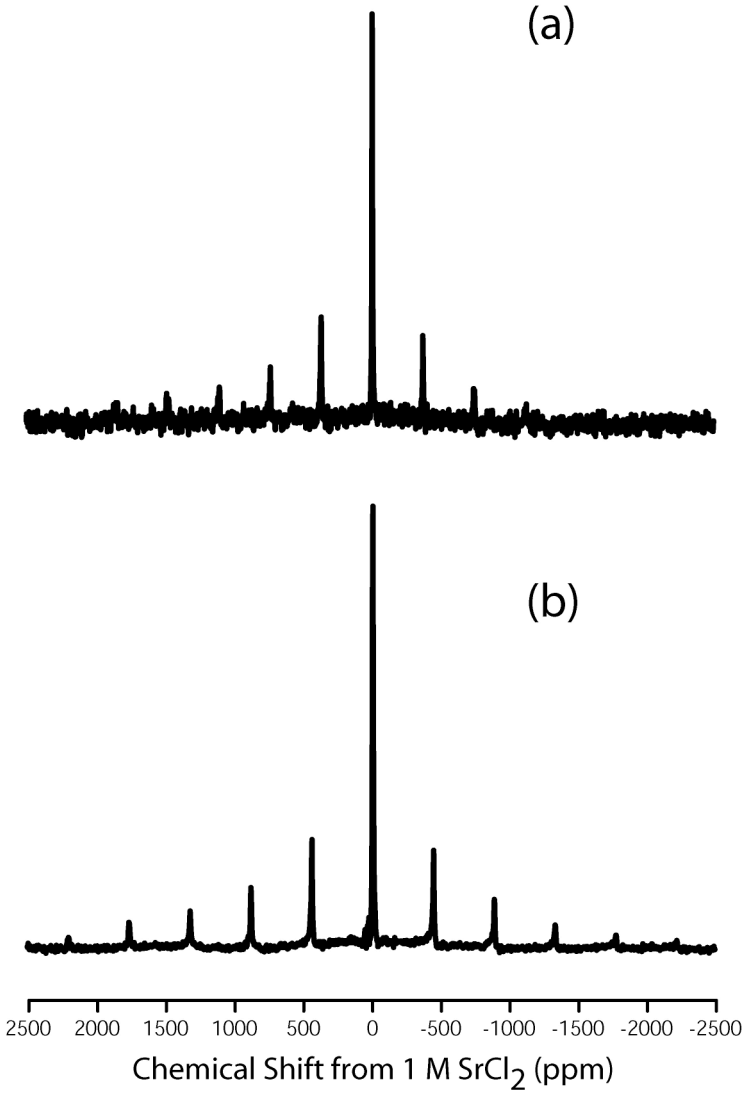

Figure **3-3**: Eight kHz ^{87}Sr MAS NMR spectrum of SrF_2 at (a) 11.74 T and (b) 9.4 T.

MAS NMR is therefore quite effective in situations where strontium possesses a symmetric coordination sphere. In all three of these systems, MAS NMR provided sufficient sensitivity to observe the isotropic resonance and the manifold of spinning

sidebands attributed to 1st order quadrupolar interactions affecting the satellite transitions. The presence of a minimal but definite quadrupolar interaction conflicts with the theory for symmetrically-coordinated strontium cations, which states that we should observe no quadrupolar effects in these samples if the ideal crystal structure holds. The observed sideband manifolds also do not map out the characteristic 1st order quadrupolar powder patterns we would expect to observe, but instead seem to map out a classic Lorentzian or Gaussian shape. To explain these anomalies, we turn to the theory of Cohen and Rief and present one potential application of ^{87}Sr MAS NMR.

3.1.3 Application: Calculation of Electric Field Gradient Distributions

Many cubic crystals (where cations possess octahedral symmetry) that contain quadrupolar nuclei display a spinning sideband manifold resulting from small first order quadrupolar couplings under MAS conditions, as we observed for SrO, SrF_2, and $SrCl_2$. One possible origin of the small quadrupolar couplings is variations in the electric field gradient at the strontium site due to defects in the crystal structure, as proposed by Cohen and colleagues.[133-136] These defects can be dislocations or point defects, which produce variations in the EFG by disrupting the cubic symmetry of the crystal.[133] Cohen and Rief show that when a small number of defects are present in a given volume, the sideband manifold due to the satellite transitions maps out a Lorenzian shape. Analyses of such sideband manifolds can provide information about the EFG distribution in the crystal system and therefore information about the defects in the crystal structure.[136]

Wadkins and Pound were the first authors to use NMR to study defects in ionic crystals, specifically the effect of applied homogeneous strain on static spectra of the ^{79}Br, ^{81}Br, and ^{127}I resonances of KBr and KI.[137] Kannert and colleagues also investigated the defects of alkali halide crystals with NMR and the lineshapes that result under each type of defect (point defects, dislocation dipoles, dislocations).[134] Similar MAS NMR methods were used to examine aluminum nuclei dissolved in a rutile (TiO_2) matrix and their proximity to defect sites.[138] Of particular interest to the field of solid-state NMR, crystal defects have been shown to be responsible for the sideband pattern that makes KBr a useful sample for setting the magic angle (utilizing either ^{79}Br or ^{81}Br MAS NMR).[139] Numerous authors have made use of NMR to study defects in semiconductor materials,[136,140-143] and Han *et al*. used a MAS NMR sideband analysis to calculate the EFG distribution due to point defects in group III-V semiconductors.[136] Other authors have examined the dislocation dynamics of defects through NMR spectroscopy.[144-146] In this sub-section, we calculate the EFG distribution about strontium nuclei in SrO, $SrCl_2$, and SrF_2 from the spinning sideband manifold observed in the MAS NMR spectra to illustrate one practical use of ^{87}Sr MAS NMR.

3.1.3.1 Theory – Calculating the EFG Distribution

To review, the quadrupolar interaction measured in a high-field NMR experiment occurs between a nucleus with a non-spherically symmetric charge distribution and the electric field gradient at the nucleus. The effect of this interaction on the NMR time

domain signal can be found by tracing the evolution of an ensemble of nuclear spins under the quadrupolar Hamiltonian, which in Cartesian coordinates is represented by:

$$H_q = \bar{I} \cdot \overline{\overline{Q}} \cdot \bar{I} \tag{3.1}$$

$$\overline{\overline{Q}} = \frac{eQ}{2I(2I-1)} \overline{\overline{V}} \tag{3.2}$$

where Q is the nuclear electric quadrupole moment, e is the charge on an electron, I is the spin quantum number of the quadrupolar nucleus, and $\overline{\overline{V}}$ is the electric field gradient tensor.[48] In the case of perfect cubic crystals (octahedral symmetry) or fluorite analogues (symmetric eight-coordinate cations), the distribution of local electric charge around a cation site in the crystal is symmetric enough that the EFG at every site would be zero, negating any measurable quadrupolar interaction.

In practice, crystals have a distribution of point defects and/or dislocations within their structure.[133] As noted, the influences of these defects on an NMR spectrum have been rigorously described by Cohen and Reif, and will be summarized briefly herein.[133] When a defect is proximal to a quadrupolar nucleus, the distribution of electrons about the nucleus is distorted, producing a small local EFG and therefore a small local quadrupolar interaction. It is known that imperfect cubic crystal systems in fact produce a distribution of quadrupolar couplings based on the number of defects and distance between defects in the crystal. Cohen and Reif show that if the number of defects in the crystal structure is large, an appreciable EFG is felt by nearly all the quadrupolar nuclei of interest. This causes larger quadrupolar couplings (usually characterized by the quadrupolar coupling constant, $C_q = \frac{e^2 qQ}{h}$) at the nuclei of interest manifested as a

second order quadrupolar broadening and a frequency shift of the central transition. This situation also produces first order quadrupolar broadenings of the satellite transitions, but the coupling is large enough that the satellite resonances are too broad for detection by conventional NMR methods. If a small number of defects are present in the sample, the quadrupolar couplings are small, producing a narrow isotropic resonance, and the impact of this EFG distribution is observable only in the first order quadrupolar broadening of the satellite transitions. In this case, the distribution of EFGs can be mapped by integrating the sideband intensities and plotting the integrated intensity against the frequency shift.[136]

Cohen and Reif showed that when small concentrations of defects are present, the shape of each satellite transition under static conditions is described by:[133,135]

$$g(\nu) = \frac{1}{\pi}\frac{\Gamma}{\Gamma^2 + \upsilon^2} \text{ for } \nu < \nu_c \tag{3.3}$$

$$\text{where:} \qquad \Gamma = \left(\frac{4\pi^2}{9\sqrt{3}}\right) NC\nu_C \tag{3.4}$$

$$\text{and} \quad \nu_C = (2m-1)\left(\frac{3e^2qQ}{4I(2I-1)h}\right) \quad . \tag{3.5}$$

Here Γ is the full width at half height (FWHH) of the resulting resonance line, eq corresponds to the electric field gradient (rigorously, eV_{zz} where V_{zz} is the z component of the electric field gradient tensor), m is defined based on the transition $m \rightarrow m\text{-}1$ corresponding to the satellite transition of interest, ν is the independent variable (frequency in this case), N is the number of defects per unit volume, C is a multiplication

factor, and the other parameters are defined as for equation 3.2. Note that the expression for the line shape takes the form of a Lorentzian distribution function (equation 3.3).

In order to map the EFG distribution over the entire sample from the series of spinning sidebands in a MAS experiment, Oldfield *et al*. show that we must calculate the width of the Lorentzian function corresponding to the sum of all the satellite transitions ($\overline{\Gamma}_m$), which can be accomplished by replacing (2*m*-1) in the expression for ν_c with a weighting factor related to the relative probability of each transition, $\overline{(2m-1)}$. If this is the case, the resulting line width is related to the number of defects per unit volume in the sample by:

$$\overline{\Gamma}_m = \left|\overline{2m-1}\right| \frac{4\pi^2}{3\sqrt{3}} \frac{NCe^2qQ}{4I(2I-1)h} \tag{3.6}$$

where $\overline{\Gamma}_m$ is the full width at half height of the Lorentzian distribution that results from fitting a Lorentzian to the integrated intensities of each sideband, $\left|\overline{2m-1}\right|$ is a weighting factor related to the relative probability of an $m \leftrightarrow m$ -1 ($m \neq ½$) transition, and *N*, *C*, *e*, *q*, and *Q* are defined as before.[135] In principle, with this equation one may calculate the number of defect sites in a sample from the FWHH of the resulting sideband fit. Unfortunately, only the product *NC* can be calculated from the Lorentzian fit without prior knowledge of the *C* values of the sample, which require a series of experiments/analysis with samples of known defect number density *N*.[136]

3.1.3.2 Calculation Results

To increase the quality of the fits, the MAS NMR experiments at a spin rate of 5 kHz (where more spinning sidebands are present) were used to determine the electric field gradient distributions. The sideband intensities were determined by least-squares iterative fitting of Lorentzian functions to each sideband using the program DMfit by the Massiot group.[129] EFG distributions were determined by plotting the integrated intensity of each sideband as a function of frequency and, as suggested in Han *et al*.,[136] a least-squares fit of these data with a Lorentzian lineshape, performed here with Origin software.

The lack of second-order quadrupolar character was confirmed for SrO by iterative fitting of the isotropic resonance, which has clearly defined Lorentzian character rather than a quadrupolar shape, and the best-fit Lorentzian line is centered at ~ 340 ppm at 9.4 T. It is also clear that little spin exchange is occurring for strontium at room temperature as the lineshape would be Gaussian if exchange was appreciable.[147,148] Since the resonance line lacks significant second-order quadrupolar character and the sideband pattern lacks sharp edges associated with first-order quadrupolar patterns (Figure **3-4**), we conclude that the sideband manifold is a result of 1st order quadrupolar effects due to a distribution of EFGs caused by a small concentration of defects in the SrO sample. The integrated sideband intensities from the 5 kHz MAS data are well fit by a Lorentzian function (R^2 = 0.9939), as expected for quadrupole couplings due to a small number of defects. The characteristics of the EFG distribution (FWHH) for strontium oxide and the

other compounds are compiled in Table **3-1** along with the isotropic chemical shifts for each sample.

Table **3-1**: Chemical shift and EFG distribution parameters

Sample	δ_{iso} (ppm)	FWHH EFG dist. (kHz)	R^2 EFG dist.
SrO	340 ± 1	50.4 ± 2.5	0.9939
$SrCl_2$	45.9 ± 1.2	30.9 ± 1.4	0.9987
SrF_2	-13.0 ± 1.2	104 ± 18	0.9508

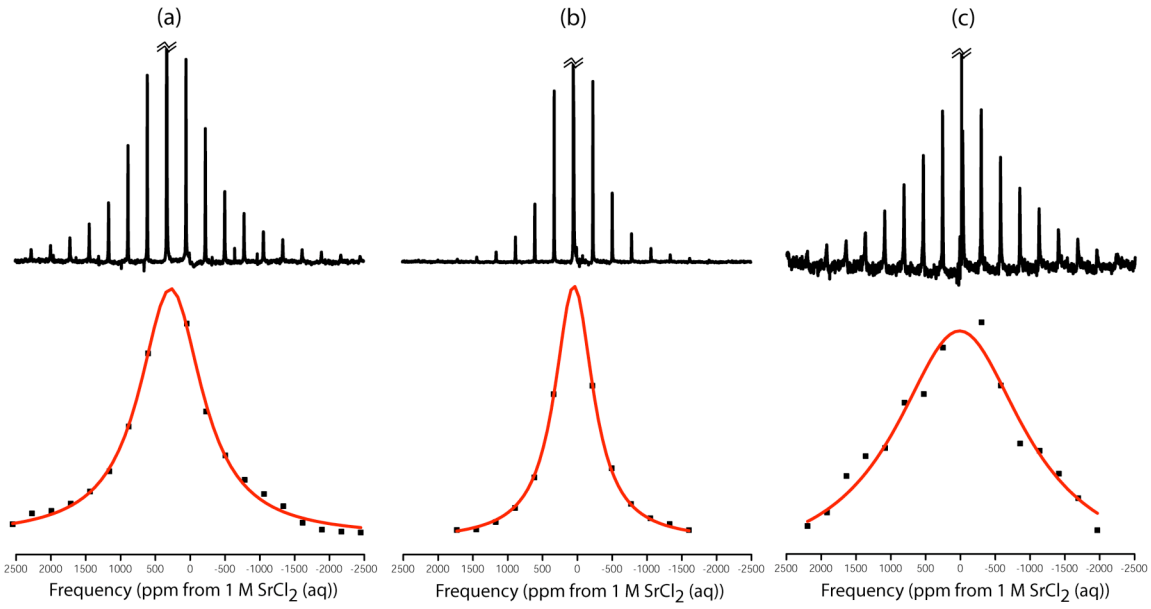

Figure **3-4**: Electric field gradient distributions (bottom row) of (a) SrO, (b) $SrCl_2$, and (c) SrF_2. The top row contains the 5 kHz ^{87}Sr MAS NMR results with the centerband cut to enhance the appearance of the spinning sideband manifold.

The isotropic resonance for $SrCl_2$ is again well fit by a Lorentzian function, indicating no appreciable spin exchange at room temperature. The sideband intensities of this sample are fit closely by a Lorentzian distribution ($R^2 = 0.9987$), again indicating a small concentration of defects as the source of the first order quadrupolar sideband manifold. This distribution has a much narrower width than the distribution for the strontium oxide sample (30.9 ± 1.4 kHz vs. 50.4 ± 2.5 kHz), which may indicate the presence of fewer defects in the strontium chloride. In order to clearly reach this conclusion, the value of *eq* arising from the defect sites in each material and the value of *C* for each sample must be known.

MAS NMR produces a sideband manifold displaying the characteristics of an EFG distribution due to a small defect concentration for the strontium fluoride sample as well. The isotropic peak of SrF_2 is well fit with a Lorentzian function, as for the other low-EFG samples, and the sideband manifold is similar in shape and breadth to that displayed by strontium oxide. The intensities from the strontium fluoride 5 kHz MAS sidebands do not provide as good a match as SrO or $SrCl_2$ to the Lorentzian distribution function expected for a point defect-based EFG distribution. The FWHH of the fluoride distribution is much larger than either the chloride or oxide samples, which may indicate that strontium fluoride has the greatest number of defect sites per unit volume depending on the values of *eq* and *C* for the three materials. The higher degree of scatter in the sideband intensity plot is likely a function of the difficulty in accurately estimating the peak areas at this S/N ratio.

3.1.4 Conclusions – Low Electric Field Gradient MAS NMR

The results presented in section 3.1 represent the first MAS NMR study of strontium nuclei in natural abundance, focusing on crystalline samples with symmetric electron environments around the strontium nuclei. In each sample studied, MAS NMR provided sufficient sensitivity enhancement to observe the isotropic strontium resonance free of second order quadrupolar effects. The NMR spectrum of each sample also featured a manifold of spinning sidebands that lacked features associated with first order quadrupolar or CSA powder patterns. The frequency shifts of the isotropic resonance at 9.4 T and 11.74 T were within the uncertainty of the shift measurements and these resonances were well-fit by a Lorentzian function, confirming that there are negligible second-order quadrupolar interactions for strontium in these materials. These observations are consistent with crystal systems that contain a low concentration of defects in their crystal structure, producing a distribution of EFGs in the sample. The electric field gradient distributions were calculated according to the method of Han *et al*. for low-defect crystalline materials. Further studies are necessary to determine the multiplication factor C and enable the calculation of the number of defects per unit volume N directly from the NMR results. Nonetheless, determination of the EFG distribution due to crystal defects does demonstrate one potential use of ^{87}Sr MAS NMR.

3.2 MAS of Moderate to Large Electric Field Gradient Materials

In a majority of crystal systems, strontium nuclei are located at lattice sites where the electric field gradient is non-zero. Strontium-87 has a relatively large nuclear electric

quadrupole moment (as compared to commonly studied quadrupolar nuclei such as ^{23}Na or ^{27}Al) in addition to its low gyromagnetic ratio and relatively large spin quantum number, meaning that strontium quadrupolar couplings are quite large when moderate EFGs are present. In these situations, the ^{87}Sr NMR spectra are dominated by the quadrupolar interaction and the resulting central transition ^{87}Sr resonances can be tens to hundreds of kHz wide. The ability of MAS NMR to increase sensitivity and resolution in these situations depends on the particular combination of quadrupolar coupling, spin rate, and magnetic field strength. In this section, we examine some well-characterized systems with moderate EFGs by MAS NMR and SIMPSON simulation to ascertain the limiting conditions of quadrupolar coupling at readily available field strengths and spin rates.

Strontium nitrate and strontium carbonate have both been shown to have moderate quadrupolar couplings (15.4 MHz and 8.6 MHz, respectively) by other authors and were selected as good model compounds for these MAS feasibility studies. The samples were analyzed with echo experiments at 11.74 T with a 9 kHz spin rate and at 21.14 T with a 20 kHz spin rate. It was found that the strontium carbonate resonance was readily narrowed at both field strengths, though the sensitivity enhancement was not very large. In the case of strontium nitrate, 9 kHz MAS at 11.74 T was not suitable as a sensitivity enhancing method, nor did it provide improvements in resolution or interpretability of the spectrum. The 20 kHz experiments at 21.14 T were more effective at narrowing the nitrate resonance, but produced a clutter of overlapping sidebands and sensitivity enhancements that are inferior to those produced by the QCPMG methods presented in the remaining chapters. In the final section, theoretical simulations performed with the SIMPSON[47] simulation program are used to confirm the experimental

observations and provide an estimate of the limiting cases of quadrupolar coupling under each set of experimental conditions.

3.2.1 Experimental

Samples of $Sr(NO_3)_2$ (99.97% metals basis) and $SrCO_3$ (99.99% metals basis) were obtained from Alpha-Aesar. Static and 9 kHz MAS θ–2θ echo experiments were performed on the 11.74 T Varian/Chemagnetics Infinity spectrometer in the Penn State NMR facility using the low channel of a commercial 5mm TR probe. The echo sequences made use of the sixteen-step phase cycle proposed by Oldfield *et al.*[149] A $\theta = \pi/2$ pulse width of 3 μs was used in combination with a pulse delay of 1 s to collect 204,800 transients for each sample. For strontium carbonate, 1024 points were acquired per scan and with a sweep width of 500 kHz. Strontium nitrate data were acquired with 2048 points per scan and a sweep width of 200 kHz. In the static experiments, delays of 60 μs and 55 μs applied before and after the inversion pulse (respectively) were found empirically to minimize the effects of acoustic ringing and ensure the collection of the echo maximum. When 9 kHz MAS was employed, the delays around the refocusing pulse were adjusted to produce a rotor-synchronized echo. By using delays of 121 μs and 117 μs, each pulse is applied with the rotor in the same rotational orientation in the stator, which also causes the echo maximum to form at that rotational orientation. The shorter second delay ensures that the echo maximum is collected. Processing began by phasing the FID and removing early data points until the first data point corresponded to the echo maximum. Each static and MAS spectrum received the equivalent of 1500 Hz of

Lorenzian apodization and was zero filled to twice the original number of acquisition points before being transformed to the frequency domain.

MAS Oldfield echo experiments with a spin rate of 20 kHz were performed on the same samples using the 21.14 T Varian Inova spectrometer available in the High Field Magnetic Resonance User Facility (HFMRF) at the Pacific Northwest National Laboratory. These data were collected with a facility-built 3.2mm DR MAS probe using the low channel tuned to the ^{87}Sr resonance frequency of 39.009 MHz at this field. A spectral width of 1 MHz was used for fast data acquisition with a smaller 400 kHz filter bandwidth to reduce the noise acquired due to the large spectral width. A $\theta = \pi/2$ pulse width of 3.3 μs was used with a pulse delay of 0.5 s to collect 40,000 transients for strontium carbonate and 80,000 transients for strontium nitrate. The delays around the re-focusing pulses were set to 100 μs to ensure rotor synchronization (2 rotor periods per delay cycle) while minimizing acoustic ringing. Both data sets involved the acquisition of 10,000 data points that were zero filled to a total of 16,384 points before Fourier transformation. The strontium carbonate spectrum received 500 Hz of Lorenzian apodization pre-transformation while the strontium nitrate required a larger 2000 Hz apodization to produce an interpretable spectrum.

Signal to noise ratios were calculated using NUTS software from Acorn. Each data set was zero filled to produce the same frequency resolution and then transformed without apodization. The signal to noise ratio was calculated over a region of ± 100 kHz from the reference frequency.

3.2.2 Strontium Carbonate

Strontium carbonate has the smaller quadrupolar coupling and should therefore be more amenable to study with ^{87}Sr MAS NMR. Static echo experiments with $SrCO_3$ produced a classic 2nd order quadrupolar powder pattern with a basal width of roughly 34 kHz at 11.74 T.

As expected, both of the spinning experiments provided substantial reduction in linewidth, as shown in Figure **3-5**. The 20 kHz MAS experiments at 21.14 T produced a resonance with a width of only 5.2 kHz, a 7-fold reduction in width over the static echo from 11.74 T and roughly 3-fold reduction in width over a static echo acquired at 21.14 T. The high-field experiment also produced zero spinning sidebands, meaning that 20 kHz MAS at 21.14 T will provide a significant improvement in resolution for quadrupolar couplings of 9 MHz and less. The lack of sidebands also indicates that 20 kHz MAS maximizes the MAS-related sensitivity enhancement at this field: when corrected for variations in the number of transients acquired, the calculated signal to noise ratio is 68.56 for the 20 kHz MAS compared to the 11.74 T static echo signal to noise of 13.5, equivalent to a greater than twenty five-fold reduction in acquisition time.

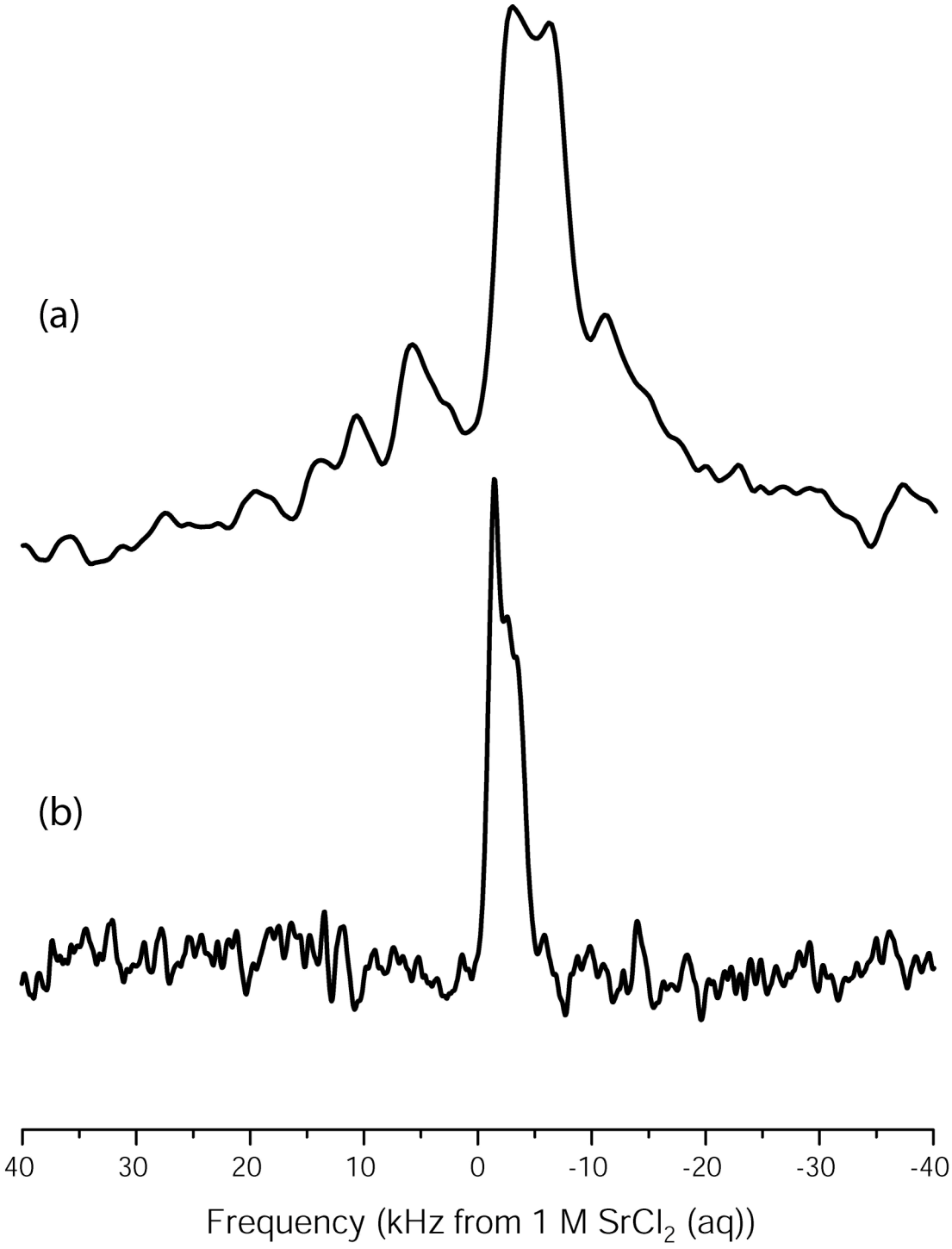

Figure **3-5**: ^{87}Sr MAS NMR spectra of strontium carbonate collected at (a) 9 kHz MAS, 11.74 T and (b) at 20 kHz MAS, 21.14 T.

With the moderate MAS spin rate of 9 kHz, the basal width was reduced from 34 kHz (static conditions) to 20 kHz at 11.74 T. Unlike 20 kHz MAS at 21.14 T, the experiment at 11.74 T does show some degree of spinning sidebands, none of which produces a recognizable quadrupolar pattern. Despite the presence of sidebands, the centerband is readily identifiable at the lower spin rate and has a signal to noise ratio 50% higher than the static echo at the same field. Despite a decreased sensitivity enhancement provided by 9 kHz MAS at 11.74 T, the 40% reduction in line width will produce improvements in resolution that could be useful in complex minerals with strontium quadrupolar couplings of 9 MHz and less.

3.2.3 Strontium Nitrate

Strontium nitrate has a single strontium environment with a quadrupolar coupling constant of 15.4 MHz and an asymmetry parameter of 0.03 as reported by Larsen *et al*.[97] This represents an intermediate level of strontium quadrupolar coupling based on the literature available at the start of this study and the logical next step for evaluating ^{87}Sr MAS NMR. Strontium nitrate produces a cylindrically symmetric 2nd order quadrupolar powder pattern under static echo conditions with a width in excess of 75 kHz at 11.74 T.

The width of the strontium nitrate resonance at 11.74 T exceeds the excitation bandwidth at a single transmitter frequency and is broad enough that 9 kHz MAS seems to provide little to no reduction in linewidth at 11.74 T. The MAS spectrum decreases the basal width of the resonance from 75 kHz to 74 kHz at a single transmitter frequency, providing little improvement in resolution under the experimental conditions (Figure **3-**

6). Additionally, line widths under both static and 9 kHz MAS conditions require the experimentalist perform identical experiments at a second transmitter frequency, significantly increasing the required acquisition time at 11.74 T. The 9 kHz MAS spectrum appears as a broad peak interrupted by the narrow resonance due to the upfield singularity of the powder pattern. The signal to noise ratio for the 9 kHz MAS spectrum is only 22% larger than for the static echo and the calculated improvement is primarily a result of the increase in intensity of the singularity. Since 9 kHz MAS at 11.74 T does not provide substantial improvement to sensitivity or to the interpretability of the spectrum, it is concluded that 9 kHz MAS at 11.74 T is insufficient to benefit resonances with quadrupole couplings of 15 MHz and greater.

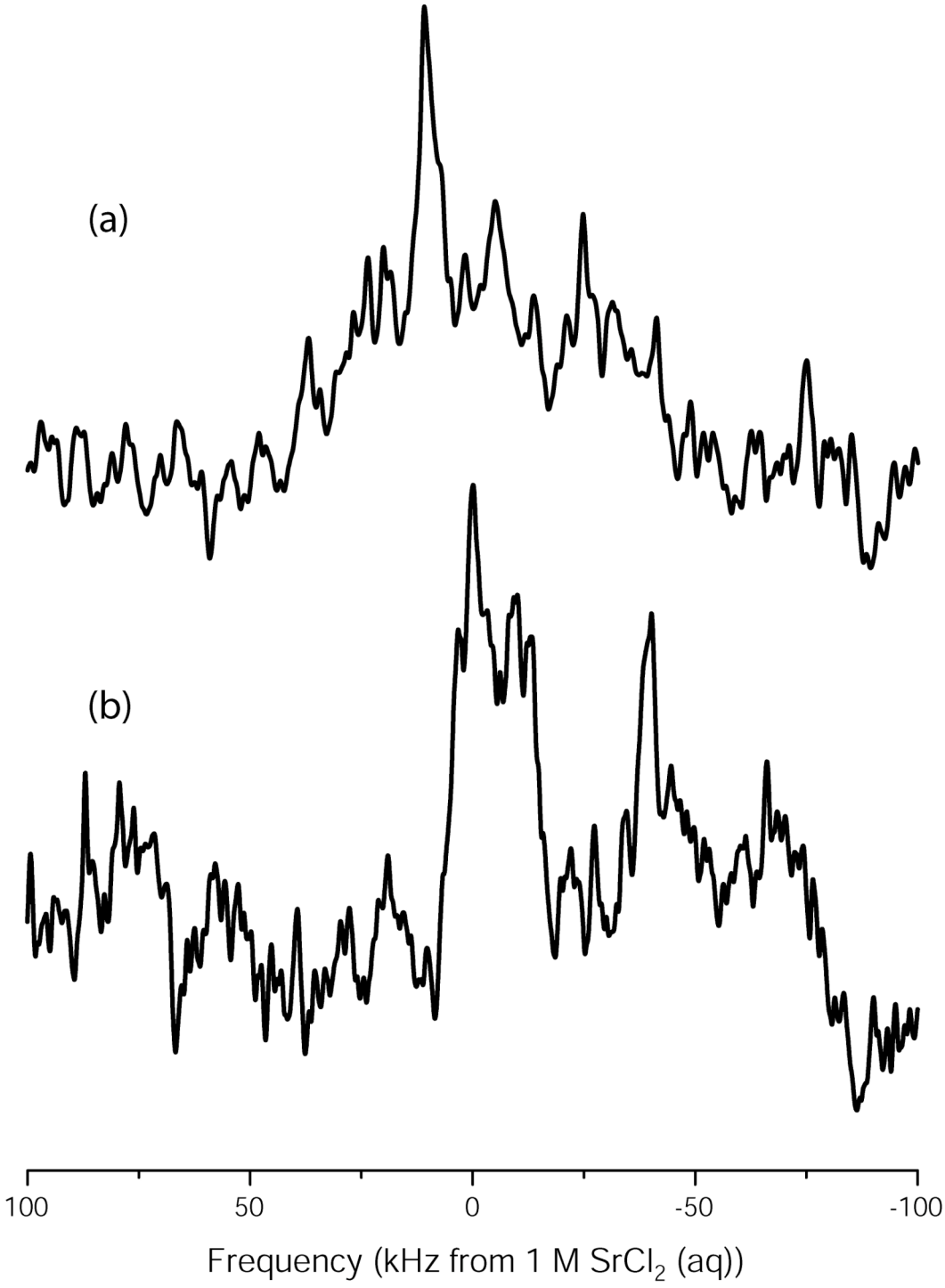

Figure **3-6**: ^{87}Sr MAS NMR spectra of strontium nitrate collected (a) at 9 kHz MAS, 11.74 T and (b) at 20 kHz MAS, 21.14 T.

The 20 kHz MAS experiments at 21.14 T produced a resonance with a basal width of 24 kHz, roughly 60% of the basal width of a static echo experiment at 21.14 T and significantly less than the static echo at 11.74 T. An improvement to the signal to noise ratio also occurs: when corrected for variations in the number of transients, 20 kHz MAS at 21.14 T results in a signal to noise ratio 2.67 times higher than the 11.74 T static echo (S/N ratio, 20 kHz MAS = 4.8 vs. 1.8 for the 11.74 T static echo). However, the resulting MAS spectrum yields a very complicated line-shape that is nearly impossible to interpret. The complex shape is likely a result of central transition spinning sidebands overlapping with the centerband. There may also be slight shape perturbations due to partial excitation of the two nearest satellite transitions under the particular set of pulse conditions. Based on the results at 21.14 T, 20 kHz MAS provides some sensitivity enhancement but is inadequate at improving the interpretability of strontium spectra when the quadrupolar coupling exceeds 15 MHz.

3.2.4 MAS Limitations

The experiments in sub-sections 3.2.2 and 3.2.3 show that there is a relationship between the applied field strength, the spin rate, and the ^{87}Sr quadrupole coupling that is directly related to the effectiveness of MAS NMR. A somewhat poor intuitive feel for the limiting conditions of quadrupole coupling can be extracted from the empirical results, namely that ^{87}Sr quadrupole couplings of 9 MHz and less can be studied with conventional MAS instrumentation while larger couplings seem not to benefit from readily available MAS conditions. Ideally, MAS experiments would be performed on

samples with a wider range of ^{87}Sr quadrupole couplings to improve the quality of our understanding, but factors such as the availability of samples and instrument time make this a difficult task. To alleviate this dilemma, SIMPSON[47] was used to calculate strontium MAS NMR spectra at a variety of spin rates and quadrupolar couplings at applied fields of 11.74 T and 21.14 T.

Samples of the simulation input files may be found in Appendix A, examples A.4.5 and A.4.6. Calculations were performed on a home-built, dual 3.0 GHz Xeon computer with 3 GB of available memory running Red Hat Enterprise Linux WS 3.0. Simulations were performed at MAS spin rates of 5 kHz, 10 kHz, 15 kHz, and 20 kHz for quadrupolar coupling constants of 10 MHz, 15 MHz, 20 MHz, and 30 MHz at both fields. The initial state of the system was specified as *I1x*, meaning that the net magnetization existed purely in the *x*-*y* plane and the detect parameters were set to observe only the central transition (making the assumption of only I_x magnetization valid). Each simulated spectrum therefore contains the central transition centerband and associated central transition spinning sidebands only; satellite effects are not observed. Each simulation was performed with a built-in crystal file containing 986 crystallite orientations determined by the ZCW method (see appendix A). The number of gamma angles was varied such that the spin rate multiplied by the number of gamma angles provided a sweep width of roughly 500,000 kHz for each simulation. The compute time for each calculation directly depended on the number of gamma angles used in the calculation, with higher numbers of gamma angles leading to longer simulations. The simulated time-domain signals were processed with NUTS software where apodizations equivalent to 500 Hz, 500 Hz, 1000 Hz, and 2000 Hz of Lorenzian line-broadening were

applied to the simulations with quadrupolar coupling constants of 10 MHz, 15 MHz, 20 MHz, and 30 MHz, respectively. Multiplication factors required to normalize the intensities of each simulation were calculated by assigning the maximum intensity of the C_q = 10 MHz, 20 kHz MAS spectrum at each field a value of 1.0.

Figure **3-7** contains the simulation results at an equivalent field strength of 11.74 T. Initially, we observe that the C_q = 10 MHz, 10 kHz MAS spectrum is very similar in appearance to the experimental spectrum obtained for strontium carbonate. This is expected since this set of simulation conditions mimic those applied in the strontium carbonate experiment and confirm that these conditions do enhance sensitivity and resolution. We may safely conclude that spin rates of 10 kHz and greater are sufficient at 11.74 T to improve the sensitivity and resolution of a C_q = 10 MHz resonance from these data. On the opposite end of the spectrum, we observe that the C_q = 30 MHz resonances resemble static powder patterns at all the MAS speeds involved in the calculations at 11.74 T. The sensitivity improvement due to 20 kHz MAS conditions for C_q = 30 MHz is really a product of the intense singularity near -150 kHz and therefore sensitivity is not improved at this range of MAS speeds for broad resonances. For the intermediate values of quadrupolar coupling, we observe that MAS at any spin rate seems to complicate the resulting spectrum rather than improving its interpretability with the possible exception of the C_q = 15 MHz, 20 kHz MAS spectrum. We also note that the sensitivity of the spectrum drops significantly as the quadrupolar coupling constant increases, suggesting that alternative methods of sensitivity enhancement should be explored. The simulation results confirm the conclusions from the empirical studies: MAS NMR at 11.74 T is not

effective for strontium resonances with quadrupolar coupling constants much larger than 10 MHz.

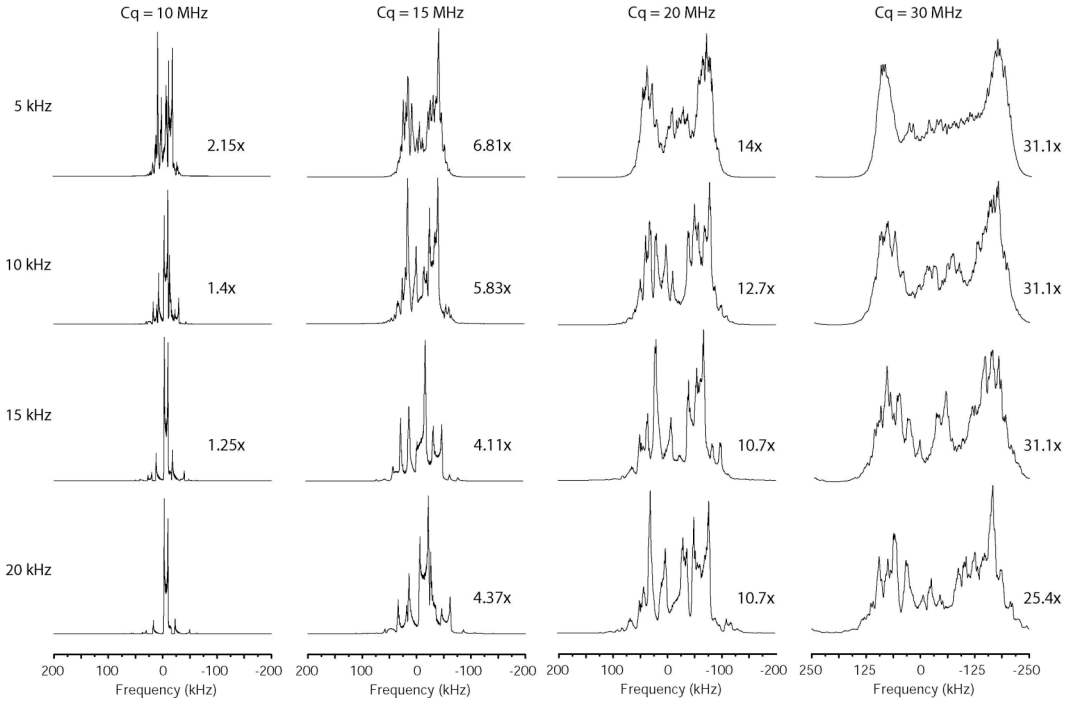

Figure **3-7**: ^{87}Sr MAS NMR simulations with an applied field of 11.74 T.

Figure **3-8** contains the simulation results from 21.14 T. At this field, the resonances will all be narrower since the second order quadrupolar linewidth scales inversely with applied field. Resonances that are not as broad should increase the effectiveness of MAS, a fact that is readily apparent in Figure 3-8. We observe that all of the applied spin rates increase the resolution and interpretability of the data for the C_q = 10 MHz spectra. In fact, spinning the sample at 20 kHz yields no central transition spinning sidebands, again in agreement with the experimental strontium carbonate spectrum acquired under similar conditions. The simulations show that resonances of C_q

= 15 MHz can be effectively observed with spin rates greater than 15 kHz at 21.14 T and that 20 kHz MAS can improve the interpretability and sensitivity up to C_q = 20 MHz resonances. These results do not quite match with the experimental results for strontium nitrate, which were difficult to interpret at this field under 20 kHz MAS. Perhaps interferences from satellite transitions ignored in the simulations are the source of the empirical complications. Once again, MAS does not seem to provide any reasonable enhancements in the case of resonances with quadrupolar coupling constants of 30 MHz and greater, though in this case only the 5 kHz and 10 kHz MAS resonances appear similar to static powder patterns at 21.14 T. As one would suspect, the sensitivity of the simulations from 21.14 T are all greater than those from 11.74 T. A roughly 30% improvement in sensitivity becomes apparent solely due to the reduction in line width at the higher field. The advantages of increasing the field strength will be explored further in the following chapter. The simulations show that MAS NMR is more effective at 21.14 T and that resonances with quadrupolar coupling constants up to 20 MHz seem to benefit from MAS at this static field.

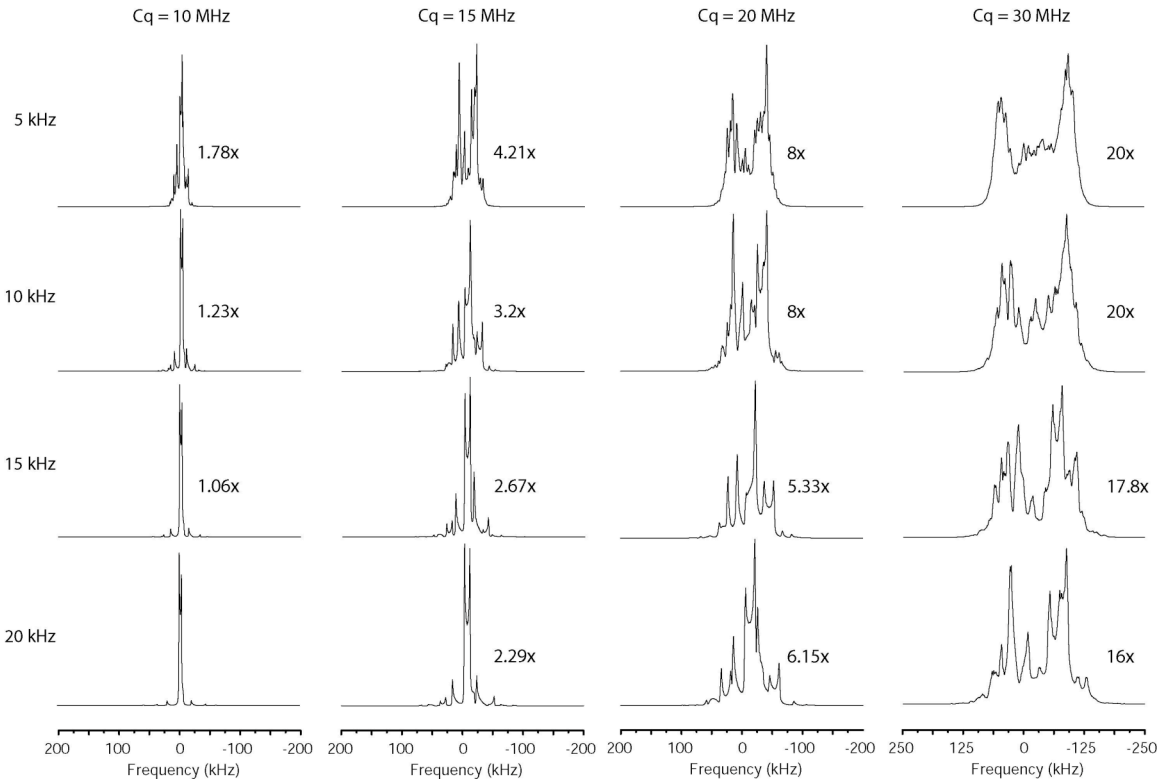

Figure **3-8**: ^{87}Sr MAS NMR simulations with an applied field of 21.14 T.

3.2.5 Conclusions – ^{87}Sr MAS NMR with Moderate to Large EFGs

Through experiment and calculations, the effectiveness of ^{87}Sr MAS NMR was explored for quadrupolar couplings of 9 to 30 MHz. Both empirically and from simulation results, it was found that MAS NMR at 11.74 T is not an effective method for samples with ^{87}Sr quadrupolar coupling constants of greater than 10 MHz. Spin rates greater than 10 kHz at this field can provide some benefit for samples with quadrupolar

couplings smaller than 10 MHz. MAS NMR is more effective at 21.14 T, and may benefit samples with quadrupolar couplings up to 20 MHz when 20 kHz MAS is employed. At both fields, a slight sensitivity enhancement was observed experimentally, but 20 kHz MAS NMR experiments at 21.14 T did not permit observation of strontium sorbed in phyllosilicate minerals. More aggressive sensitivity enhancing NMR methods proved necessary to achieve this goal, as discussed in the remaining chapters.

Chapter 4

Enhancing the Sensitivity of ^{87}Sr NMR

As discussed in chapter 2, numerous methods other than MAS may be used to improve the sensitivity of low-γ quadrupolar nuclei. These methods may be classified into three general categories: (i) multiple pulse sequences, (ii) preparatory pulse sequences that re-arrange the spin populations, and (iii) specialized hardware. Many of the pulse-related techniques, such as the quadrupolar Carr-Purcell-Meiboom-Gill (QCPMG) sequence and double frequency sweep (DFS) preparation pulse, have shown great potential in studies with other quadrupolar nuclei.[78,82,83,97,98,100-103,105,110,115,116,150,151] A new generation of ultra high-field spectrometers, such as the 21.14 T instrument at the Pacific Northwest National Laboratory (PNNL), have become available in recent years and are ideal for studying low-γ quadrupolar nuclei. In this chapter, the sensitivity enhancing properties of QCPMG and DFS-QCPMG NMR at a static field of 21.14 T will be explored for ^{87}Sr nuclei in simple crystalline phases.

Section 4.1 focuses on the advantages of high-field ^{87}Sr QCPMG NMR over the static Hahn-echo method. The strontium cations in three inorganic compounds (strontium nitrate and the natural minerals strontianite ($SrCO_3$) and celestine ($SrSO_4$)) are analyzed with Hahn-echo experiments at two fields and with QCPMG NMR at 21.14 T. QCPMG at 21.14 T provided sensitivity enhancements of roughly two orders of magnitude over static echo experiments performed at 11.74 T, equating to the appearance of a strontium resonance 10,000 times faster. The strontium quadrupolar parameters are

extracted from the NMR spectra and related back to the crystal structure determined from X-ray diffraction (XRD) analyses. The results show that the ^{87}Sr quadrupolar parameters (particularly the asymmetry parameter) are highly sensitive to the nature of the nearest neighbor coordination sphere and thus can be used to characterize the local strontium binding structure in more complex materials.

The second section (4.2) explores the additional sensitivity enhancement obtained by including DFS preparation with QCPMG NMR at 21.14 T. Inclusion of the DFS pulse is found to provide an additional order of magnitude reduction in acquisition time, permitting time-efficient studies of materials that cannot be observed with QCPMG alone. DFS-QCPMG is then used to analyze a number of more complicated inorganic and organic crystal systems. In the first application of DFS-QCPMG, an inorganic compound that contains multiple phases with varying degrees of hydration will be examined. The results provide insight into the effects that hydration may have on the strontium NMR spectrum of environmentally relevant strontium sorption materials. The second set of studies examines strontium-bearing organic compounds that include both strontium and protons. Strontium binding in these simple organic compounds reveals potential strontium interactions with soil organic matter that may affect the rate of strontium transport. Through the lessons learned from these relatively simple systems, it will be possible to perform more detailed analyses of strontium binding in phyllosilicates and other complex materials in chapters 5 and 6.

4.1 Quadrupolar Carr-Purcell-Meiboom-Gill at 21.14 T (This section contains excerpts of reference 99, copyright the Elsevier publishing group)

Despite the availability of techniques for overcoming the sensitivity limitations of low-γ quadrupolar nuclei, in only two cases have sensitivity enhancing NMR methods been applied to ^{87}Sr prior to the work presented here.[75,97] The majority of the literature regarding solid-state ^{87}Sr NMR consists of studies with strontium nuclei in highly symmetric environments, as discussed at the beginning of chapter 3.[75,152,153] To review, Weber and Allen studied the changes in strontium quadrupolar parameters in strontium titanate (cubic symmetry around the strontium nuclei) as the material went through a phase change at 110 K.[152] More recently, Gervais *et al*. examined mixed barium-strontium titanates at various barium to strontium ratios and presented preliminary ^{87}Sr NMR data showing that the narrow strontium resonance became broader with increasing barium content until they could no longer detect a strontium signal with Hahn-echo methods.[153]

Only two publications (excluding those associated with the research presented in this and the following chapters) have used solid-state ^{87}Sr NMR to examine systems where a moderate electric field gradient is present. Bastow published a study examining the electric field gradient at the cation site in alkaline earth carbonates with static Hahn-echo methods in which he reports the ^{87}Sr spectrum and quadrupolar parameters of the strontium site in strontium carbonate.[154] Larsen *et al.* published the only work (other than the Bowers and Mueller ^{87}Sr MAS paper discussed in chapter 3) where a sensitivity enhancing NMR technique is applied to ^{87}Sr.[97] Larsen and colleagues extracted the quadrupolar and chemical shift parameters of ^{87}Sr in $Sr(NO_3)_2$ and $SrMoO_4$ from spectra

acquired with the quadrupolar Carr-Purcell-Meiboom-Gill (QCPMG) pulse sequence at 14.09 T (ν_0^{1H} = 600 MHz).

The QCPMG experiment used by Larsen *et al.* is one of the most promising methods for the general examination of low-γ quadrupolar nuclei with solid-state NMR. A number of authors have shown that the QCPMG sequence provides up to an order of magnitude sensitivity enhancement over conventional echos (at constant field strength) for quadrupolar nuclei.[81,83,97,110] To review the discussion in Chapter 2, a QCPMG experiment involves a θ-2θ echo sequence and half-echo acquisition followed by a series of 2θ pulses with a full-echo acquisition after each 2θ pulse (Figure 2-6).[84] The Fourier transform of the resulting NMR signal is a series of sharp peaks that map out the static powder pattern, providing gains in sensitivity without sacrificing the information contained in the powder pattern. QCPMG NMR provides an additional advantage in that the sensitivity of the experiment increases by a factor of $\sqrt{2n}$ due to the acquisition of n full echos (rather than half echos) over the course of the n echo loops. Many data processing methods also exist that further improve the sensitivity of QCPMG experiments[81], as described in detail by Lefort.[105] Larsen and colleagues have also used QCPMG to study ^{67}Zn in metalloproteins, organic, and inorganic compounds as well as ^{39}K, ^{25}Mg, and ^{87}Rb in inorganic salts.[78,97,103] QCPMG experiments have also been used by other authors to study ^{25}Mg in organic compounds[81,102], ^{91}Zr in organic compounds[100], and ^{35}Cl and ^{37}Cl in organic hydrochloride salts.[101]

In this section, the stable 21.14 T magnetic field available at the Pacific Northwest National Laboratory will be used to examine strontium nuclei with QCPMG

NMR. As stated in chapter 2, high static magnetic fields are known to provide three advantages for low-γ quadrupolar nuclei: a reduction in the quadrupolar line-width due to an inverse relationship between line-width and applied magnetic field, an increased population difference of the central transition as predicted by the Curie magnetization law, and an increase in the EMF produced by the coil due to the increase in the Larmor frequency of the nucleus.[48] The goals for this section are to (i) quantify the sensitivity enhancement QCPMG and the field provide over static echos at 11.74 T, (ii) accurately report the quadrupolar parameters of strontium in strontianite ($SrCO_3$) and celestine ($SrSO_4$), and (iii) determine if QCPMG at 21.14 T (ν_0^{1H} = 900 MHz) can be used to study strontium cations in saturated clays and zeolites.

4.1.1 Experimental

4.1.1.1 X-ray Diffraction

Samples of $Sr(NO_3)_2$ (99.97% metals basis) and $SrCO_3$ (99.99% metals basis) were obtained from Alpha-Aesar. Strontium sulfate ($SrSO_4$, 99.9% metals basis) was obtained from Sigma-Aldrich. X-ray diffraction (XRD) patterns were obtained on a Phillips X'pert MPD diffractometer in the Pennsylvania State University Materials Characterization Laboratory to confirm the identity and purity of each powdered sample as received. Scans were made from 10°-90° 2θ in steps of 0.03° 2θ with a Cu-Kα source and a collection rate of one degree per minute. Experimental patterns were compared to

reference patterns in the International Center for Diffraction Data (ICDD) database to confirm the identity of each compound and identify any impurities.

4.1.1.2 Strontium NMR

All NMR spectra in this chapter were referenced to a 1 M aqueous solution of $SrCl_2$ prepared from $SrCl_2 \cdot 6H_2O$ (obtained from Sigma-Aldrich). QCPMG experiments were performed with a double resonance, cross-coil 5 mm static probe[80] on a Varian Inova 21.14 T spectrometer located at the Pacific Northwest National Laboratory (PNNL) in Richland, Washington. A selective $\theta = \pi/2$ pulse width of 3.8 μs was used in combination with τ delays of $\tau_1 = \tau_\alpha = 100$ μs and $\tau_2 = \tau_\beta = 102.5$ μs and a pulse delay of 0.5 s. The inter-pulse delays were selected to remove the effects of probe ringing from the spectra and to account for the instrumental filter delay, ensuring that the first data point collected corresponds to an echo maximum. A sampling rate of 1 MHz was used in conjunction with a receiver bandwidth of 400 kHz to allow for rapid digitization with the filter bandwidth restricted to a region just outside of the excitation profile. For strontium carbonate, 20,000 scans were acquired with twenty echo loops per scan and 1000 data points acquired per half echo. The strontium nitrate resonance was acquired over 40,000 scans with forty echo loops and 500 data points per half-echo, yielding a spikelet spacing of 1 kHz. For celestine, the resonance was too broad to excite uniformly at a single transmitter frequency. It was determined experimentally that a region of ±20 kHz around the spectrometer frequency was capable of providing NMR signals without attenuation due to the excitation or tuning profile. As such, the celestine resonance was acquired in

pieces by stepping the spectrometer frequency in 30 kHz increments. Twenty-five thousand transients were acquired at each transmitter frequency with eighty echo loops and a 2 kHz spikelet spacing. These pieces were then combined with a sky projection to produce the overall celestine resonance.[155] The QCPMG spectra were apodized with a "comb filter" scheme originally proposed by Lipton, Sears, and Ellis that involves applying an exponential apodization to each individual echo rise and decay, maintaining the signal intensity of each echo maximum while reducing the noise level between maxima.[81] The equivalent of 2000 Hz of exponential broadening was applied to each echo rise and decay, as this was found to maximize the signal-to-noise (S/N) ratio without distorting the lineshape severely.

Static θ–2θ echo experiments were performed on an 11.74 T instrument within the Penn State NMR Facility and on the 21.14 T spectrometer at PNNL in order to differentiate the sensitivity enhancements attributed to QCPMG and the 21.14 T field strength. The echo sequences made use of the sixteen-step phase cycle proposed by Oldfield *et al.*[149] A 90° pulse width of 3.8 μs was used in combination with τ delays of 60 and 50 μs or 80 and 70 μs (to minimize ringing and ensure collection of echo maximum) on the 11.74 T and 21.14 T instruments, respectively, with pulse delays of 1 s. For strontium nitrate, 204,800 transients were acquired with 1024 points per scan and with a sweep width of 200 kHz at 11.74 T while 100,000 transients were sufficient under identical conditions at 21.14 T. Strontium carbonate was acquired over 204,800 scans with 1024 points per scan and a sweep width of 500 kHz at 11.74 T while only 10,000 acquisitions were necessary at 21.14 T. Data points were removed from the beginning of each FID until the first data point corresponded to the echo maximum prior to any other

processing steps. Each spectrum received the equivalent of 500 Hz of exponential apodization followed by a single zero fill prior to Fourier transformation.

4.1.1.3 Simulations and Calculations

In order to estimate the sensitivity enhancement quantitatively, signal-to-noise (S/N) ratios of non-apodized QCPMG and echo spectra were obtained using Acorn NUTS software. The S/N ratio was calculated over identical frequency regions for each sample and corrected for variations in acquisition time by dividing each S/N ratio by the square root of the number of acquisitions n for each sample:

$$\left(S/N\right)_{norm} = \frac{\left(S/N\right)}{\sqrt{n}}.$$

The strontium sites in these materials were characterized by extracting the quadrupolar parameters (C_q and η) and isotropic chemical shift (δ_{iso}) through iterative simulations of the QCPMG spectra with the SIMPLEX method provided in the SIMPSON solid-state NMR simulation package.[47] Chemical shift anisotropy was not incorporated into the simulation results presented in this section since the spectral features were accurately reproduced by a single quadrupolar powder pattern. Calculations where the effects of CSA were included did not significantly affect the simulation results. Simulations were performed on a Beowulf cluster at PNNL (composed of 23-Racksaver Dual P4 2.4 GHz Xeon nodes and 8-Racksaver Dual Pentium III 1.26 GHz nodes) running the Rocks clustering software utilizing a gigabit Ethernet connection. The simulations of the strontianite and strontium nitrate accounted

for finite pulse effects while good agreement was found for celestine under ideal pulse conditions.

4.1.2 Sensitivity Enhancement

There was a substantial improvement in the sensitivity of ^{87}Sr NMR measurements made with the QCPMG sequence at 21.14 T (Table **4-1**). In the case of strontium carbonate, a single transmitter frequency is required to excite the entire resonance at 11.74 T and 21.14 T. However, moving to 21.14 T reduced the static line-width from roughly 35 kHz to 18 kHz, which in combination with the Curie effect led to a signal to noise ratio enhancement of 37.3. Even greater sensitivity was obtained with the QCPMG sequence using a 500 Hz spikelet spacing: when processed with a 2,000 Hz comb filter, an additional enhancement to the signal to noise ratio of 7.5 was produced. Similar sensitivity enhancements were found in the case of strontium nitrate. The strontium nitrate resonance proved too broad to be excited fully with a single transmitter frequency at 11.74 T but can be excited quite readily at 21.14 T, yielding a line width of roughly 40 kHz. An echo experiment with $Sr(NO_3)_2$ at 21.14 T therefore takes half the acquisition time of an echo experiment at 11.74 T through the reduction in the number of necessary transmitter frequencies. The 21.14 T strontium nitrate QCPMG experiment enhanced the signal-to-noise ratio by a factor of 500 compared to Hahn-echos at 11.74 T. Based on the enhancements in these two test cases, 1/10,000 of the acquisition time for a general ^{87}Sr NMR experiment is required with QCPMG at 21.14 T to achieve the same signal to noise ratio provided by Hahn-echos at 11.74 T.

Table **4-1**: Corrected signal-to-noise ratios of strontium NMR resonances

Sample	Echo 11.74 T	Echo 21.14 T	QCPMG 21.14 T
Carbonate	3.56	133	992
Nitrate	3.42	27.6	1630

Strontium sulfate was also examined with QCPMG NMR at 21.14 T. Hahn echo experiments at 11.74 T were not capable of producing a strontium signal despite three days of acquisition with one second pulse delays. However, QCPMG at 21.14 T produced a strontium signal with an acceptable signal to noise ratio in only four hours of acquisition time at a single transmitter frequency. The strontium sulfate resonance was particularly broad, requiring acquisition at eight transmitter frequencies with the transmitter stepped in 30 kHz increments to map out the entire 240 kHz central transition powder pattern. Based on observed enhancements from the nitrate and carbonate samples, performing an identical experiment with Hahn-echos on the 11.74 T spectrometer at Penn State would require a minimum of 36.5 years of acquisition. QCPMG NMR at 21.14 T is thus a highly effective method for observing strontium in systems where strontium is relatively abundant.

4.1.3 Characterization of the NMR Spectra

In order to test the experimental and computational methods, detailed characterizations of the strontium sites began with an examination of the strontium nitrate spectrum. As stated in the introduction to section 4.1, the quadrupolar and chemical shift parameters for ^{87}Sr in cubic strontium nitrate have been reported by Larsen, Skibsted, Jakobsen, and Nielsen (C_q = 15.4 MHz and η = 0.03).[97] The powder XRD pattern of the strontium nitrate sample as received was an excellent match for the reference pattern of cubic strontium nitrate in the ICDD database and thus similar values for C_q and η should be obtained from our analysis. The experimental and simulated NMR spectrum of strontium nitrate is contained in Figure **4-1** and the quadrupolar parameters obtained from simulations of the compounds analyzed in this chapter are listed in Table **4-2**. The strontium nitrate resonance is roughly 40 kHz wide at 21.14 T and by observation should have an asymmetry parameter of nearly zero. The simulated spectrum is an excellent match to our experimental spectrum aside from oscillations in the magic angle feature present in the experimental spectrum resulting from non-ideal excitation. Our values of C_q and η are nearly identical to those reported by Larsen *et al.* and validate the accuracy of our experimental and computational methods.

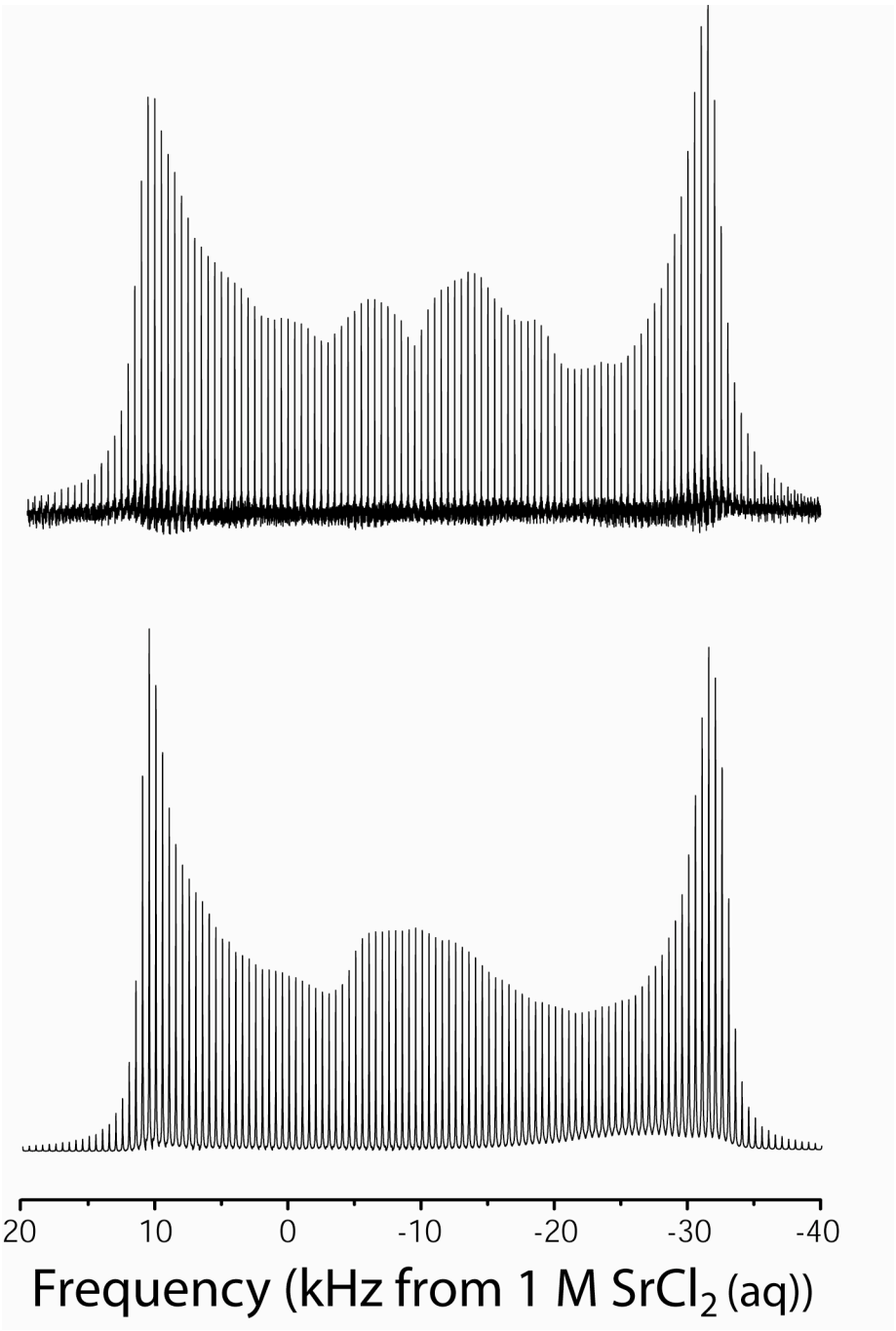

Figure **4-1**: QCPMG ^{87}Sr NMR spectrum of strontium nitrate acquired at 21.14 T. The top spectrum corresponds to the experimental data and the bottom is the simulated spectrum calculated with SIMPSON.

Table **4-2**: Strontium quadrupolar parameters and isotropic chemical shift

Sample	C_q (MHz)	η	δ_{iso} (ppm)
$Sr(NO_3)_2$	15.3	0.03	- 323
$SrCO_3$	8.91	0.14	- 133
$SrSO_4$	28.1	0.71	- 47
$SrZrO_3$	39.1	0.73	0
$SrBr_2$ – Resonance 1	9.07	0.15	-
$SrBr_2$ – Resonance 2	25.9	0.30	-
$SrHPO_4$	14.8	0.65	-
SrC_2O_4	12.2	0.75	- 3.4

The experimental and simulated spectra of the strontium carbonate sample are presented in Figure **4-2**. The XRD pattern of the strontium carbonate obtained from Sigma-Aldrich was an excellent match for orthorhombic strontianite. Strontianite is a natural mineral commonly found as a co-precipitated phase with calcium carbonate in soils corresponding to regions where ancient saline bodies of water once existed.[156-158] It is also produced in conjunction with aragonite (a phase of $CaCO_3$) by corals and other marine invertebrates.[159-162] Again, the experimental and simulated spectra are in good

agreement, though slightly different values for C_q and η are obtained from this analysis than those reported by Bastow from Hahn-echo results.[154] The optimized value of C_q is 0.31 MHz higher than the 8.6 MHz previously reported. A more significant disparity was found for the asymmetry parameter, η, where a value of 0.15 was obtained from the QCPMG results rather than 0.27. The source of this discrepancy lies in the resolvability of quadrupolar features: the quadrupolar characteristics of the QCPMG spectrum are better resolved than in the Hahn-echo acquired by Bastow and are thus better suited to accurate simulation.

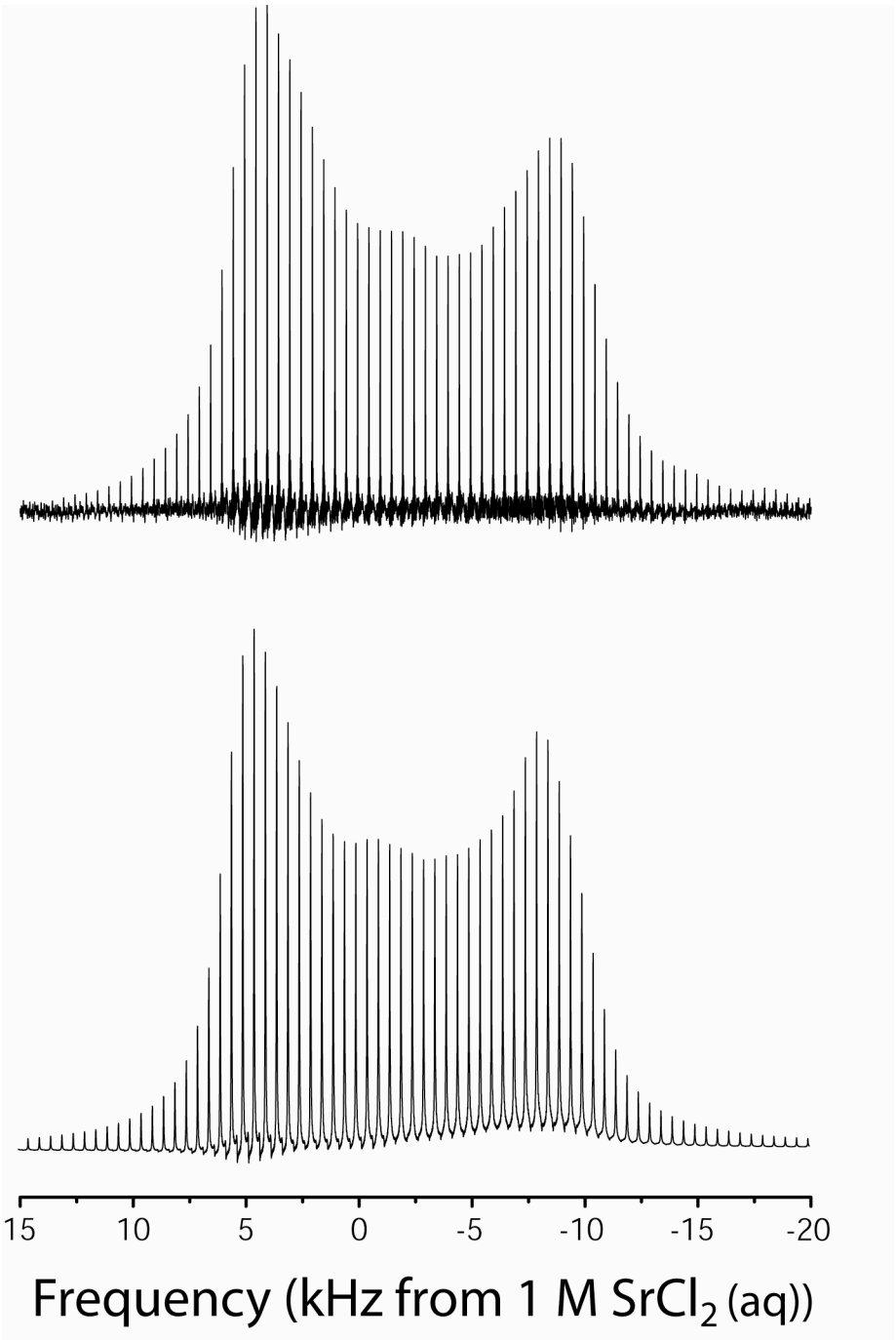

Figure **4-2**: QCPMG ^{87}Sr NMR spectrum of strontium carbonate acquired at 21.14 T. The top spectrum corresponds to the experimental data and the bottom is the simulated spectrum calculated with SIMPSON.

The XRD results for strontium sulfate indicated that the sample was a good match for orthorhombic celestine with a minor impurity phase that appeared to match with strontium hydroxide hydrate. Celestine is also a naturally occurring mineral and is commonly found in tertiary marine sediments and in conjunction with barite, strontianite, calcite, and dolomite in nearly any system that contains these minerals.[163-168] The experimental and simulated QCPMG spectra of celestine are presented in Figure **4-3**. The quadrupolar coupling constant of celestine is much larger than either of the other strontium compounds examined in this study (see Table 4.2) and the asymmetry parameter describes a highly non-symmetric local electric field gradient.

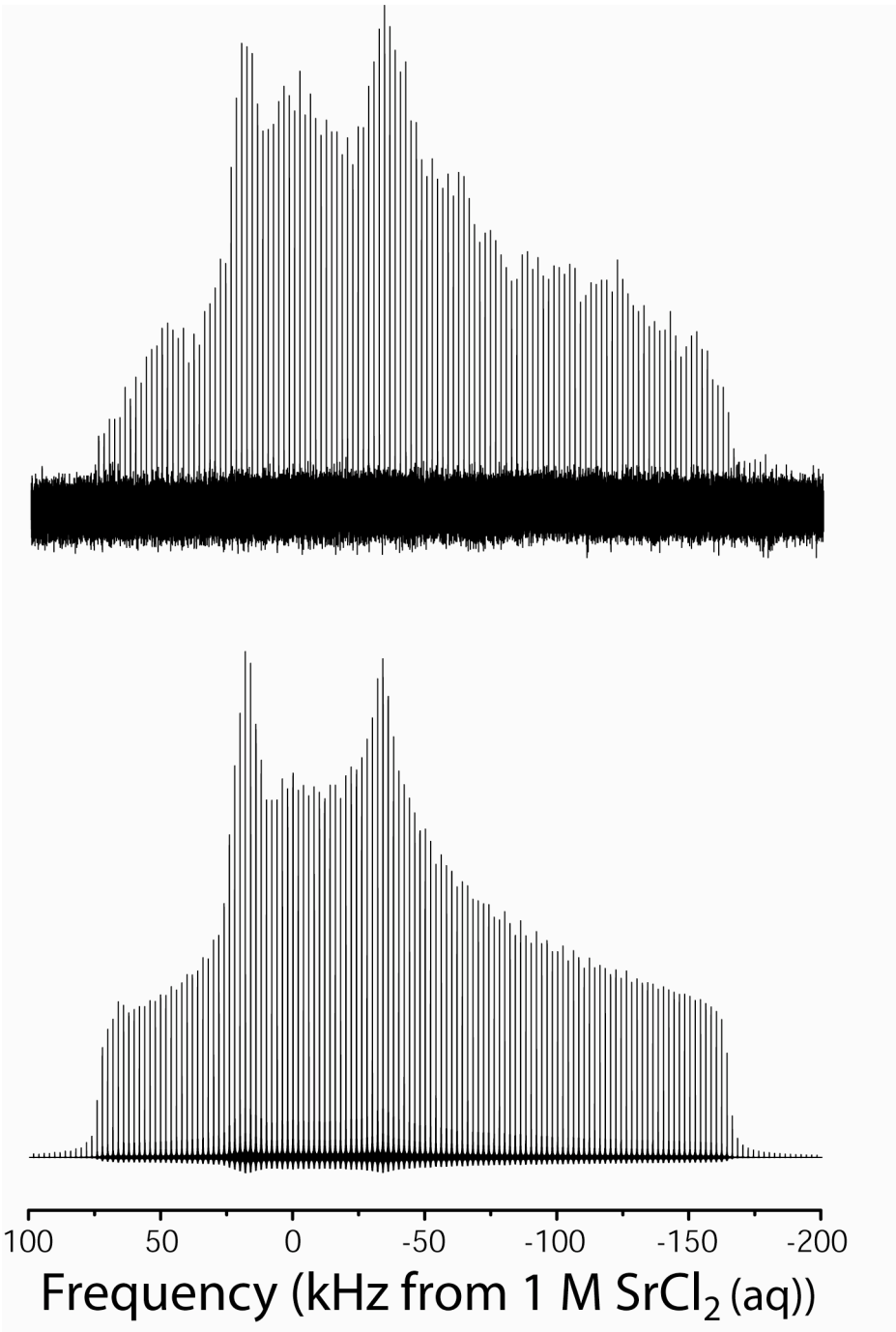

Figure **4-3**: QCPMG ^{87}Sr NMR spectrum of strontium sulfate acquired at 21.14 T. The top spectrum corresponds to the experimental data and the bottom is the simulated spectrum calculated with SIMPSON.

4.1.4 Crystal Structure and NMR Parameters

A close examination of the ^{87}Sr quadrupolar parameters and the crystal structure of each sample reveals that the quadrupolar parameters (particularly the quadrupolar asymmetry parameter) are highly sensitive to the symmetry of the strontium coordination environment. The coordination environments of the strontium nuclei derived from literature XRD patterns are displayed in Figure **4-4**. Based on the structural refinement of Nowotny and Heger for cubic strontium nitrate, there should be a single strontium environment where each strontium atom is coordinated to six nitrate groups via two oxygen atoms.[169] The nitrate groups also appear to be arranged in a relatively uniform spatial fashion around the strontium nucleus. The fairly uniform spatial arrangement of the coordination sphere produces a resonance that has a relatively small quadrupolar asymmetry parameter (η = 0.03). In strontianite, the strontium nuclei coordinate to nine oxygen atoms according to the X-ray structure.[170] These oxygen atoms are provided by six neighboring carbonate groups; three coordinated to strontium by two shared oxygen atoms and three coordinated through a single shared oxygen. The coordinating carbonate groups sit in two planes, one above and one below the strontium atom, with one plane containing five of the coordinating oxygens and the other plane four. This arrangement is not as symmetric as the coordination environment in strontium nitrate, but still maintains a moderate level of spatial symmetry. The quadrupolar asymmetry parameter of strontianite (η = 0.15) reflects this variation in coordination symmetry by being larger than the asymmetry parameter reported for strontium nitrate. The crystal structure of celestine is quite complex and represents the most distorted strontium coordination

environment of the three samples.[171] The strontium nuclei in celestine are once again coordinated to twelve oxygen atoms; ten of the coordinating oxygens come from five sulfate tetrahedra and the remaining two coordinating oxygens come from interactions with an additional two sulfate tetrahedra. The two sulfate groups that contribute a single coordinating oxygen appear relatively close together in space and four of the five remaining sulfate tetrahedra appear on the opposite side of the strontium atom, causing an irregularly spaced coordination sphere. This distorted coordination environment results in a much higher quadrupolar asymmetry parameter than in the other compounds examined here (η = 0.71). We conclude that the quadrupolar parameters will be a sensitive probe of the strontium binding environment in clay minerals, especially dehydrated phases where binding to mineral surfaces will produce a change in the electric field gradient at the strontium nucleus.

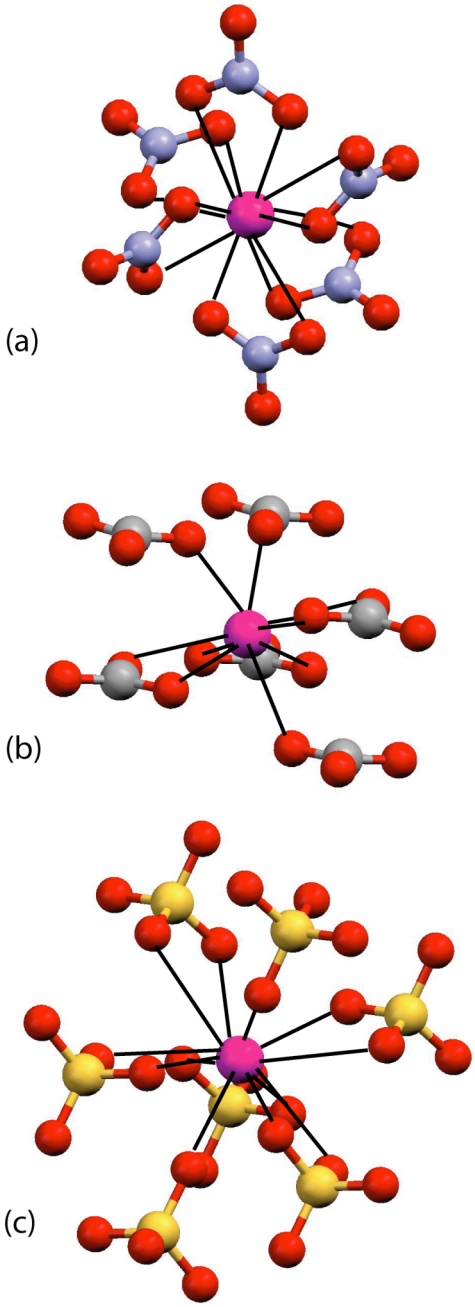

Figure **4-4**: Strontium coordination environments as determined from XRD patterns. (a) represents 12-coordinate strontium nitrate, (b) represents 9-coordinate strontium carbonate, and (c) represents 12-coordinate strontium sulfate. Graphic presentations come from the XRD results of references 169-171.

4.1.5 Conclusions – QCPMG at 21.14 T

QCPMG NMR at 21.14 T effectively manages many of the sensitivity issues that historically have plagued ^{87}Sr solid-state NMR and is a useful method for studying strontium in mineral systems where strontium is abundant. In combination with the iterative simulation capabilities of the SIMPSON package, this technique is ideally suited to characterize the quadrupolar and chemical shift parameters for strontium nuclei in solid samples. Greater than two orders of magnitude enhancement to the signal-to-noise ratio over Hahn-echo experiments at 11.74 T was observed in strontianite and strontium nitrate. We also were able to extract accurate quadrupolar parameters for strontium nuclei in the simple minerals strontianite and celestine as well as observe a strong relationship between the quadrupolar parameters and the symmetry of the strontium site in these materials. Despite success in the minerals celestine and strontianite, initial room-temperature QCPMG experiments at 21.14 T were not capable of detecting strontium bound in strontium-saturated phyllosilicates and zeolites, nor other inorganic crystal systems such as $SrZrO_3$. Additional methods of sensitivity enhancement such as low-temperature NMR or preparatory pulse schemes will be necessary in order to observe strontium in more structurally complicated materials.

4.2 Double Frequency Sweep QCPMG at 21.14 T

Using low temperature NMR to achieve the necessary additional sensitivity enhancement carries a few significant drawbacks. The first is that specialized equipment is necessary, such as cryoprobes or cryoamplifiers, which involve considerable capital

expense and consume expensive resources such as liquid nitrogen or helium during daily operation. Additionally, as the temperature is decreased, the relaxation rates decrease, which may necessitate increasing the recycle delay to the point that any sensitivity advantage gained by decreasing the temperature is nullified. The relaxation effects can be moderated by introducing paramagnetic dopants into the samples, but dopant addition requires additional sample preparation and can affect the NMR results if one does not maintain careful control over the doping procedure. The use of preparatory pulse schemes such as DFS and RAPT provide an alternative means to increase sensitivity without requiring specialized equipment or special sample preparation. Because of the observed enhancement of 2*I* reported in the literature and the successful mating of DFS and QCPMG in the past[83,115], the additional enhancement provided by DFS preparation prior to QCPMG at 21.14 T will be explored in this section.

To review, double-frequency sweeping makes use of a single amplitude-modulated pulse that effectively sweeps adiabatically through a range of frequencies around the transmitter frequency, thereby saturating or inverting the outer transitions of a quadrupolar nucleus and increasing the population difference of the central transition.[83,114,116,150] DFS results in a theoretical maximum sensitivity enhancement of 2*I* (9 in the case of ^{87}Sr) and can therefore significantly reduce the acquisition time required to produce a quality strontium NMR resonance. In section 4.2.2, DFS-QCPMG at 21.14 T will be applied to strontium carbonate in order to quantify the sensitivity enhancement due to DFS preparation. The extra enhancement from this method will also be highlighted by using DFS-QCPMG to examine the ^{87}Sr resonance in strontium zirconate, which was not possible with QCPMG at 21.14 T alone.

The remaining sub-sections of this chapter involve interrogations of the strontium environment(s) in a series of samples containing strontium and structural or hydration-based protons using DFS-QCPMG at 21.14 T. The motivation behind these studies is that phyllosilicate minerals in the Hanford sediments are exposed to moisture and in some cases, directly to the aqueous tank waste. Under these conditions, the minerals will likely incorporate waters of hydration on their external surfaces and in the interlayer (depending on the structure of the mineral in question). In fact, all extended X-ray absorption fine structure (EXAFS) studies of strontium sorption by mineral phases report the existence of hydrated strontium species on external surfaces and in the interlayers.[172-175] Before analyzing ^{87}Sr sorption in phyllosilicate minerals, it is thus necessary to have some knowledge of potential proton-strontium interactions and the degree to which they affect ^{87}Sr NMR spectra. Section 4.2.3 explores the effects that hydration may have on inorganic systems by examining a mixture of strontium bromide and strontium bromide hydrate phases with ^{87}Sr NMR. In section 4.2.4, proton-decoupled DFS-QCPMG at 21.14 T is used to examine strontium in a pair of simple organic systems. The experiments with the organic compounds (i) show that the trends observed in the inorganic systems apply to organic systems as well and (ii) provide a first insight into the minimum number of ^{87}Sr spins required to produce a resonance with DFS-QCPMG at 21.14 T.

4.2.1 Experimental

4.2.1.1 Materials and Sample Handling

Samples of $SrZrO_3$, anhydrous $SrBr_2$ (99.99% metals basis), strontium oxalate (SrC_2O_4, 99.999% metals basis), and strontium acetylacetonate ($SrC_{10}H_{14}O_4$, 97% metals basis) were obtained from Sigma-Aldrich. All of the samples save strontium zirconate were stored under vacuum in a dessicator, regardless of their sensitivity to moisture. The hygroscopic strontium bromide sample was packed and sealed under nitrogen prior to transport for NMR or XRD experiments. The other samples, being less sensitive to moisture, were packed under atmospheric conditions.

4.2.1.2 X-ray Diffraction

X-ray diffraction (XRD) patterns were obtained for each material on a Rigaku Geigerflex diffractometer in the Pennsylvania State University Materials Characterization Laboratory to confirm the identity of each sample. Scans were made from 10°-90° 2θ in steps of 0.03° 2θ with a Cu-Kα source and a collection rate of one degree per minute. The samples were exposed to atmospheric moisture during data acquisition. The XRD results were compared to reference patterns in the ICDD database to identify the phase(s) present in the sample.

4.2.1.3 Strontium NMR

DFS-QCPMG experiments using the 5 mm double-resonance cross-coil static probe were performed on the 21.14 T spectrometer located at PNNL. For each sample (excluding strontium zirconate and strontium carbonate), a proton decoupling field was generated by applying a 200 W continuous wave pulse to the proton channel during the data acquisition periods. The DFS preparation period consisted of a single amplitude-modulated pulse (of equal power to the $\pi/2$ pulse) designed to sweep through a frequency range from ± 1.5 MHz to ± 50 kHz from the transmitter frequency in the case of strontium carbonate and from ± 1.5 MHz to ± 100 kHz for the other samples. These frequency limits were selected to leave a 100 or 200 kHz window centered at the transmitter frequency for the central transition strontium resonance and to operate within the bandwidth of the probe's low-frequency channel. An optimum DFS pulse width of 1 ms was identified by varying this parameter until the sensitivity enhancement was maximized. A selective $\theta = \pi/2$ pulse width of 3.8 μs was used in combination with τ delays of $\tau_1 = \tau_\alpha$ =100 μs and $\tau_2 = \tau_\beta$ = 105 μs and a pulse delay of 1 s for all of the experiments. A sampling rate of 1 MHz was used in conjunction with a receiver bandwidth of 200 kHz to acquire the ^{87}Sr NMR resonances. Each individual transient involved the acquisition of 40 echo loops with 500 data points per half echo, leading to a spikelet spacing of 1 kHz in the frequency spectrum. It was possible in only three samples (strontium carbonate, strontium oxalate, and strontium acetylacetonate) to collect the full ^{87}Sr resonance at a single transmitter frequency. With the optimized DFS-QCPMG experiment at 21.14 T, these materials required 64, 500, and 80,000 transients

(respectively) to produce the spectra displayed in this chapter. For the remainder of the materials, acquisitions at multiple transmitter frequencies were necessary to map out the entire powder pattern, as was the case for celestine in section 4.1. For strontium zirconate, 20,000 transients were acquired at each of nine transmitter frequencies spaced by 30 kHz increments. The strontium bromide experiment required the acquisition of only 1,000 transients at each of five transmitter frequencies spaced in 30 kHz increments. Each spectrum received 2000 Hz of comb filter apodization before transformation to the frequency domain. For the very broad resonances, the segments acquired at each transmitter frequency were combined with the aforementioned sky projection algorithm following apodization and Fourier transformation.[81,155] Iterative fitting of the ^{87}Sr resonances was performed using the SIMPSON simulation package running on 32 AMD Athalon processors in Penn State's LionXO supercomputing cluster to extract the strontium quadrupolar parameters. When necessary, signal-to-noise (S/N) ratios of the spectrum with and without DFS were obtained using Acorn NUTS software in a similar procedure to that described in section 4.1.1.3.

4.2.2 Sensitivity Enhancement

As can clearly be observed in Figure **4-5**, DFS produces a significant sensitivity enhancement in the case of strontium carbonate. The signal-to-noise ratio of the optimized DFS-QCPMG experiment is 5.6 times greater than without DFS, corresponding to a 31-fold reduction in acquisition time over a QCPMG experiment at this field. An optimized DFS-QCPMG experiment at 21.14 T can thus produce

interpretable ^{87}Sr resonances approximately 300,000 times faster than with Hahn-echo experiments at a more conventional 11.74 T field strength.

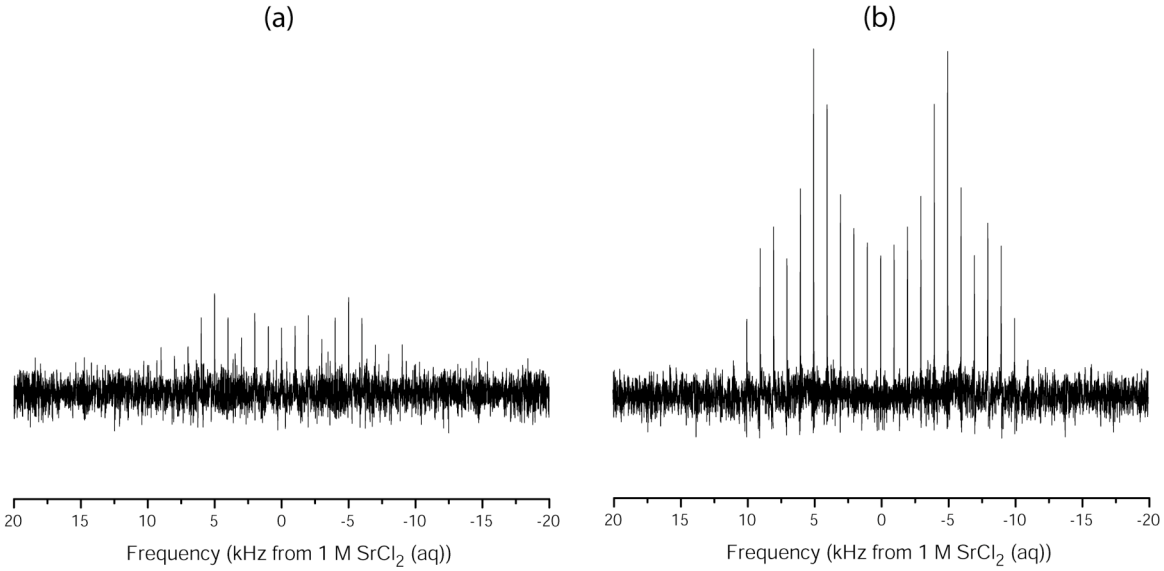

Figure **4-5**: QCPMG (a) vs. DFS-QCPMG (b) of strontium carbonate acquired at 21.14 T. Spectra are plotted on identical intensity scales after an identical number of transients were acquired.

A few additional aspects of the strontium carbonate DFS experiment warrant further comment. First, the observed enhancement is quite a bit below the theoretical maximum enhancement of 2*I* normally attributed to DFS preparation. The reason for this is that the practical enhancement in a given system is limited by the tuning bandwidth of the NMR probe and the magnitude of the quadrupolar coupling. Because the probe is not capable of operating in a region greater than 1.5 MHz from the transmitter frequency, any satellite transitions that extend beyond ± 1.5 MHz will not be completely inverted by the DFS preparation used here. Likewise, without advanced knowledge of the central transition line-width, the lower limit of the DFS pulse must be set to a value such that the DFS sweep has a low chance of overlapping the central transition. The implication of the

second restriction is that any satellite components with frequencies less than the lower limit will also not invert fully. Applying this discussion to the strontium carbonate example, satellite components that occur at frequencies less than 50 kHz or greater than 1.5 MHz from the transmitter will not be fully inverted.

Because the strontium carbonate resonance is relatively narrow with a known line-width, this test case represents the optimum sensitivity enhancement DFS can provide for ^{87}Sr NMR with the 5 mm cross-coil probe on the 21.14 T instrument. The relatively small quadrupolar coupling implies that the DFS conditions will fully invert more satellites in strontium carbonate than in a sample with a larger quadrupolar coupling constant. In addition, it is known from section 4.1 that the strontium resonance can exceed 200 kHz in width, meaning that the lower bound of the DFS pulse must be adjusted to at least 100 kHz from the transmitter frequency before analyzing a previously unexplored strontium sample. Any resonances significantly less than 200 kHz in width will therefore receive reduced inversion of the inner satellites compared to strontium carbonate.

Despite these limitations, the sensitivity enhancement of DFS-QCPMG at 21.14 T is sufficient to permit ^{87}Sr NMR studies impossible with QCPMG alone, even in the case of very broad resonances. For example, strontium zirconate is an orthorhombic system analogous in structure to $CaTiO_3$ perovskite. In this structure, the strontium atoms are surrounded by zirconate octahedra, producing a single eight-coordinate strontium environment containing only oxygen atoms in the coordination sphere. The zirconate octahedra have been shown by neutron diffraction to tilt ≈ 7.6° about the *c* axis of the orthorhombic unit cell and ≈ 11.2° about the *b* axis, pushing the strontium atoms away

from the center of the coordination sphere to produce an asymmetric strontium environment.[176] Initial attempts to detect the strontium resonance in this sample failed under MAS conditions at both 11.74 T and 21.14 T as well as with QCPMG at 21.14 T. The additional sensitivity produced by a DFS sweep from ±1.5 MHz to ±100 kHz from the transmitter did permit an interrogation of the strontium environment, producing the resonance shown in Figure **4-6**. This spectrum required six hours of acquisition at nine different transmitter frequencies to map out the 310 kHz-wide resonance. Iterative simulations show that the quadrupolar coupling constant for this strontium environment was 31.9 MHz with a quadrupolar asymmetry parameter of 0.73, the largest values detected for ^{87}Sr to date.

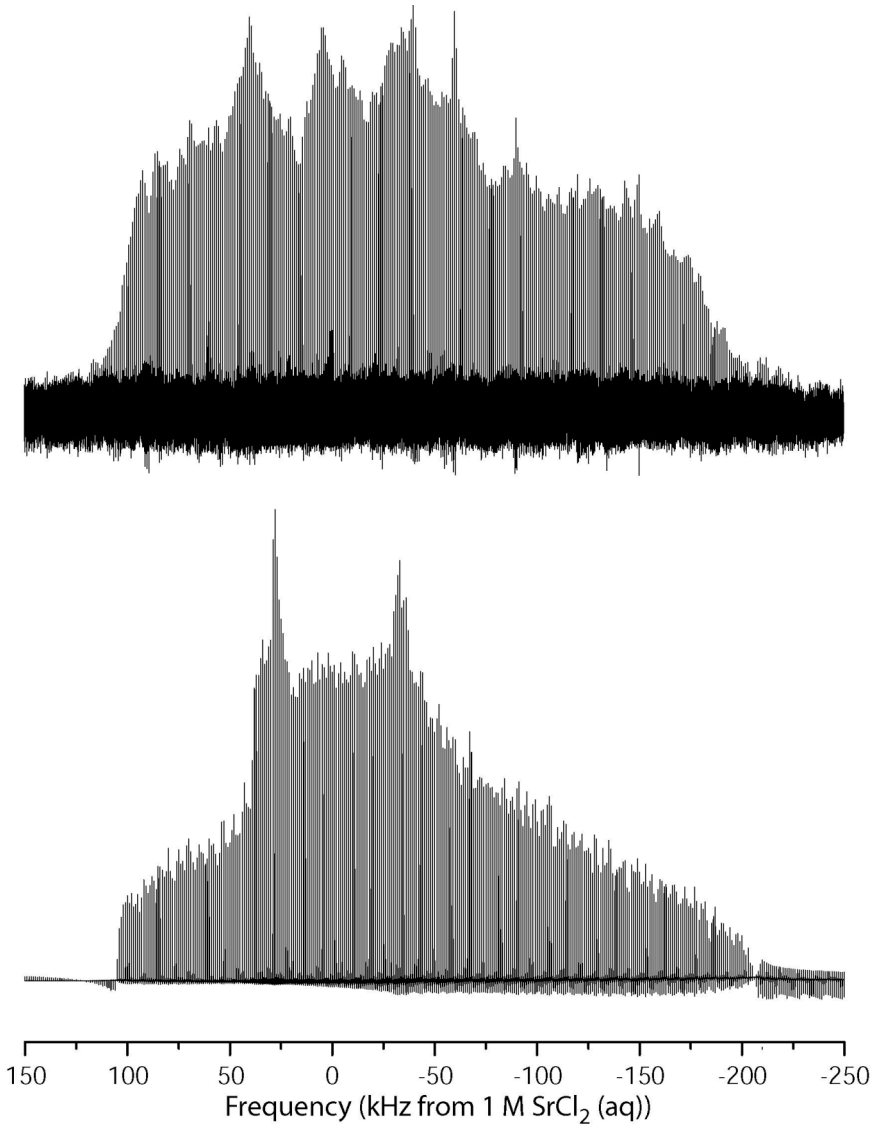

Figure **4-6**: DFS-QCPMG ^{87}Sr spectrum of strontium zirconate acquired at 21.14 T. The top spectrum includes the experimental results and the bottom the calculated simulation with SIMPSON. The center singularity in the experimental spectrum represents the magic angle feature.

It is worth noting that the intensity of the singularities in the zirconate spectrum is not nearly as high as the singularities in the iterative simulation results. The source of this discrepancy lies in the fact that the detected resonance extends beyond the width of

the central transition window provided by the DFS conditions. The DFS pulse therefore overlaps the central transition resonance, skewing the resulting line shape such that the singularities are not of the appropriate intensity. In this particular case, the width of the calculated pattern and position of the singularities correlates well with the experimental spectrum despite the DFS overlap, allowing an accurate determination of the ^{87}Sr quadrupolar parameters. It will be shown in the remainder of this and subsequent chapters that DFS-QCPMG at 21.14 T provides suitable enhancement to study strontium in additional simple and complex materials.

4.2.3 Effect of Hydration on Strontium in Inorganic Crystals

As detailed in section 4.2.1, the highly hygroscopic strontium bromide sample was stored as received under controlled atmospheric conditions to minimize its exposure to atmospheric moisture. Samples for XRD and NMR analyses were also prepared and sealed under a nitrogen atmosphere before being shipped to the designated testing facilities. However, it was necessary to perform XRD analysis under ambient atmospheric conditions and a phase attributable to anhydrous strontium bromide was not definitively observed. Two known strontium bromide phases were positive matches for the XRD results: strontium bromide monohydrate and strontium bromide hexahydrate. Additional peaks appeared in the XRD spectrum that may be ascribed to either in-situ hydration or to a small fraction of anhydrous strontium bromide (no reference diffraction pattern exists for anhydrous strontium bromide in the ICDD database) persisting throughout the experiment. No significant impurities were observed by XRD, but it may

not be stated conclusively from these data that the original material was pure anhydrous strontium bromide.

Because of the rate at which strontium bromide sorbed moisture during the XRD experiment, great care was taken with the packing, transportation, and storage of the NMR sample. The NMR experiments at PNNL were performed on a sample sealed in a 5 mm OD glass NMR tube, which was stored in a secondary, CaSO4 dessicant-filled plastic vial before exiting the glove bag (Figure **4-7**). The secondary plastic vial was packed in a larger dessicant filled bag before being shipped to PNNL. Upon removing the sample in Washington, visual observation of the dessicant color confirmed that no significant moisture penetrated the plastic vial, suggesting that the strontium bromide sample remained in a primarily anhydrous state through the beginning of the NMR experiment. Despite the efforts to control moisture uptake, two ^{87}Sr resonances with vastly different quadrupolar parameters were observed in the proton-decoupled DFS-QCPMG experiment at 21.14 T (Figure **4-8**). The narrower of the two resonances spanned a region of roughly 20 kHz, corresponding to a quadrupolar powder pattern with a quadrupolar coupling of 9.07 MHz and an asymmetry parameter of 0.15. Though this fit is not ideal, including chemical shift anisotropy, a single spin ^{1}H-^{87}Sr dipolar coupling, and varying the pulse power did not improve the quality of the fit. The second, broader resonance covered a region of 160 kHz, corresponding to a single quadrupolar resonance with a quadrupolar coupling constant of 25.9 MHz and an asymmetry parameter of 0.30.

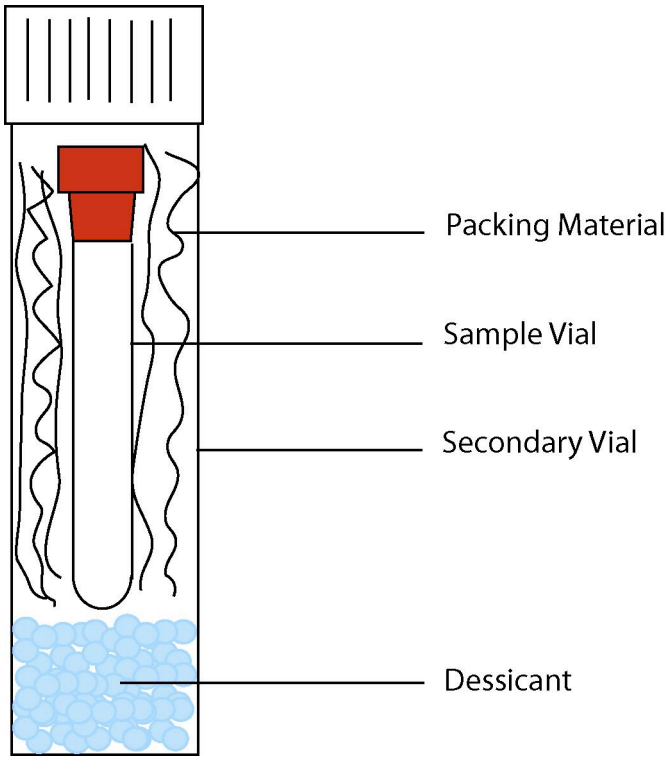

Figure **4-7**: Diagram of the packing system for the moisture sensitive samples. The outer secondary vial is then placed in a large bag filled with additional $CaSO_4$ dessicant material.

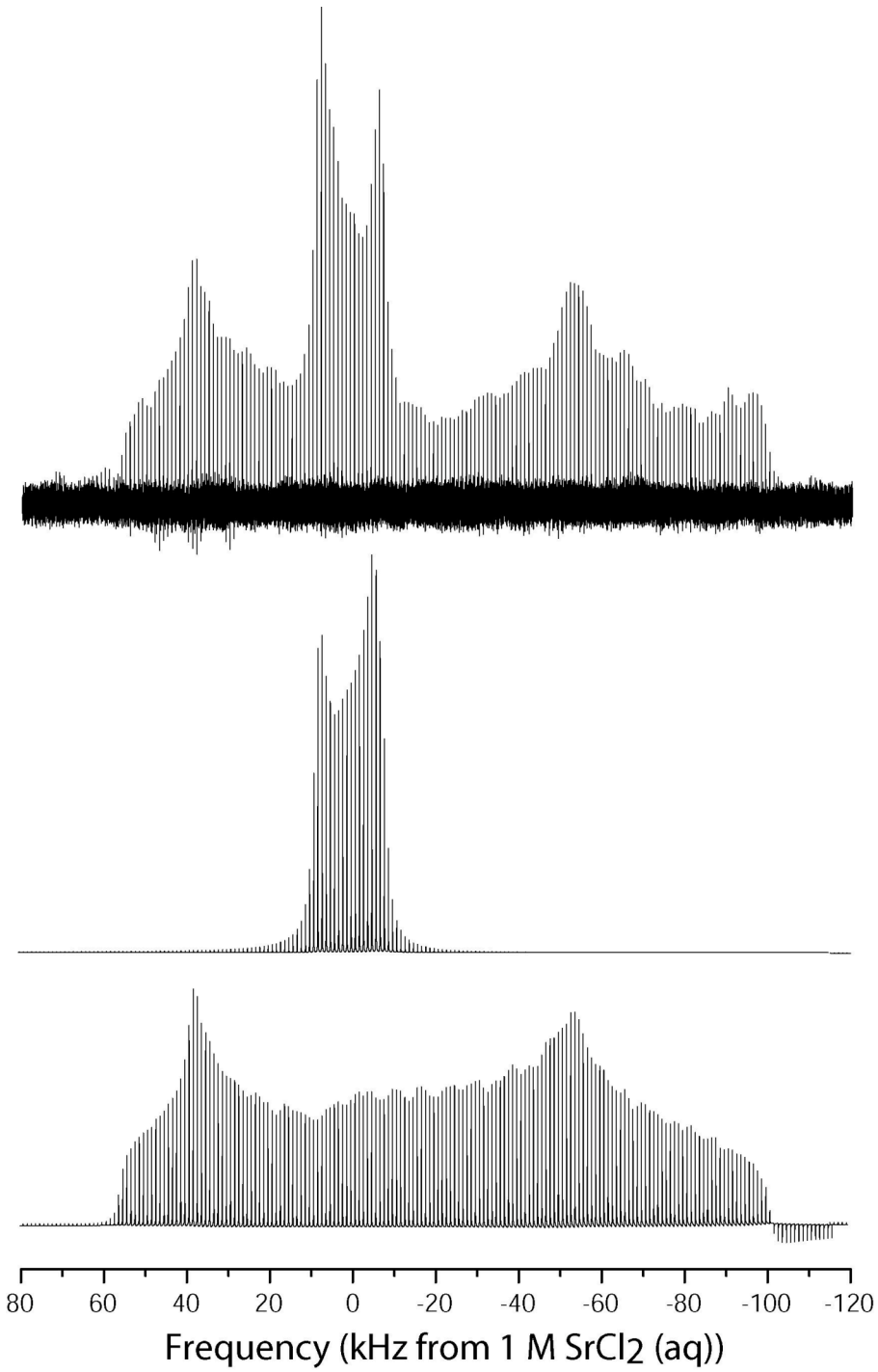

Figure **4-8**: DFS-QCPMG ^{87}Sr spectrum of strontium bromide mixed hydrate acquired at 21.14 T. The top spectrum includes the experimental results and the bottom two the calculated simulations with SIMPSON for the two sites.

These results support the conclusion that waters of hydration do indeed have a strong effect on the strontium NMR spectrum. Anhydrous strontium bromide is a highly hygroscopic inorganic compound where each strontium atom is coordinated electrostatically by seven nearest-neighbor bromine atoms in a slightly asymmetric arrangement.[177] The incorporation of a small number of water molecules should perturb this basic structure only slightly, producing a strontium coordination environment with a higher level of asymmetry than in the anhydrous state. In the case of a hexahydrate phase, the presence of six water molecules per unit cell will significantly perturb the strontium bromide structure and likely produce a strontium coordination environment with an even higher degree of asymmetry. From this perspective, it is reasonable in light of the trends observed earlier in this chapter to assign the wider of the two resonances to a more hydrated phase and the narrower to either anhydrous strontium bromide or strontium bromide monohydrate. This is contrary to popular opinion in many hydrated quadrupolar systems, where the more narrow resonances are typically associated with the more hydrated species due to dynamic effects. Regardless of the specific assignment of each resonance, structural changes due to the incorporation of water in this crystalline system can affect the ^{87}Sr quadrupolar coupling (and therefore the linewidth) dramatically. Based on the magnitude of change observed here, it is possible that hydrating water with restricted mobility can increase the quadrupolar coupling to the point that a resonance may become non-detectable. The hydration state of strontium will clearly have a significant effect on the observed NMR spectrum and associated binding structure in mineral phases.

4.2.4 Strontium in Organic Systems and the Sensitivity Limits of DFS-QCPMG

Soil organic matter (SOM) is an important component of the global carbon cycle and the global energy cycle as well. Though the carbon content of biota and marine sediments greatly exceeds that of terrestrial soils, a greater quantity of carbon is partitioned into soils as organic matter than into the atmosphere as CO_2 and volatile hydrocarbons.[35] While some carbohydrates, lipids, proteins, and organic acids with known composition may be found in soils, soil organic matter (SOM) is primarily of humic origin and the many components of SOM do not have well defined chemical compositions. Despite the relative abundance of SOM, very little is actually known about the structure of the humic fraction and scientists are only beginning to realize the importance of SOM in many environmental processes. It is thought that SOM plays an important role in environmentally important oxidation-reduction chemistry and in the sorption of some toxic metals.[178-183] Strontium cations traveling through the Hanford sediments will likely encounter organic material in the course of migrating from source to eventual fate. If SOM can sorb strontium from the soil solution, the affinity of these humic and bio-organic materials for strontium as well as the mechanisms they use to sorb strontium must be incorporated into accurate strontium reactive transport models.

Before delving into studies with SOM, detailed solid-state ^{87}Sr NMR studies of strontium/organic interactions must begin on a small scale with organic systems of known composition. The use of simple organic systems is necessary from a sensitivity point of view, as sensitivity will become a significant problem if the number of sorption sites per unit volume decreases, as one would expect for large SOM components. In

addition, the unknown structure of the large humic fraction will make it difficult to extract structural details of the strontium binding mechanism in natural SOM samples. In this section, proton-decoupled ^{87}Sr DFS-QCPMG NMR at 21.14 T is used to examine the local structure of strontium in the small organic compounds strontium oxalate and strontium acetylacetonate with the goals of (i) characterizing the binding environment of strontium in a representative organic molecule and (ii) gaining insight into the minimum number of strontium spins per unit volume necessary to achieve a detectable ^{87}Sr NMR resonance for a given C_q and η.

4.2.4.1 Strontium Oxalate

Strontium oxalate is a very simple small organic compound and thus contains a large number of strontium nuclei per unit volume. XRD analysis confirmed that the sample as received consists of purely tetragonal strontium oxalate. In tetragonal strontium oxalate, a single strontium environment is present where each strontium atom has eight nearest-neighbor oxygen atoms contributed by six different oxalate groups (Figure **4-9**).[184] The pair of oxalate groups that contribute two oxygen atoms to the strontium coordination sphere are on opposite faces of the strontium cation, oriented perpendicularly relative to one another. The remaining oxalate groups contributing a single oxygen atom are positioned non-uniformly around the strontium atom such that none of the strontium-oxygen distances in this material are identical. If the trends of section 4.1 hold true for organic systems, a reasonably high value of the quadrupolar asymmetry parameter would be expected from such a structure.

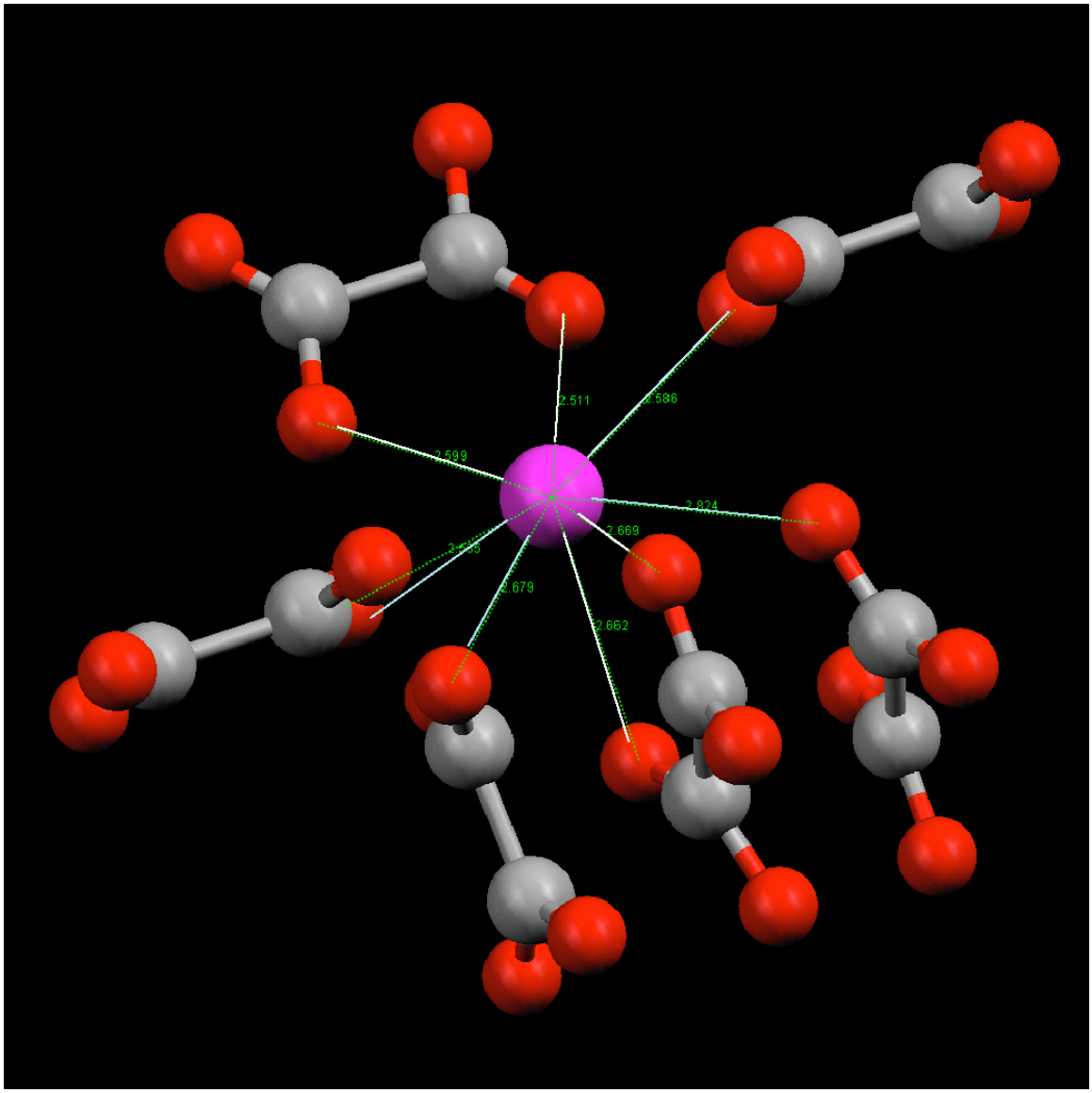

Figure **4-9**: Coordination environment of the strontium atom in strontium oxalate (derived from the crystal structure presented in reference 184).

As hypothesized, a single strontium resonance with a high quadrupolar asymmetry parameter was observed (Figure **4-10**). The resonance is roughly 40 kHz wide and is a nearly perfect match to a classic quadrupolar powder pattern with a quadrupolar coupling constant of 12.2 MHz and a quadrupolar asymmetry parameter of 0.75. These parameters compare quite well with the qualitative trends reported in section

4.1. Additionally, this spectrum required only 500 acquisitions with proton-decoupled DFS-QCPMG at 21.14 T to achieve the level of signal-to-noise displayed in Figure 4.10. DFS-QCPMG at 21.14 T thus appears to provide sufficient sensitivity to permit studies of ^{87}Sr nuclei in small organic compounds (MW ≈ 143 amu).

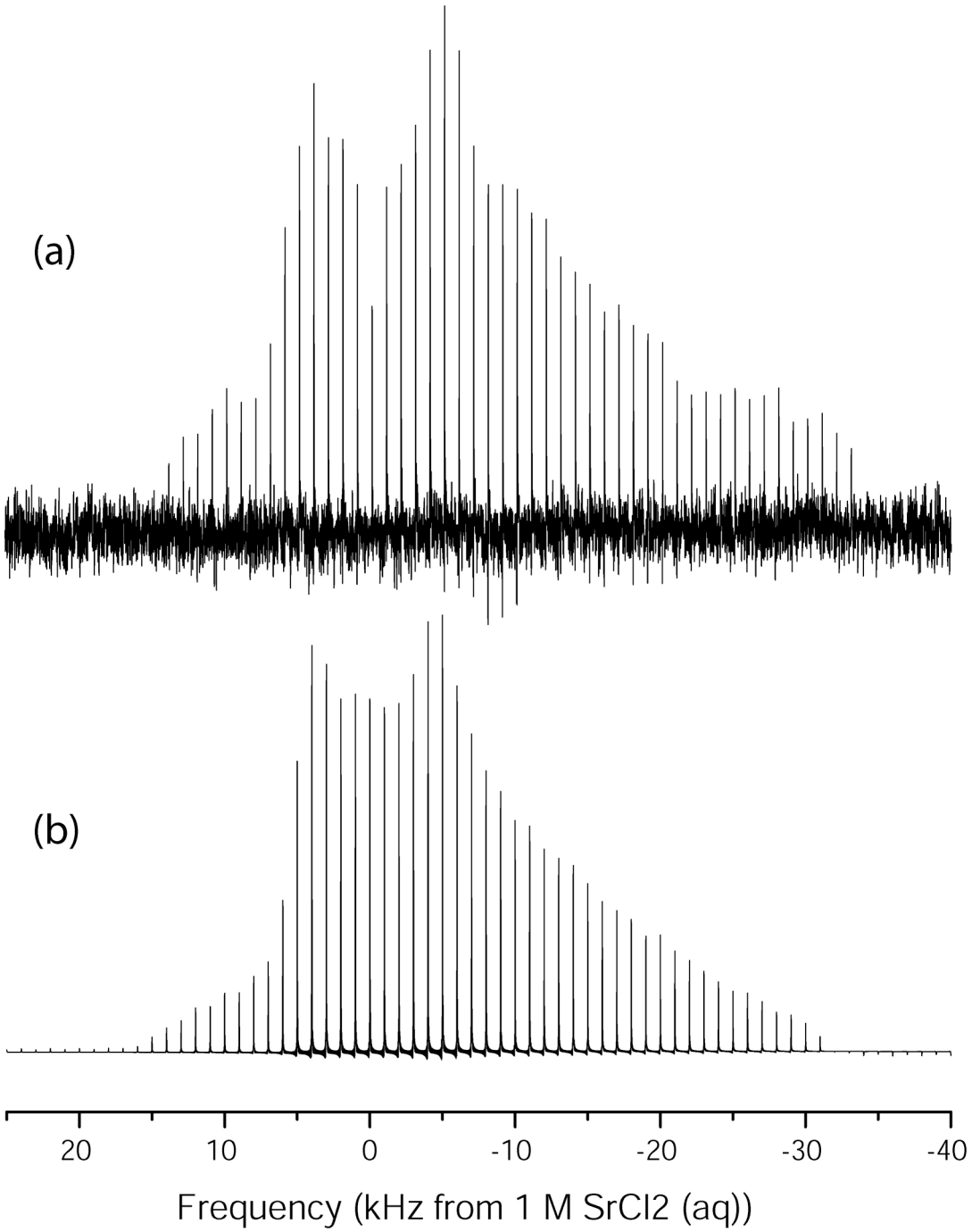

Figure **4-10**: DFS-QCPMG ^{87}Sr NMR spectrum of strontium oxalate (a) acquired at 21.14 T and (b) the iterative simulation results calculated with SIMPSON.

4.2.4.2 Strontium Acetylacetonate

Strontium acetylacetonate is a significantly larger compound (MW ≈ 285.84 amu) and thus has a much lower number of strontium atoms per unit volume than strontium oxalate. The detailed crystal structure of this material has yet to be refined and there is no reference pattern in the ICDD database. The intensity of the ^{87}Sr signal is quite low in the NMR spectrum (Figure **4-11**) despite acquiring a greater number of transients than for strontium oxalate. The resonance in Figure 4.11 could not be fit well with a single quadrupolar powder pattern, single chemical shift anisotropy (CSA) pattern, or a combination of the two anisotropic interactions. Attempts to fit the resonance to multiple strontium environments were also fruitless. A quick examination of the powder spectrum shows that the resonance tails toward the downfield region of the spectrum, possibly indicating that only part of the spectrum is being excited and that acquisitions at multiple transmitter frequencies may be required to map out the entire powder pattern. Unfortunately, time did not permit further experimentation with this sample, and additional NMR studies will be necessary to characterize the strontium environment of strontium acetylacetonate in detail.

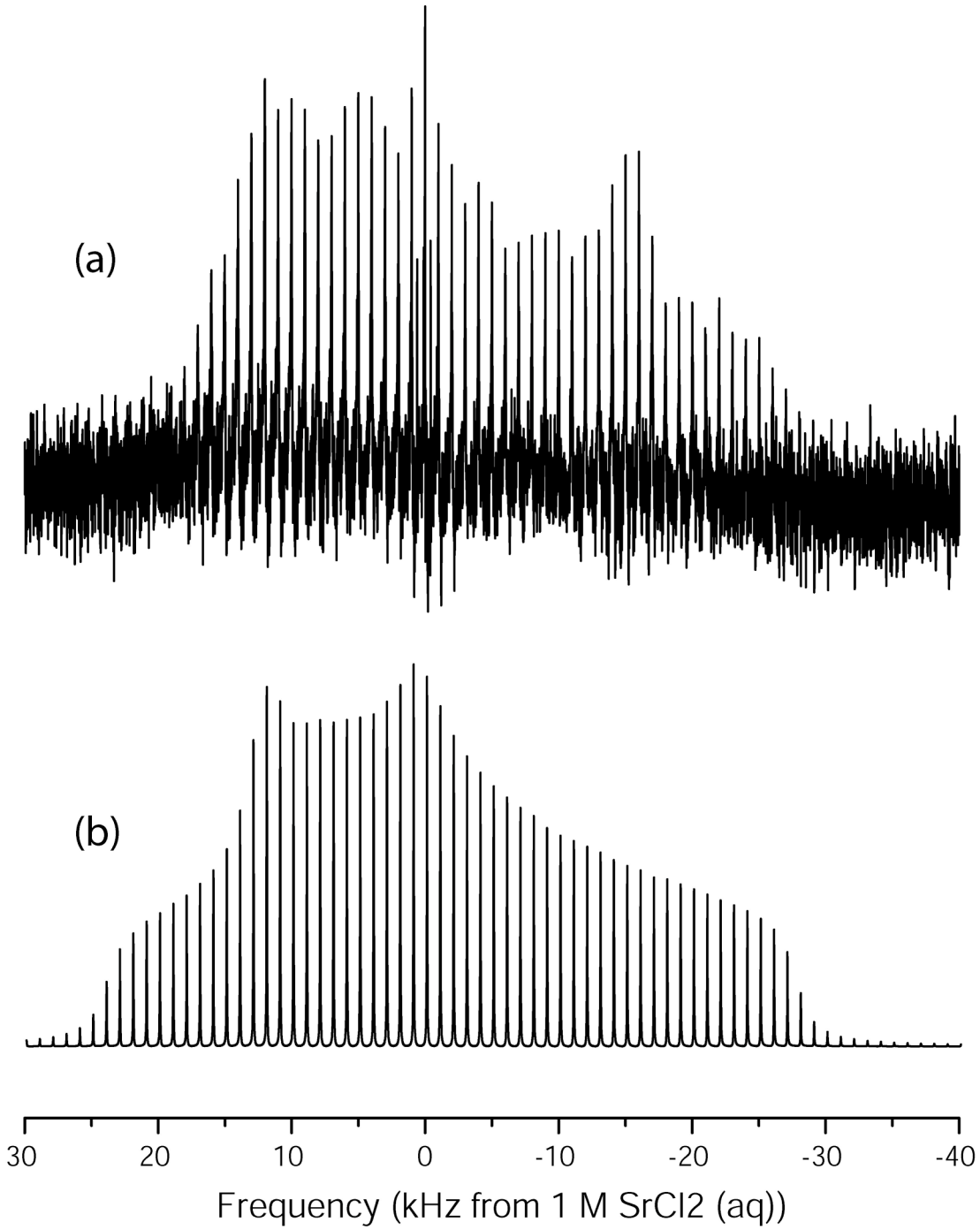

Figure **4-11**: DFS-QCPMG ^{87}Sr NMR spectrum of strontium acetylacetonate (a) acquired at 21.14 T and (b) the iterative simulation results calculated for a single quadrupolar site with SIMPSON. Note that the simulation is not a very good match to the experimental resonance.

Despite yielding an un-interpretable resonance, the low signal to noise ratio obtained for strontium acetylacetonate indicates that this sample is near the lower limit of detection provided by proton decoupled DFS-QCPMG at 21.14 T. We can therefore calculate the number of ^{87}Sr spins contributing to the resonance in Figure 4.11 from the weight of the sample, natural abundance of ^{87}Sr, and molecular weight of strontium acetylacetonate. In this case, 1.3 x10^{19} spins contributed to the ^{87}Sr NMR spectrum. While this is not an absolute limit of detection, it does suggest that somewhere on the order of 10^{18} to 10^{19} spins are necessary to detect a strontium resonance in a reasonable acquisition period with DFS-QCPMG at 21.14 T if the resonance is on the order of 50 kHz. It would be difficult to achieve this number of strontium spins in a sample of natural SOM where an average molecular weight would be thousands to tens of thousands of grams, suggesting that strontium studies in natural SOM samples will require additional sensitivity enhancing techniques, such as low temperature NMR. Additional evidence regarding the strontium limit of detection will be presented in the next chapter.

4.2.5 Conclusions – DFS-QCPMG at 21.14 T

Inclusion of DFS preparation with the QCPMG pulse sequence at 21.14 T provided greater than an order of magnitude additional reduction in acquisition time necessary to acquire the ^{87}Sr NMR spectrum of strontium carbonate. While the specific enhancement for other samples will likely not be as large as in this test case, the strontium zirconate example demonstrates that DFS-QCPMG at 21.14 T is the most

appropriate general method investigated thus far for examining a sample with an unknown strontium environment. DFS-QCPMG at 21.14 T was used to study the strontium environment in a hydrated inorganic material and a pair of organic compounds; studies that were not possible with QCPMG at 21.14 T alone. DFS-QCPMG NMR analyses of strontium bromide demonstrated that incorporating waters of hydration into the crystal structure can distort the strontium coordination sphere, affecting the quadrupolar coupling. DFS-QCPMG examinations of strontium-bearing organic compounds demonstrated that the trends observed in section 4.1 generally hold true for organic systems as well and provided an initial insight into the ^{87}Sr limit of detection of DFS-QCPMG at 21.14 T.

Chapter 5

Strontium Binding in Phyllosilicates

In the previous chapter, ^{87}Sr DFS-QCPMG NMR at 21.14 T was shown to enhance the signal-to-noise ratio by two to three orders of magnitude compared to conventional echo methods at 11.74 T. With the sensitivity enhancement afforded by this technique, it is possible to study the strontium binding environment in strontium-saturated minerals. The interlayer strontium binding environments of two mineral classes are investigated using solid-state ^{87}Sr NMR and other techniques, and will be reported in the first section of chapter 5.

One class of materials investigated is a series of strontium-saturated synthetic micas designed by Komarneni and colleagues specifically to sequester strontium and radium from contaminated waste plumes.[185-187] These materials are tri-octahedral with a very high charge per formula unit due to Al^{3+} substitution for Si^{4+} in the tetrahedral sheet and contain sodium as the charge-balancing cation rather than potassium. The synthesis procedures are also designed specifically to exclude hydrogen atoms from the mica structure: each Mg-OH species one would expect to find in the di-trigonal cavity of the tri-octahedral mica is replaced with a Mg-F moiety. After exchanging parent sodium for strontium, heat treatment leads to irreversible dehydration of the interlayer and cation sequestration[188,189], making these micas promising strontium remediation materials. Therefore, strontium-saturated versions of the micas will be heat treated and analyzed

with ^{87}Sr DFS-QCPMG NMR, XRD, and ^{19}F MAS NMR to characterize the interlayer strontium binding environment.

The second group of samples is composed of two natural montmorillonites that are strontium-saturated, one with sodium as the original charge-balancing cation and the second with calcium serving in the same capacity. The montmorillonites received a similar heat treatment which did not collapse the interlayer or fully dehydrate the interlayer cations. A ^{87}Sr NMR signal was not observed from interlayer strontium in the montmorillonites (or the hydrated micas), consistent with other evidence that strontium nuclei with restricted mobility and water in their coordination sphere may not be observable with direct ^{87}Sr NMR. However, ^{87}Sr NMR was able to identifiy a secondary precipitated phase in one of the strontium-exchanged montmorillonites that was not observable by X-ray methods.

In the second section, preliminary research into indirect detection of hydrated strontium cations via ^{1}H-^{87}Sr TRAPDOR NMR will be presented. In the heat treated micas, strontium cations closely associated with protons exist only on the exterior mica surfaces. In the case of the non-heated micas and the montmorillonites, both interlayer and surface strontium species will be hydrated, potentially producing resonances in the TRAPDOR difference spectrum. Though it will be demonstrated that indirect detection of strontium is nearly as challenging as direct methods, successful TRAPDOR experiments in a few cases contribute toward a better overall picture of strontium binding in the minerals examined here. The data and conclusions presented in this chapter represent significant achievement in ^{87}Sr NMR and are directly relevant to modelers of strontium reactive transport and waste remediation strategists at the DOE.

5.1 Direct Detection of ^{87}Sr (This section contains excerpts of reference 127, copyright the American Chemical Society)

To date, only extended X-ray absorption fine structure (EXAFS) and related X-ray techniques have been used to investigate the coordination environment of strontium cations in layered minerals. Chen *et al*. performed both EXAFS and other X-ray absorption spectroscopy (XAS) studies of strontium bound by kaolinite, illite, hectorite, and montmorillonite after varying the pH and ionic strength of the electrolyte exchange solution.[190-192] In all cases, they conclude that the strontium-oxygen distances in the first shell are consistent with strontium sorption as a six-coordinate outer-sphere complex in hydrated forms of these minerals. Sahai *et al.* examined three systems with EXAFS where the only available cation sorption sites are on external surfaces (kaolinite, goethite, and amorphous silica) and also conclude that strontium sorption occurs via outer-sphere complexation.[174] Their EXAFS data suggest that surface-sorbed strontium cations are coordinated by nine water molecules and that iron-rich surfaces promote the nucleation of strontium carbonate.[174] O'Day *et al*. studied strontium sorbed by the natural zeolite heulandite with EXAFS and determined that strontium is sequestered as a partially hydrated inner-sphere complex at the Ca2 site of the zeolite's *B* channel.[175] None of the available EXAFS literature includes studies of fully *dehydrated* minerals with unique interlayer and surface sorption sites available to strontium.

As alluded to in previous chapters, an alternative and often complementary tool to EXAFS for molecular-level structure determination is solid-state NMR. The ability of NMR to distinguish among unique cation environments in a model-free manner, especially in cases where each site produces a unique set of spectral features, makes this

technique ideally suited for studying strontium binding by minerals. As we observed in Chapter 4, NMR parameters such as the quadrupolar coupling constant (C_q) and quadrupolar asymmetry parameter (η) are highly sensitive to changes in the local electronic environment of ^{87}Sr.[99] These parameters therefore provide a means to directly probe the binding mechanism and binding structure(s) of strontium sorbed by (alumino)silicate minerals in both model and real (heterogeneous) systems. However, despite the successful implementation of high-field ^{87}Sr QCPMG and DFS-QCPMG NMR experiments in studies of inorganic and organic salts[97,99], direct observation of strontium nuclei in complex minerals has remained elusive to date.

In this section, the interlayer binding environment of strontium will be probed in hydrated and de-hydrated phyllosilicate minerals through ^{87}Sr DFS-QCPMG NMR at 21.14 T. The ^{87}Sr quadrupolar parameters will be extracted from DFS-QCPMG experiments involving heat-treated synthetic micas and will be used along with XRD data, ^{19}F MAS NMR, and spatial/electrostatic arguments to detail the interlayer strontium binding structure in these materials. Evidence will be presented that hydrated and partially hydrated strontium nuclei with restricted mobility are difficult or impossible to observe with direct ^{87}Sr NMR methods. In light of these facts, the lack of a ^{87}Sr NMR signal in the montmorillonite samples will be used along with XRD to assign the interlayer strontium binding mechanism in these natural minerals as well. It will also be shown that ^{87}Sr NMR can be sensitive to the presence of strontium carbonate that is not observable by standard X-ray techniques.

5.1.1 Experimental

5.1.1.1 Mineral Preparation and XRD

Samples of the strontium-selective micas were synthesized by Ramesh Ravella, a graduate student in the laboratory of Prof. Sridhar Komarneni at Penn State. Na-4 mica ($Na_4Mg_6Al_4Si_4O_{20}F_4$) was prepared according to a modified procedure of Komarneni *et al.*[185] and Paulus *et al.*[193]. The Na-3 mica (nominally $Na_3Mg_6Al_3Si_5O_{20}F_4$) was synthesized from kaolinite, fumed silica, magnesium chloride, and sodium fluoride according to the procedure of Kodama *et al.*[189] Na-2 mica ($Na_2Mg_6Al_2Si_6O_{20}F_4$) was synthesized from kaolinite, silica gel, magnesium fluoride, and sodium chloride in a modified version of Kodama *et al.*'s procedure.[194] Following synthesis, the micas were saturated with Sr^{2+} by ion exchange with concentrated strontium electrolyte solutions. Full saturation with strontium yields a theoretical loading of roughly 468 meq of strontium per 100 g of mica in Na-4 mica and 247 meq per 100 g for the Na-2 mica, with the strontium exchange capacity of Na-3 mica falling in between these values.

Samples of a Na- and Ca-montmorillonite were obtained from the Source Clay Minerals Repository, now located at Purdue University. In montmorillonite, the layer charge comes about primarily from Mg substitution for Al in the octahedral sheet and the interlayer typically contains fully hydrated cations to balance this charge.[35] The Na-montmorillonite used here has actual composition $(Ca_{.12}Na_{.32}K_{.05})[Al_{3.01}Fe(III)_{.41}Mn_{.01}Mg_{.54}Ti_{.02}][Si_{7.98}Al_{.02}]O_{20}(OH)_4$ with a cation exchange capacity of 76 meq per 100 g clay. Ca-montmorillonite has a cation exchange capacity of 84.4 meq per 100 g of clay and composition $(Ca_{.27}Na_{.04}K_{.01})[Al_{2.41}Fe(III)_{.09}Mg_{.71}Ti_{.03}]$

$[Si_{8.00}]O_{20}(OH)_4$. Both of the montmorillonites were strontium saturated prior to XRD, ICP, and NMR analyses.

Since we know strontium is sequestered by these materials following dehydration of the interlayer[188,189,194], it is necessary to heat the micas with a temperature program capable of removing all loosely and tightly sorbed water. To identify a suitable set of dehydrating conditions, thermo-gravimetric analysis (TGA) was performed on the strontium-saturated Na-4 mica. Based on the mica TGA results, a portion of each mica was heated at 500°C for four hours to drive off interlayer and surface-sorbed water. Though montmorillonite is a markedly different mineral, a portion of the strontium-saturated forms were subjected to the same heat treatment. X-ray diffraction (XRD) analyses were performed to monitor the *d*-spacing of these materials before and after heat treatment using a Scintag diffractometer operated at 35 kV with a 30 mA current and Cu-Kα radiation (λ = 1.54178 Å).

5.1.1.2 ICP

Elemental analysis was performed to quantify the strontium uptake of each mineral during the ion exchange process. ICP-AES (atomic emission spectroscopy) experiments were performed in the Penn State Materials Characterization Laboratory on a Leeman Labs PS3000UV ICP spectrometer. The minerals were digested in a lithium metaborate fusion prior to analysis and the weight percent of aluminum oxide, calcium oxide, iron (III) oxide, magnesium oxide, sodium oxide, silicon dioxide, and strontium oxide were determined. Each mineral sequestered significant quantities of strontium

during the exchange procedure (replacement of the parent cation is nearly complete in the two montmorillonites), though some of the parent sodium proved non-exchangable in the swelling micas. In addition, ICP revealed that the mica samples are virtually iron-free while the montmorillonites contain relatively significant amounts of iron substitution (3.4 mass % in the Na-montmorillonite and 1.5 mass % in the Ca-montmorillonite). ICP results also confirm that there is considerably more magnesium in the Ca-montmorillonite, consistent with the higher cpfu of this clay reported by the Source Clays Repository.

5.1.1.3 Solid-State NMR

5.1.1.3.1 ^{87}Sr DFS-QCPMG

The NMR experiments used to directly probe the ^{87}Sr nuclei incorporated a double frequency sweep (DFS) preparatory scheme[116] combined with the quadrupolar Carr-Purcell-Meiboom-Gill (QCPMG) pulse sequence[84,85] and ^{1}H decoupling (Figure 2.6). The experiments were performed using the 5 mm cross-coil static probe[80] and 21.14 T Varian Inova spectrometer at the Pacific Northwest National Laboratory. At the beginning of each acquisition cycle, frequency regions of 1.5 MHz (ν_l) to 50 kHz (ν_h) from the transmitter frequency were swept over a period of one millisecond using a central transition ν_{rf} of 65 kHz. This set of sweep conditions was found empirically to maximize the sensitivity enhancement provided by DFS using a sample of strontianite. A data sampling rate of 1 MHz was used in conjunction with a receiver bandwidth of 200

kHz to rapidly digitize the data with the filter bandwidth restricted to a region near the edges of the excitation profile. A selective $\theta = \pi/2$ pulse width of 3.8 μs was used in combination with τ delays of $\tau_1 = \tau_\alpha = 100$ μs and $\tau_2 = \tau_\beta = 105$ μs. The evolution periods after each pulse are longer than those before the pulses to account for the delay associated with the particular filter window; the additional delay of 5 μs ensures the first data point in the NMR signal corresponds to an echo maximum. After the initial $\pi/2 - \pi$ echo sequence and half echo acquisition, forty refocusing pulses were applied where each pulse is followed by the acquisition of a full echo. A spikelet spacing of 1 kHz was produced by acquiring 500 data points per half echo, resulting in a total acquisition length of 40,500 points. Prior to Fourier transformation, zeros were appended to the data until the total data set contained 262,144 points. Proton decoupling was applied during data acquisition using a continuous wave pulse at a power level of 200 W. A total of 150,000 transients were collected over a period of 67 hours to produce the final strontium spectrum for the heated Na-4 mica. The heated Na-3 mica required the acquisition of 240,000 transients and the heated Na-2 mica did not produce an interpretable ^{87}Sr signal after the acquisition of 250,000 transients. One-hundred twenty thousand transients were acquired for both heated montmorillonites. The "comb filter" apodization scheme originally proposed by Lipton, Sears, and Ellis[81] was applied to each signal before transformation to the frequency domain. In the case of Na-4 mica, 4 kHz of exponential apodization was applied to each individual echo rise and decay, maintaining the signal intensity of each echo maximum while reducing the noise level between maxima. The other phyllosilicates received 3 kHz of apodization with the comb filter function. Spectra are referenced to a 1 M aqueous solution of $SrCl_2$ prepared from $SrCl_2 \bullet 6H_2O$ (obtained

from Sigma-Aldrich). Iterative simulations of the spectra were performed using real pulse conditions and 8,000 repulsion-based crystallite orientations using the SIMPSON program by Bak, Rasmussen, and Nielsen.[47] The full simulations required six hours to complete on the Lion-XO computing cluster at the Pennsylvania State University using 32 2.4 GHz AMD Opteron processors with 8 GB of RAM allocated to each processor.

5.1.1.3.2 ^{19}F MAS

Quantitative ^{19}F MAS NMR experiments were performed on the synthetic micas using a 4 mm DR MAS probe on the home-built 9.4 T Tecmag Libra spectrometer at Penn State. A Bloch-decay experiment was performed at a spin rate of 10 kHz using a fluorine resonance frequency of 376.346 MHz and a $\pi/2$ pulse width of 3.25 μs. For each sample, 4,096 data points were acquired using a receiver bandwidth of 100 kHz with a pulse delay of 15 s. Sixty-four transients were acquired for each sample. The time-domain data received the equivalent of 50 Hz of Lorentzian apodization prior to Fourier transformation. Spectra are referenced to $CFCl_3$ through a secondary standard of sodium trifluoroacetate (Na-TFA). Peak integrals were determined for each site (centerband and spinning sidebands) using the SIMPLEX-based peak fitting routine in the NUTS NMR data processing software.

5.1.2 Effect of the Heat Treatments

The TGA trace of Na-4 mica shows an initial weight loss of approximately 7% that occurs below a temperature of approximately 120°C (Figure **5-1**) associated with the removal of loosely-bound water molecules. A similar weight loss has been reported in the literature for a pure Na-4 mica phase and was attributed to the removal of 3.6 ± 0.3 water molecules per unit cell; a nearly stoichiometric amount of interlayer water.[195] A second broad peak occurs in the derivative TGA curve with a minimum near 400°C, corresponding to the loss of residual tightly-sorbed water. No additional losses occur through roughly 1100°C, at which point the mica begins to decompose. Based on these results, full dehydration of the minerals should be accomplished with a four hour heat treatment at 500°C.

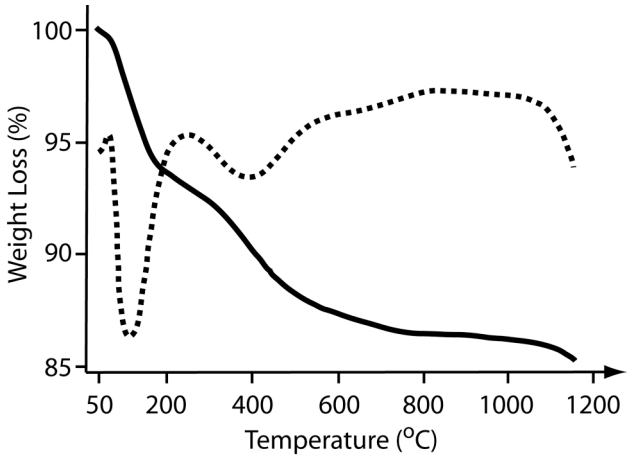

Figure **5-1**: TGA (solid line) and derivative TGA (dashed line) results for the Na-4 mica. Note the two minima in the derivative curve below a temperature of 450°C associated with the loss of all water from the system.

To confirm that each mineral is fully dehydrated by this treatment, the *d*-spacing of each phyllosilicate was monitored by XRD before and after heating. The *d*-spacing in

the micas and montmorillonites should collapse to 9.4 - 9.8 Å with the loss of all interlayer water. Indeed, the Sr-saturated Na-4 mica showed a *d*-spacing of 12.1 Å that collapsed to approximately 9.52 Å (a change in interlayer spacing from 2.7 Å to 0.12 Å) upon heating, consistent with the removal of all interlayer water molecules (Figure **5-2**). The Na-3 mica showed a similar collapse, shrinking from an initial *d*-spacing of 12.07 Å to a final spacing of 9.60 Å. The Na-2 mica changed from an initial spacing of 12.2 Å to a final spacing of 9.4 Å upon heating, confirming that all three micas fully dehydrate with the proposed heat treatment.

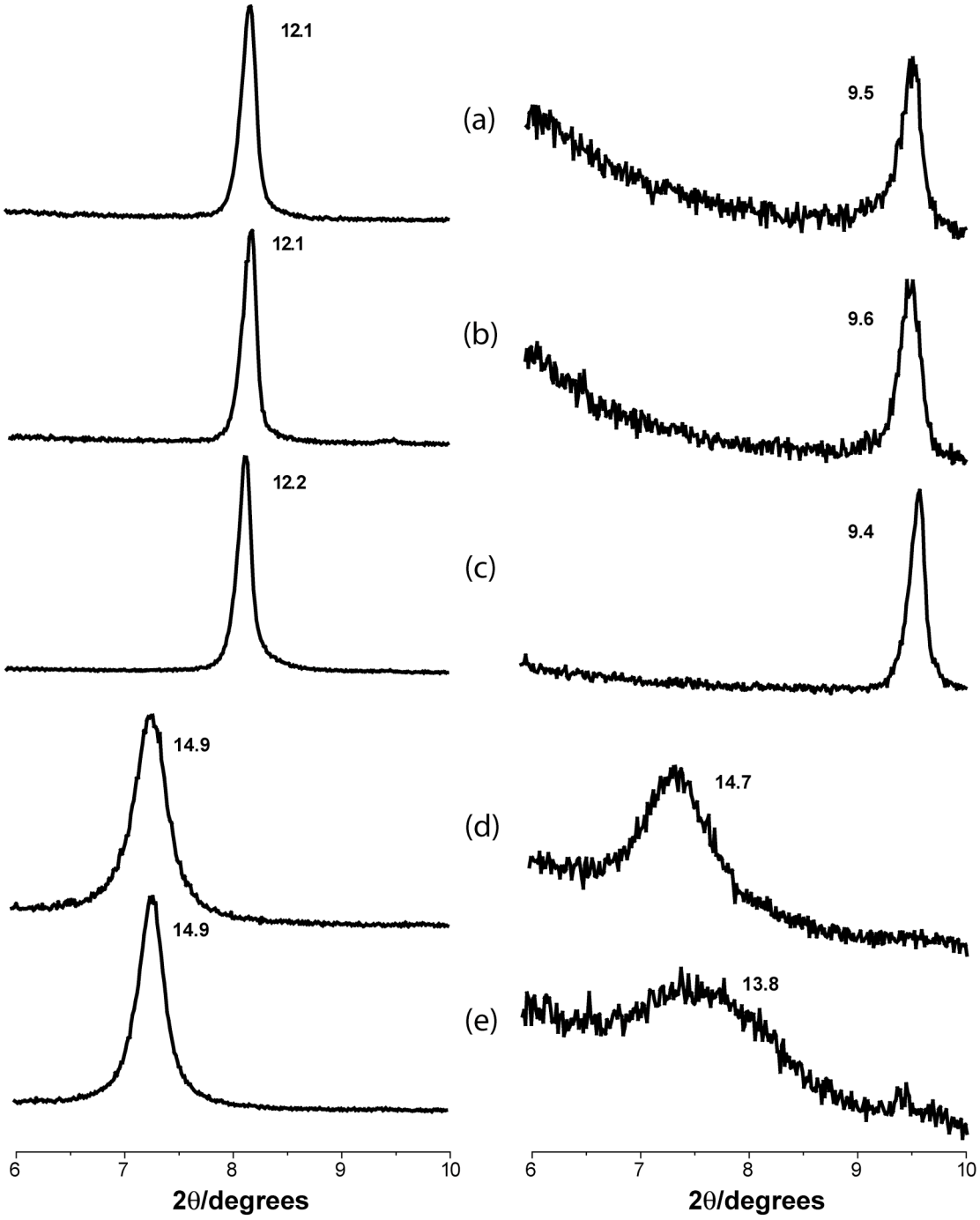

Figure **5-2**: XRD data for (a) Na-4 mica, (b) Na-3 mica, (c) Na-2 mica, (d) Ca-montmorillonite, and (e) Na-montmorillonite before heat treatment (left) and after heat treatment at 500°C for four hours (right).

Heat treatment at the same conditions did not have the same effect on the montmorillonite samples. Based on the XRD results, it appears that (i) the heat treatment is insufficient to de-hydrate these materials and/or (ii) the montmorillonites re-hydrate spontaneously upon exposure to atmospheric moisture. The latter point is consistent with the nature of montmorillonite: these minerals are part of the smectite family, which are also known as swelling clays due to their affinity for moisture. Additional evidence supporting the first conclusion may also be found in the literature, where multiple forms of montmorillonite are reported to fully dehydrate at temperatures in excess of 600°C.[35] Despite heating well below this temperature, the strontium-saturated sodium montmorillonite did collapse to some degree, from an initial spacing of 14.9 Å to a final value of 13.75 Å. This partial collapse suggests that partial dehydration occurred, though the montmorillonite will likely re-hydrate fully upon sustained exposure to atmospheric moisture. The calcium form of the strontium-saturated montmorillonite was found to have a consistent *d*-spacing of 14.9 Å before and after heat treatment. From the literature data and observed *d*-spacings, it is reasonable to conclude that the heated and non-heated montmorillonite samples will contain fully hydrated strontium species in the interlayer.

5.1.3 Interlayer Strontium Binding in the Synthetic Micas

5.1.3.1 Na-4 Mica

Two of the unique features of Na-4 mica were discussed in the chapter introduction, specifically the lack of structural protons in the mica and the inclusion of

sodium as a charge balancing cation rather than potassium. Because the mica contains sodium, a single layer of water is readily sorbed into the interlayer, expanding the interlayer spacing from 0.4 Å to 2.8 Å. In the expanded state, strontium or radium can enter the interlayer and exchange with the sodium cations. A third unique aspect of Na-4 mica is that successive layers are offset from each other by roughly one-third of the unit cell *b* dimension. This produces steric restrictions that make it unlikely for large divalent cations to coordinate with the oxygen atoms of the di-trigonal holes on opposite interlayer faces. However, in a recent report focusing on radium binding[196], strong electrostatic interactions between the radium and the interlayer surfaces were shown to force water out of the interlayer without heating, collapsing it to 0.6 Å. Komarneni has hypothesized that this collapse is also accompanied by a shift of the adjacent layers, eliminating the offset and producing a twelve coordinate radium cation spanning the interlayer gap.[196] This type of binding environment renders interlayer radium non-exchangable, making Na-4 mica a successful radium remediation material. The objectives of the ^{87}Sr NMR investigation of Na-4 mica are to (i) determine whether a similar layer shift and twelve-coordinate interlayer binding environment exists for strontium in heat treated Na-4 mica and (ii) if not, determine what the interlayer strontium binding structure and binding mechanism are in this material.

As indicated in Figure **5-3**, a single strontium resonance was observed from de-hydrated Na-4 mica after a 67 hour acquisition period using ^{1}H decoupled DFS-QCPMG at 21.14 T. *A priori*, one would predict the existence of at least two unique strontium environments in the heat treated Na-4 mica; an anhydrous interlayer site and at least one type of hydrated surface-sorbed species. The resonance observed by solid-state ^{87}Sr

NMR is readily assigned to anhydrous strontium cations bound in the interlayer, since (i) a vast majority of the strontium will be found in the interlayer, (ii) the number of available surface sites is likely too small for surface-sorbed strontium to be observed in a ^{87}Sr NMR experiment, and (iii) the resonance has too great a quadrupolar character to have resulted from hydrated strontium.

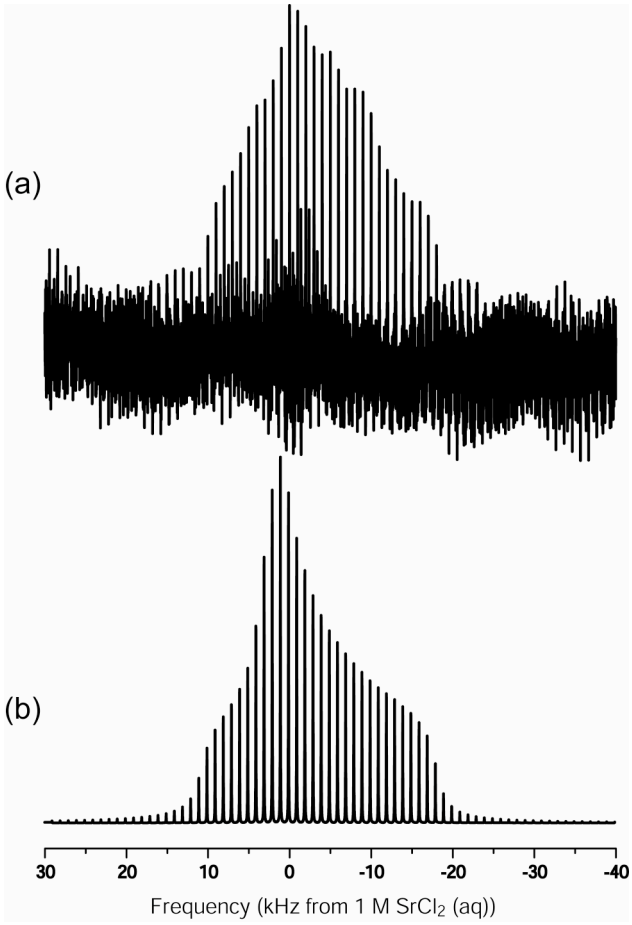

Figure **5-3**: The (a) experimental ^{87}Sr DFS-QCPMG spectrum of Na-4 mica acquired at 21.14 T and (b) the iterative simulation results obtained from SIMPSON.

The quadrupolar parameters extracted from this resonance provide significant insight into the interlayer strontium binding environment in heated Na-4 mica. If the twelve coordinate binding model proposed for radium were true for interlayer strontium,

the strontium cation will be located at the center of a highly symmetric coordination environment where quadrupolar effects should be negligible, leading to a narrow ^{87}Sr lineshape. However, the strontium resonance observed in the heat-treated mica has significant quadrupolar character and was well fit by a single quadrupolar lineshape with a coupling constant of 9.02 MHz and an asymmetry parameter of 1.0 (Figure 5.3).[127] Furthermore, if the strontium cations span the interlayer space as in the dehydrated radium model, we would expect to observe an interlayer spacing between 0.3 and 0.4 Å rather than the 0.12 Å that is observed with XRD. Thus, one may safely conclude that the binding mechanism of the interlayer strontium is not the same as the twelve-coordinate interlayer radium binding model.[196]

A quadrupolar asymmetry parameter of this magnitude has been associated only with highly distorted strontium coordination environments[99], suggesting that the strontium cations contributing to the resonance possess an asymmetric coordination sphere. Within the anhydrous interlayer, such an asymmetry can be envisioned for strontium cations bound through electrostatic interactions within the pockets formed by the di-trigonal holes (where a large electron density is available). In this situation, strontium cations will coordinate to the six oxygens of the di-trigonal hole and the adjacent fluorine atom found at the base of the di-trigonal pocket. Strontium bound in the di-trigonal pocket would not span the interlayer space, eliminating the driving force of strong electrostatic interactions across the interlayer required to induce a layer shift. To facilitate full charge compensation in a non-shifted case, the interlayer strontium cations are expected to include the two nearest oxygen atoms on the opposite interlayer surface in the coordination sphere, producing an electrostatically-driven nine-coordinate

asymmetric strontium binding site (Figure **5-4**). This type of coordination environment is also consistent with the 0.12 Å interlayer spacing observed with XRD and basic steric considerations arguing that the ionic radius of strontium cations allow them to fit in the di-trigonal pocket.

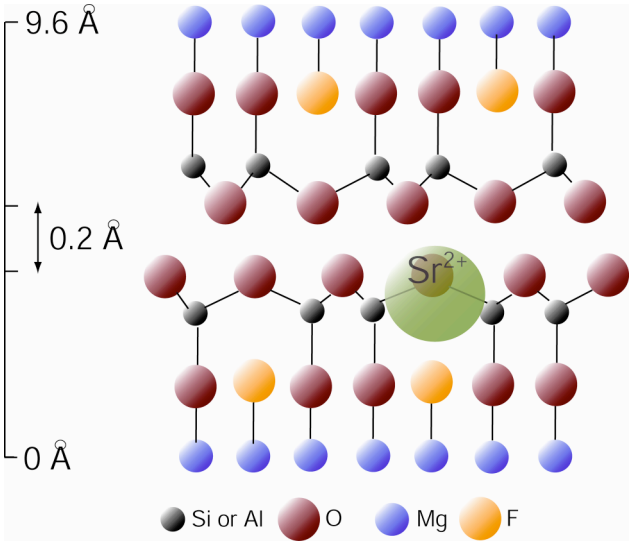

Figure **5-4**: Model of the strontium binding environment in Na-4 mica determined from the XRD and NMR results. The drawing is not to scale.

5.1.3.2 Na-3 Mica

Fewer details are known about the specific crystal structures of the Na-3 and Na-2 micas, primarily due to the difficulty in preparing single crystals for XRD refinement. The basic structure of both materials will be very similar to the Na-4 mica, evident from the similar *d*-spacing of all three hydrated and strontium-exchanged micas. The primary differences between the three micas are (i) the cation exchange capacity and (ii) the presence/extent of a layer offset. It is believed that the Na-3 mica contains an offset in

the unit cell *b*-dimension, though the extent of this offset is currently unknown. Based on the successful observation of strontium in the Na-4 mica, it is expected that anhydrous strontium will be observable in the Na-3 mica using ^{87}Sr DFS-QCPMG NMR at 21.14 T.

The ^{87}Sr spectrum from the heated Na-3 mica appears to be a single resonance with a quadrupolar coupling similar to interlayer strontium in the Na-4 mica (Figure **5-5**). Iterative simulation was able to achieve a acceptable fit despite the low signal-to-noise ratio using a single quadrupolar resonance defined by a coupling constant of 8.52 MHz and an asymmetry parameter of 0.48. The ^{87}Sr quadrupolar asymmetry parameter in the Na-3 mica is not nearly as high as that observed in the Na-4 mica, indicative of a more spatially uniform coordination environment. The quadrupolar nature of this resonance supports the proposed existence of a layer offset in the Na-3 mica and indicates that the layer shift is not eliminated upon strontium sorption and dehydration, just as for the Na-4 mica.

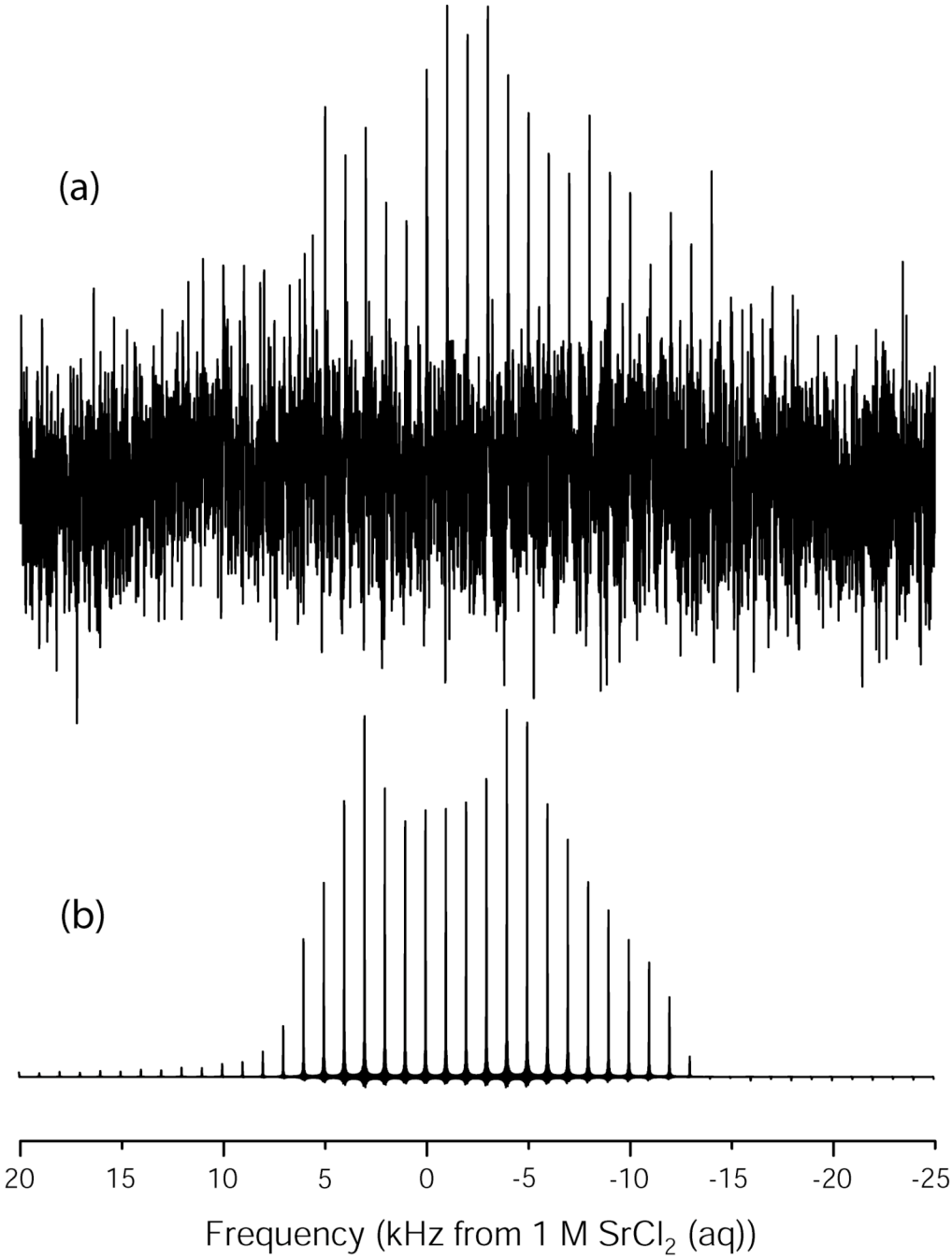

Figure **5-5**: The ^{87}Sr NMR spectrum of heated Na-3 mica from (a) experiment and (b) SIMPSON simulation.

The observed strontium quadrupolar parameters do not indicate, however, whether the layer offset is larger or smaller in the Na-3 mica. If the layer offset is reduced in Na-3 mica, it is possible that the strontium cation extends further into the interlayer space and coordinates with oxygen atoms composing the di-trigonal holes on each face of the interlayer. The presence of a slight offset in this scenario would tend to distort the strontium coordination sphere, leading to a quadrupolar coupling and asymmetry in the NMR spectrum. A less likely but still possible scenario in the case of a smaller layer offset is that the strontium cation resides in the di-trigonal pocket, but that the smaller layer shift produces a less distorted electric field gradient at the strontium nucleus (it is more likely that this situation would increase the quadrupolar parameters). At the opposite end of the spectrum, if the layer offset is larger than $b/3$, it is unlikely that the strontium cation will span the interlayer space, leading to electrostatically-driven binding in the di-trigonal pocket. With a larger offset (e.g., $b/2$), the coordinating oxygen atoms on the opposite face of the interlayer position to form a more spatially symmetric coordination sphere, leading to a reduction in the strontium quadrupolar parameters. The *d*-spacing from XRD does not point to a reduced or increased offset: the spacing is slightly larger than in the Na-4 mica (by 0.08 Å), which could be due to any of the proposed strontium binding arrangements (within the limits of uncertainty). From the ^{87}Sr NMR, we conclude that interlayer strontium in the Na-3 mica is bound through electrostatic interactions and that the layer offset is not eliminated. More detailed comment on the extent of the layer offset cannot be deduced from ^{87}Sr NMR and XRD alone.

5.1.3.3 Na-2 Mica

The Na-2 mica will likely have no layer offset as synthesized and resemble a typical brittle mica. In this structure, there is no steric restriction to strontium spanning the interlayer space, reducing the driving force for strontium sorption in the di-trigonal pocket. The Na-2 mica also has the lowest theoretical charge per formula unit and exhibits the lowest cation exchange capacity of the three micas. As the XRD results indicate, the heat-treated form will contain anhydrous interlayer strontium species, but may have a low enough strontium concentration to be unobservable by DFS-QCPMG at 21.14 T. Indeed, the Na-2 mica failed to produce an interpretable strontium resonance over a five day acquisition period, yielding only a few spikelets barely discernable above the noise level. Instrument time limitations prevented the acquisition of a better spectrum from this sample for detailed structural characterization. However, the low sensitivity observed in this experiment provides another opportunity to calculate a lower limit of ^{87}Sr detection for DFS-QCPMG at 21.14 T. With the assumption that half of the sample contained within the 5 mm NMR tube is located within the coil (roughly accurate based on visual observation), 2.8 x 10^{18} ^{87}Sr spins were present in the coil during this experiment. This is nearly an order of magnitude lower than the limit calculated in chapter 4 and likely represents the extreme lower limit of sensitivity. Based on the strontium acetylacetonate and Na-2 mica results, one may state with reasonable certainty that a minimum of 1 x 10^{19} ^{87}Sr spins (or roughly 0.001 moles of Sr) are necessary to produce an interpretable resonance during a five-day DFS-QCPMG NMR experiment at 21.14 T.

5.1.3.4 Strontium-Fluorine Interactions in the Swelling Micas

As stated earlier, the nine-coordinate interlayer binding model proposed for the Na-4 mica incorporates the fluorine at the base of the di-trigonal cavity into the strontium coordination sphere. If this model is correct, strontium bound in the di-trigonal pocket will attract charge from the electron-rich fluorine, de-shielding the nucleus and inducing an upfield frequency shift in the ^{19}F spectrum of the mica after heat treatment. Likewise, if strontium resides in the di-trigonal pocket of the Na-3 mica, it should also draw electron density from the coordinating fluorine and affect the ^{19}F NMR signature. Therefore, ^{19}F MAS NMR offers a mechanism to confirm the Na-4 interlayer binding model and may permit the unambiguous assignment of the interlayer strontium binding structure of the Na-3 mica.

The ^{19}F MAS NMR spectra of the three swelling micas before and after heat treatment are presented in Figure **5-6**. In the non-heated materials, a single fluorine peak appears in the spectrum of all three micas at a chemical shift of -142 ppm flanked by two up-field and two down-field spinning sidebands. From XRD, it is known that the non-heated micas have a larger interlayer space than the heated micas and can accommodate the strontium cation in the interlayer. The most likely strontium binding environment in the non-heated case is a partially hydrated species that is coordinated to the oxygen atoms composing the di-trigonal holes on adjacent sheets. There is no driving force for strontium to approach fluorine in the di-trigonal pocket without heat treatment, and thus a chemical shift of -142 ppm is assigned to fluorine on the octahedral sheet that is un-perturbed by interlayer strontium.

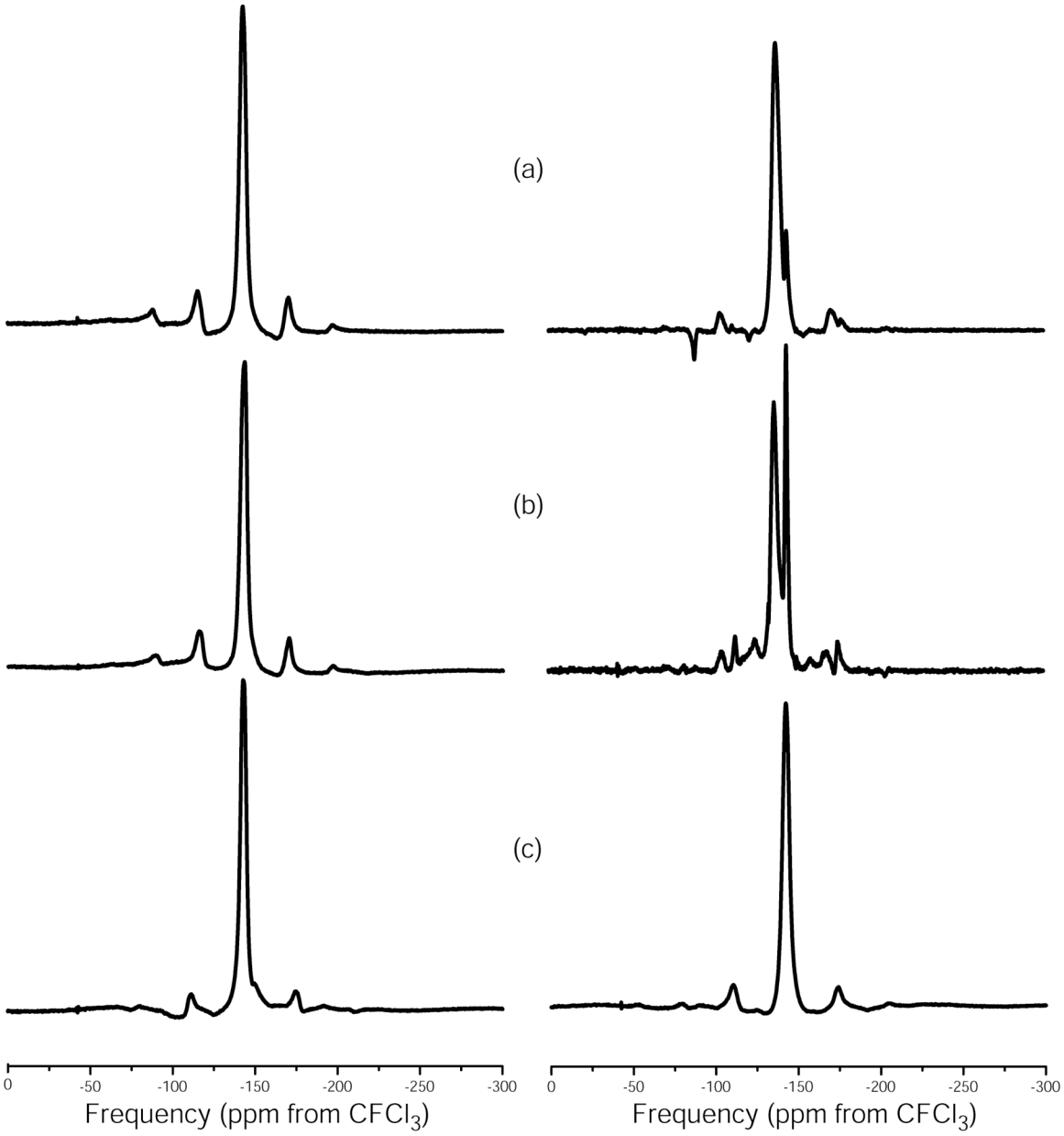

Figure **5-6**: The ^{19}F MAS NMR spectra of the non-heated (left) and heated (right) strontium-saturated swelling micas. Note the peak at -136 ppm on (a) Na-4 mica and (b) Na-3 mica indicative of fluorine close to strontium in the pocket formed by the di-trigonal hole. This peak is absent in Na-2 mica (c), where no layer offset that forces strontium into the di-trigonal cavity is present.

After heating, two peaks appear in the fluorine spectrum of Na-4 mica, each of which has a single spinning sideband up- and down-field. One of the peaks is centered at a chemical shift of -142 ppm and the other, larger peak is centered at a chemical shift of -136 ppm. A similar two-peak spectrum results for heated Na-3 mica (resonances centered at -136 ppm and -143 ppm) while the Na-2 mica has a single fluorine resonance at -142 ppm in the heated and non-heated case. To assign these peaks, we turn to the difference in layer offset between the three micas. As stated earlier, with no offset in the Na-2 mica, there are no steric restrictions forcing strontium cations deep in the di-trigonal pockets upon interlayer collapse. The interlayer strontium of the heated and non-heated Na-2 mica will likely span the interlayer space as in the proposed radium binding model and not coordinate to fluorine on the octahedral sheet. If this postulated structure is true, we would predict the appearance of a single resonance in the fluorine NMR spectrum of the heated Na-2 mica at the un-perturbed fluorine shift, as observed in Figure 5.6. However, in the other two heated micas, there is a layer offset that provides a steric restriction preventing strontium from spanning the interlayer space once the interlayer is collapsed. The steric hindrance combined with the large electron density available in the di-trigonal pocket drives the interlayer strontium close to the fluorine in the heated Na-4 and Na-3 mica, where it will shift the resonance frequency upfield. The peak at a chemical shift of -136 ppm is thus assigned to fluorine on the octahedral sheet that is perturbed by adjacent strontium cations residing in the di-trigonal cavity. The ^{19}F MAS NMR results confirm the binding structure proposed for the Na-4 mica and is consistent with two earlier conclusions about the Na-3 mica: (i) the predicted layer offset must exist and (ii) interlayer strontium is also bound deep in the di-trigonal cavity of the heated Na-

3 mica. Additional insight into the magnitude of the layer offset in Na-3 mica can not be deduced from the ^{19}F MAS NMR results.

The fluorine results also suggest that not all of the fluorine atoms in either heated Na-3 or Na-4 mica are associated with strontium cations. The single-pulse ^{19}F MAS results are quantitative, meaning that the integrated intensity of each peak (and sidebands) is proportional to the number of ^{19}F spins in each environment. The strontium occupancy of the di-trigonal cavities in the Na-3 and Na-4 micas can therefore be calculated from the ratio between the peak area of the -136 ppm resonance and the total peak area. For the Na-4 mica, integrations show that 85.3% of the di-trigonal cavities are filled with strontium nuclei. The percentage of filled cavities is reduced for the Na-3 mica (65.0%), correlating well with the reduction in strontium sorption capacity versus the Na-4 mica.

Having confirmed the close spatial relationship of interlayer strontium and fluorine in the Na-4 and Na-3 micas, it is reasonable to wonder whether strong ^{19}F-^{87}Sr dipolar couplings will form and affect the ^{87}Sr NMR spectrum. To determine the extent of such effects, the two spin ^{19}F-^{87}Sr dipolar coupling was calculated as a function of inter-nuclear distance according to the following equation (Figure **5-7**):

$$D = \left(\frac{\mu_0 h}{16\pi^3} \right) \frac{\gamma_{Sr}\gamma_F}{r_{Sr-F}^3} \tag{5.1}$$

where μ_0 is the magnetic permittivity of free space, γ_x is the gyromagnetic ratio of nucleus x, and r is the distance between the coupled nuclei in meters. The magnitude of this interaction was found to be only 613 Hz at the shortest possible inter-nuclear distance of 2.04 Å (fluorine atomic radius = 0.72 Å and strontium ionic radius = 1.32 Å). This

coupling strength is significantly less than the ≈ 9 MHz quadrupolar coupling that leads to the static linewidth of 20 to 30 kHz observed for the Na-4 and Na-3 micas. A dipolar coupling of this magnitude should therefore have little effect on the strontium NMR spectrum. To confirm this assertion, SIMPSON simulations of the strontium resonance incorporating this maximal dipolar coupling were performed. The simulation results did not show a significant effect in the shape or width of the ^{87}Sr NMR spectrum, permitting us to conclude that the presence of fluorine in the strontium coordination sphere does not significantly influence the strontium NMR resonance.

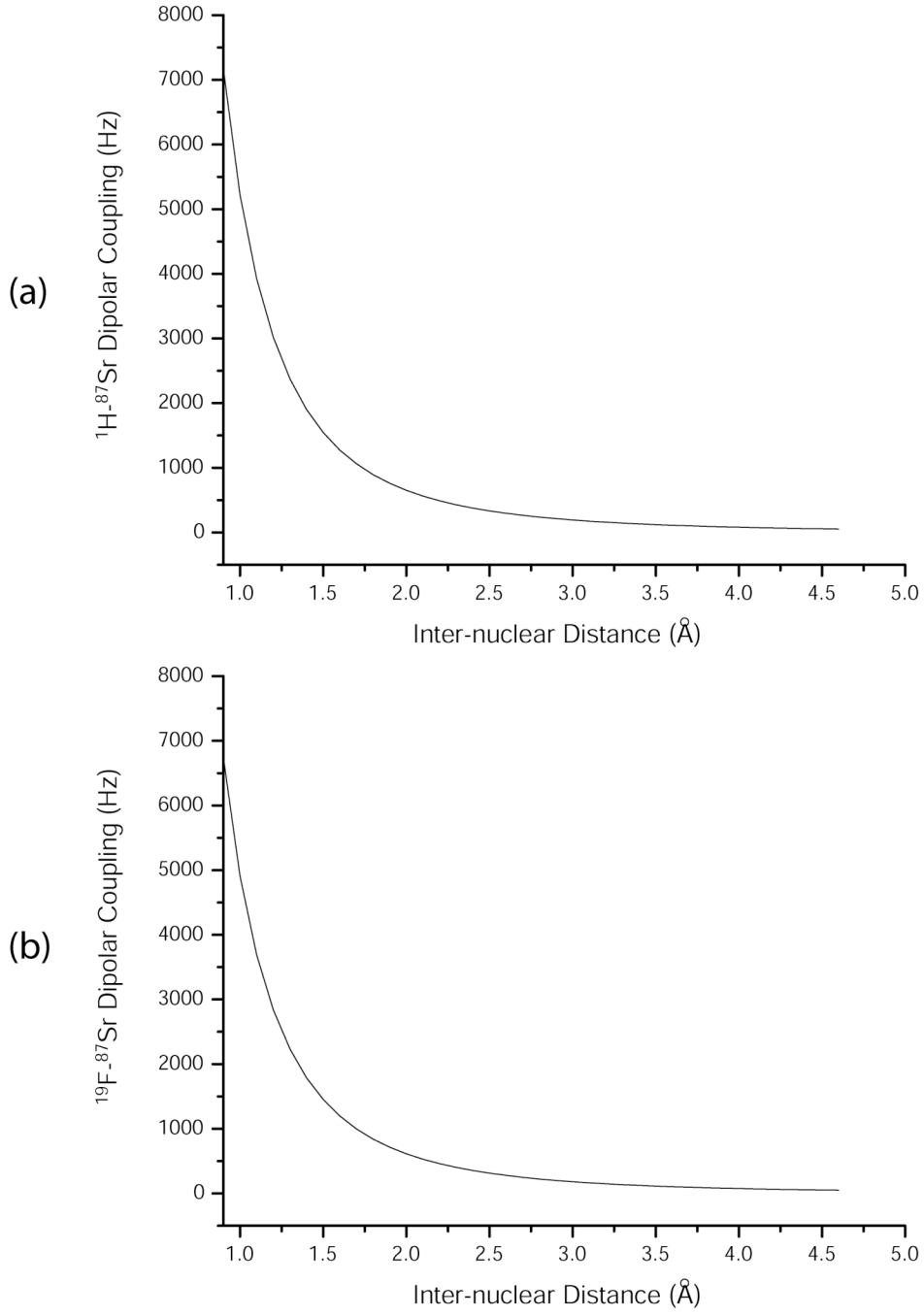

Figure **5-7**: Plots of the (a) proton-strontium and (b) fluorine-strontium two spin dipolar coupling as a function of inter-nuclear distance. The dipolar coupling rapidly rises to many thousands of Hz at distances below 0.9 Å.

5.1.4 Coordinating Water and Invisible ^{87}Sr

Before discussing the interlayer strontium binding environment in the montmorillonites (where strontium is expected to be hydrated), it is necessary to explore strontium-water interactions in more detail. Strontium in solution is generally considered to be nine-coordinate, highly mobile, and is readily observable by ^{87}Sr NMR. However, mounting experimental evidence suggests that strontium nuclei with water in the coordination sphere and a low degree of mobility can not be observed so easily. Hydration effects plagued early strontium experiments, such as ^{87}Sr MAS NMR investigations of strontium chloride hexahydrate (Figure **5-8**). Initial studies of the hexahydrate produced no detectable signal with or without proton decoupling; however, as time passed, a narrow resonance appeared that increased in intensity over time. This time-dependent resonance in the "hexahydrate" is attributed to strontium cations that become fully solvated through the incorporation of additional atmospheric moisture and increasingly mobile in the crystal network. MAS NMR experiments performed on damp, re-crystallized strontium chloride hexahydrate re-produced the strontium resonance from the latter time point in Figure 5-8 quite well (not shown), supporting this assertion. In addition to the strontium chloride hexahydrate results, crystalline strontium hydroxide octahydrate also failed to produce a detectable strontium resonance under static and MAS conditions as received. These data suggest that strontium nuclei with low mobility and water in their coordination sphere cannot be detected in simple crystals by direct ^{87}Sr NMR with these methods.

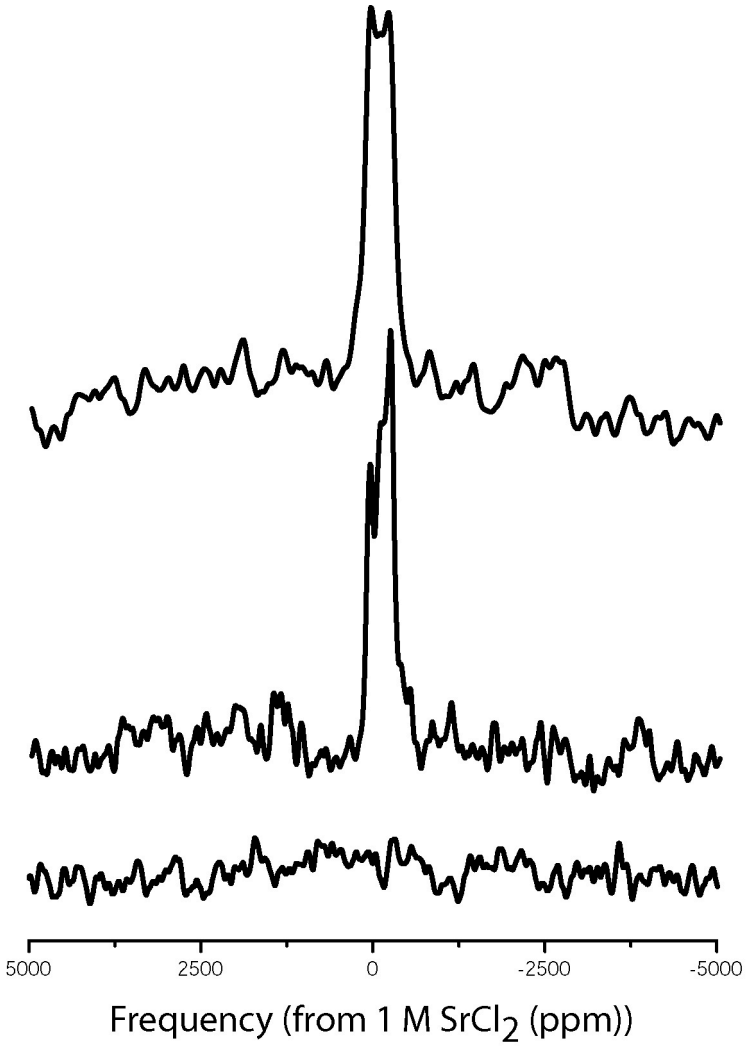

Figure **5-8**: Normalized ^{87}Sr MAS NMR spectra of strontium chloride hexahydrate as a function of time. The bottom spectrum was acquired from a fresh bottle opened on 1/19/04, the middle spectrum was acquired on 2/12/04, and the top spectrum on 3/24/04.

A similar limitation has been observed in ^{87}Sr NMR studies of the hydrated micas and montmorillonites. To date, a strontium NMR signal has yet to be detected in any phyllosilicate mineral where the surface-sorbed and interlayer strontium are at least

partially hydrated. The interlayer strontium cations in the hydrated micas are anticipated to have restricted mobility due to steric restrictions and electrostatic considerations. Similarly, hydrated interlayer strontium cations in the montmorillonites may also have low mobility since the systems studied here are strontium-saturated. The surface sorbed strontium species are likely to be fully hydrated with a reasonably high degree of mobility in the micas and montmorillonites; however, as noted in section 5.1.3.1, the surface strontium spin population is far too low to be detected with any direct ^{87}Sr NMR method. In addition, a strontium NMR signal has yet to be detected in any strontium-saturated tectosilicate minerals, where partially hydrated strontium species are expected to exist, lending additional weight to the hypothesis that hydrated and relatively non-mobile strontium can not be observed with ^{87}Sr NMR.

One potential source of the invisible strontium effect may be strong ^{1}H-^{87}Sr dipolar couplings between hydrating waters and the strontium nuclei that broaden the ^{87}Sr resonance to the point that it is un-detectable. Fortunately, this theory can be tested by calculating the magnitude of the dipolar coupling interaction as a function of proton-strontium inter-nuclear distance with equation 5.1. Even if a proton is located directly at the 1.3 Å ionic radius of a strontium atom (an unreasonably low distance), one finds that the dipolar coupling is only 2.3 kHz and rapidly decreases as distance increases (Figure 5.7). Considering that the smallest ^{87}Sr quadrupolar coupling observed in non-zero EFG materials is on the order of 9 MHz (≈ 20 kHz central transition line width at 21.14 T), single-spin ^{1}H-^{87}Sr dipolar coupling can not be responsible for the invisible strontium phenomenon. A second possibility is that water dramatically decreases the strontium relaxation rate, leading to saturation of the strontium resonance over the course of the

experiment. However, hydration typically modulates the EFG more rapidly, increasing the relaxation rate and making saturation effects an unlikely source of the invisible strontium phenomenon. Yet another possibility is that the incorporation of water into the strontium coordination sphere induces (i) strontium or (ii) water motion with a correlation time that renders strontium unobservable with direct room temperature ^{87}Sr NMR. If this explanation is correct, using variable temperature NMR to freeze out the motion will permit detection of a strontium resonance in these hydrated systems. An investigation of this possibility will form the basis of a future proposal for instrument time at PNNL.

In theory, the ^{87}Sr quadrupolar coupling provides a fourth potential source of the invisible strontium effect. Recall that in section 4.2.3, hydration of the $SrBr_2$ crystal significantly affected the strontium *quadrupolar* coupling. With dipolar coupling and saturation effects unlikely, it is tentatively concluded that water profoundly distorts the strontium coordination sphere, producing strong quadrupolar couplings. The precise relationship between hydration, mobility, and quadrupolar coupling is currently unknown and will require additional experimentation as well as detailed computational analyses to resolve. However, this phenomenon can also be used advantageously when studying the strontium binding mechanism in minerals, as we will see in the case of the montmorillonites.

5.1.5 Strontium Binding in the Heated Montmorillonites

5.1.5.1 Ca-Montmorillonite

Calcium is the typical charge balancing cation found in soil montmorillonites. It is believed to exist in the interlayer as a six-coordinate, fully hydrated outer-sphere complex and produces a *d*-spacing of roughly 14.8 - 14.9 Å (Figure **5-9**).[35] The ionic radii of Ca^{2+} and Sr^{2+} are somewhat similar when the cations are coordinated by six water molecules, 1.14 Å and 1.32 Å respectively. Because of the relative similarity in size and charge, it is reasonable to assume that interlayer strontium will also exist as a six-coordinate hydrated complex in this material (as reported by Chen *et al.*[191]), leading to a similar *d*-spacing. Recall that the *d*-spacing observed in the heated and non-heated strontium-saturated forms of Ca-montmorillonite is 14.9 Å, consistent (within uncertainty limits) with the presence of six-coordinate hydrated interlayer strontium. Despite the full hydration shell, the mobility of the interlayer strontium cations may be somewhat restricted due to the saturated state of the system. If the mobility is restricted, the invisible strontium hypothesis dictates that interlayer strontium in the strontium-saturated Ca-montmorillonite will not produce a resonance in a direct ^{87}Sr NMR experiment. In fact, the heat-treated strontium-rich Ca-montmorillonite did not produce an observable resonance in a ^{87}Sr DFS-QCPMG NMR experiment at 21.14 T, consistent with interlayer strontium sorption as a fully hydrated outer-sphere complex.

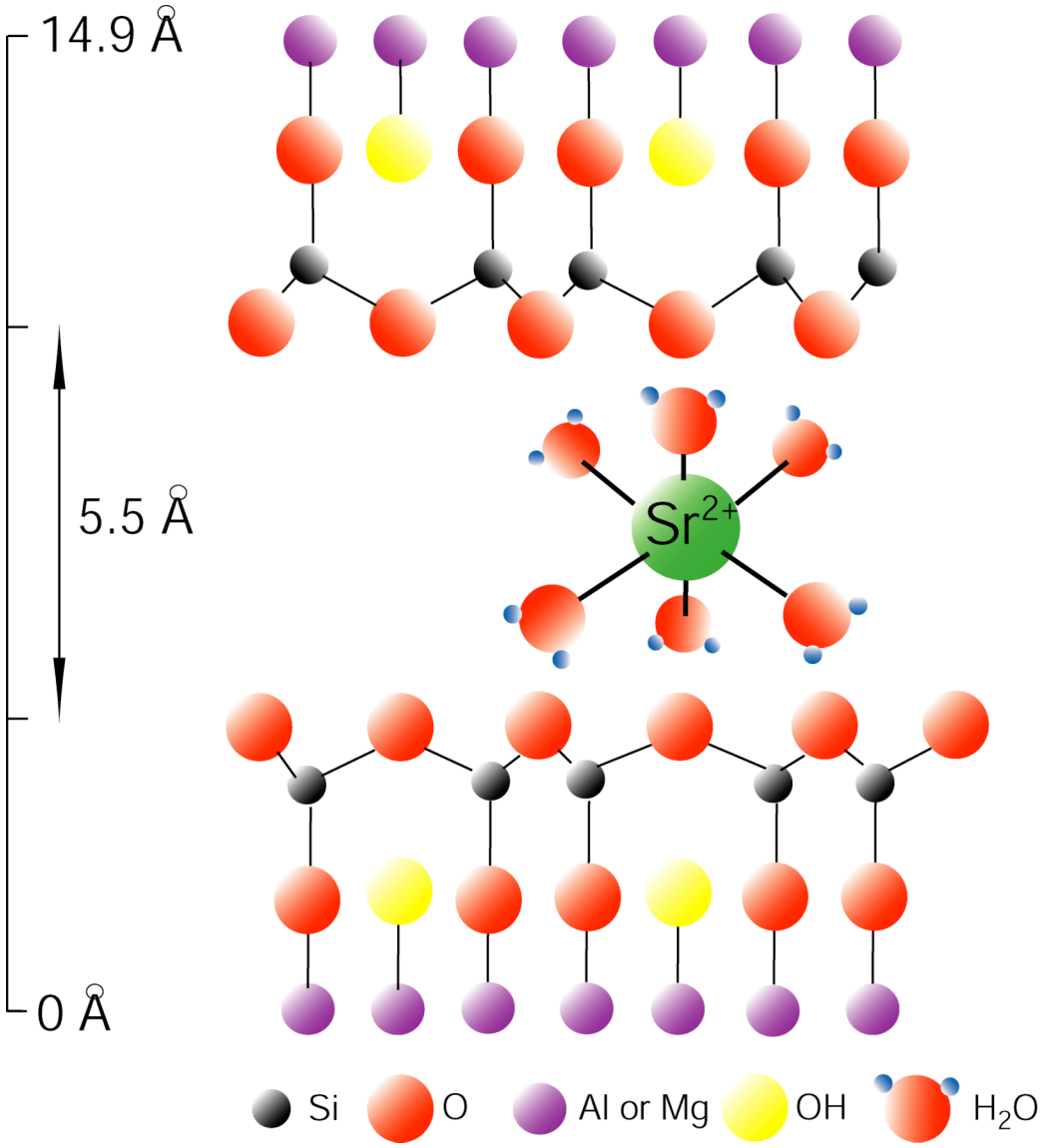

Figure **5-9**: Structural schematic of montmorillonite showing the hydrated interlayer strontium species. Drawing not to scale.

5.1.5.2 Na-Montmorillonite

The ionic radius of sodium in a six-coordinate hydrated configuration is 1.16 Å, only 2 pm larger than the ionic radius of calcium. The initial *d*-spacing of the Na-montmorillonite should be quite similar to that of Ca-montmorillonite, implying that interlayer sodium will also be present as a six coordinate hydrated complex that will readily exchange with hydrated strontium cations. Based on these similarities, we would predict that strontium-saturated Na-montmorillonite should therefore have a *d*-spacing similar to the strontium-saturated Ca-montmorillonite. Indeed, the *d*-spacing after strontium saturation is nearly identical for the two montmorillonites (14.9 Å) prior to heat treatment, allowing us to conclude that interlayer strontium in Na-montmorillonite is also bound as a six-coordinate hydrated complex. However, unlike the Ca-montmorillonite, the *d*-spacing after heat treatment showed a slight collapse corresponding to a reduction of the interlayer spacing from 5.5 Å to 4.4 Å. Presumably, this collapse is related to the partial removal of water from the interlayer, suggesting that the Na-montmorillonite has a lower dehydration temperature than the Ca-form. Whether the interlayer strontium cations are partially or fully hydrated, the invisible strontium hypothesis predicts that the heated Na-montmorillonite will not produce a strontium resonance in a ^{87}Sr DFS-QCPMG experiment. However, a single strontium resonance was detected in the heated montmorillonite that is moderately well fit with a single quadrupolar line shape using a quadrupolar coupling constant of 9.17 MHz and a quadrupolar asymmetry parameter of 0.32 (Figure **5-10**).

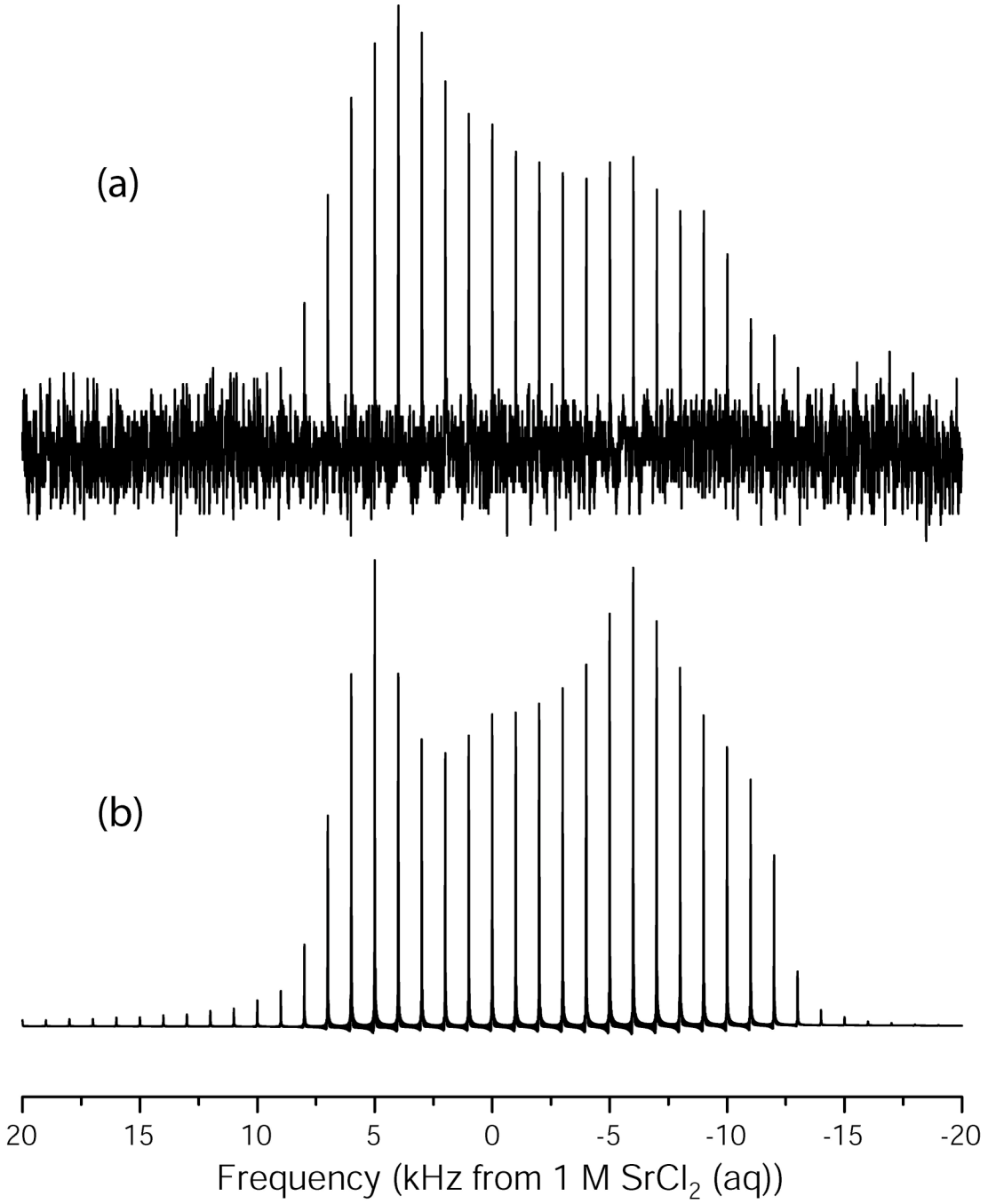

Figure **5-10**: The ^{87}Sr DFS-QCPMG spectrum of (a) heat-treated and strontium-saturated Na-montmorillonite and (b) SIMPSON simulation.

To explain the appearance of this strontium resonance, we turn to the ICP elemental analyses of the montmorillonites. The primary differences between these two members of the smectite family are the much greater Fe(III) content of the Na-montmorillonite and the degree of magnesium substitution for aluminum in the octahedral sheet (and therefore the cpfu and cation exchange capacity). ICP shows that there is between half and two-thirds as much magnesium substitution in the Na-montmorillonite, correlating well with the lower cation exchange capacity reported by the Source Clays Repository and implying that the Na-montmorillonite should sequester less strontium than the Ca-montmorillonite. Furthermore, since monovalent sodium is exchanging with divalent strontium and the layer charge is conserved, Na-montmorillonite would be expected to sorb even less strontium compared to the Ca-montmorillonite. However, the ICP results also show that the Na-montmorillonite sample contains a *greater* mass percent of strontium than the Ca-montmorillonite. The excess strontium can not be located in the mica interlayer without causing a charge imbalance, suggesting that the strontium must be sorbed to the exterior montmorillonite surfaces.

Since the available surface sorption sites are low in number with respect to interlayer sorption sites, the excess strontium is likely reacting to form a secondary strontium-bearing phase on the clay surface. The most likely secondary precipitated phase would be strontium carbonate, which is known to nucleate from concentrated strontium solutions under non-CO_2 free conditions.[197,198] The strontium spectrum of the Na-montmorillonite appears quite similar to the shape of the carbonate resonance (Figure **5-11**), though the quadrupolar parameters are slightly different. These

differences may be related to the crystallinity of the secondary carbonate phase or they may arise from interactions between the strontium carbonate and the montmorillonite surfaces. A literature precedent exists for the former of these two hypotheses, as the formation of an amorphous sodium carbonate phase on an aluminoborosilicate surface was reported by Egan *et al*.[199] An amorphous strontium carbonate phase would also explain the absence of strontium carbonate peaks in the XRD pattern of the strontium-saturated Na-montmorillonite. Recalling the high iron content of this material, a significant degree of iron substitution for silicon in the tetrahedral sheet may produce iron-rich regions that catalyze the formation of strontium carbonate, as reported in the EXAFS literature.[174] The assignment of the NMR resonance to strontium carbonate also explains the relative ease with which a ^{87}Sr NMR signal was acquired in a sample where a majority of the strontium should be hydrated. The strontium resonance observed from the heat-treated and strontium saturated Na-montmorillonite is thus assigned to a strontium carbonate phase forming on the external mineral surface, and is not related to hydrated interlayer strontium.

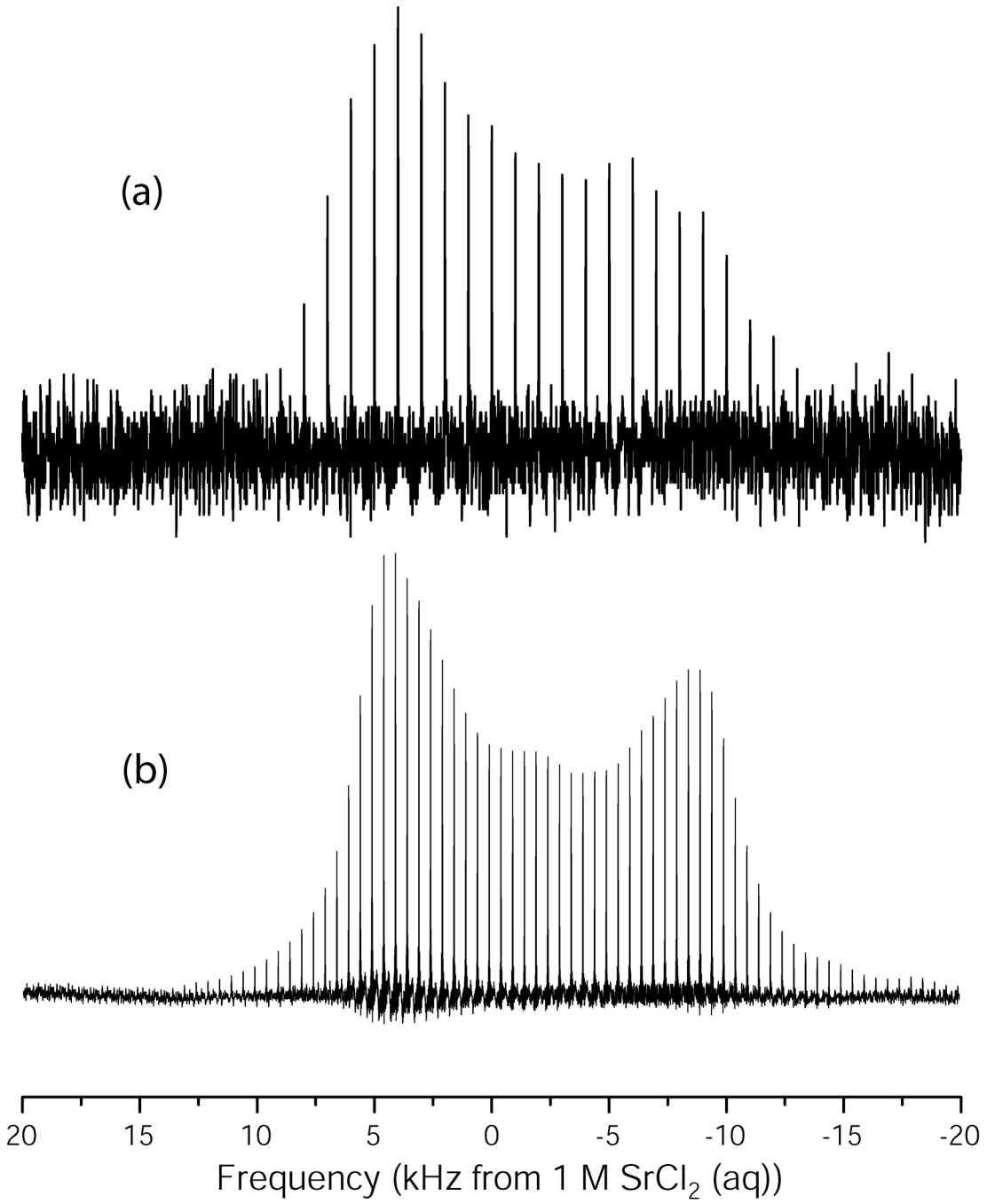

Figure **5-11**: The ^{87}Sr DFS-QCPMG spectrum of (a) heat-treated and strontium-saturated Na-montmorillonite and (b) strontium carbonate. Aside from the spikelet spacing, note the similarity in the two resonances.

5.1.6 Conclusions – ^{87}Sr DFS-QCPMG of Phyllosilicates

DFS-QCPMG at 21.14 T provides the sensitivity necessary to observe interlayer strontium resonances in dehydrated mineral phases. Background knowledge of the relationship between ^{87}Sr quadrupolar parameters and local structure allowed a detailed characterization of the interlayer strontium binding sites in heat-treated micas using XRD, ^{87}Sr NMR, and ^{19}F NMR. The interlayer strontium in heated Na-4 and Na-3 mica is bound through electrostatic interactions in the di-trigonal pockets as nine-coordinate complexes. Specific assignment of the heated Na-2 mica was not possible based on the sensitivity limits of ^{87}Sr NMR, but ^{19}F MAS experiments and XRD support the hypothesis that strontium spans the interlayer gap in Na-2 mica to form a twelve-coordinate species as in the radium binding model. Based on empirical evidence that strontium with water in the coordination sphere and restricted cation mobility cannot be observed with direct ^{87}Sr NMR methods, the ^{87}Sr NMR and XRD results support the assignment of six-coordinated, hydrated strontium species within the montmorillonite interlayer regardless of heat treatment. ^{87}Sr NMR was also used to identify an amorphous strontium carbonate phase on the Na-montmorillonite surface that was not observable by XRD.

5.2 Indirect Detection – ^{1}H-^{87}Sr TRAPDOR

Double-resonance NMR methods, such as the transfer of populations by double resonance (TRAPDOR) technique,[66,200,201] can be used to determine through-space interactions between nuclei and may be capable of detecting strontium indirectly via

interactions (dipolar coupling, scalar coupling) with other, more abundant, spins. Despite the weak proton-strontium dipolar couplings calculated in section 5.1, this interaction will be present to some extent (i) when water is a component of the strontium coordination sphere or (ii) when surface-bound protons are near strontium nuclei on the mineral exterior. Thus, ^{1}H-^{87}Sr TRAPDOR NMR may allow indirect observation of surface and interlayer hydrated strontium species reported in the EXAFS literature and invisible to direct ^{87}Sr NMR.

In this section, preliminary results of ^{1}H-^{87}Sr TRAPDOR studies with the hydrated and de-hydrated phyllosilicates are presented. For the heated Na-4 mica, on-resonance and off-resonance TRAPDOR NMR confirm the presence of a hydrated surface strontium environment. Results with the hydrated Na-4 mica are different and may originate from partially-hydrated interlayer strontium cations. The results with the Na-3 and Na-2 micas are less straightforward to interpret and should be investigated further with computational and XAS methods. For the montmorillonites, ^{1}H-^{87}Sr TRAPDOR shows the presence of hydrated interlayer strontium in the heated and non-heated Ca-form, but no signal results for the Na-form. The reasons behind these observations will be discussed, highlighting the inherent difficulties of double-resonance methods involving ^{87}Sr and the need for further research in this area.

5.2.1 Experimental

TRAPDOR NMR experiments[200,201] with proton detection and strontium dephasing were performed on an 11.74 T Varian Infinity spectrometer using the ^{1}H and

low-frequency channels of a 5 mm triple resonance MAS probe. To review the discussion from chapter 2, ^{1}H nuclei that are strongly coupled to strontium nuclei through the direct dipolar interaction (which has an inverse r^3 dependence on the internuclear distance r) can be identified in the ^{1}H-^{87}Sr TRAPDOR difference spectrum. A ^{1}H $\pi/2$ pulse width of 6 μs was used with a sweep width of 100 kHz to acquire both the S_o and S_f signals (Figure 2-6). The spin rate and inter-pulse delays were set at 10 kHz and 100 μs, respectively, to keep the experiment synchronized with the rotor period. One thousand transients for both S_o and S_f were acquired with 5 and 20 second pulse delays in the case of the Na-4 mica. The experiment was also repeated 5 kHz off-resonance to ensure the difference peaks were authentic and not the results of spectrometer or probe-related problems. Based on the Na-4 results, off-resonance TRAPDOR with a 20 second pulse delay was performed on the remaining micas and montmorillonites. For the figures, exponential apodization corresponding to 300 Hz of Lorentzian line-broadening was applied to the time domain signals before Fourier transformation and calculation of the TRAPDOR difference spectrum. Since TRAPDOR is a difference experiment, the proton background of the system is automatically cancelled during data processing and thus is not an issue. Chemical shifts are referenced to tetra-methyl silane (TMS) through a secondary standard from the residual ^{1}H species in D_2O at 298 K.

5.2.2 Na-4 Mica

5.2.2.1 Heated Mica

Though the interlayer irreversibly de-hydrates in the heated Na-4 mica, the external surfaces will spontaneously hydrate upon exposure to atmospheric moisture, an effect reported for a number of soil minerals in the available EXAFS literature.[174,191] Despite the low abundance of surface strontium and weak ^{1}H-^{87}Sr dipolar coupling, it may be possible to acquire a ^{1}H-^{87}Sr TRAPDOR signal from the surface strontium, providing indirect evidence of its existence. Two small peaks appear in the TRAPDOR difference spectrum of heated Na-4 mica (Figure **5-12**), one at a chemical shift of 3.6 ppm and the other at roughly 0.5 ppm.

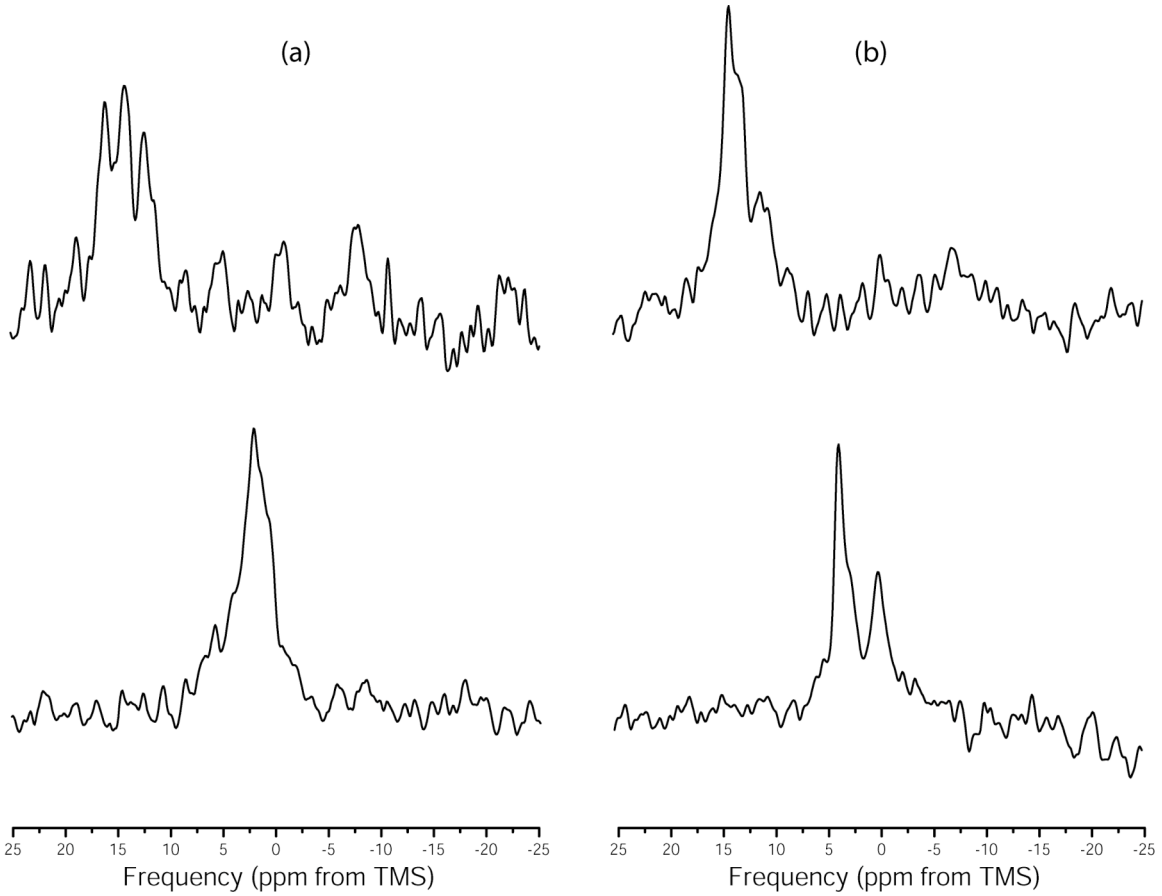

Figure **5-12**: The ^{1}H-^{87}Sr TRAPDOR NMR spectrum of strontium-saturated Na-4 mica (a) before and (b) after heat treatment. The top spectra were acquired 5 kHz off-resonance to eliminate any electronic glitches at the transmitter frequency.

The non-apodized TRAPDOR difference spectrum (not shown) contains peaks of very low intensity, which is expected based on the weak coupling and low natural abundance of the ^{87}Sr isotope. Recall that the maximum dipolar coupling will be on the order of a few hundred Hz (Figure 5-7), a relatively weak pathway for energy transfer. Since ^{87}Sr is only 7% abundant, only 7 out of every 100 strontium atoms will de-phase the associated proton peaks in the ^{1}H NMR spectrum. Additionally, the strontium dephasing efficiency is unknown under this set of experimental conditions and may be

quite low. Unfortunately, weak signals may also be generated by electronic interferences, timing errors, etc. rather than dephasing through a true proton-strontium coupling. Many of these electronic interferences occur at the transmitter frequency and can be eliminated by performing a duplicate experiment off-resonance. Any TRAPDOR difference peaks due to real ^{1}H-^{87}Sr interactions will shift approximately 10 ppm with respect to the transmitter frequency in our off-resonance experiment and indeed, the small TRAPDOR difference signal appears at the appropriate chemical shift. Upon apodization, one can clearly observe that both resonances are present in the off-resonance difference spectrum of the heated Na-4 mica, validating the on-resonance results.

The peak at 3.6 ppm is tentatively assigned to the protons on water molecules sorbed to the external silica surfaces of the Na-4 mica particles: it is well documented in the solid-state NMR literature that proton peaks shift upfield with increasingly strong hydrogen bonding interactions and proton shifts of ~3.5 ppm have been assigned to waters sorbed by silica surfaces.[202] The origin of the second peak is not as clear and can not be discussed in detail from these data alone. Some potential sources of this second resonance include (i) waters of hydration on the strontium nucleus that behave like bulk water, (ii) interactions of silanol groups on the mica surfaces with strontium cations, or (iii) minor impurity phases containing hydrated strontium cations. Because TRAPDOR is not inherently quantitative and there are a number of potential sources of ^{1}H-^{87}Sr interactions, the number of unique external strontium environments also cannot be deduced from the TRAPDOR data and will not be speculated upon here. However, the TRAPDOR results do support the existence of surface-sorbed and partially hydrated strontium in the heated Na-4 mica, in agreement with the mineral EXAFS literature.

5.2.2.2 Non-heated Mica

In the case of the non-heated mica, ^{1}H-^{87}Sr TRAPDOR peaks may arise from any of the possible surface species as well as from partially hydrated interlayer strontium. Although TRAPDOR is not quantitative, it is worth noting that the TRAPDOR signal from interlayer strontium in the Na-4 mica may be minimal at best. Interlayer strontium in the non-heated mica will not have a complete hydration sphere: based on the XRD spacing, only four water molecules at most may interact with each interlayer strontium cation. In reality, probably fewer nearest neighbor water molecules are found in the mica interlayer, exacerbating the abundance-related dephasing issue discussed in the previous sub-section. In addition, the proton-strontium inter-nuclear distances may be quite different in the interlayer than for fully hydrated external strontium species, which will affect the dephasing efficiency.

The on-resonance ^{1}H-^{87}Sr TRAPDOR data for the hydrated Na-4 mica show a shouldered peak with a maximum at a chemical shift of 2.68 ppm and a second, weaker peak at a shift of 6.8 ppm (Figure 5-12). The off-resonance difference spectrum has a reduced signal-to-noise ratio (speaking to the difficulty of ^{1}H-^{87}Sr TRAPDOR), making it difficult to assign an accurate peak count. Assuming that the three peaks are valid, one is located at a similar chemical shift to the sorbed water protons in the heated Na-4 mica spectrum (3.7 ppm). The second and third peaks (1.9 ppm and 5.65 ppm) may be associated with partially hydrated interlayer strontium species or surface environments that are not present in the heated Na-4 mica. XAS or first-principles calculations are necessary to accurately assign the peaks for the non-heated mica. It is difficult to draw

any conclusions from these TRAPDOR results due to the variations in the on- and off-resonance difference spectra. However, it does appear that at least one strontium surface environment is present in the non-heated Na-4 mica as well.

5.2.3 Na-3 and Na-2 Mica

Based on the successful implementation of ^{1}H-^{87}Sr TRAPDOR NMR in the heated Na-4 mica, one would expect TRAPDOR to be straightforward in the Na-3 mica and Na-2 mica. However, off-resonance TRAPDOR experiments failed to produce a difference spectrum in either of these two micas, regardless of heat treatment. The precise reason behind this observation is unclear and demonstrates that additional method development is necessary before indirect strontium detection is applied routinely to complex materials.

One possible explanation for the lack of a difference signal from interlayer water may be that no significant quantities of water are associated with strontium in either of these two materials. This is not a likely explanation for the non-heated micas, given the *d*-spacing and the lack of a ^{87}Sr signal (despite the sorption of a suitable amount of strontium in the Na-3 mica). A related concern would be that interlayer water is present, but at reduced levels in the Na-3 and Na-2 mica interlayers, which will also weaken the TRAPDOR difference signal. Thermo-gravimetric analysis of the hydrated micas and dehydrated micas exposed to atmospheric moisture should allow an estimate of the interlayer water content, addressing this possibility. Another explanation may be that the proton-strontium distances are quite different in the interlayer of the three micas: a larger

inter-nuclear distance will reduce the magnitude of the dipolar coupling, negatively impacting the efficiency of the TRAPDOR experiment. Repeating the TRAPDOR studies with longer dephasing times (either through multiple rotor cycle dephasing periods or by using additional spin rates) will help identify if variations in inter-nuclear distance are a major source of interference.

Regarding hydrated surface strontium species, the number of sorption sites may vary significantly between the three micas. The surface area and particle size distributions are related to the number of surface sorption sites, as is the surface pH. Measuring these properties will help characterize variations in the surface binding sites. The surface binding mechanisms may also be a source of variance between the micas and affect the TRAPDOR efficiency. To resolve these issues and increase the general utility of the method, a long-term ^{1}H-^{87}Sr TRAPDOR optimization study with the six mica samples and additional hydrated mineral phases should be performed.

5.2.4 Montmorillonites

5.2.4.1 Ca-Montmorillonite

In section 5.1.5.1, interlayer strontium in the heated and non-heated Ca-montmorillonite was assigned as a six coordinate hydrated strontium species based on the ^{87}Sr NMR and XRD data. Thus, fully hydrated strontium species are expected to exist on the external montmorillonite surfaces and in the montmorillonite interlayer, maximizing the potential for proton-strontium interactions in both environments. It is reasonable to

expect a strong and nearly identical TRAPDOR difference signal from interlayer protons if hydrated interlayer species are present in heated and non-heated Ca-montmorillonite.

A broad difference signal is observed in both samples with a maximum at -1.0 ppm for the non-heated sample and at -0.96 ppm for the heated sample (Figure **5-13)**. There is also a shoulder on the downfield side of the resonances, located at -3.7 and -3.5 ppm for the non-heated and heated sample, respectively. The chemical shifts and difference intensities are nearly identical for the two samples, as predicted for a fully hydrated interlayer strontium model regardless of heating. The shifts are also quite a bit different than those reported for the Na-4 mica difference spectrum, suggesting that these peaks do not originate from surface-bound strontium species. In addition, a majority of the hydrated strontium species will be found in the interlayer space, leading to the tentative assignment of the strong resonance near -1 ppm to interlayer strontium sorbed by outer-sphere complexation (again, without knowledge of the TRAPDOR efficiency, an assignment made on the basis of peak intensity can not be made with absolute certainty). The origin of the shoulder near -3.6 ppm is not precisely known and could be any number of surface sites, contaminant minerals, or perhaps even variations in the interlayer strontium coordination number. Though specific assignment of all peaks cannot be performed, the ^{1}H-^{87}Sr TRAPDOR experiment is consistent with the earlier assignment of outer-sphere strontium sorption in the Ca-montmorillonite interlayer.

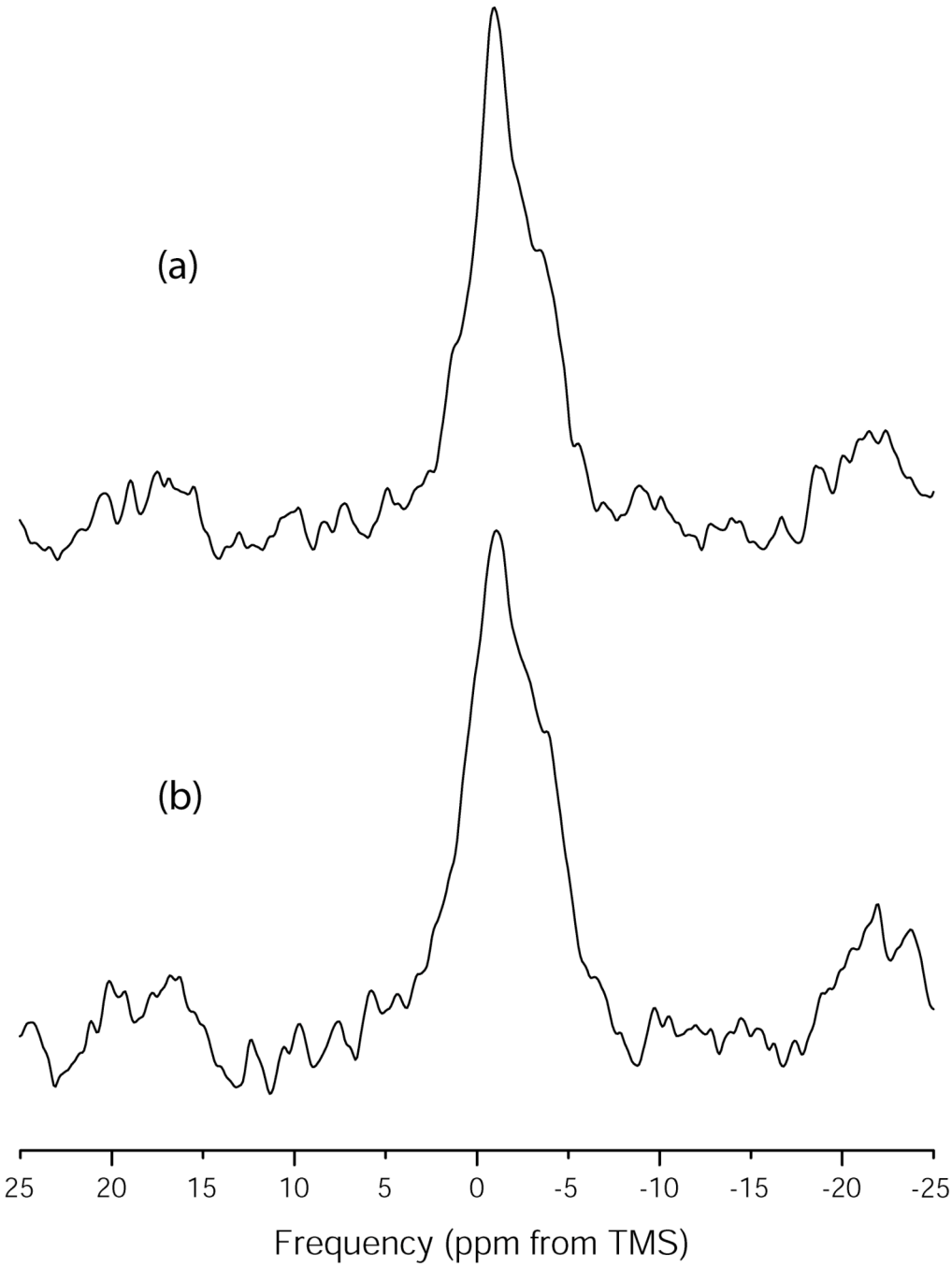

Figure **5-13**: The ^{1}H-^{87}Sr TRAPDOR NMR spectrum of strontium-saturated Ca-montmorillonite (a) before and (b) after heat treatment.

5.2.4.2 Na-Montmorillonite

Unlike the strontium-saturated Ca-montmorillonites, the heated and non-heated Na-montmorillonite samples did not produce a resonance in the ^{1}H-^{87}Sr TRAPDOR difference spectrum. Two additional interferences are present in the Na-montmorillonite that contribute to the lack of signal: (i) the surface nucleation of strontium carbonate and (ii) the relatively high paramagnetic iron content. Two potential problems arise from strontium carbonate formation. The first results when strontium carbonate coats the outer surface of the montmorillonite particles. If the edge sites become covered with this material, it may interfere with the interlayer cation exchange process, limiting the number of hydrated interlayer strontium nuclei that contribute to the TRAPDOR spectrum. Full or partial coverage of the planar silica surfaces will significantly reduce the number of surface-sorbed hydrated species as the number of available binding sites will be reduced. Furthermore, if the kinetics of strontium carbonate formation are rapid compared to the cation exchange kinetics, it is possible that the exchangeable strontium will be used to produce strontium carbonate rather than exchanging with sodium in the montmorillonite interlayer. While these hypotheses explain the lack of signal associated with hydrated surface species, the ICP results show a nearly full exchange of sodium for strontium in the interlayer, suggesting that strontium carbonate formation does not affect the interlayer ion exchange process significantly.

The lack of an observable ^{1}H-^{87}Sr TRAPDOR signal from the interlayer species likely lies with the iron content of the sample: there is greater than twice as much iron in the Na-montmorillonite than in the Ca-montmorillonite. The paramagnetic electrons

from structural iron can interfere with the ^{1}H NMR signal originating from interlayer proton species via the electron-nuclear hyperfine interaction. This type of interaction leads to severe broadening of the interlayer proton resonances and generally results in the appearance of a broad spinning sideband manifold. Both of these features are exhibited in the proton spectrum collected from the heated and non-heated Na-montmorillonite (Figure **5-14**). It is also worth pointing out that the signal-to-noise ratio of the Na-montmorillonite proton spectra is many orders of magnitude lower than the Ca-montmorillonite or the micas, which is readily explainable by severe broadening of the proton resonance(s). We conclude that paramagnetic broadening obscures the interlayer ^{1}H-^{87}Sr TRAPDOR difference signal in strontium-saturated Na-montmorillonite.

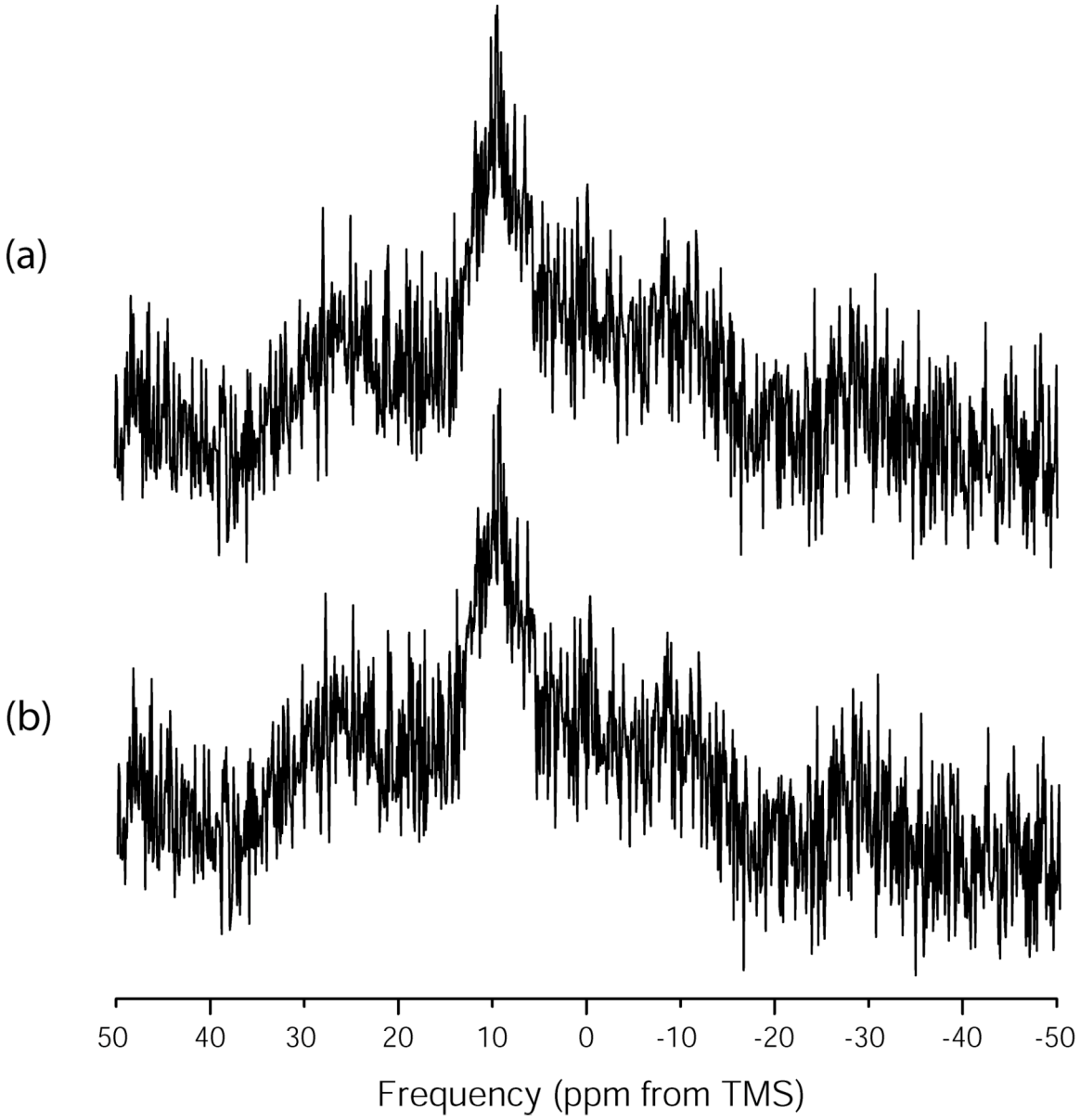

Figure **5-14**: The ^{1}H NMR spectrum of (a) strontium-saturated Na-montmorillonite before and (b) after heat treatment. Note the width of the resonance and the low signal-to-noise ratio.

5.2.5 Conclusions – ^{1}H-^{87}Sr TRAPDOR NMR

Though ^{1}H-^{87}Sr TRAPDOR NMR is experimentally challenging due to the low abundance of ^{87}Sr and the relatively weak ^{1}H-^{87}Sr dipolar coupling, it can be useful in studies of strontium sorption by mineral phases. In the case of the Na-4 micas, ^{1}H-^{87}Sr TRAPDOR NMR was able to confirm the presence of hydrated or partially hydrated surface species regardless of heating. However, acquisition and interpretation of the TRAPDOR difference spectrum can be difficult, as demonstrated in the case of the Na-3 and Na-2 micas. ^{1}H-^{87}Sr TRAPDOR was more useful for the montmorillonite samples, where it was readily capable of detecting hydrated interlayer strontium species in the Ca-montmorillonite. The lack of a signal in the Na-montmorillonite highlighted the importance of strontium carbonate formation in that system and the effects that iron can have on an NMR spectrum. To help establish ^{1}H-^{87}Sr TRAPDOR NMR as a viable method for strontium detection in minerals, additional low-iron systems must be studied and the TRAPDOR conditions optimized for a number of standard minerals. A means of sensitivity enhancement, such as enriching the ^{87}Sr content of a sample, may be a more appropriate technique for increasing the effectiveness of ^{1}H-^{87}Sr TRAPDOR.

Chapter 6

Conclusions and the Future of ^{87}Sr NMR

In the previous three chapters, solid-state NMR was used to probe the relationship between ^{87}Sr quadrupolar parameters and the local binding structure in inorganic crystals, organic crystals, and phyllosilicate minerals. We learned that ^{87}Sr DFS-QCPMG at 21.14 T provides much greater sensitivity enhancement than MAS, reducing the acquisition time by a factor of at least 100,000 versus static echos at 11.74 T. We also learned that the ^{87}Sr quadrupolar parameters are highly sensitive to variations in the strontium coordination sphere and that a particularly strong relationship exists between the quadrupolar asymmetry parameter and the spatial symmetry of the coordination environment. Ultimately, ^{87}Sr DFS-QCPMG NMR at 21.14 T was used along with XRD and other techniques to characterize the interlayer strontium binding environment in strontium-saturated phyllosilicate minerals. A series of synthetic, strontium-selective Na-fluorophlogopite micas were found to sequester interlayer strontium through strong electrostatic interactions deep in the di-trigonal pockets following heat treatment at moderate temperatures, effectively immobilizing the strontium in an anhydrous form. In the natural minerals that were studied, it appears that interlayer strontium is bound through outer-sphere complexation, in agreement with published XAS results. These hydrated strontium species were non-observable with direct ^{87}Sr NMR methods in these minerals, inorganic crystals, or tectosilicate minerals, presumably due to extreme quadrupolar broadening or dynamic effects. In addition, ^{87}Sr NMR proved highly

sensitive to the formation of strontium carbonate on the relatively iron-rich surface of a strontium-saturated Na-montmorillonite. Evidence was also presented that hydrated surface and interlayer environments may be detected through indirect double resonance techniques, such as ^{1}H-^{87}Sr TRAPDOR, though more development is necessary to make double resonance strontium detection routine. These studies provided insight into strontium-mineral interactions that will affect strontium remediation strategies and augment reactive transport models, accomplishing the mission of this research project.

They also demonstrate the potential of high-field strontium NMR to resolve structural questions about strontium coordination in other complex materials, such as strontium ion exchange media and high-temperature superconductors. In particular, strontium interactions with strontium sorbants involved in the current waste remediation strategies, secondary phase precipitates in waste-exposed soils, and apatite minerals (the primary mineral component of bone) are also poorly understood at the molecular level and are relevant to the US DOE. This chapter will present preliminary ^{87}Sr DFS-QCPMG investigations of these three material classes, laying the groundwork for future research in the Mueller group.

In the first section, NMR is used to probe strontium sequestration by a pair of strontium selective synthetic titanate minerals.[203,204] These materials are currently part of the DOE plan for high-level waste remediation at the Savannah River site in South Carolina, where they will be used to concentrate strontium and actinides from the aqueous waste prior to vitrification. Aside from high strontium selectivity exhibited by the titanates under the harsh waste chemistry, very little is known about the bulk or available cation binding structure(s), nor is the mechanism with which strontium is

sequestered by these materials known. Solid-state ^{87}Sr NMR is used to support a number of conclusions reached from XAS studies by a collaborator and provides additional insight into strontium sequestration by these materials. This project will be continued via high-field ^{87}Sr and $^{47/49}$Ti NMR studies of synthetic titanosilicate strontium sorbants in the summer of 2006.

The second section will explore the molecular-level interactions of strontium with secondary precipitated phases formed during the weathering of soil minerals under near-field exposure to tank waste.[31] A strontium-rich simulated tank waste solution is prepared and seeded with colloidal silicon to mimic the precipitation of secondary phases in the field without interferences accompanying silicon release by parent soil minerals. The precipitate formed in the batch reactors is collected after a 30 day incubation period and characterized with XRD, ICP, and ^{87}Sr DFS-QCPMG at 21.14 T. The composition of the precipitate and sequestration of strontium is discussed. Plans are also presented for a more detailed precipitate research project.

The final section of the chapter introduces preliminary ^{87}Sr NMR investigations into strontium sequestration by synthetic apatite. A successful high-field investigation of a mixed strontium hydrogen phosphate material is reported. Based on these results, a series of apatites with varying Ca/Sr ratios were prepared by Ramesh Ravella in Prof. Sridhar Komarneni's laboratory. Unfortunately, these samples did not yield a strontium resonance during DFS-QCPMG experiments at 21.14 T and could not be analyzed with double-resonance NMR techniques. More detailed analyses of the apatites will be necessary before a detailed research project may be formulated.

6.1 Strontium Binding in Synthetic Titanate Minerals

The Savannah River site in South Carolina is another location where the United States operated a plutonium production facility during the Cold War era. Currently, Savannah River storage facilities contain roughly 130 million liters of high-level waste in underground storage tanks similar to those used at Hanford.[205] The Hanford and Savannah River wastes have similar chemistry and the waste tanks at both facilities contain a mixture of sludge, salt cake, and aqueous solution. Current Savannah River remediation plans involve a three-step process: (i) dissolving the solid tank waste, (ii) concentrating the cesium, strontium, and actinides in exchange materials, and (iii) vitrifying the concentrated waste. Monosodium titanate (MST) is the sorbant material currently designated for the concentration phase of the remediation procedure. Both MST (similar to $NaTi_2O_5 \bullet xH_2O$) and the related sodium nonatitanate (SNT, $Na_4Ti_9O_{20} \bullet xH_2O$) are stable in highly alkaline solutions and will selectively sequester strontium, uranium, plutonium, and neptunium from solutions with significant Na^+ concentrations.[204-206] Unfortunately, the structure of these ion exchange media and their associated strontium binding mechanism(s) and site(s) are poorly understood.[203,206,207] XAS studies with MST suggest that strontium is sorbed to the surface of MST particles as a partially hydrated inner sphere complex, though evidence was also found supporting outer-sphere sorption.[205] Solid-state NMR studies of strontium and titanium in these materials will help to identify the number of sorption sites and strontium sorption mechanism in MST and SNT, contributing toward the design of better titanate sorbants as well as more efficient waste processing procedures. In this section, preliminary ^{87}Sr

NMR data from strontium loaded forms of SNT and MST is presented and a framework for future NMR studies of these materials is formulated.

6.1.1 Experimental

6.1.1.1 Synthesis and Cation Exchange

Both the Sr-MST and Sr-SNT samples were donated by Abe Clearfield at Texas Agricultural and Mechanical University and David Hobbs at Savannah River National Laboratory. The Sr-SNT sample was prepared according to the synthesis procedure of Clearfield and Lehto.[203,207] MST was prepared according to the procedure in Hobbs *et al*., a modification of a synthesis developed at Sandia National Lab.[204,208] A portion of the SNT and MST was exposed to a 1 mg/L strontium solution for one week under constant stirring to facilitate strontium exchange. In research reported by Duff *et al*. with MST prepared and exchanged in an identical fashion, the Sr-MST sample was shown to sorb 95% of the strontium from solution.[205] The MST and Sr-MST were analyzed with high resolution transmission electron microscopy (HR-TEM) and energy dispersion spectroscopy (EDS) using a 400 keV JEOL 4000EX instrument. Both strontium X-ray absorption near edge structure (XANES) and EXAFS analyses were performed on K-edge data collected from the X23a2 and X26a beamlines at the National Synchrotron Light Source at Brookhaven National Laboratory. Similar XAS analyses with SNT and Sr-SNT are currently in progress in the Hobbs laboratory.

6.1.1.2 NMR

Proton-decoupled ^{87}Sr DFS-QPCMG experiments were performed at PNNL under identical conditions to those presented in section 5.1.1. The Sr-MST and Sr-SNT both required averaging of 120,000 transients at a single transmitter frequency. A comb filter apodization equivalent to 2 kHz of exponential apodization for each half echo was applied before transformation to the frequency domain. The spectra are referenced to a 1 M aqueous solution of $SrCl_2$ prepared from $SrCl_2 \bullet 6H_2O$ (obtained from Sigma-Aldrich). Iterative simulations to extract the ^{87}Sr quadrupolar parameters were performed using real pulse conditions and 8,000 repulsion-based crystallite orientations with the SIMPSON program by Bak, Rasmussen, and Nielsen.[47] The full simulations required six hours to complete on the Lion-XO computing cluster at the Pennsylvania State University using 32 2.4 GHz 64-bit AMD Opteron processors with 8 GB of RAM allocated to each processor.

6.1.2 Strontium Mono-sodium Titanate

Though the bulk structure of MST has yet to be refined from X-ray or neutron diffraction, TEM analyses reveal that MST exists primarily as spherical particles consisting of a central glassy amorphous phase with fiber-like material on the outer surface.[205] From energy dispersive spectroscopy (EDS), strontium appears to sequester only in the fibrous structure without affecting the morphology of this phase. The role of the glassy material in strontium sorption is not well understood, though it appears from TEM and EXAFS to be passive in nature. Analysis of the strontium XAS results

demonstrated that the strontium nuclei sorbed by MST have an average coordination number of 6 (5.2 to 6.9) and are best fit by a model with two titanium environments in the second shell. These titanium environments have different strontium-titanium distances and may indicate partially hydrated inner-sphere adsorption and/or outer-sphere adsorption of a fully hydrated strontium complex.

If strontium is present as a partially hydrated inner sphere complex, it should be invisible to ^{87}Sr NMR, as discussed in chapter 5. Any strontium sorbed as an outer sphere complex may (i) be unobservable if the mobility of the hydrated complex is low or (ii) produce a fairly narrow resonance, such as that observed for strontium chloride hexahydrate under conditions of high mobility (Figure 5.8). However, the ^{87}Sr NMR signal in Sr-MST displays a classic quadrupolar powder pattern roughly 18 kHz in width (Figure **6-1**). It is reasonably well fit with a single quadrupolar line-shape having a coupling constant of 8.9 MHz and a quadrupolar asymmetry parameter of 0.16. The position, shape, and quadrupolar parameters of this resonance are strikingly similar to the strontium carbonate resonance presented in chapter 4. Though Duff *et al*. did not report the presence of strontium carbonate based on the XAS and HR-TEM studies, actinide carbonates were shown to form at the surfaces of MST, indicating that strontium carbonate formation is feasible under the exchange conditions.[205] Furthermore, at low strontium loading, Duff *et al*. reported a coordination number of nine that did not correlate well with the nine-coordinate strontium species found in aqueous solution. This nine-coordinate strontium could represent a strontium carbonate phase and suggests that strontium carbonate nucleation may be the dominant form of sorption at low loadings. The intensity of the ^{87}Sr NMR spectrum in our Sr-rich MST after a three day acquisition

period indicates that a relatively small quantity of strontium carbonate is formed on MST, which may explain why the XAS techniques did not detect this phase. The resonance observed in the ^{87}Sr DFS-QCPMG experiment is thus assigned to strontium carbonate forming on the MST surface. The lack of any additional strontium resonances in the NMR spectrum are consistent with the assignments made by Duff *et al*., suggesting that a partially hydrated inner-sphere complex and/or an outer-sphere complex with restricted mobility may also be present in Sr-MST.

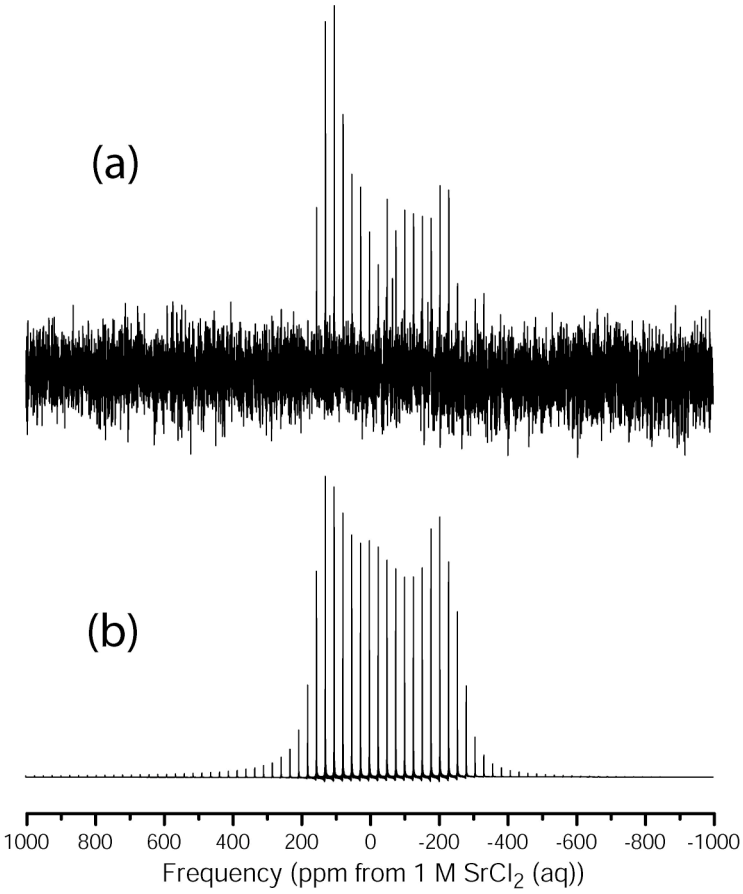

Figure **6-1**: The ^{87}Sr DFS-QCPMG pattern for Sr-MST (a) collected from experiment and (b) from the iterative simulation results.

6.1.3 Strontium Sodium-nonatitanate

Strontium-SNT is another titanate sorbant that is particularly strontium-selective at alkaline pH and high ionic strength. The bulk structure of this material has not been determined to date, though an attempt at refinement was made by Clearfield *et al*.[203] While the full structure was not solvable, SNT is believed to be a layered material with a *d*-spacing that depends on the water content, analogous to an expansive clay. If Sr-SNT is heated, it decomposes to a mixture of $SrTiO_3$ and TiO_2 phases rather than experiencing a heat-induced collapse of the postulated interlayer. XRD patterns of SNT and Sr-SNT show no variation as a result of strontium substitution for sodium[207], suggesting either (i) a water-rich interlayer environment incorporating hydrated strontium or (ii) that the strontium is not sorbed in the SNT interlayer. XAS analyses are currently in progress by colleagues at Savannah River National Lab to explore the strontium binding environment in this material on the molecular level.

The ^{87}Sr NMR spectrum for Sr-SNT is displayed in Figure **6-2**. The resonance in this material is once again very similar to the spectrum of Sr-MST and of strontium carbonate. It is well fit with a single quadrupolar powder pattern corresponding to a quadrupolar coupling of 8.5 MHz and an asymmetry parameter of 0.13, slightly smaller than the parameters observed for pure strontium carbonate. This discrepancy may indicate that the strontium carbonate formed on SNT is of a slightly altered morphology compared to natural strontianite. The spectrum from Sr-SNT is also more intense than that of Sr-MST, implying that the formation of strontium carbonate on the SNT surface is a more significant strontium sorption mechanism in this case. Again, there is still the

possibility that either (a) a partially hydrated inner-sphere strontium complex and/or (b) an outer-sphere complex with limited mobility is present in Sr-SNT based on the ^{87}Sr NMR. A more detailed structural analysis requires the completion of XAS measurements and theoretical analyses.

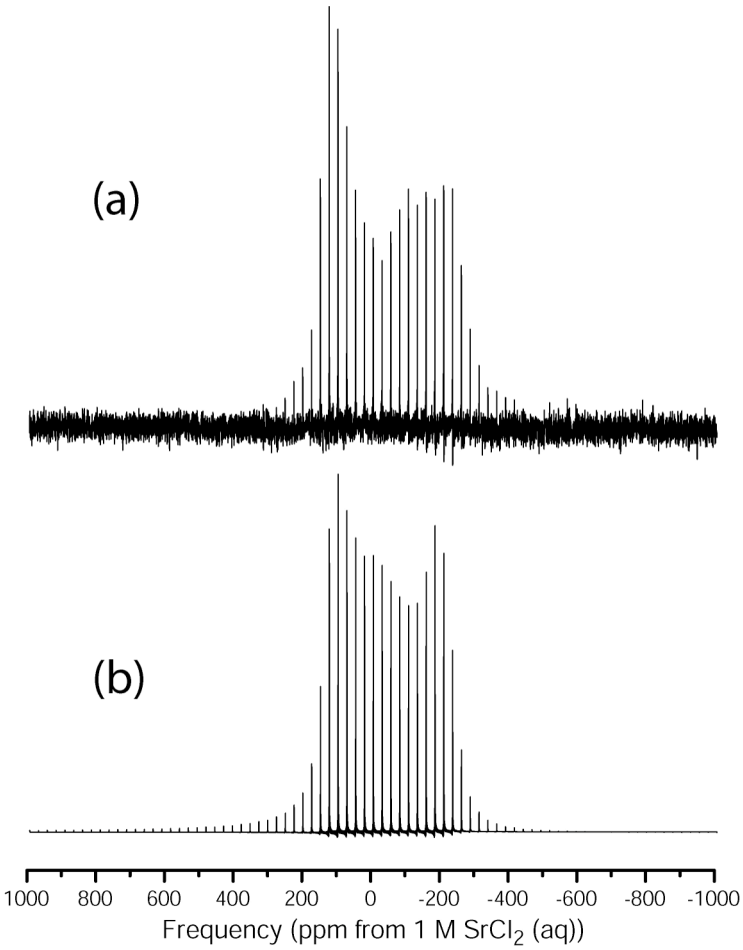

Figure **6-2**: The ^{87}Sr DFS-QCPMG pattern for Sr-SNT (a) collected from experiment and (b) from iterative simulation results.

6.1.4 Continuing Studies

While it was difficult to propose an actual binding structure for strontium in these materials based on the ^{87}Sr NMR results, a strontium carbonate phase not observed by XAS was found in MST and SNT with NMR. It is also reasonable to conclude that strontium carbonate formation is an important strontium sequestration mechanism for SNT based on the intensity of the carbonate resonance. Beyond the observation of a strontium carbonate phase, the NMR data are consistent with the assignment of hydrated or partially hydrated strontium species in SNT and MST (as reported by Duff *et al*.). The next step in a detailed NMR study of these materials would be $^{47/49}$Ti NMR to examine the titanium component of SNT and MST. Both NMR-active titanium isotopes are low-γ quadrupolar nuclei that will also benefit from DFS-QCPMG at 21.14 T. There should be an observable difference in the titanium quadrupolar parameters before and after strontium loading if strontium is sorbed as an inner-sphere complex. Formation of an outer-sphere complex may also affect the titanium NMR signal from SNT and MST, and in a different fashion than inner-sphere strontium sorption. The proposed titanium NMR experiments at PNNL are planned for the coming summer. In addition, Hobbs and co-workers at Savannah River National Lab are studying a pair of titanosilicate strontium/actinide sorbants that have tunable strontium vs. cesium selectivity. Similar preliminary ^{87}Sr and $^{47/49}$Ti NMR analyses of these two materials are planned for the remainder of 2006, with the hope of forming a larger, collaborative research project to examine the cesium and strontium binding structures as a function of Cs/Sr selectivity.

6.2 Strontium Synthetic Tank Waste Precipitate

Chorover and colleagues have examined the weathering behavior of individual soil minerals under near-field exposure to simulated tank waste leachate (STWL).[31] Under the high pH conditions characteristic of the waste solution, silicon and aluminum are released from the tetrahedral and octahedral sheets as the minerals weather. When the silicon concentration in the soil solution reaches a solubility limit, fully tetrahedral aluminosilicate phases precipitate and sequester ions from the soil solution.[209-211] The neo-formed materials may be selective for cesium and/or strontium, in which case they will impact the transport of these species through the sub-surface soils and the remediation of those soils. It is therefore desirable to identify the precipitated phase(s) and determine their selectivity for strontium. Unfortunately, it is difficult, if not impossible, to separate the cation sequestration properties of the parent clay from the neoformed phases in the mineral weathering experiments. In addition, research has shown that multiple tetrahedral minerals are formed through this dissolution/re-precipitation process, further compounding the above mentioned problem.[212]

To overcome these complications, it is desirable to induce the precipitation of secondary phases without the presence of the parent minerals. One can achieve such a scenario by seeding STWL with varying levels of colloidal silicon, thus providing the raw material for neophase formation without including the parent clays. This type of experiment was performed in the Chorover lab (results yet to be published) and analyses by an inter-disciplinary group revealed that the precipitated products were very similar in structure to the neoformed weathering products, particularly at low parent solution silicon

to aluminum (Si/Al) ratios. However, the strontium concentration in solution was kept very low (10^{-5} to 10^{-3} *m*) in keeping with the known Hanford tank compositions; values that are far too low to detect a strontium signal in these phases by DFS-QCPMG NMR at 21.14 T.

To increase the number of ^{87}Sr spins in the precipitated material and enable study with ^{87}Sr NMR, one option is to repeat the precipitation experiments using a strontium-rich STWL. To a first approximation, only the strontium-specific weathering products should precipitate from Sr-STWL and these materials should contain a high enough strontium concentration to facilitate study with ^{87}Sr NMR. The formulation of strontium-rich STWL for use in identical nucleation experiments is reported in this section. The resulting precipitates formed after a 30 day incubation period are analyzed with ICP, XRD, and ^{87}Sr NMR. It appears that amorphous silica and strontium carbonate are the two primary reaction products of silica-induced precipitation in Sr-STWL. These preliminary results suggest that a more detailed Sr-STWL precipitation study will help identify (i) strontium selective neophases formed in Hanford sediments and (ii) the formation kinetics of these phases.

6.2.1 Experimental

6.2.1.1 Strontium Simulated Tank Waste Preparation

As stated in the first chapter, the chemical composition of each waste tank at Hanford varies slightly. However, the general chemical makeup of the waste is an

aqueous solution of high alkalinity (pH ≈ 13.5) and high ionic strength (due to molar quantities of Na^+ and NO_3^-) with a significant quantity of free aluminum. Jon Chorover and colleagues at the University of Arizona have developed a process for making a synthetic tank waste solution[31] based on the waste chemistries reported by McKinley *et al*.[30] Here, a modified version of that procedure is reported for preparing a STWL mimic with Sr^{2+} as the dominant cation in solution.

The first step is to prepare a $Sr(NO_3)_2$ stock solution that is 6 *m* in nitrate and a stock solution that is saturated with $Sr(OH)_2$. The nitrate solution is prepared by dissolving 317.4 g of $Sr(NO_3)_2$ in 500 g of MilliQ water under constant stirring for roughly 15 minutes. The appropriate amount of saturated strontium hydroxide solution can be prepared by dissolving 99.6 g of strontium hydroxide octahydrate in 350 g of MilliQ water in a poly-propylene (PP) bottle. The bottle should be heated to 90°C in a water bath under conditions of constant and rapid stirring until all of the strontium hydroxide octahydrate is dissolved. Allow the solution to cool to room temperature while continuing to stir. As the solution cools, excess strontium hydroxide will precipitate, leaving a saturated room-temperature caustic solution. Once the solution has completely cooled, allow the precipitated $Sr(OH)_2$ to settle under gravity for 24 hours or centrifuge the stock solution until the supernatant is clear.

The Sr-STWL should be prepared from these stock solutions and sodium aluminate in a second PP bottle. First, add 3.09 g of $NaAlO_2$ (produces a final Sr-STWL Al^{3+} concentration of 0.05 mol/kg) to the second PP bottle. Add 194.0 g of the nitrate stock solution to the bottle, place it on a magnetic stir plate, and stir rapidly. Next, carefully decant all of the strontium hydroxide stock solution into the PP bottle

containing the nitrate/aluminate solution, making sure to transfer as little precipitated strontium hydroxide as possible. Mix this solution for at least one hour to ensure that the aluminate is fully dissolved (the solution may appear cloudy during this process). After the one hour mixing period, centrifuge the Sr-STWL solution to remove any remaining solids from the solution.

6.2.1.2 Homogeneous Nucleation Procedure

6.2.1.2.1 Preparation and Reaction

Reactions should all be performed in 30 mL PP bottles to ensure that silicon and unwanted cationic species are not leached from laboratory glassware. Add approximately 18 g of Sr-STWL to each reaction bottle (reactions should be performed in triplicate for statistical purposes) and two additional bottles that will serve as blanks. Transfer 5.01 g of MilliQ water to each bottle and then titrate one of the two blank solutions with standardized 0.1 M HCl solution to determine the hydroxide concentration. Values will typically be in the 0.05 mol/kg range, providing a reaction mixture pH of 12.75. For a parent solution Si/Al ratio of 1:1, add 1.99 g of Ludox HS-40 colloidal silicon solution to each reaction bottle. Note that the blank not used for the titration should not be seeded with silicon. Upon addition of the silicon, a gelatinous, milky suspension may appear in the reaction bottles. Shake each bottle vigorously for roughly 5 seconds to disperse the suspension and then place the bottles on a shaking apparatus. Allow the reaction to

proceed for 30 days, checking on the bottles each day to ensure proper mixing is occurring and note any changes in the appearance of the solutions, blank, or precipitate.

6.2.1.2.2 Product Processing

At the conclusion of the 30 day reaction period, remove the bottles from the shaker and transfer the full contents (liquid and precipitate) of each bottle to a clean 30 mL PP centrifuge tube. Centrifuge the samples at 2500 rpm for five minutes to separate particulates larger than 1.25 μm from the solution phase. Allow the contents of each tube to settle for 30 minutes. Collect approximately 10 mL of the supernatant from each tube in a separate 30 mL PP bottle and refrigerate. Centrifuge the remaining solution at 13,500 rpm for 20 minutes. Extract the remaining supernatant into a second set of 30 mL PP bottles and acidify each bottle with nitric acid until the pH is between 1 and 2. Record the initial pH, final pH, and weight of the liquid in each bottle before and after acidification, then store these bottles in the refrigerator as well. Re-suspend the particulate remaining in the centrifuge tubes in 10 mL of a 95% ethanol solution adjusted to pH 10 with additional saturated strontium hydroxide solution. Shake the centrifuge tubes on a reciprocal shaker at 200 rpm for 5 minutes and then centrifuge at 13,500 rpm for 20 minutes, discard the supernatant, and repeat the re-suspension and wash procedure two additional times with 95% ethanol that has no pH adjustment. After the final wash, discard the supernatant and place the centrifuge tubes in an oven for approximately 12 hours at 70°C. Collect and weigh the precipitated material.

6.2.1.3 ICP and XRD

The above procedure was used to prepare five replicates of strontium precipitate from a parent solution Si/Al ratio of 1:1. Elemental analysis of one replicate was performed with ICP-AES in the Penn State Materials Characterization Laboratory. The sample was digested in a lithium metaborate fusion and analyzed for the oxides of Si, Sr, Al, Ba, Ca, K, Mg, Mn, Na, P, and Ti on a Leeman Labs PS3000UV ICP spectrometer. The precipitate was also analyzed by XRD to determine whether the sample was crystalline or amorphous and to identify any crystalline phases by comparison with the ICDD database. XRD patterns were collected using Cu-Kα radiation on a Rigaku Geigerflex diffractometer scanning from 4° to 65° 2θ at a rate of 0.03° per second.

6.2.1.4 NMR

The ^{87}Sr NMR spectrum was acquired using DFS-QPCMG at 21.14 T. The frequency sweep and pulse conditions were identical to those presented in section 5.1.1. One-hundered twenty thousand transients were acquired at a single transmitter frequency with forty refocusing pulses per transient. A comb filter equivalent to 2 kHz of exponential apodization was applied and the data were zero filled to 262,144 data points before Fourier transformation. The spectrum is referenced to a 1 M aqueous solution of $SrCl_2$ prepared from $SrCl_2 \cdot 6H_2O$ (obtained from Sigma-Aldrich). Iterative simulations to extract the ^{87}Sr quadrupolar parameters were performed using real pulse conditions and 8,000 repulsion-based crystallite orientations with SIMPSON on the Lion-XO cluster.

6.2.2 Precipitate Characterization

Elemental analysis determined that the precipitate is 81wt% silicon, 5.6 wt% strontium, 0.31 wt% barium, with trace amounts of aluminum as well as other mono-, di-, and tri-valent cations (note that elemental carbon was not determined). The XRD spectrum (Figure **6-3**) shows the presence of an amorphous phase along with a few peaks associated with a more crystalline material. Comparison with the ICDD database identified the more crystalline phase as strontium carbonate. The precipitate did yield at least one ^{87}Sr NMR resonance over a 3 day acquisition period with DFS-QCPMG on the 21.14 T spectrometer (Figure **6-4**). The resonance is moderately well fit by a quadrupolar pattern roughly 20 kHz wide (C_q = 9.32 MHz, η = 0.15) and corresponds to the spectrum acquired for pure strontium carbonate, aside from an intensity difference in the singularities. This could be due to the formation of a carbonate phase with a slightly different morphology, the presence of multiple strontium phases, or perhaps a disordered carbonate phase. We conclude that the primary products of the modified homogeneous nucleation experiment are an amorphous silicate material that may or may not contain strontium and a second strontium carbonate phase detectable by XRD and NMR. This supports the assertion that strontium carbonate formation in soil systems exposed to the tank waste may be an important strontium-sequestering process. In addition, nucleation of strontium carbonate on the outer silicate surface of soil minerals may inhibit weathering reactions and affect the transformation kinetics, factors that must be included in reactive transport models.

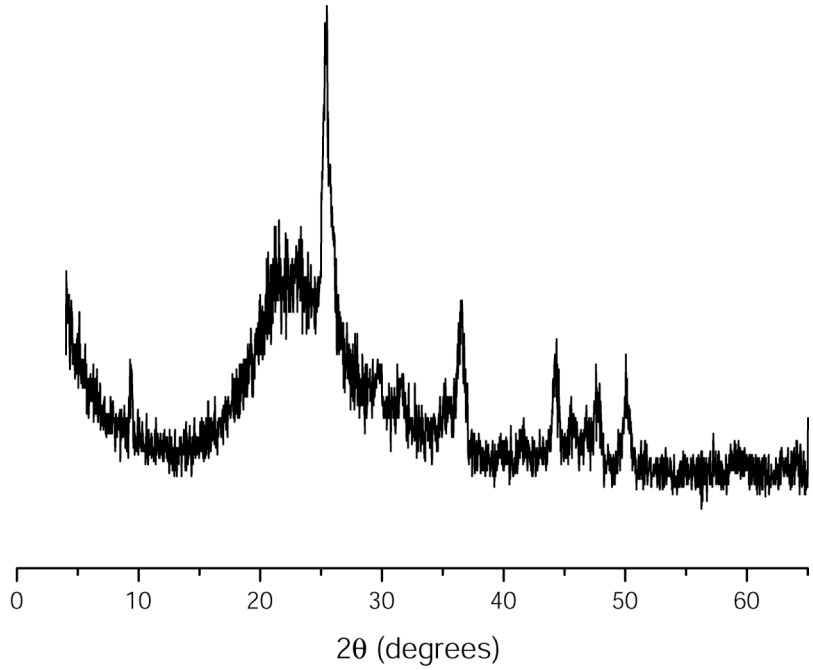

Figure **6-3**: XRD pattern for the strontium precipitate, showing a broad peak associated with an amorphous material and a series of weak crystalline peaks associated with strontium carbonate.

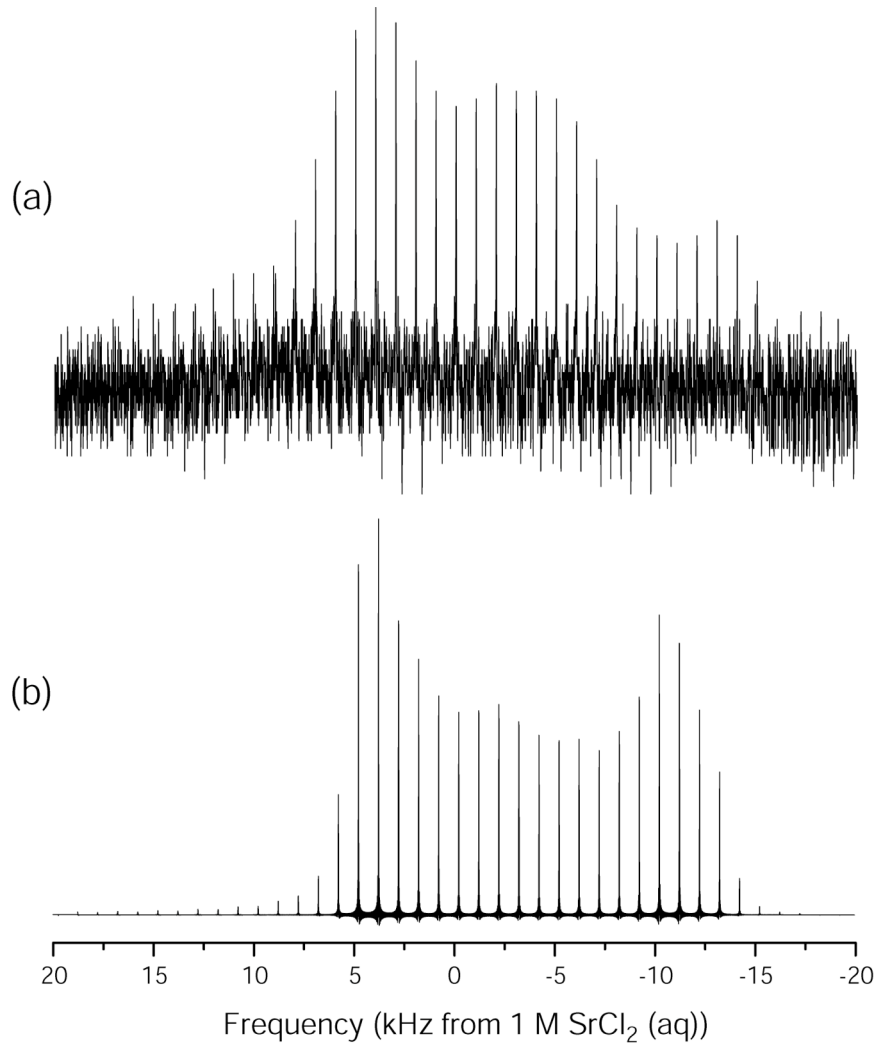

Figure **6-4**: The ^{87}Sr DFS-QCPMG pattern for the Sr-STWL precipitate collected (a) from experiment and (b) from iterative simulation results.

6.2.3 Continuing Studies

Though the Sr-STWL is not an exact duplicate of the tank waste chemistry or conditions, the preliminary study supports EXAFS hypotheses that strontium carbonate formation is an important factor in strontium sequestration (and perhaps weathering

kinetics) at Hanford-relevant chemical conditions.[174] As such, performing a more complete Sr-STWL precipitate study where the parent solution Si/Al ratio and the length of the reaction period are varied seems warranted. Adjusting the Si/Al ratio will help determine if the silicon concentration in solution affects the nature of the precipitated material and varying the reaction period will allow a kinetic investigation of product formation. Replicates should be performed in the presence of atmospheric CO_2 and under CO_2-free conditions to determine the rate of strontium carbonate formation under atmospheric conditions and to identify the strontium environments that form when carbon dioxide is absent from the system. In addition, SEM/EDS should be included in the analysis scheme to (i) examine precipitate morphology as a function of time and (ii) determine whether strontium carbonate nucleates on the amorphous silicon surface or as a separate entity. Repeating the entire set of proposed studies with Sr-STWL and with the strontium content in the Sr-STWL reduced by a factor of ten should also be explored to generate results more applicable to the field while balancing the time efficiency of ^{87}Sr NMR experiments.

6.3 Structural Role of Strontium in Apatite Minerals

As mentioned previously, ^{90}Sr is the second most abundant radioactive contaminant contained in the Hanford tank waste and is responsible for a significant amount of the waste radioactivity.[1] Perhaps more disturbingly, radio-strontium has been detected in the Columbia river, though the waste storage facility is remote from the river.[17,206] These finding suggest that strontium is quite mobile in the Hanford sediments

and potentially could migrate into the ground water, where it would become available to plants, local wildlife, and thus the human population in the Tri-citites region.[213] Though strontium is not sorbed into the blood stream as easily as cesium, roughly 15% of strontium that is metabolized becomes sequestered in bone mass. Once sequestered, this β-emitter may become a persistent radiation source within the body, increasing the risk of cancer in adults and adversely affecting bone growth in children.[22]

The kinetics of strontium uptake by bone and the affects of strontium sequestration on the bulk structure have been examined by numerous authors in the literature.[22-26,214-217] Studies by multiple authors have shown that strontium levels tend to build in the blood stream of exposed rats and beagles, peaking at seven to fourteen days post-oral or nasal exposure and clearing the bloodstream completely after 180 days.[23,26] The levels in bone tend to peak four weeks following exposure with varying clearing times reported in the literature. Beyond the clearing rates, disagreement is also found in the literature regarding the mechanism of strontium incorporation by bone. In the 2001 review article by Dahl *et al*., they suggest that strontium is sequestered primarily in new, callous bone and that it is present primarily on the bone surface.[23] This finding is supported by the work of Rokita and colleagues, where strontium EXAFS studies are also consistent with strontium sequestration primarily on the bone surface and indicate that the coordination environment appears to be different for adults and children.[215] However, other authors have reported the formation of strontium/calcium solid solutions in bone apatite, tooth enamel, and in a simple β-tricalcium phosphate crystals.[24,25,214] Investigating the local strontium binding environment in apatites on the molecular level using solid-state NMR will help resolve these discrepancies.

In this section, preliminary data is presented regarding the feasibility of solid-state ^{87}Sr NMR investigations of strontium-bearing apatite minerals. The effectiveness of ^{87}Sr DFS-QCPMG at 21.14 T will first be demonstrated in a crystalline sample of strontium hydrogen phosphate. Successful observation of strontium in this system prompted the synthesis of hydroxyapatite minerals with varying strontium to calcium (Sr/Ca) ratios. Unfortunately, direct strontium NMR studies of these materials did not reveal a strontium resonance with DFS-QCPMG at 21.14 T. Double resonance methods also proved unsuccessful in the synthetic apatites due to electronic issues. Potential reasons behind the failures with apatite minerals will be explored and demonstrate that there are still obstacles to overcome in solid-state ^{87}Sr NMR.

6.3.1 Experimental

6.3.1.1 Materials

Strontium hydrogen phosphate (99.98% metals basis) was obtained from Sigma-Aldrich. Strontium hydrogen phosphate has a general composition that is comparable to an apatite crystal ($SrHPO_4$ vs. $Ca_5(PO_4)_3OH$), contains a large quantity of strontium, and can be obtained readily. As such, this material represents a good starting point for evaluating the feasibility of strontium NMR experiments in apatite minerals. XRD analyses confirmed that the sample is a mixture of two known strontium phosphate forms, β-$SrHPO_4$ and $Sr_2P_2O_7$ (strontium pyrophosphate). Samples of Ca-apatite, Sr-

apatite, and 1:1 Ca/Sr-apatite were synthesized by Ramesh Ravella in the laboratory of Prof. Sridhar Komarneni at Penn State using a proprietary procedure.

6.3.1.2 NMR

The ^{87}Sr NMR experiments were performed using DFS-QPCMG at 21.14 T as described in section 5.1.1. The strontium hydrogen phosphate spectrum required the acquisition of 50,000 transients with proton decoupling at three different transmitter frequencies. A comb filter equivalent to 2 kHz of exponential apodization was applied and the data were zero filled to 262,144 data points before Fourier transformation and combination with a sky projection. Roughly 40,000 transients were acquired for the Sr and 1:1 Ca/Sr apatite samples without any sign of a strontium NMR signal. The data are referenced to a 1 M aqueous solution of $SrCl_2$ prepared from $SrCl_2 \cdot 6H_2O$ (obtained from Sigma-Aldrich). Iterative simulations to extract the ^{87}Sr quadrupolar parameters were performed using real pulse conditions and 8,000 repulsion-based crystallite orientations with SIMPSON on the Lion-XO computing cluster as described previously.

6.3.2 Strontium Hydrogen Phosphate

Strontium hydrogen phosphate is known to exist in a variety of allotropic morphologies[218-220], some of which are well characterized while the detailed structures of others have yet to be explored. As stated in the experimental section, XRD analyses reveal that the strontium hydrogen phosphate sample received from Sigma-Aldrich is a

mixture of two known forms: β-$SrHPO_4$ and $Sr_2P_2O_7$. The latter of these two phases is known to form upon high-temperature heating of $SrHPO_4$ and the former is the low-temperature form of $SrHPO_4$.[221] Though a diffraction pattern has been determined for β-$SrHPO_4$ that is substantially different than the pattern observed for α-$SrHPO_4$ or γ-$SrHPO_4$, the structural details of the β-form have yet to be determined through single-crystal XRD or other methods. Few structural details are available in the literature regarding strontium pyrophosphate as well, which render an accurate interpretation of the strontium NMR spectrum difficult.

Despite the un-availability of detailed structures for these two phases, it is reasonable to anticipate the presence of two unique strontium sites in the ^{87}Sr NMR spectrum associated with the two allotropes. However, only a single strontium resonance appears in Figure **6-5** that is well fit with a single quadrupolar lineshape involving a quadrupolar coupling constant of 14.8 MHz and an asymmetry parameter of 0.65. This suggests that the strontium nuclei are located in a fairly distorted coordination environment, though somewhat less distorted than the environment in celestine. Unfortunately, specific assignment of this resonance to one phase or the other is not possible without additional single crystal XRD, neutron diffraction, or XAS data from pure forms of the two phases. The absence of the second resonance could be due to many factors, such as (i) an extremely large quadrupolar coupling in one phase versus the other, (ii) a relatively low abundance of either phase in the NMR sample, (iii) a very similar strontium environment in the two phases, etc. Despite limited interpretability, the presence of a relatively strong NMR signal suggests that strontium NMR studies of strontium apatite will be feasible with DFS-QCPMG at 21.14 T.

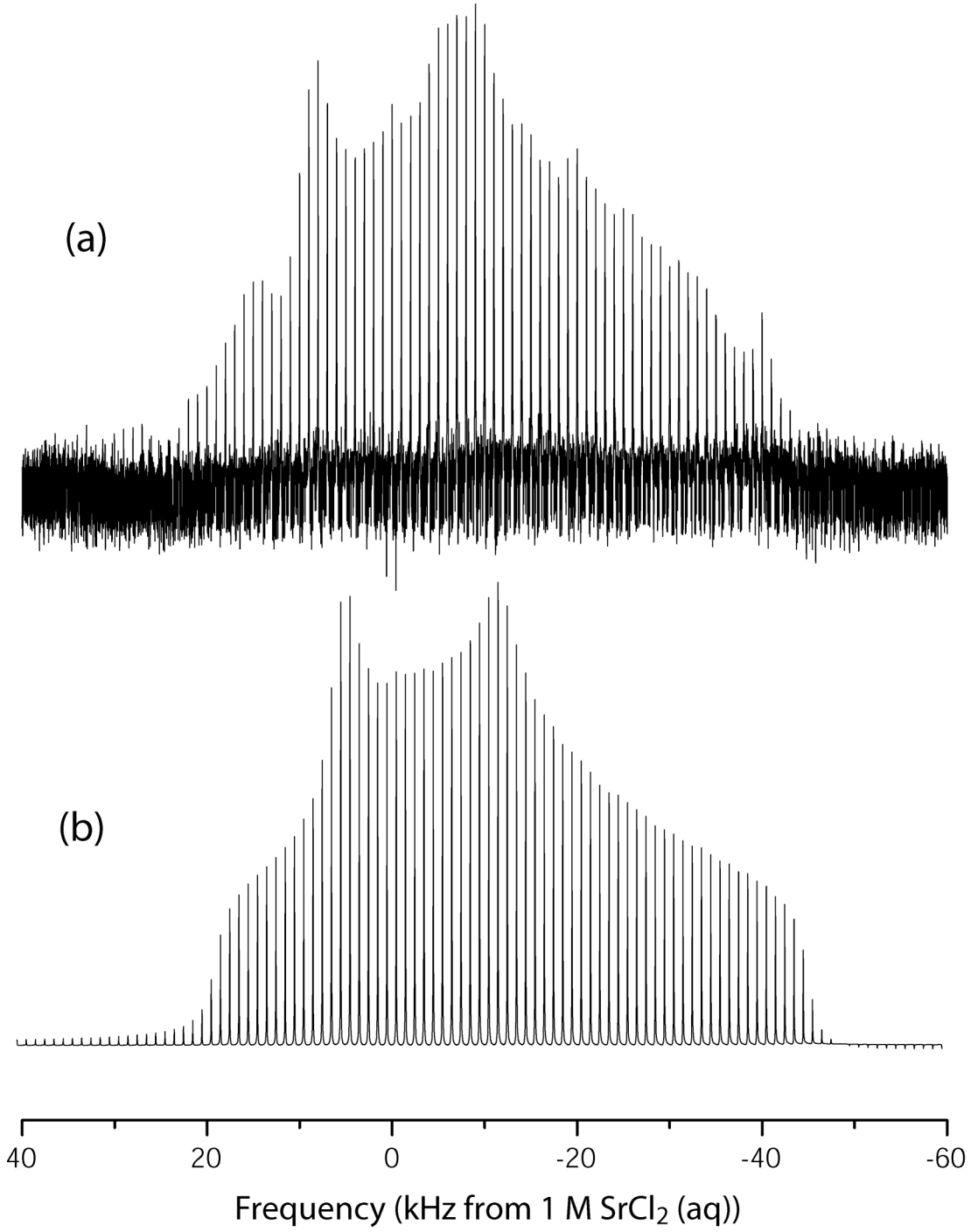

Figure **6-5**: The ^{87}Sr DFS-QCPMG spectrum of the $SrHPO_4$ sample received from Sigma-Aldrich from (a) experiment and (b) iterative simulation.

6.3.3 Apatites

Unfortunately, none of the experiments with the synthetic apatite minerals produced any strontium spikelets in a 24 hour acquisition period. This is quite surprising, as the strontium content of the 100% strontium apatite should be high enough to facilitate detection easily up to fairly large quadrupolar couplings. Additionally, double resonance experiments proved impossible with any of the apatites due to probe tuning limitations. It was not possible to tune the proton channel to the appropriate resonance frequency with any of the three apatite minerals loaded in the coil at either 21.14 T or 11.74 T, indicative of a sample with strong dielectric properties.

These data suggest that some sort of interference is present in the apatite samples that obscures the strontium resonance. This complication is not likely a result of proton-strontium dipolar coupling; the single spin dipolar coupling calculated in chapter 5 applies in this system as well and the proton-strontium distances in the apatite are likely larger than 2 Å. It is possible that multiple unique strontium environments exist in one unit cell, effectively decreasing the strontium population contributing to the NMR resonance. However, even in this situation, it seems unlikely that no strontium signal would appear to any degree in a 24 hour DFS-QCPMG NMR experiment given the response of the strontium hydrogen phosphate and micas (which have a lower strontium content than the 100% Sr apatite). The presence of contaminant species that interact strongly with strontium is a possibility and elemental analysis/XRD are in progress to evaluate this explanation. Again, supporting XAS and computational data would greatly

improve our understanding of how ^{87}Sr DFS-QCPMG at 21.14 T failed in the synthetic apatite studies.

6.3.4 Continuing Studies

Based on the results presented here, a detailed NMR investigation of strontium apatites cannot be proposed at this time. Successful study of the strontium hydrogen phosphate phase suggests that strontium investigations of apatite minerals will be possible. Crystallographic, elemental, thermo-gravimetric, and XAS analyses of these materials must be performed to determine why the strontium signal was not detectable with DFS-QCPMG at 21.14 T. If necessary, the materials should be synthesized again with a different procedure and re-analyzed with solid-state NMR prior to forming a detailed research plan.

6.4 Conclusions – Preliminary Studies and Future Challenges

These preliminary studies highlight some of the remaining challenges in solid-state ^{87}Sr NMR. Understanding water-strontium interactions and the resulting effect on the NMR spectrum is the most prominent obstacle for continuing strontium studies in phyllosilicate and tectosilicate minerals. Computational, XAS, and variable temperature NMR experiments should help advance our comprehension of this limitation and may help identify an experimental technique for overcoming the invisible strontium phenomenon. The length of a strontium NMR experiment is still fairly substantial in

some cases, even with the benefits of DFS-QCPMG at 21.14 T. In fact, the limit of detection calculated in this dissertation suggests that this method will not be applicable to studies of strontium binding at environmentally relevant strontium concentrations. Despite this limitation of the techniques described in this dissertation, the future of ^{87}Sr NMR is still quite promising, as many additional methods for improving strontium NMR have yet to be explored in detail. Ultra-low temperature experiments provide a mechanism to potentially increase the sensitivity beyond what is possible with DFS-QCPMG at 21.14 T alone. Synchronized QCPMG-MAS experiments may also improve sensitivity as a result of the line-narrowing properties of MAS NMR. Indirect detection may also be useful for future studies, though additional development work is necessary with these techniques as well.

Bibliography

(1) Marceau, T. E.; Harvey, D. W.; Stapp, D. C.; Cannon, S. D.; Conway, C. A.; Deford, D. H.; Freer, B. J.; Gerber, M. S.; Keating, J. K.; Noonan, C. F.; Weisskopf, G. "History of the Plutonium Production Facilities at the Hanford Site Historic District, 1943-1990," Hanford Cultural and Historic Resources Program, United States Department of Energy, 2002.

(2) Gosling, F. G. "The Manhattan Project: Making the Atomic Bomb," United States Department of Energy, 1999.

(3) Sublette, C. "Nuclear Weapons Frequently Asked Question, Section 10.0 Chronology for the Origin of Atomic Weapons," High Energy Weapons Archive, 1997.

(4) Hahn, O.; Strassmann, F. *Naturwissenschaften* **1939**, *27*, 89-95.

(5) Meitner, L.; Frisch, O. R. *Nature (London, United Kingdom)* **1939**, *143*, 239-240.

(6) Anderson, H. L.; Fermi, E.; Hanstein, H. B. *Physical Review* **1939**, *55*, 797-798.

(7) Anderson, H. L.; Fermi, E.; Szilard, L. *Physical Review* **1939**, *56*, 284-286.

(8) Bohr, N.; Wheeler, J. A. *Physical Review* **1939**, *56*, 1065-1066.

(9) Seaborg, G. T. *Chemical & Engineering News* **1945**, *23*, 2190-2193.

(10) Seaborg, G. T.; McMillan, E. M.; Kennedy, J. W.; Wahl, A. C. *Physical Review* **1946**, *69*, 366-367.

(11) Seaborg, G. T. *Record Chem. Progress* **1946**, *7*, 1-12.

(12) Fermi, E. *Proc. Am. Phil. Soc.* **1946**, *90*, 20-24.

(13) Anderson, H. L.; Fermi, E.; Marshall, L. *Physical Review* **1946**, *70*, 815-817.

(14) Jones, V. C. *Manhattan: The Army and the Atomic Bomb*; Center of Military History, US Army: Washington, 1988.

(15) "Plutonium: The First 50 Years, United States Plutonium Production, Acquisition, and Utilization from 1944 to 1994," US DOE, 1996.

(16) Ahearne, J. F. *Phys Today* **1997**, *50*, 24-29.

(17) Zachara, J. M.; Smith, S. C.; Liu, C. X.; McKinley, J. P.; Serne, R. J.; Gassman, P. L. *Geochim Cosmochim Ac* **2002**, *66*, 193-211.

(18) Choppin, G. R.; Rydberg, J. *Nuclear Chemistry: Theory and Applications*; 1st ed.; Pergamo Press Ltd: Elmsford, New York, 1980.

(19) Robertson, D. E.; Fix, J. J. "Association of Hanford origin radionuclides with Columbia River sediment," USA. Field Url:, 1977.

(20) Serne, R. J.; Zachara, J. M.; Burke, D. S. *PNNL-11495 UC-510* **1998**.

(21) Schmidt, H. W.; Neiler, J. H.; Walter, F. J.; Chetham-Strode, A. *Phyiscal Review Letters* **1962**, *9*, 427-429.

(22) Upton, A. C.; et al. "Implications to man of irradiation by internally deposited strontium-89, strontium-90, and cesium-137," Federal Radiation Council,Washington,DC,USA. FIELD URL:, 1964.

(23) Dahl, S. G.; Allain, P.; Marie, P. J.; Mauras, Y.; Boivin, G.; Ammann, P.; Tsouderos, Y.; Delmas, P. D.; Christiansen, C. *Bone (New York, NY, United States)* **2001**, *28*, 446-453.

(24) Das, R.; Nanda, B.; Patel, P. N. *Journal of the Indian Chemical Society* **1983**, *60*, 693-694.

(25) Baud, C. A.; Very, J. M. *Colloques Internationaux du Centre National de la Recherche Scientifique* **1975**, *230*, 405-410.

(26) Jones, R. K.; Boecker, B. B.; Pickrell, J. A.; Hobbs, C. H.; McClellan, R. O. *ERDA Symposium Series* **1976**, *37*, 83-89.

(27) Smith, S. *Fiz. Szemle* **1960**, *10*, 275-281.

(28) Gerber, M. S. "Plutonium Production Story at the Hanford Site: Processes and Facilities History," Westinghouse Hanford Corporation, 1996.

(29) McCabe, W. L.; Smith, J. C.; Harriott, P. *Unit operations of chemical engineering*; 6th / ed.; McGraw Hill: Boston, 2001.

(30) McKinley, J. P.; Zeissler, C. J.; Zachara, J. M.; Serne, R. J.; Lindstrom, R. M.; Schaef, H. T.; Orr, R. D. *Environ Sci Technol* **2001**, *35*, 3433-3441.

(31) Chorover, J.; Choi, S. K.; Amistadi, M. K.; Karthikeyan, K. G.; Crosson, G.; Mueller, K. T. *Environ Sci Technol* **2003**, *37*, 2200-2208.

(32) Liu, C.; Zachara, J. M.; Qafoku, O.; Smith, S. C. *Environmental Science and Technology* **2003**, *37*, 2640-2645.

(33) Conner, J. C. "High-heat tank safety issues evaluation," Westinghouse Hanford Co.,Richland,WA,USA. FIELD URL:, 1993.

(34) DeFigh-Price, C.; Wang, O. S. "Action plan for response to excessive temperature in high heat source waste tank 241-C-106 at the Hanford Site," Westinghouse Hanford Co.,Richland,WA,USA. FIELD URL:, 1992.

(35) Dixon, J. B.; Weed, S. B., Eds. *Minerals in Soil Environments*; Second ed.; Soil Science Society of America: Madison, 1989.

(36) Lindsey, K. A.; Connelly, M. P. "Geological Setting of the 200 West Area: An Update," Westinghouse Hanford Company, 1991.

(37) Price, W. H.; Fecht, K. R. "Geology of the 241-SX Tank Farm," Atlantic Richfield Hanford Company, 1976.

(38) Serne, R. J.; Legore, V. L.; Last, G. V.; Schaef, H. T.; O'Hara, M. J.; Smith, S. C.; Bjornstad, B. N.; Brown, C. F.; Lindenmeier, C. W.; Williams, C. A.; Parker, K. E.; Zachara, J. M.; Lanigan, D. C.; Kutnyakov, I. V.; Burke, D. B.; Horton, D. G.; Serne, J. N.; Clayton, R. E.; Mitroshkov, A. V. "Characterization of Uncontaminated Sediments from the Hanford Reservation - RCRA Borehole Core Samples and Composite Samples," United States Department of Energy, 2002.

(39) Bauer, A.; Velde, B.; Berger, G. *Appl Geochem* **1998**, *13*, 619-629.

(40) Bauer, A.; Berger, G. *Appl Geochem* **1998**, *13*, 905-916.

(41) Carroll-Webb, S. A.; Walther, J. V. *Geochim Cosmochim Ac* **1988**, *52*, 2609-2623.

(42) Bauer, A.; Velde, B. *Clay Miner* **1999**, *34*, 259-273.

(43) Eberl, D. D.; Velde, B.; Mccormick, T. *Clay Miner* **1993**, *28*, 49-60.

(44) Komarneni, S.; White, W. B. *Clays and Clay Minerals* **1983**, *31*, 113-121.

(45) Su, Y.; Wang, L.; Bunker, B. C.; Windisch, C. F. *Materials Research Society Symposium Proceedings* **1997**, *465*, 465-472.

(46) Qafoku, N. P.; Ainsworth, C. C.; Szecsody, J. E.; Qafoku, O. S. *Geochim Cosmochim Ac* **2004**, *68*, 2981-2995.

(47) Bak, M.; Rasmussen, J. T.; Nielsen, N. C. *J Magn Reson* **2000**, *147*, 296-330.

(48) Slichter, C. P. *Principles of Magnetic Resonance*; 3rd ed.; Springer-Verlag Berlin: Heidelberg, 1990.

(49) Ernst, R. R.; Bodenhausen, G.; Wokaun, A. *Principles of nuclear magnetic resonance in one and two dimensions*; Clarendon Press ; Oxford University Press: Oxford [Oxfordshire] New York, 1987.

(50) Mehring, M. *Principles of High-Resolution NMR in Solids*; 2nd ed.; Springer-Verlag: Heidelberg, 1983.

(51) Mehring, M.; Weberruss, V. A. *Object-Oriented Magnetic Resonance*; 1st ed.; Academic Press: London, UK, 2001.

(52) Levitt, M. H. *Spin Dynamics: Basics of Nuclear Magnetic Resonance*; John Wiley & Sons, Ltd.: West Sussex, England, 2001.

(53) Cohen-Tannoudji, C.; Diu, B.; Laloe, F. *Quantum Mechanics*; Hermann: Paris, France, 1977.

(54) Haeberlen, U.; Waugh, J. S. *Physics Reviews* **1968**, *175*, 453.

(55) Haeberlen, U. *High Resolution NMR in Solids: Selective Averaging*; Academic Press: New York, 1976.

(56) Magnus, W. *Communications on Pure Applied Mathematics* **1954**, *7*, 649.

(57) Wilcox, R. M. *Journal of Mathematical Physics* **1967**, *8*.

(58) Bak, M.; Nielsen, N. C. *J Magn Reson* **1997**, *125*, 132-139.

(59) Alderman, D. W.; Solum, M. S.; Grant, D. M. *J Chem Phys* **1986**, *84*, 3717.

(60) Wang, D.; Hanson, G. R. *Journal of Magnetic Resonance A* **1995**, *117*, 1.

(61) Zaremba, S. K. *Ann. Mat. Pura Appl.* **1966**, *4-73*, 293.

(62) Conroy, H. *J Chem Phys* **1967**, *47*, 5307.

(63) Cheng, V. B.; Suzukawa, H. H. J.; Wolfsberg, M. *J Chem Phys* **1973**, *59*, 3992.

(64) Pines, A.; Gibby, M. G.; Waugh, J. S. *The Journal of Chemical Physics* **1973**, *59*, 569-590.

(65) Gullion, T. *Chem Phys Lett* **1995**, *246*, 325-330.

(66) Grey, C. P.; Vega, A. J. *J Am Chem Soc* **1995**, *117*, 8232-8242.

(67) Casimir, H. B. G.; Teyler's Tweede Genootschap: Haarlem, 1936.

(68) Cook, R. L.; De Lucia, F. C. *Americal Journal of Physics* **1971**, *39*, 1433.

(69) Sakurai, J. J. *Modern Quantum Mechanics*; Addison-Wesley Publishing Company, Inc.: Redwood City, California, 1985.

(70) Samoson, A.; Kundla, E.; Lippmaa, E. *J Magn Reson* **1982**, *49*, 350.

(71) Bloch, F.; Hansen, W. W.; Packard, M. *Physical Review* **1946**, *70*, 474-485.

(72) Bloch, F. *Physical Review* **1946**, *70*, 460-474.

(73) Oldfield, E.; Timken, H. K. C.; Montez, B.; Ramachandran, R. *Nature (London, United Kingdom)* **1985**, *318*, 163-165.

(74) Kunwar, A. C.; Turner, G. L.; Oldfield, E. *Journal of Magnetic Resonance (1969-1992)* **1986**, *69*, 124-127.

(75) Bowers, G. M.; Mueller, K. T. *Physical Review B* **2005**, *71*, 224112. Copyright American Physics Society.

(76) Alemany, L. B.; Steuernagel, S.; Amoureux, J.-P.; Callender, R. L.; Barron, A. R. *Solid State Nucl Mag* **1999**, *14*, 1-18.

(77) Amoureux, J.-P.; Morais, C.; Trebosc, J.; Rocha, J.; Fernandez, C. *Solid State Nucl Mag* **2003**, *23*, 213-223.

(78) Larsen, F. H.; Jakobsen, H. J.; Ellis, P. D.; Nielsen, N. C. *Mol Phys* **1998**, *95*, 1185-1195.

(79) Ashbrook, S. E.; Wimperis, S. *J Magn Reson* **2003**, *162*, 402-416.

(80) Lipton, A. S.; Heck, R. W.; Sears, J. A.; Ellis, P. D. *J Magn Reson* **2004**, *168*, 66-74.

(81) Lipton, A. S.; Sears, J. A.; Ellis, P. D. *J Magn Reson* **2001**, *151*, 48-59.

(82) Kentgens, A. P. M.; Verhagen, R. *Chem Phys Lett* **1999**, *300*, 435-443.

(83) Schurko, R. W.; Hung, I.; Widdifield, C. M. *Chem Phys Lett* **2003**, *379*, 1-10.

(84) Garroway, A. N. *Journal of Magnetic Resonance (1969-1992)* **1977**, *28*, 365-371.

(85) Cheng, J. T.; Ellis, P. D. *J Phys Chem-Us* **1989**, *93*, 2549-2555.

(86) Yao, Z.; Kwak, H. T.; Sakellariou, D.; Emsley, L.; Grandinetti, P. J. *Chem Phys Lett* **2000**, *327*, 85-90.

(87) Kwak, H. T.; Prasad, S.; Yao, Z.; Grandinetti, P. J.; Sachleben, J. R.; Emsley, L. *J Magn Reson* **2001**, *150*, 71-80.

(88) Smith, M. E. In *Encyclopedia of Nuclear Magnetic Resonance*; Grant, D. M., Harris, R. K., Eds.; John Wiley: Chichester, New York, 1996, pp 607-619.

(89) Hoult, D. I. *Concept Magnetic Res* **1989**, *1*, 1.

(90) Andrew, E. R.; Bradbury, A. J.; Eades, R. G. *Nature* **1958**, *182*, 1659.

(91) Lowe, I. *Phyiscal Review Letters* **1959**, *2*, 285.

(92) Andrew, E. R.; Bradbury, A. J.; Eades, R. G. *Nature* **1959**, *183*, 1802.

(93) Gutowsky, H. S.; Pake, G. E. *J Chem Phys* **1948**, *16*, 1164.

(94) Gutowsky, H. S.; Pake, G. E. *J Chem Phys* **1950**, *18*, 162.

(95) Meiboom, S.; Gill, D. *Review of Scientific Instruments* **1958**, *29*, 6881.

(96) Larsen, F. H.; Jakobsen, H. J.; Ellis, P. D.; Nielsen, N. C. *J Phys Chem A* **1997**, *101*, 8597-8606.

(97) Larsen, F. H.; Skibsted, J.; Jakobsen, H. J.; Nielsen, N. C. *J Am Chem Soc* **2000**, *122*, 7080-7086.

(98) Larsen, F. H.; Jakobsen, H. J.; Ellis, P. D.; Nielsen, N. C. *J Magn Reson* **1998**, *131*, 144-147.

(99) Bowers, G. M.; Lipton, A. S.; Mueller, K. T. *Solid State NMR* **2006**, *29*, 95-103. Copyright Elsevier.

(100) Hung, I.; Schurko, R. W. *J Phys Chem B* **2004**, *108*, 9060-9069.

(101) Bryce, D. L.; Gee, M.; Wasylishen, R. E. *J Phys Chem A* **2001**, *105*, 10413-10421.

(102) Hung, I.; Schurko, R. W. *Solid State Nucl Mag* **2003**, *24*, 78-93.

(103) Larsen, F. H.; Lipton, A. S.; Jakobsen, H. J.; Nielsen, N. C.; Ellis, P. D. *J Am Chem Soc* **1999**, *121*, 3783-3784.

(104) Larsen, F. H.; Lipton, A. S.; Jakobsen, H. J.; Nielsen, N. C.; Ellis, P. D. *J Am Chem Soc* **1999**, *121*, 3783-3784.

(105) Lefort, R.; Wiench, J. W.; Pruski, M.; Amoureux, J. P. *J Chem Phys* **2002**, *116*, 2493-2501.

(106) Kentgens, A. P. M. *J Magn Reson* **1991**, *95*, 619-625.

(107) Van Veenendaal, E.; Meier, B. H.; Kentgens, A. P. M. *Mol Phys* **1998**, *93*, 195-213.

(108) Haase, J.; Conradi, M. S.; Grey, C. P.; Vega, A. J. *J Magn Reson Ser A* **1994**, *109*, 90-97.

(109) Haase, J.; Conradi, M. S. *Chem Phys Lett* **1993**, *209*, 287-291.

(110) Siegel, R.; Nakashima, T. T.; Wasylishen, R. E. *Chem Phys Lett* **2004**, *388*, 441-445.

(111) Brauniger, T.; Madhu, P. K.; Pampel, A.; Reichert, D. *Solid State Nucl Mag* **2004**, *26*, 114-120.

(112) Brauniger, T.; Ramaswamy, K.; Madhu, P. K. *Chem Phys Lett* **2004**, *383*, 403-410.

(113) Vega, S.; Naor, Y. *J Chem Phys* **1981**, *75*, 75.

(114) Schafer, H.; Iuga, D.; Verhagen, R.; Kentgens, A. P. M. *J Chem Phys* **2001**, *114*, 3073-3091.

(115) Iuga, D.; Kentgens, A. P. M. *J Magn Reson* **2002**, *158*, 65-72.

(116) Iuga, D.; Schafer, H.; Verhagen, R.; Kentgens, A. P. M. *J Magn Reson* **2000**, *147*, 192-209.

(117) Widdifield, C. M.; Schurko, R. W. *J Phys Chem A* **2005**, *109*, 6865-6876.

(118) Vega, A. J. *Solid State Nucl Mag* **1992**, *1*, 17-32.

(119) van Eck, E. R. H.; Janssen, R.; Maas, W. E. J. R.; Veeman, W. S. *Chem Phys Lett* **1990**, *174*, 428-432.

(120) Grey, C. P.; Veeman, W. S.; Vega, A. J. *J Chem Phys* **1993**, *98*, 7711-7724.

(121) Liu, H. M.; Kao, H. M.; Grey, C. P. *J Phys Chem B* **1999**, *103*, 4786-4796.

(122) Tsomaia, N.; Brantley, S. L.; Hamilton, J. P.; Pantano, C. G.; Mueller, K. T. *Am Mineral* **2003**, *88*, 54-67.

(123) Zeng, Q.; Nekvasil, H.; Grey, C. P. *J Phys Chem B* **1999**, *103*, 7406-7415.

(124) Brouwer, D. H.; Chezeau, J.-M.; Fyfe, C. A. *Micropor Mesopor Mat* **2006**, *88*, 163-169.

(125) Huang, Y.; Kirby, C. W.; Richer, R. *Studies in Surface Science and Catalysis* **2004**, *154B*, 1471-1477.

(126) Huang, Y.; Yan, Z. *J Am Chem Soc* **2005**, *127*, 2731-2740.

(127) Bowers, G. M.; Ravella, R.; Komarneni, S.; Mueller, K. T. *J Phys Chem B* **2006**, *110*, 7159-7164. Copyright American Chemical Society.

(128) Oldfield, E.; Kirkpatrick, R. J. *Science* **1985**, *227*, 1537-1544.

(129) Massiot, D.; Fayon, F.; Capron, M.; King, I.; Le Calve, S.; Alonso, B.; Durand, J.-O.; Bujoli, B.; Gan, Z.; Hoatson, G. *Magnetic Resonance in Chemistry* **2002**, *40*, 70-76.

(130) Wilson, T. A. *Physical Review* **1928**, *31*, 1117.

(131) Ott, H. *Zeitschrift fuer Kristallographie, Kristallgeometrie, Kristallphysik, Kristallchemie* **1926**, *63*, 222-230.

(132) Ferrari, A. *Atti III congresso naz. chim. pura applicata* **1930**, 452-460.

(133) Cohen, M. H.; Reif, F. In *Solid State Physics: Advances in Research and Applications*; Turnbull, D., Seitz, F., Eds.; Academic Press: New York, 1957; Vol. 5, pp 321-438.

(134) Kanert, O.; Kotzur, D.; Mehring, M. *Physica Status Solidi* **1969**, *36*, 291-300.

(135) Cohen, M. H. *Philosophical Magazine (1798-1977)* **1958**, *3*, 564.

(136) Han, O. H.; Timken, H. K. C.; Oldfield, E. *J Chem Phys* **1988**, *89*, 6046-6052.

(137) Watkins, G. D.; Pound, R. V. *Physical Review* **1953**, *89*, 658.

(138) Stebbins, J. F.; Famaon, I.; Klabunde, U. *Journal of the American Ceramic Society* **1989**, *72*, 2198-2200.

(139) Frye, J. S.; Maciel, G. E. *J Magn Reson* **1982**, *48*, 125-131.

(140) Suemitsu, M.; Nakajo, N. *Journal of Applied Physics* **1989**, *66*, 3178-3186.

(141) Hester, R. K.; Sher, A.; Soest, J. F.; Weisz, G. *Physical Review B: Solid State* **1974**, *10*, 4262-4273.

(142) Hon, J. F.; Bray, P. J. *Physics and Chemistry of Solids* **1959**, *11*, 149-169.

(143) Stallworth, P. E.; d'Espinose de la Caillerie, J. B.; Maquet, J.; Babonneau, F.; Guillemoles, J. F.; Powalla, M.; Lyakovitskaya, V.; Yakushev, M.; Tomlinson, B. *Thin Solid Films* **2001**, *387*, 235-238.

(144) Yesinowski, J. P.; Purdy, A. P. *J Am Chem Soc* **2004**, *126*, 9166-9167.

(145) Xie, Z. H.; Smith, M. E.; Strange, J. H.; Jaeger, C. *Journal of Physics: Condensed Matter* **1995**, *7*, 2479-2487.

(146) De Hosson, J. T. M. *Dislocat. Solids, [Proc. Yamada Conf.], 9th* **1985**, 261-270.

(147) Ruderman, M. A.; Kittel, C. *Phyiscs Reviews* **1954**, *96*, 99.

(148) Van Vleck, J. H. *Phyiscs Reviews* **1948**, *74*, 1168.

(149) Kunwar, A. C.; Turner, G. L.; Oldfield, E. *J Magn Reson* **1986**, *69*, 124-127.

(150) Kentgens, A. P. M.; Iuga, D.; Kalwei, M.; Koller, H. *J Am Chem Soc* **2001**, *123*, 2925-2926.

(151) Hung, I.; Schurko, R. W. *Solid State Nucl Mag* **2003**, *24*, 78-93.

(152) Weber, M. J.; Allen, R. R. *The Journal of Chemical Physics* **1962**, *38*, 726-729.

(153) Gervais, C.; Veautier, D.; Smith, M. E.; Babonneau, F.; Belleville, P.; Sanchez, C. *Solid State Nucl Mag* **2004**, *26*, 147-152.

(154) Bastow, T. J. *Chem Phys Lett* **2002**, *354*, 156-159.

(155) Lipton, A. S.; Wright, T. A.; Bowman, M. K.; Reger, D. L.; Ellis, P. D. *J Am Chem Soc* **2002**, *124*, 5850-5860.

(156) Xu, J.; Xie, Y.; Li, J.; Hou, Z. *Progress in Natural Science* **2001**, *11*, 833-837.

(157) Kowalski, W.; Osmolski, T.; Pilichowska, E. *Archiwum Mineralogiczne* **1980**, *36*, 29-46, 22 plates.

(158) Harder, H. *Beitr. Mineral. Petrog.* **1964**, *10*, 198-215.

(159) Kao, T. S.; Chang, Y. M.; Kung, K. H. *Kexue Tongbao (Chinese Edition)* **1981**, *26*, 932-935.

(160) Thompson, G.; Livingston, H. D. *Earth and Planetary Science Letters* **1970**, *8*, 439-442.

(161) Buchardt, B.; Fritz, P. *Science (Washington, DC, United States)* **1978**, *199*, 291-292.

(162) Katz, A.; Sass, E.; Starinsky, A.; Holland, H. D. *Geochim Cosmochim Ac* **1972**, *36*, 481-496.

(163) Hanor, J. S. *Reviews in Mineralogy & Geochemistry* **2000**, *40*, 193-275.

(164) Martin, J. M.; Ortega-Huertas, M.; Torres-Ruiz, J. *Sedimentary Geology* **1984**, *39*, 281-298.

(165) Rivkina, E. M.; Lein, A. Y.; Samarkin, V. A. *Geokhimiya* **1981**, 418-429.

(166) Srebrodol'skii, B. I. *Doklady Akademii Nauk SSSR* **1980**, *250*, 1445-1446 [Mineral.].

(167) Mogarovskii, V. V. *Izvestiya Akademii Nauk Tadzhikskoi SSR, Otdelenie Fiziko-Matematicheskikh i Geologo-Khimicheskikh Nauk* **1979**, 118.

(168) Baikov, A. A.; Golikov-Zavolzhenskii, I. V.; Golikova-Zavolzhenskaya, A. A.; Sedletskii, V. I.; Shvedov, V. N. *Litologiya i Poleznye Iskopaemye* **1978**, 77-86.

(169) Nowotny, H.; Heger, G. *Acta Crystallographica* **1983**, *C39*, 952-956.

(170) de Villiers, J. P. R. *Am Mineral* **1971**, *56*, 758-767.

(171) Jacobsen, S. D.; Smyth, J. R.; Swope, R. J.; Downs, R. T. *The Canadian Mineralogist* **1998**, *36*, 1053-1060.

(172) Nakano, M.; Uchida, K. *Kobe Daigaku Nogakubu Gakujutsu Hokoku* **2001**, *25*, 1-8.

(173) Axe, L.; Bunker, G. B.; Anderson, P. R.; Tyson, T. A. *J Colloid Interf Sci* **1998**, *199*, 44-52.

(174) Sahai, N.; Carroll, S. A.; Roberts, S.; O'Day, P. A. *J Colloid Interf Sci* **2000**, *222*, 198-212.

(175) O'Day, P. A.; Newville, M.; Neuhoff, P. S.; Sahai, N.; Carroll, S. A. *J Colloid Interf Sci* **2000**, *222*, 184-197.

(176) Ahtee, A.; Ahtee, M.; Glazer, A. M.; Hewat, A. W. *Acta Crystallographica* **1976**, *B32*, 3243-3246.

(177) Kamermans, M. A. *Zeitschrift fuer Kristallographie, Kristallgeometrie, Kristallphysik, Kristallchemie* **1939**, *101*, 406-411.

(178) Nurmi, J. T.; Tratnyek, P. G. *Environmental Science and Technology* **2002**, *36*, 617-624.

(179) Geckeis, H.; Rabung, T.; Kim, J. I. "Kinetic aspects of the metal ion binding to humic substances," Inst. Nukleare Entsorgungstechnik,Forschungszentrum Karlsruhe G.m.b.H.,Karlsruhe,Germany. FIELD URL:, 1999.

(180) Tanaka, T.; Nagao, S.; Ogawa, H. *JAERI-Conf* **2002**, *2002-004*, 651-658.

(181) Seibert, A.; Mansel, A.; Marquardt, C. M.; Keller, H.; Kratz, J. V.; Trautmann, N. *Radiochimica Acta* **2001**, *89*, 505-510.

(182) Nagasaki, S. *Studies in Surface Science and Catalysis* **2001**, *132*, 829-832.

(183) Cory, R. M.; McKnight, D. M. *Environmental Science and Technology* **2005**, *39*, 8142-8149.

(184) Vanhoyland, G.; Van Bael, M. K.; Mullens, J.; Van Poucke, L. C. *Powder Diffraction* **2001**, *16*, 224-226.

(185) Komarneni, S.; Pidugu, R.; Amonette, J. E. *Journal of Materials Chemistry* **1998**, *8*, 205-208.

(186) Komarneni, S.; Kozai, N.; Paulus, W. J. *Nature* **2001**, *410*, 771-771.

(187) Komarneni, S.; Kodama, T.; Paulus, W. J.; Carlson, C. *Journal of Materials Research* **2000**, *15*, 1254-1256.

(188) Kodama, T.; Harada, Y.; Ueda, M.; Shimizu, K.-i.; Shuto, K.; Komarneni, S. *Langmuir* **2001**, *17*, 4881-4886.

(189) Kodama, T.; Nagai, S.; Hasegawa, K.; Shimizu, K.-I.; Komarneni, S. *Separation Science and Technology* **2002**, *37*, 1927-1942.

(190) Chen, C. C.; Hayes, K. F.; Papelis, C. *Book of Abstracts, 214th ACS National Meeting, Las Vegas, NV, September 7-11* **1997**, GEOC-048.

(191) Chen, C.-C.; Papelis, C.; Hayes, K. F. *Adsorption of Metals by Geomedia* **1998**, 333-348.

(192) Chen, C.-C.; Hayes, K. F. *Geochimica et Cosmochimica Acta* **1999**, *63*, 3205-3215.

(193) Paulus, W. J.; Komarneni, S.; Roy, R. *Nature* **1992**, *357*, 571-573.

(194) Kodama, T.; Higuchi, T.; Shimizu, T.; Shimizu, K.-i.; Komarneni, S.; Hoffbauer, W.; Schneider, H. *Journal of Materials Chemistry* **2001**, *11*, 2072-2077.

(195) Park, M.; Lee, D. H.; Choi, C. L.; Kim, S. S.; Kim, K. S.; Choi, J. *Chem Mater* **2002**, *14*, 2582-2589.

(196) Frazer, L. *Environmental Health Perspectives* **2002**, *110*, A528-A531.

(197) Malollari, I. X. H.; Klepetsanis, P. G.; Koutsoukos, P. G. *Journal of Environmental Protection and Ecology* **2000**, *1*, 399-406.

(198) Prieto, M.; Fernandez-Gonzalez, A.; Putnis, A.; Fernandez-Diaz, L. *Geochim Cosmochim Ac* **1997**, *61*, 3383-3397.

(199) Egan, J. M.; Mueller, K. T. *J Phys Chem B* **2000**, *104*, 9580-9586.

(200) Vaneck, E. R. H.; Janssen, R.; Maas, W. E. J. R.; Veeman, W. S. *Chemical Physics Letters* **1990**, *174*, 428-432.

(201) Grey, C. P.; Veeman, W. S. *Chem Phys Lett* **1992**, *192*, 379-385.

(202) Bronnimann, C. E.; Zeigler, R. C.; Maciel, G. E. *J Am Chem Soc* **1988**, *110*, 2023-2026.

(203) Clearfield, A.; Lehto, J. *Journal of Solid State Chemistry* **1988**, *73*, 98-106.

(204) Lynch, R. W.; Dosch, R. G.; Johnstone, J. K.; Nowak, E. J. In *Management of Radioactive Wastes from the Nuclear Fuel Cycle*; IAEA, Ed.: Vienna, Austria, 1976; Vol. 1, pp 360-372.

(205) Duff, M. C.; Hunter, D. B.; Hobbs, D. T.; Fink, S. D.; Dai, Z.; Bradley, J. P. *Environ Sci Technol* **2004**, *38*, 5201-5207.

(206) Beherens, E. A.; Sylvester, P.; Clearfield, A. *Environ Sci Technol* **1998**, *32*, 101-107.

(207) Lehto, J.; Clearfield, A. *Journal of Radioanalytical and Nuclear Chemistry* **1987**, *118*, 1-13.

(208) Hobbs, D. T.; Barnes, M. J.; Pulmano, R. L.; Marshall, K. M.; Edwards, T. B.; Bronikowski, M. G.; Fink, S. D. *Separation Science and Technology* **2005**, *40*, 3093-3111.

(209) Hackbarth, K.; Fechtelkord, M.; Buhl, J.-C. *Reaction Kinetics and Catalysis Letters* **1998**, *65*, 33-39.

(210) Lin, D.-C.; Xu, X.-W.; Zuo, F.; Long, Y.-C. *Micropor Mesopor Mat* **2004**, *70*, 63-70.

(211) Buhl, J.-C.; Taake, C.; Stief, F.; Fechtelkord, M. *Reaction Kinetics and Catalysis Letters* **2000**, *69*, 15-21.

(212) Crosson, G. S.; Choi, S. K.; Chorover, J.; Amistadi, M. K.; Mueller, K. T. *J Phys Chem B* **2006**, *110*, 723-732.

(213) Grodzinskaya, A. A.; Kuchma, N. D. *International Journal of Medicinal Mushrooms* **2004**, *6*, 361-368.

(214) Bigi, A.; Foresti, E.; Gandolfi, M.; Gazzano, M.; Roveri, N. *J Inorg Biochem* **1997**, *66*, 259-265.

(215) Rokita, E.; Cichocki, T.; Meyer-Klaucke, W.; Tabor, Z.; Taton, G. *Trace Elements and Electrolytes* **1999**, *16*, 142-146.

(216) Rokita, E.; Hermes, C.; Nolting, H. F. *Trace Elements in Medicine* **1992**, *9*, 136-138.

(217) Torizuka, K. *Naika Hokan* **1959**, *6*, 84-95.

(218) Boudjada, A.; Masse, R.; Guitel, J. C. *Acta Crystallographica B* **1978**, *34*, 2692-2695.

(219) Ben Taher, L.; Smiri, L.; Laligant, Y.; Maisonneuve, V. *Journal of Solid State Chemistry* **2000**, *152*, 428-434.

(220) Mooney, R. W.; Aia, M. A.; Hoffman, C. W. W.; Ropp, R. C. *J Am Chem Soc* **1959**, *81*, 826.

(221) Kreidler, E. R.; Hummel, F. A. *Inorganic Chemistry* **1967**, *6*, 884-891.

(222) Windig, W.; Antalek, B. *Chemometr Intell Lab* **1997**, *37*, 241-254.

(223) Windig, W.; Hornak, J. P.; Antalek, B. *J Magn Reson* **1998**, *132*, 298-306.

(224) Windig, W.; Antalek, B.; Robbins, M. J.; Zumbulyadis, N.; Heckler, C. E. *J Chemometr* **2000**, *14*, 213-227.

(225) Windig, W. *Chemometr Intell Lab* **1992**, *16*, 1-16.

(226) Antalek, B.; Windig, W. *J Am Chem Soc* **1996**, *118*, 10331-10332.

(227) Antalek, B.; Hornak, J. P.; Windig, W. *J Magn Reson* **1998**, *132*, 307-315.

Appendix A

Simpson Simulations

A.1 Brief Review of SIMPSON

For a detailed discussion of the theoretical concepts involved in a SIMPSON calculation, one is referred back to chapter 2. The goal of this appendix is to address more practical aspects of SIMPSON simulations, such as software installation and the dissection of a SIMPSON input file. In this first section, a brief overview of the utility of the SIMPSON program is presented to motivate the practical discussions in the remainder of Appendix A.

As stated in chapter two, the SIMPSON simulation package authored by Bak, Rasmussen, and Nielsen simulates an NMR spectrum by evolving the density matrix through time under the influence of internal interactions and the pulse sequence specified by the user.[47] Evolution is achieved by calculating the density operator at various discrete time intervals with the Liouville von Neumann equation (discussed in chapter 2) using the appropriate time evolution operators for each crystallite orientation in the crystal file followed by rotation into the laboratory frame. The resulting individual frequency components are then combined to produce the simulated NMR signal, the Fourier transform of which produces the simulated powder spectrum. The SIMPSON code also contains features that allow users to process experimental and simulated data, read in ASCII data files in the *spe* or *fid* format, and produce ASCII output files in the

spe or *fid* format. SIMPSON calculations can be performed on stand-alone computers or run in parallel mode on clusters. SIMPSON clusters can contain Mac, LINUX/UNIX, and/or Windows computers, provided each computer has been configured appropriately. Another useful function of SIMPSON is the ability to perform iterative simulations of experimental spectra, allowing the user to extract relevant NMR parameters such as C_q, η, relative orientations of tensors, and other important properties. The iterative simulation routine makes SIMPSON especially relevant to this dissertation.

A.2 Installing and Configuring SIMPSON on a PC/Linux Computer

Before SIMPSON can be used on a personal computer or on a cluster, the user must configure all the relevant computers appropriately. Regardless of the basic operating system, SIMPSON essentially runs in a Unix shell equipped with the TCL script language. For example, on a Mac, SIMPSON runs from a terminal window on the underlying Darwin form of Unix and on a PC running Windows, installing Cygwin is necessary to use SIMPSON. Cygwin is a free program written by the producers of Red Hat Linux, providing a Linux shell operating environment that is executable from the Windows environment. A very important consideration is, therefore, that the environment to be used for SIMPSON calculations contains the necessary components to recognize and interpret TCL script as well as the associated supporting libraries. Most LINUX systems will already contain the necessary components, though a full install of the operating system (OS) may be necessary. PC users running Cygwin should download the FULL version of Cygwin (multiple GB of files) to ensure that all necessary support

software is installed. Installation and configuration of SIMPSON is discussed in the following sub-sections.

A.2.1 Installation

After all the required libraries are installed, two methods of downloading/installing SIMPSON may be employed. The authors of the program provide compiled binary versions of SIMPSON for Linux, Darwin, Cygwin, and Sun OS on the web or the user can download the source code and compile their own version of SIMPSON for their operating environment. The latter of these two options relies heavily on supporting components/libraries and should be avoided by the novice LINUX/UNIX user. As such, this method will not be discussed further. The interested user should download the source code and examine all *readme* and *installation* files for specifics on compiling a computer-specific version of SIMPSON.

Upon downloading the appropriate SIMPSON binary *.tar* file for your operating environment from the website, the user should move the *tar* archive to the */usr/local/bin* directory (see indented commands below). Next, expand the archive in this location, which will produce one folder containing all the compiled components of SIMPSON in */usr/local/bin*. Enter this directory and move all of its contents up one level to the */usr/local/bin* directory. This will enable the user to run *simpson*, *simplot*, and *simdps* from the command prompt in any directory, simplifying file organization and use of the SIMPSON programs. The following are the series of commands on the LINUX/Cygwin operating system that will perform the suggested operations:

```
mv simpson_xxxxxxxxxxxxxxxxxxxx.tar.gz /usr/local/bin
cd /usr/local/bin
tar –zxvf simpson_xxxxxxxxxxxxxxxxxx.tar.gz
cd simpson_xxxxxxxxxxxxxxxxxx
mv * /usr/local/bin
```

Occasionally, the *tar* command will not recognize the *–z* flag. If this occurs, simply replace the single *tar* line above with the following two lines:

```
gunzip simpson_xxxxxxxxxxxxxxxxxx.tar.gz
tar –xvf simpson_xxxxxxxxxxxxxxxxxx.tar
```

After these operations are completed, one should execute SIMPSON on the provided test code to make sure that SIMPSON is installed properly on your system. This can be performed by typing "simpson test.in" or "./simpson test.in" at the command prompt in the */usr/local/bin* directory.

A.2.2 Multi-processor Configuration

For computers with multiple processors or to run SIMPSON calculations on a cluster of computers, one must configure each system to recognize calls from the host computer for SIMPSON execution. SIMPSON uses the ethernet card to communicate with each processor, even if the processors are contained on the same motherboard. Configuration therefore requires the user to specify ports, services, and server names in various network configuration files. In this section, the instructions for a LINUX computer running Red Hat WS 3.0 will be provided as a general setup guide. The specific instructions for multi-processor configuration vary a bit from system to system and OS version to OS version. It should also be mentioned that these instructions are

NOT readily available in the SIMPSON documentation or on the web to the inexperienced user.

The first task in multi-processor configuration is to specify a SIMPSON port and define a SIMPSON service so that the computer knows "where to listen" for a call to run SIMPSON and what to do when it receives such a call. To create the service, change directories to the */etc/xinetd.d* directory. Here, you will make a file called "simpson". At the command prompt, type vi to enter the vi text editor and enter the following:

```
service simpson
{
disable = no
socket_type = stream
port = 3265
wait = no
user = <your user name here>
protocol = tcp
server = /usr/local/bin/simpson
server_args = -server
}
```

Make sure to specify your specific user name in the service file. Also, be aware that a different port number may be used, but the port number you choose must (i) not be assigned to another service and (ii) must be the same on each computer in the cluster. Exit and save the file as "simpson" by typing:

```
<esc> :w simpson <enter>
: q <enter>
```

Next, you must add the port number specified in the service file to your *xinetd.conf* file in the */etc* directory. Change to the */etc* directory and type "vi xinetd.conf" to begin editing the file. Add the following line to the bottom of the *xinetd.conf* file:

simpson 3265 tcp

where 3265 is whatever port number was assigned in the service file and then exit *xinetd.conf* by typing ":wq". This adds the name of the service, the port number, and the protocol (tcp) to the network configuration files.

There is a security danger in creating this particular port. At this point, an intruder can potentially access your computer through the SIMPSON port and compromise the operating system or damage information on the hard disk. There are a few approaches to minimize the security risk. One option is to specify a specific user name in the */etc/xinetd.d/simpson* file so that only a single username can access the port. You may even desire to create a dummy user that has very limited privileges for the express purpose of executing SIMPSON jobs, though this method can make the implementation of SIMPSON clustered calculations more complicated. A more significant security measure is to use the *hosts.allow* and *hosts.deny* files located in the */etc* directory. In the *hosts.allow* file, you can specify that only certain host names are allowed to access a particular service, like the SIMPSON service. The *hosts.deny* file allows the user to specify usernames that are not allowed to access certain services. The highest security option for the SIMPSON service would be to add the following line to the *hosts.deny* file:

simpson: ALL EXCEPT 128.118.56.91 128.118.56.90

with as many IP addresses as you like following the EXCEPT flag. It is recommended that this security option be used if you intend to use the multi-processor functions of SIMPSON.

A.3 Parts and Functions of a SIMPSON Input File

The SIMPSON input file syntax is based on the TCL scripting language and contains functions recognized by the SIMPSON calculation software. For more information on TCL, the interested reader should consult a TCL scripting language book. There are five basic sections that make up any SIMPSON input file and an additional sixth section used for iterative fitting with SIMPSON. The five basic sections are the *cluster, spinsys, par, proc pulseq*, and *proc main* sections, which must be present in an input file in that order. The *proc fitfunction* section is used for fitting routines and is only included if fitting is necessary. This section of Appendix A will present some general points about each of the sections in the input file and discuss their function. For a full and detailed discussion of the available commands in SIMPSON input files, the reader is referred to the paper by Bak, Rasmussen, and Nielsen.[47]

A.3.1 Cluster

If the calculation is to be performed on a stand-alone, single processor computer, the *cluster* section is not a necessary component of the input file. The *cluster* section is where the user specifies the locations of processors to be used in parallel calculations (whether they are within one computer or on multiple clustered computers), which is done by listing the IP addresses or DNS names corresponding to the computers involved in the calculation (see examples A.4.3 and A.4.4). If you are working on a multi-processor computer, you must specify the DNS name or IP address of your computer twice in the *cluster* section, once for each processor. In theory, there is no limit to the

number of processors that can be used in a SIMPSON calculation (to the author's knowledge). In addition to including the processor locations in the *cluster* section, multi-processor calculations require the user to specify the calculation port number in the *par* section and to turn the cluster flag on. This is done by adding the following lines to the *par* section:

```
use_cluster 1
cluster_port <put port number here>
```

If the SIMPSON program detects the presence of the cluster section, it divides the number of crystallites in the calculation evenly between the specified processors. Each processor then calculates its share of the crystallite orientations and sends the results to the interface computer where the finalized NMR signal is assembled and processed.

A.3.2 Spinsys

The *spinsys* section is where the user specifies the initial spin system and the NMR interactions present in the system. This includes specifying the identity and number of unique nuclear environments in the system, the channels on the virtual spectrometer, and the homo- and hetero-nuclear internal interactions present in the system. Example A.4.1 represents a simulation of a static Bloch-decay experiment for a system with a single ^{31}P nuclear environment that evolves solely under the influence of the chemical shielding interaction. Looking at the example, the first line specifies that there is one phosphorus nucleus and assigns it the index 1 for the remainder of the *spinsys* section. The second line establishes that the virtual spectrometer has a phosphorus channel. The third line specifies the chemical shift interaction for nucleus 1 such that the

isotropic component is 1.9 ppm, the chemical shift anisotropy is 60.4 ppm, the chemical shift asymmetry parameter is 0.15, and the Euler angles (α, β, and γ) are 0, 0, and 0. The Euler angles need not be specified explicitly in this example because only a single interaction is present, permitting us to align the orientation of the chemical shift tensor with the orientation of the particular crystallite being calculated. If a second anisotropic interaction were present, such as the quadrupolar interaction, the Euler angles relating the orientation of the chemical shift tensor to the electric field gradient tensor would have to be specified for the less dominant interaction. It should also be mentioned that SIMPSON makes use of the Haeberlen convention for specification of chemical shift anisotropy in the *spinsys* section.

A.3.3 Par

The *par* section contains global variables and parameters necessary to finish specifying the initial density matrix and experimental parameters. Experimental details such as the number of crystallite orientations to use, whether the experiment is under spinning conditions, and the initial and detect states of the density matrix are also entered in *par*. This is also the location where more efficient calculation methods can be specified (when applicable) to reduce compute time. All examples listed in this Appendix are calculated with the *direct* method, but in some instances the *gcompute* method is applicable and can reduce compute time. As a sample *par* section, we return to example A.4.1, where the first line specifies a sweep width of 100 kHz. The start and detect operators are specified as *I1z* and *I1p*, meaning that the density matrix for nucleus

1 starts along the I_z axis and that the detected signal is the I_+ component for nucleus 1. The use of a built-in crystal file with 4,180 crystallite orientations is specified on the next line. A number of pre-built crystal files calculated with various methods (REPULSION, Zaremba-Conroy-Wolfsberg, etc.)[58,61] are available with the standard SIMPSON build. A list of these files can be obtained by entering an inappropriate crystal file name and attempting to run the simulation. Other key specifications in the par section are the proton frequency (method by which external field strength is specified), the level of interaction with the user during the calculation (through the verbose line), and additional variables. For example, here the user specifies a variable for the rf power in the parameters section that they will use in subsequent SIMPSON sections. Variables can also be declared within a particular sub-section, but global variables are most easily specified in the *par* section.

A.3.4 Proc Pulseq {}

The *proc pulseq {}* section is where the desired pulse sequence is entered. This section should always begin with the "global par" line found in example A.4.1. The next component of the *pulseq* section is usually a calculation of the dwell time and pulse widths (also delays if necessary) followed by the pulse sequence as a series of pulses, delays, and acquisition periods. Pulses can either be entered as ideal pulses or as finite pulses with the *pulseid* and *pulse* commands, respectively. The first entry after either pulse command lists the pulse width, the second the pulse power (in units of Hz), and the third entry represents the phase of the pulse. Acquisition can be programmed in a variety

of styles, the most conceptually straightforward being the loop form presented in example A.4.1. Here, the *acq* command collects a single data point, followed by the loop that collects an additional data point every dwell time until the specified number of points has been acquired.

It should be noted that in addition to multiple data acquisition schemes, there are multiple valid syntaxes for pulse sequences (depending on the experience of the user) that require different amounts of compute time. For example, calculations that essentially re-use certain results can be written with either (a) a straight calculation of the result every time it is needed or (b) store the result of a single calculation in a propagator and call the propagator every time the calculation is needed. One can see an example of (a) and (b) in the QCPMG calculations of example A.4.3 and A.4.4, respectively. Example A.4.3 calculates the density matrix and acquires points over the entire series of echo loops, essentially meaning the same half-echo is calculated directly $2N + 1$ times, where N is the number of echo loops. Example A.4.4 calculates the first half echo and stores it in a propagator, which is then recalled, duplicated, and flipped as needed to generate each of the N echo maxima in the full QCPMG NMR signal. Both methods re-produce the same QCPMG NMR signal and the second method generally requires less compute time (depending on the where the bottleneck is in your computer system).

A.3.5 Proc Main {}

The final necessary section of the input file is the *proc main {}* section. This section actually executes the SIMPSON program and has features available for data

processing and input/output control. The main section should always begin with the line "global par" to make the *par* section variables accessible to the *main* section. The command "set f [fsimpson]" executes the SIMPSON program and stores the results of the calculation in the variable *f*. The other commands present in example A.4.1 save the resultant fid stored in *f* as a *.fid* file; an ASCII file with the appropriate headers to be opened in the companion SIMPLOT program. The particular syntax of the "fsave" commands used in this example saves the file with the same name as the input file, but with the *.fid* or *.spe* format and extension. The next two lines zero fill the data set to a total of 8192 points and then apply 500 Hz of Lorenzian apodization to the NMR signal. The user can control the degree of Gaussian and Lorenzian apodization by changing the final number in the *faddlb* command, which represents the Gaussian/Lorenzian ratio of the apodization function. The next line in example A.4.1 performs a Fourier transformation on the now processed data set stored in *f* that is subsequently written to an ASCII file with the *spe* format and *.spe* extension in the final *fsave* line.

A.3.6 Proc Fitfunction {}

One of the more useful aspects of the SIMPSON program is the ability to iteratively simulate an experimental spectrum, permitting the user to extract useful NMR parameters from real data. Fitting is performed by including the *proc fitfunction {}* section in the SIMPSON input file prior to the *proc main* section. When fitting with SIMPSON, the initial parts of the input file (the *cluster, par*, and *proc pulseq {}* sections) will be programmed as already described. Substantial changes to the *main* section as

well as the addition of the *fitfunction* section are the primary modifications necessary to use the SIMPLEX fitting routine in SIMPSON. Section A.3.6 will guide the reader through the pieces of the *fitfunction* section and other changes to the input file; a sample *fitfunction* can be found in example A.4.4.

The *fitfunction* section should begin with the line "proc fitfunction {val} {". The array variable *val* is included in the first set of brackets so that the values of the varied parameters can be passed between the *main* and *fitfunction* sections of the input file after every iteration. The variable *val* is understood by the SIMPSON code to be a list variable involved in the iterative fitting input file and does not need special declaration. We will return to the *val* variable when discussing the proc main section in a few paragraphs. The main text of the *fitfunction* section begins with a declaration of the global variables (this section must always include *par* and *stop)*. Other global variables can also be declared; for example, input file A.4.4 also declares the variables *exp* (contains the experimental data) and *exp2* (controls the exponential apodization applied to the final NMR signal) global. Variables can be calculated in this section just as in the *proc pulseq* or *proc main* sections, as shown by the third and fourth lines of *proc fitfunction* in A.4.4.

The next lines of the *fitfunction* section begin to manage the variables that will be manipulated during the iterative procedure. The initial step of this process is to assign a value to each varied parameter every time the *fitfunction* is called. The general format for these variable assignments is as follows:

```
set cq1 [lindex [lindex $val 0] 1]
```

Remember that the list *val* was passed from the main section to the *fitfunction* section in brackets during the function call. The *lindex* command is used to extract an element from

a list variable. In the sample input line, the inner *lindex* command tells the SIMPSON code extract the value at position 0 in the list variable *var* (the first value in the list). The outer *lindex* command says to assign that value of *cq* to the non-list variable *cq1*. This syntax can be used to vary values of any parameters that can be specified in the *spinsys* section, the degree of apodization, scaling in the case of multiple-resonance simulations, and others calculation variables.

The second step of parameter management is to pass the values for each variable parameter to the *spinsys* section at the start of each iteration. This is performed by calling SIMPSON with the following sample input line:

```
set f [fsimpson [list quadrupole_1_aniso $cq1] ]
```

In this input line, the value stored in *cq1* is substituted for the quadrupolar coupling of the nucleus with index 1 in the *spinsys* section prior to the simulation calculations. The most important aspect of this second step in variable management is that only specific keywords result in the replacement of parameters in the *spinsys* section (for example, it is necessary to use the line *quadrupole_1_aniso* to specify the quadrupolar coupling constant of nucleus 1). These keywords are not listed anywhere in the original SIMPSON documentation; however, the example that was chosen for section A.4.4 was selected specifically to present as many of the correct keywords as possible.

In example A.4.4, the next set of *for* commands build the QCPMG NMR signal from the single echo calculated in the *proc pulseq* section, followed by some data processing. The next two *set* commands convert the QCPMG spectrum into a standard powder pattern by integrating each 500 Hz region to produce a single data point. The syntax of this particular input file uses the calculated static powder pattern in the

comparison phase rather than the actual QCPMG calculation. Next, the actual QCPMG simulation results are stored in the file (name*)-sim.spe*. The line that begins with *set rms* calculates the root mean squared error between the experiment and the fit results, stores the root mean squared error in the variable *rms*, and places a * at the beginning of the line in the output file if the *rms* value from the current iteration is the lowest *rms* in the calculation. The *funload* command removes the current calculation results from the variable *f* and the following *puts* commands writes the parameters from the current iteration and the root mean squared error to the output file (name)*.out*.

The final step of the variable management procedure occurs in the *proc main* section. First, one declares the various global parameters again at the beginning of the *proc main* section. The next line of the main section in example A.4.4 specifies the iterative fitting method; for most calculations, choosing SIMPLEX is appropriate. For information on other fitting methods available in SIMPSON, the interested reader should consult the Bak paper.[47] The next line sets the name of the *fitfunction* section; there is no need to call this section anything other than *fitfunction* for the novice user. The fourth line of the main section loads the experimental data into the variable *exp*. The next three lines provide user control over the convergence criteria, specifically the initial value of *bestrms*, the maximum value of *rms*, and the number of iterations to perform in each simulation. The most important change to the main section is the next set of lines, where the initial values of each varied parameter are specified. The line *set par(values) {...}* creates the list variable *var* mentioned above and assigns the values within the squiggly brackets to indices *0 - x* of the list variable *var*. This list must contain each varied parameter in the same order that they appear in the assignment commands discussed in

paragraph 3, section A.3.6. Each line in the *set par(values)* list begins with a declaration of the variable name, followed by the starting value of the parameter, the initial step size for the variation, and ends with a 1 and close bracket. The remaining lines of the *main* section perform additional integration, processing, and finally the *fit par* line to initiate the successive iterations.

A.4 SIMPSON Input Files

A.4.1 Sample State CSA Simulation

This simulation calculates a static spectrum of a single phosphorus environment under the influence of only the chemical shift interaction. It does so by the direct method and is an example of a straightforward way to simulate a basic experiment.

```
spinsys {
  nuclei 31P
  channels 31P
  shift 1 1.9p 60.4p 0.15 0 0 0
}

par {
  sw 100000
  start_operator I1z
  detect_operator I1p
  crystal_file zcw4180
  np 1024
  proton_frequency 500e6
  verbose 1101
  variable rfpow 500
}

proc pulseq {} {
  global par

  set tdwell [expr 1.0e6/$par(sw)]
  set t90 [expr 0.25e6/$par(rfpow)]

  pulseid $t90 $par(rfpow) x
```

```
  acq
  for {set i 1} {$i < $par(np)} {incr i} {
    delay $tdwell
    acq
  }
}

proc main {} {
  global par

  set f [fsimpson]
  fsave $f $par(name).fid
  fzerofill $f 8192
  faddlb $f 500 0
  fft $f
  fsave $f $par(name).spe
}
```

A.4.2 Sample MAS CSA Simulation

This simulation calculates a magic angle spinning spectrum of the same single phosphorus environment calculated in example A.4.1. It does so by the direct method and is an example of a straightforward way to simulate a basic MAS experiment.

```
spinsys {
  nuclei 31P
  channels 31P
  shift 1 1.9p 60.4p 0.15 0 0 0
}

par {
  spin_rate 6000
  gamma_angles 16
  sw spin_rate*gamma_angles
  start_operator I1z
  detect_operator I1p
  crystal_file rep168
  np 1024
  proton_frequency 500e6
  verbose 1101
  variable rfpow 50000
}

proc pulseq {} {
  global par

  maxdt 1
```

```
  set tdwell [expr 1.0e6/$par(sw)]
  set t90 [expr 0.25e6/$par(rfpow)]

  pulseid $t90 $par(rfpow) x
  acq
  for {set i 1} {$i < $par(np)} {incr i} {
    delay $tdwell
    acq
  }
}

proc main {} {
  global par

  set f [fsimpson]
  fsave $f $par(name).fid
  fzerofill $f 8192
  faddlb $f 500 0
  fft $f
  fsave $f $par(name).spe
}
```

A.4.3 Sample QCPMG Simulation

This simulation calculates a static QCPMG spectrum of a single strontium environment dominated by the quadrupolar interaction. Only an isotropic chemical shift is involved in the calculation; no CSA is accounted for. This simulation calculates the QCPMG NMR signal directly in the pulse sequence section as a series of pulses and delays. A faster method for performing this calculation is demonstrated in example A.4.4.

```
cluster {
dirac.chem.psu.edu
dirac.chem.psu.edu
}

# Static QCPMG

spinsys {
  channels 87Sr
  nuclei 87Sr
  quadrupole 1 2 8.96e6 0.10 0 -20 0
```

```
  shift 1 -338p 0 0 0 0 0
}

par {
  spin_rate        0
  sw               1000000
  crystal_file     zcw4180
  start_operator   I1z
  detect_operator  I1c
  verbose          1101
  proton_frequency 900e6
  variable rf      83333
  variable rf2     83333
  variable N       1000
  variable R       20
  use_cluster         1
  cluster_port        5535
}

proc pulseq {} {
  global par

  set tsw  [expr 1.0e6/$par(sw)]
  set t90  [expr 0.25e6/$par(rf)/5]
  set t180 [expr 0.5e6/$par(rf)/5]


  set t1 85.0
  set t2 85.0
  set t3 85.0

  reset
  delay  $tsw
  store 1

  reset
  pulse $t90 $par(rf) x
  delay $t1
  pulse $t180 $par(rf) y
  delay $t2
  acq $par(N) 1 -y
  for {set j 1} {$j < $par(R)} {incr j} {
    delay $t3
    pulse $t180 $par(rf) y
    delay $t3
    acq [expr 2*$par(N)-1] 1 -y
  }
  acq $par(N) 1 -y
}


proc main {} {
  global par

  set par(np) [expr (2*$par(N)-1)*$par(R)+$par(N)]
```

```
  set f [fsimpson]

  fsave $f $par(name).fid
  fzerofill $f 262144
  faddlb $f 40 0
  fft $f
  fsave $f $par(name).spe
      }
```

A.4.4 Sample QCPMG Iterative Fitting Simulation

This is an example of the iterative fitting routine in SIMPSON. Here, a single strontium environment in the experimental spectrum "SrAcAcdfs.spe" is simulated by SIMPSON using the SIMPLEX method. Many of the elements of the basic QCPMG calculation are performed in this simulation. This example also highlights the changes needed to each section of the input file to initiate an iterative simulation.

```
cluster {
dirac.chem.psu.edu
dirac.chem.psu.edu
}

# Static qcpmg
# simulate 87Sr at 20.5 T
# optimization of 1 independent sites

spinsys {
  channels 87Sr
  nuclei 87Sr
  quadrupole 1 2 12e6 0.7 0 0 0
  shift 1 -200p 200p 0.2 14.0 88.0 48.0
}

par {
  spin_rate        0
  sw               1000000
  crystal_file /home1/gmb189/rep8000.cry
#  crystal_file /home1/gmb189/zcw28656.cry
  start_operator   I1z
  detect_operator  I1c
  verbose         0
  proton_frequency 900e6
  variable rf      41800
  variable N       500
```

```
  variable R       40
  use_cluster      1
#  cluster_port     6287
}

proc pulseq {} {
  global par

  set tsw  [expr 1.0e6/$par(sw)]
  set t90  [expr 0.25e6/$par(rf)]
  set t180 [expr 0.5e6/$par(rf)]


  set t1 100.0
  set t2 100.0
  set t3 100.0

  matrix set 1 totalcoherence {1 -1}

  reset
  delay  $tsw
  store 1

  reset
  pulse $t90 $par(rf) x
  filter 1
  delay $t1
  pulse $t180 $par(rf) y
  filter 1
  delay $t2
  acq $par(N) 1 -y
}


proc fitfunction {val} {
  global par stop exp exp2

  set par(np) [expr (2*$par(N))*$par(R)+$par(N)]
  set N2 [expr 2*$par(N)]
      set cq1           [lindex [lindex  $val 0] 1]
      set etaq1   [lindex [lindex  $val 1] 1]
      set shift1  [lindex [lindex  $val 2] 1]
      set csa           [lindex [lindex  $val 3] 1]
      set etacs   [lindex [lindex  $val 4] 1]
      set alpha   [lindex [lindex  $val 5] 1]
      set beta    [lindex [lindex  $val 6] 1]
      set gamma   [lindex [lindex  $val 7] 1]
  set lb2 1000
  set lb 15

  set f [fsimpson [list [list quadrupole_1_aniso $cq1 ] \
              [list quadrupole_1_eta $etaq1] [list shift_1_iso $shift1]
\
            [list shift_1_aniso $csa] [list shift_1_eta $etacs] \
            [list shift_1_alpha $alpha] [list shift_1_beta $beta] \
```

```
            [list shift_1_gamma $gamma]  ]]
      faddlb $f $lb2 0

for  {set i 1} {$i <= $par(N)} {incr i} {
    set c [findex $f [expr $i]]
    set re [lindex $c 0]
    set im [lindex $c 1]
    set im2 [expr -1*$im]
    fsetindex $f [expr 1+2*$par(N)-$i] $re $im2
    fsetindex $f [expr 2*$par(N)+$i] $re $im
    }

  for {set i 1} {$i <= $N2} {incr i} {
    set c [findex $f [expr $i + $par(N)]]
    set re [lindex $c 0]
    set im [lindex $c 1]
    for {set j 1} {$j < $par(R)} {incr j} {
      fsetindex $f [expr $i+$j*$N2+$par(N)] $re $im
    }
  }

      faddlb $f $lb 0
      fzerofill $f 262144
      fft $f
      fphase $f -rp -5


set f2 [fssbint $f 500 0 500]
set scale [fautoscale $f2 $exp2]

  fsave $f $par(name)-sim.spe


set rms [frms $f2 $exp2 [list -re] [list {-60000 10000}]]
if {$rms < $par(bestrms) } {
      set par(bestrms) $rms
      fsave $f2 $par(name)-best.spe
      puts -nonewline "*"
}
funload $f
puts "$par(iter) $rms $par(bestrms) scale= $scale $val"
if {$stop || $rms < $par(maxrms) ||
      $par(iter) > $par(maxiter)} {
     exit
}
return $rms
}

proc main {} {
  global par exp exp2

set par(fitmethod) simplex
set par(function) fitfunction
set exp [fload SrAcAcdfs.spe]
set par(bestrms)  1e6
```

```
set par(maxrms)         0.5
set par(maxiter)  100

set par(values) {
      {cq1              12.5e6      0.1e6 1}
      {etaq1            0.60  .05   1}
      {shift1           -384  50    1}
      {csa              10000 1000  1}
      {etacs            0.02  0.05  1}
      {alpha            10.0  25    1}
      {beta             60.0  25    1}
      {gamma            60.0  25    1}
}
set exp2 [fssbint $exp 500 0 500]
fsave $exp2 $par(name)-exp.spe
fit par
}
```

A.4.5 Sample ^{87}Sr MAS NMR Simulation – C_q = 10 MHz, Spin Rate = 5 kHz

This is a sample of the ^{87}Sr MAS simulations used to generate parts of figure 3.7. Here, only the quadrupolar interaction is of interest and is thus the only interaction present during the calculation.

```
cluster {
dirac.chem.psu.edu
dirac.chem.psu.edu
}

spinsys {
    nuclei 87Sr
    channels 87Sr
    quadrupole 1 2 10e6 0.1 0 0 0
}

par {
    start_operator   I1x
    detect_operator  I1c
    spin_rate        5000
    gamma_angles     100
    sw               gamma_angles*spin_rate
#    crystal_file     rep168
    crystal_file     zcw986
#    crystal_file     /usr/local/bin/rep8000.cry
#    crystal_file     /usr/local/bin/zcw28656.cry
    np               2048
    proton_frequency 500e6
```

```
    verbose      1101
    use_cluster      1
    cluster_port     5535
}

proc pulseq {} {
    global par

    maxdt 1

    set tdwell [expr 1.0e6/$par(sw)]
    acq
    for {set i 1} {$i < $par(np)} {incr i} {
        delay $tdwell
        acq
    }
}

proc main {} {
    global par

    set f [fsimpson]
    fsave $f $par(name).fid
    fzerofill $f 4096
    faddlb $f 100 0
    fft $f
    fsave $f $par(name).spe
}
```

A.4.6 Sample ^{87}Sr MAS NMR Simulation – C_q = 30 MHz, Spin Rate = 20 kHz

This is a sample of the ^{87}Sr MAS simulations used to generate parts of figure 3.8. It is identical to example A.4.5, but shows the user how to vary the spin rate, quadrupolar coupling, and field strength.

```
cluster {
dirac.chem.psu.edu
dirac.chem.psu.edu
}

spinsys {
    nuclei 87Sr
    channels 87Sr
    quadrupole 1 2 30e6 0.1 0 0 0
}

par {
```

```
    start_operator   I1x
    detect_operator  I1c
    spin_rate        20000
    gamma_angles     25
    sw               gamma_angles*spin_rate
#    crystal_file     rep168
    crystal_file     zcw986
#    crystal_file     /usr/local/bin/rep8000.cry
#    crystal_file     /usr/local/bin/zcw28656.cry
    np               2048
    proton_frequency 900e6
    verbose      1101
    use_cluster      1
    cluster_port     5535
}

proc pulseq {} {
    global par

    maxdt 1

    set tdwell [expr 1.0e6/$par(sw)]
    acq
    for {set i 1} {$i < $par(np)} {incr i} {
        delay $tdwell
        acq
    }
}

proc main {} {
    global par

    set f [fsimpson]
    fsave $f $par(name).fid
    fzerofill $f 4096
    faddlb $f 100 0
    fft $f
    fsave $f $par(name).spe
}
```

Appendix B

Other Computer Codes

B.1 QCPMG Pulse Sequence for Chemagnetics Infinity Systems

During the course of this research, the QCPMG pulse sequence was programmed on the Varian/Chemagnetics Infinity 500 console. The pulse programmer on this instrument requires the sequence is written in P-code, a proprietary language. The pulse program and corresponding acquisition file are included below.

B.1.1 Pulse Program

```
name        "qcpmg";
title       "nonint quad spikelet echo";

!  COMPILED WITH OPTIMIZATION ON
!  $Header: /usr2/users/applab/CFR/ppg/oldfield_echo.s,v 1.4 1998/07/23
22:28:45 applab Exp $

!     ref. A.C. Kunwar, G.L. Turner, E. Oldfield, J. Magn. Reson.,
69:124-127 (1986).
!   pulse program works with 90/180, or with 45/90 pulse widths.
!   Modified by ASLipton for ENI gating (7/7/2000) and for spikelet
echo (7/7/2000)
!   Also ASLipton added decoupling 8/4/2000

    NMRchnls    RF: ch1 ch2; NMRacq;

! ----------------------------------------
! .data section is for compiler definitions
! ----------------------------------------
.data

    .time autofix extern tau2 "post-refocus tau" = 30us;
      .time rof2 = 20us;

      .time TAU3;
```

```
      .time TAU4;
      .time TAU;

      .long extern nloop = 1;
      .long extern ndp = 256;
      .long i = 1;
    .long ndpacqfecho = 512;

!This is no phase cycling whatsoever
!.phase           list X90[]=0;
!.phase           list X180[]=90;
!.phase           list Xtrain[]=90;
!.long      extern      list abph[]=0;

!This is a simple phase cycle from cs echo
!.phase                 list X90[]  = 0,180,90,270;
!.phase                 list X180[] =   90,90,180,180;     ! refocus
pulse phase list
!.phase                 list Xtrain[]= 90,270,180,0;
!.long      extern      list abph[] = 0,2,1,3;  !rcvr cycle list

!This is the phase list from Andy Lipton's code
.phase list X90[]=0,0,0,0,90,90,90,90,180,180,180,180,270,270,270,270;
.phase list X180[]=0,90,180,270;
.phase list
Xtrain[]=90,90,90,90,180,180,180,180,270,270,270,270,0,0,0,0,
270,270,270,270,0,0,0,0,90,90,90,90,180,180,180,180;

.long extern list
abph[]=0,2,0,2,3,1,3,1,2,0,2,0,1,3,1,3,0,2,0,2,3,1,3,1,
2,0,2,0,1,3,1,3;

!This is the phase cycle from Larsen, JPCA,1997,pg. 8601
!.phase list X90[]=0,90,180,270;
!.phase list X180[]=90,0,90,0,270,180,270,180;
!.phase list
Xtrain[]=90,0,90,0,270,180,270,180,270,180,270,180,90,0,90,0;

!.long extern list abph[]=2,3,0,1;

include "../includes/STANDARD_PARAMS";
include "../includes/1D.inc";

! -----------------------------------------------------
! Define error codes specific to this pulse program
! -----------------------------------------------------
define PW180_ERR 0x100
define PW180_ERROR_CODE USER_ERROR_BASE + PW180_ERR
comment "ERROR "PW180_ERROR_CODE "pw180X too long or tau1 too short";

!-------------------------------------------------------
! UPDATES calculate parameters, report values to acq panel.
!-------------------------------------------------------

! .update "rb=1.30*sw";
```

```
.update "al = ndp + (ndp*2+1)*nloop"; !calculates total npts
.update "aqtm=(dw*al)";
.update "extm=(pw90X+tau+tau2+rd+aqtm+pd)";
.update "txduty1=(pw90X+pw180X)/extm";
.update "time1d=((na+dp)*extm)/60.0";

!--------------------------------------
! executed once at start of run
!--------------------------------------

.program

dpc = dp;
TAU = tau;
TAU3 = tau2 - rd;
TAU4 = tau - (tau2 - tau);
rof2 = rd;
ndpacqfecho = 2*ndp+1;

txduty1=(pw90X+pw180X)/extm;
if (txduty1 > 0.2) {error(TXDUTY_ERR);}

if (TAU3 < 0.1us) {error(PW180_ERR);}

! -------------------------------
! actual pulse prog. runtime loop
! -------------------------------

.start
      aqph=@abph;  ! cycle rcvr phase
      out     time(3u)  ch1: SC(scX)      ch2:SC(scH);            !
output scaler
      out   time(10u)   ch1: AP(aX,@X90++);!cycle pulse phase and
amplitude
      out   pw90X       ch1:TG;                 ! output  90 degree
pulse
      out     time(TAU) ch1:P(@X180++);
      out     pw180X    ch1:TG;
      out   time(rof2) ch1:P(p) ch2: A(aH);
      out     time(TAU3)      ch1: RE|TB  ch2:TG;
      outAQ dw    ch1: RE|TB  ch2:TG,ndp;
if (nloop > 0) {
      for (i=0, i<nloop, i++)
      {
    out time(TAU4) ch1:RE|P(@Xtrain) ch2:TG;
      !out time(TAU) ch1:RE|P(@Xtrain) ch2:TG;
      out pw180X  ch1:RE|TG   ch2:TB;
      out time(rof2) ch1:RE|P(p) ch2:TG;
      out time(TAU3)  ch1:RE|TB     ch2:TG;
      outAQ dw    ch1:RE|TB   ch2:TG ,ndpacqfecho;
      }     !end of spikelet loop
}
    Xtrain++;
      abph++;
      scan pd;
```

```
.end
```

B.1.2 Acquisition Parameters

```
# spikelet3.acq
##########################################################
#  $Revision: 1.6 $  $Date: 1997/02/10 21:16:48 $
#  $Source: /usr2/users/applab/CFR/acqpars/oldfield_echo.acq,v $
#
#   This section sets the initial cmx global parameters
#
#     The file format is as follows
#
#     si_name;long name;value;units;min;max;decimal pnts;user
level;data type
#
#   a - is a blank field.
#   tabs and spaces are allowed if you wish to seperate the fields a
little
#   but a line can be only 80 characters.
#
# first line = ppfn and na
#
na;# acq's (x 16);1;-;1;100000000;0;1;long
#
# Channel assignments
#
ch1;ppg ch1;1;-;1;4;0;1;long
sf1;spect freq;21.662;MHz;1.0;800.5;7;1;float
ch2;ppg ch2;2;-;1;4;0;1;long
sf2;spect freq;499.61600;MHz;1.0;800.5;7;1;float
sf3;spect freq;20.0;MHz;1.0;800.5;6;1;float
#
# timing variables
#
tau;delay bet. pulses;50;u;.1;100000;2;1;float
pw90X;90 pulse (or 45);2;u;.1;10000;2;1;float
tau2;delay after pi pulse;45;u;.1;100000;2;1;float
pw180X;180 pulse (or 90);4;u;.1;10000;2;1;float
dw;dwell;.5;u;.2;100000;3;1;float
rd;receiver delay;15;u;.1;1000;2;1;float
sw;spectrum width;2000;kHz;.01;5001;1;1;float
pd;pulse delay;1;s;.0001;6500;3;1;float
aqtm;acq. time;0.256;m;.0005;50000;3;1;float
#
# Pulse/receiver attributes
#
aX;X rf ampl;0.0;-;0.0;1.0;4;1;float
```

```
scX;X scalar;0.1;-;0.001;1.0;4;1;float
aH;H rf ampl;0.0;-;0.0;1.0;4;1;float
scH;H scalar;0.1;-;0.001;1.0;4;1;float
#
#
# Other variable, e.g., al, loop counters
#
al;acq length;512;-;2;1048576;0;1;long
dp;dummy pulses;0;-;0;1000;0;1;long
rb;receiver bandwidth;230;khz;.2;7000;1;1;float
rg;receiver gain;500;-;1;2820;2;1;float
txduty1;trans. duty;.01;-;0.0;0.2;3;1;float
temp;Set Temp. (C);0;-;-1000;250;2;1;float;acc_array
speed;spin rate;-1;kHz;-1000;50;3;1;float;acc_array
time1d;1D time (min);1;-;0.000005;999999999;3;0;float
nloop;spikelet loops;1;-;0;500;0;1;long
ndp; half echo points;512;-;2;1048576;0;1;long
#
# si_name;long name;value;units;min;max;decimal pnts;user level;data
type
```

B.2 DECRA Code

Though not involved directly in the strontium NMR project, a series of MATLAB functions were written to analyze data sets consisting of overlapping exponentially decaying functions. The mathematical operations are known as the dynamic exponential curve resolution algorithm (DECRA) and were devised by Antalek and Windig in the mid-1990's.[222-227] This type of analysis is useful in the case of a saturation-recovery T_1 experiment where the peaks are convoluted or to extract diffusion rate constants and spectral contributions from a diffusion experiment. DECRA is capable of decomposing highly overlapped spectra for even small variations in the decay rate.

The basic input to the DECRA Matlab routine is a file containing two-dimensional NMR data saved as alternating real and imaginary FIDs in a single column (MacRMN can prepare a processed 2D data set in this format quite easily). This file should be an

ASCII text file and end with the extension *.txt* to facilitate proper handling of the input file. The computer algorithm stores the data file specified by the user and re-constructs the 2D data set as a matrix of *y* rows containing the real data while discarding the imaginary data. The matrix is converted into a pair of matrices each with *y*-1 rows of data that are used in a singular value decomposition (SVD) analysis. The SVD results are used in a general eigenvalue problem to determine the decay rates (the eigenvalues) and resolve the spectral contributions of each component (the eigenfunctions). The decay rates are stored as a column vector and the spectral contributions are stored in a matching matrix. The mathematical operations in the "*decra2.m*" function are a direct translation of the code developed by Antalek and Windig. The remaining functions were written to provide a user-friendly graphical user interface (GUI) and to accommodate the input format specified earlier.

The T_1 analysis program is called from the MATLAB command interface by typing "*decragraph*" with all of the necessary DECRA functions stored in the *~/MATLAB/toolbox/local* directory (please ensure this directory is contained in the MATLAB path). The header function will create a graphical user interface prompting the user to input parameters, such as the number of spectra in the data file. After the parameters are entered, the user should click on the "Run DECRA" button at the bottom of the GUI. At this point, the parameters are passed to the *decra2.m* function, which actually reads and manipulates the data with the help of a supporting function *vars.m*. The individual contributions to the overall spectrum calculated during the DECRA analysis are saved in a text file consisting of one data column per component. A final function, *decout.m*, creates an output GUI to display the rate constants in units of seconds

and has a series of buttons to allow the user to view (a) the overall spectrum and/or (b) the contributions of each individual component to the overall spectrum. Note: this output GUI is the only location that displays the decay constants calculated by the algorithm. **The user must write down these numbers from the screen before closing the program**. The spectral contribution corresponding to the first decay constant can be found by clicking the button "PLOTS". The figure with the lowest number in the title bar corresponds to the top decay constant, the second to the second constant in the column, etc. A sentence displaying the name of the text file containing the resolved spectral components is listed at the bottom of this final GUI.

Great care must be taken in the interpretation of the DECRA results. The user is required to provide the algorithm with the number of unique components that are contained in the sample spectra. This number must be varied manually by the user if the number of unique components is unknown *a priori*. Continue to re-run the program, increasing the number of unique components until the decay results appear as complex numbers. When this occurs, decrease the number of components by one and re-run the algorithm. The decay rates/diffusion rates that appear at this point represent the true number of resolvable components in the sample and the matching decay/diffusion rates. The user must determine from the resulting individual spectral contributions whether the number of distinguishable components provided by DECRA is correct or not. The code for each function, listed in the order they are called, follows.

B.2.1 decragraph.m

```
function decragraph()
% This function sets up a graphical user interface for use with the
DECRA
% code.  This allows the user to input all of the necessary arguments
in a
% graphical format and execute the decra code.  There will also be a
% corresponding GUI that controls the decra output and puts it into a
% format that is easily read and interpreted by the user.

% This next line of code creates the master figure onto which the gui
% controls will be placed.
Hf_decra=figure('Position',[150 150 600 600],'Name','DECRA',...
    'Color',[0.9 0.05 0.1]);
set(Hf_decra,'DefaultUicontrolUnits','normalized');

% The next set of code creates the gui controls.  This consists of a
set of
% paired uicontrols, the first creating the label for the user input
box,
% the second creating boxes into which the user can put the necessary
% parameters to run the DECRA program.
uicontrol(Hf_decra,'style','text','position',[0.4 0.9 0.2 0.04],...
    'string','DECRA for 2D','ForegroundColor',[0 0
0],'BackgroundColor',...
    [0.9 0.05 0.1]);
uicontrol(Hf_decra,'style','text','position',[0.3 0.86 0.4 0.04],...
    'string','Enter each parameter, then press <ENTER>',...
    'ForegroundColor',[0 0 0],'BackgroundColor',...
    [0.9 0.05 0.1]);

Hc_label1=uicontrol(Hf_decra,'style','text','position',...
    [0.25 0.8 0.3 0.04],'string','Number of spectra in set:',...
    'ForegroundColor',[0 0 0],'BackgroundColor',...
    [0.9 0.05 0.1]);

Hc_nspec=uicontrol(Hf_decra,'style','edit','position',...
    [0.55 0.8 0.2 0.05],'string',' ','ForegroundColor',[0 0 0],...
    'BackgroundColor',[1 1 1]);

Hc_label2=uicontrol(Hf_decra,'style','text','position',...
    [0.25 0.6 0.3 0.04],'string','Number of T1 components:',...
    'ForegroundColor',[0 0 0],'BackgroundColor',...
    [0.9 0.05 0.1]);

Hc_ncom=uicontrol(Hf_decra,'style','edit','position',...
    [0.55 0.6 0.2 0.05],'string',' ','ForegroundColor',[0 0 0],...
    'BackgroundColor',[1 1 1]);

Hc_label3=uicontrol(Hf_decra,'style','text','position',...
    [0.25 0.4 0.3 0.04],'string','Time increment:',...
    'ForegroundColor',[0 0 0],'BackgroundColor',...
```

```
    [0.9 0.05 0.1]);

Hc_time=uicontrol(Hf_decra,'style','edit','position',...
    [0.55 0.4 0.2 0.05],'string',' ','ForegroundColor',[0 0 0],...
    'BackgroundColor',[1 1 1]);

set(gcf,'UserData',[Hc_nspec Hc_ncom Hc_time]);

% The next set of code creates a button that must be pressed to
continue
% the program.  This button will implement the DECRA code, and then
cause
% the final GUI to run and display the results of the calculations.

Hc_go=uicontrol(Hf_decra,'style','push','position',[0.4 0.1 0.2
0.1],...
    'String','Run DECRA','callback','vars; close(gcf); decra2;
decout');
```

B.2.2 vars.m

```
function vars()
% This function is used by the decragraph program to execute the
callbacks
% and assign values to global variables for use by the decra code
itself.

global nspec ncom time

Hc_all=get(gcf,'UserData');
Hc_nspec=Hc_all(1);
Hc_ncom=Hc_all(2);
Hc_time=Hc_all(3);

% These lines of code assign values to the last three global variables
% based on the user input to the GUI controls in decragraph.
nspec=str2num(get(Hc_nspec,'string'));
ncom=str2num(get(Hc_ncom,'string'));
      time=str2num(get(Hc_time,'string'));
```

B.2.3 decra2.m

```
function decra2()
% fname is the filename where the data is stored.  It must be contained
% within a set of quotations, ex. 'datafile', when the function is
called
% at the command prompt.
```

```
% nspec is the numbmer of spectra contained in the 2D data set.
% rfname is the file name that you would like the scaled and resolved
% spectra to be stored to.
% ncom is a user defined number of independent T1 values beleived to be
% included in the 2D data.
% ppmval is the associated ppm values to be used for the x-axis
% time is a variable representing the total time elapsed for the T1
% experiment...this is the same value as the number of spectra in
% the data set if the time for each spectra is 1 second.

global nspec ncom time eval purspec ppmvals npts

% This section imports the data from the MacRMN program and puts it in
the
% proper format for the algorithm to run.  Input data file should be in
the
% form of a column of numbers representing alternating real/imaginary
FID's
% from the 2D data set.

[fname, pathname]=uigetfile('*.*','Open file containing Data:',...
    300, 300);
[ppmval, path3]=uigetfile('*.*',...
    'Open file containing the x-axis values:', 300, 300);

% Importing the data:
data1=dlmread(fname,' ');
data=[];
tempdat=[];
% Importing the xaxis values:
ppmvals=dlmread(ppmval,' ');
ppmvals=ppmvals';
ppmvals=fliplr(ppmvals);
% Calculating the number of data points per spectra:
nrows=nspec*2;
l=length(data1');
npts=l/nrows;
% Formation of the master matrix from the column of FID's
for i=1:1:(nspec*2)
    start=(i-1)*npts+1;
    for j=0:1:npts-1
        tempdat=[tempdat data1(start+j,:)];
    end
    data=[data; tempdat(1,:)];
    tempdat=[];
end
spec=[];
% Discarding the imaginary parts from the matrix
for i=1:2:(nspec*2)
    spec=[spec; data(i,:)];
end

% The next section is for error trapping purposes.  It steps through
the
% data matrix element by element testing for negative values, which are
```

```
not
% tolerated by the remainder of the code.  When a negative value is
found,
% it is replaced with zero and a warning message is displayed to the
user.
for a=1:1:nspec
    for b=1:1:npts
        if spec(a,b)<0
            spec(a,b)=0;
            Hf_err=figure('position',[150 150 200
150],'name','WARNING',...
                'color',[0.9 0.05 0.1]);
            set(Hf_err,'DefaultUicontrolUnits','normalized');
            Hc_err1=uicontrol(Hf_err,'position',[0.4 0.9 0.2
0.05],'style',...
                'text','string','Warning!','ForegroundColor',[0 0 0]);
            Hc_err2=uicontrol(Hf_err,'position',[0.2 0.8 0.6
0.1],'style',...
                'text','string','Negative values in real part of
spectra.',...
                'ForegroundColor',[0 0 0]);
            Hc_err3=uicontrol(Hf_err,'position',[0.2 0.4 0.6
0.3],'style',...
                'text','string',...
                'Number of spectra may be incorrect or data set is not
uniform.',...
                'ForegroundColor',[0 0 0]);
            Hc_err4=uicontrol(Hf_err,'position',[0.2 0.2 0.6
0.15],'style',...
                'text','string',...
                'Values will be replaced with zero.  Hit any key to
continue...',...
                'ForegroundColor',[0 0 0]);
            pause;
         end
     end
 end

% The following section of code is the actual DECRA math algorithm.  It
% begins by setting the range that each of the two sub-matrices will be
% based on the total set of spectra in spec.  It then computes a
singular
% value decomposition of one of the two matrices.  Results from this
% operation are truncated and then used to solve the generalized
eigenvalue
% problem.  The results of the eigenvalue problem are then used to
% calculate the T1 values and resolve the spectra.
range1=1:nspec-1;
range2=2:nspec;

[v,s,u]=svd(spec(range1,:)',0);
s=s(1:ncom,1:ncom);
u=u(:,1:ncom);
v=v(:,1:ncom);
```

```
[ev,aa]=eig(u'*spec(range2,:)*v*inv(s));
ev=fliplr(ev);
aa=flipud(diag(aa));
purspec=pinv(v*inv(s)*ev);
purint=u*ev;

eval=[];
eval=aa;
eval=log(eval);
for n=1:1:ncom
    eval(n)=-time/eval(n);
end

% This section provides a very easy way to check to see if the results
are
% correct by viewing a graph of the output spectra.  As long as there
% aren't a bunch of lines at the bottom of the graph (a noisy
spectrum),
% the calculations are correct.  The T1 values are displayed on the
Matlab
% user interface screen, and the output file is written as a text file
with
% one column of values for each T1.
tic=sum(spec(range1,:)')';
scalefactor=purint\tic;
purint=purint*diag(scalefactor);
purspec=diag(1./scalefactor)*purspec;
dlmwrite('decraout',purspec',' ');

purspec=fliplr(purspec);
```

B.2.4 decout.m

```
function decout()
% This is a GUI version of the DECRA output, that allows the user to
view
% the results of the T1 calculation, the parameters that they entered
into
% the initial GUI, and two buttons for plotting the figures of the
resolved
% spectra.

global nspec ncom time eval

% This sets up the figure window that will contain the GUI control
% structures.
Hf_decout=figure('Position',[150 150 400 600],'Name','DECRA',...
    'Color',[0.9 0.05 0.1]);
set(Hf_decout,'DefaultUicontrolUnits','normalized');

% This sets up displays of the entered values and the results of the T1
```

```
% calculations.
uicontrol(Hf_decout,'style','text','position',[0.4 0.9 0.2 0.04],...
    'string','DECRA Results','BackgroundColor',[0.9 0.05 0.1],...
    'ForegroundColor',[0 0 0]);

Hc_lab1=uicontrol(Hf_decout,'style','text','position',[0.15 0.8 0.5
0.04],...
    'string','Number of Spectra in set:','BackgroundColor',[0.9 0.05
0.1],...
    'ForegroundColor',[0 0 0]);

Hc_specout=uicontrol(Hf_decout,'style','text','position',[0.55 0.8 0.2
0.05],...
    'string',num2str(nspec),'BackgroundColor',[1 1 1],...
    'ForegroundColor',[0 0 0]);

Hc_lab2=uicontrol(Hf_decout,'style','text','position',[0.1 0.7 0.55
0.04],...
    'string','Number of T1 values in set:','BackgroundColor',[0.9 0.05
0.1],...
    'ForegroundColor',[0 0 0]);

Hc_comout=uicontrol(Hf_decout,'style','text','position',[0.55 0.7 0.2
0.05],...
    'string',num2str(ncom),'BackgroundColor',[1 1 1],...
    'ForegroundColor',[0 0 0]);

Hc_lab3=uicontrol(Hf_decout,'style','text','position',[0.15 0.6 0.5
0.04],...
    'string','Time Constant:','BackgroundColor',[0.9 0.05 0.1],...
    'ForegroundColor',[0 0 0]);

Hc_timeout=uicontrol(Hf_decout,'style','text','position',[0.55 0.6 0.2
0.05],...
    'string',num2str(time),'BackgroundColor',[1 1 1],...
    'ForegroundColor',[0 0 0]);

Hc_lab4=uicontrol(Hf_decout,'style','text','position',[0.25 0.4 0.3
0.04],...
    'string','T1 values:','BackgroundColor',[0.9 0.05 0.1],...
    'ForegroundColor',[0 0 0]);

Hc_T1=uicontrol(Hf_decout,'style','text','position',...
      [0.55 0.4-(0.04*(ncom-2)) 0.2 0.04*ncom],...
    'string',num2str(eval),'BackgroundColor',[1 1 1],...
    'ForegroundColor',[0 0 0]);

Hc_graphs=uicontrol(Hf_decout,'style','text','position',...
      [0.1 0.36-(0.04*(ncom-2))-0.06 0.8 0.09],...
    'string','To view a graph of each resolved spectra, click button
below.  First T1 value belongs to lower numbered figure.',...
    'BackgroundColor',[0.9 0.05 0.1],'ForegroundColor',[0 0 0]);

Hc_plots=uicontrol(Hf_decout,'style','push','position',[.2 0.2 0.2
0.05],...
```

```
            'string','PLOTS','ForegroundColor',[0 0 0],'callback',...
            'plotfnc;');

Hc_plots2=uicontrol(Hf_decout,'style','push','position',[.6 0.2 0.3
0.05],...
            'string','FULL SPECTRUM','ForegroundColor',[0 0
0],'callback',...
            'plotfnc2;');

Hc_stored=uicontrol(Hf_decout,'style','text','position',[0.1 0.12 0.8
0.05],...
    'string','The resolved spectra are contained in the file
''decraout''.',...
    'BackgroundColor',[0.9 0.05 0.1],'ForegroundColor',[0 0 0]);

Hc_close=uicontrol(Hf_decout,'style','push','position',...
    [0.4 0.05 0.2 0.05],'string','Close','ForegroundColor',[0 0 0],...
    'callback','close(gcf)');
```

B.3 QCPMG Processing Post-Acquisition

There are a variety of methods to further enhance the sensitivity of QCPMG NMR results, as presented by Leforte *et al*.[105] One of the most useful qualitative means to enhance sensitivity post-acquisition is to adjust the spacing of the echo maxima in the resulting QCPMG signal. This is done by removing points or adding points to the region consisting of primarily noise between the maxima. Adding points in the form of zeros causes a decrease in the spacing between spikes in the spectrum. Removing points has the opposite effect, increasing the spacing between spikes in the frequency domain. While this approach is not encouraged for publication-quality data, it can be used to find the optimum spikelet spacing for a series of samples after one spectrum has been collected. A second useful form of post-processing is to use a more specialized apodization function rather than the typical Lorentzian broadening, such as the comb

filter introduced in chapter 2. The comb filter reduces noise between the echo maxima while preserving the intensity of each echo.

The following code (B.3.1) is a MATLAB program designed to read in user data in the form of an ASCII file with two columns consisting of real and imaginary data pairs. The function is called at the MATLAB command prompt with the command *QCPMGspacing(<# of loops>, <# points desired per half echo in final data set>, <output file name in double quotes>)*. The program reads in the file and then calculates the number of points per data set. From this and the arguments, it determines whether zeros need to be added to the data or noise subtracted from each half echo and performs those operations. The output is written as columns of real and imaginary data to an ASCII file specified by the final argument in the function call.

The code in section B.3.2 is a second MATLAB function that applies the comb filter apodization scheme to a data set. This function is called from the MATLAB command prompt with the following syntax: *QCPMGproc(nloops,expbrd,nptszfill,sw,rfname)*. It simply reads in a data file, calculates the number of points in the data set, and generates a comb filter of the appropriate length and broadening. The filter is then multiplied with the real and imaginary data columns, which are then written to an output file.

B.3.1 QCPMGspacing.m

```
function QCPMGspacing(nloops,nptperecho,rfname)
% nloops is the numbmer of echo loops used in your QCPMG experiment.
% rfname is the file name that you would like the processed FID to be
stored to.
```

```
% nptperecho is the number of data points per half echo you desire in
your final
% QCPMG data set.

% This program allows you to process QCPMG data by changing the spacing
between
% echo peaks in frequency spectrum.  Keep in mind that
% this has a negative impact on one's ability to map out the static
powder
% pattern with the spikelet manifold.  The input file is assume to be
an
% ASCII data file with two columns, one containing the real data and
the
% other the imaginary data as pairs.

[fname, pathname]=uigetfile('*.*','Open file containing Data:',...
    'Location',[300 300]);

% Importing the data:
data1=dlmread(fname);
data=[];

% Calculating the number of data points per half echo:
npts=length(data1');
pthalfecho=npts/(2*nloops+1);

% This next section actually removes the points from each half echo and
% then stores the resulting echo with filename rfname.
a=1;
if nptperecho<pthalfecho
    for i=1:1:(2*nloops+1)
        for j=1:1:pthalfecho
            if j<nptperecho
                data=[data; data1(a,:)];
                a=a+1;
            end
        end
        a=i*pthalfecho;
    end
elseif nptperecho>pthalfecho
    diff=nptperecho-pthalfecho;
    for k=1:1:pthalfecho
        data=[data; data1(k,:)];
    end
    for i=1:1:nloops
        for l=1:1:(diff*2)
            data=[data; 0,0];
        end
        m=(i-1)*2*pthalfecho+pthalfecho;
        for n=1:1:(pthalfecho*2)
            data=[data; data1(m+n,:)];
        end
    end
end
```

```
dlmwrite(rfname,data,' ');
```

B.3.2 QCPMGproc.m

```
function [nuqcp]=QCPMGproc(nloops,expbrd,nptszfill,sw,rfname)
% fname is the filename where the data is stored.  It must be contained
% within a set of quotations, ex. 'datafile', when the function is
called
% at the command prompt.
% nloops is the numbmer of echo loops used in your QCPMG experiment.
% rfname is the file name that you would like the processed FID to be
stored to.
% expbrd is the broadening you wish applied to each half-echo in Hz.
% nptszfill is the number of points to zero fill between each echo;
used to
% adjust the nuqcp value and reduce the number of spikes in the
envelope.
% sw is the sweep width in kHz that you used for your QCPMG experiment.

% This program allows you to process QCPMG data in two ways.  First,
you
% can apply the special exponential apodization scheme proposed by
Lefort
% and colleagues to a QCPMG data file.  The second allows you to zero
fill
% between echo acquisitions, thereby artificially increasing the nuqcp
and
% improving the sensitivity of the resulting spectrum.  Keep in mind
that
% this has a negative impact on one's ability to map out the static
powder
% pattern with the spikelet manifold.  The input file is assume to be
an
% ASCII data file with two columns, one containing the real data and
the
% other the imaginary data as pairs.

[fname, pathname]=uigetfile('*.*','Open file containing Data:',...
    300, 300);

% Importing the data:
data1=dlmread(fname,' ');
data=[];
tempdat=[];

sw=sw*1000; % Makes sw in Hz

% Calculating the number of data points per half echo:
```

```
l=length(data1');
npts=l/2;
pthalfecho=npts/(2*nloops+1);

% The next section of code actually performs the exponential broadening
of
% each half echo.  It does so by creating a vector corresponding to the
% time point at which each data point was acquired.  This vector is
then
% transformed into a vector representing the calculated exponential
% function, which is then multiplied by the real column and the
imaginary
% column.
time=[];
time2=[];
time3=[];
brdfnc=[];
tdw=1/sw;
for j=1:1:pthalfecho
    time=[time j*tdw];
end
for k=1:1:pthalfecho
    time2=[time2 (exp(-expbrd*time(1,k)))];
end
for m=1:1:pthalfecho
    time3(1,pthalfecho-(m-1))=time2(1,m);
end
for k=1:1:(2*nloops+1)
    if rem(k,2)==0
        brdfnc=[brdfnc time3];
    else
        brdfnc=[brdfnc time2];
    end
end
temp=[];
temp2=[];
temp=data1(:,1);
temp=brdfnc.*temp;
temp2=data1(:,2);
temp2=temp2.*brdfnc;
spec(:,1)=temp;
spec(:,2)=temp2;

% This section provides a very easy way to check to see if the results
are
% correct by viewing a graph of the output spectra.  As long as there
% aren't a bunch of lines at the bottom of the graph (a noisy
spectrum),
% the calculations are correct.  The T1 values are displayed on the
Matlab
% user interface screen, and the output file is written as a text file
with
% one column of values for each T1.

dlmwrite(rfname,spec,' ');
```

```
nuqcp=2*pthalfecho*tdw
```

VITA

Education

Ph.D., Chemistry, The Pennsylvania State University, University Park, PA, 2006 (anticipated).
- Dissertation topic: Characterization of Strontium Interactions in Environmental and Inorganic Systems with Solid-State ^{87}Sr NMR

B.S., Chemical Engineering with Chemistry Minor, Purdue University, West Lafayette, IN, 2002.
- Co-operative Education Certificate

Indiana Academic Honors Diploma, Brebeuf Jesuit Preparatory School, Indianapolis, IN, 1997.

Research Experience

Graduate Student, Department of Chemistry, The Pennsylvania State University, 2002-present.
- Solid-State ^{87}Sr, ^{27}Al, ^{29}Si, ^{1}H and ^{23}Na NMR of strontium compounds, clay minerals, zeolites, and glass systems

Research and Development Co-op Student, Raytech Composites, 1998-2001.
- Development, optimization, and formulation of friction materials and processing techniques
- Analytical and mechanical analyses of friction materials

Long-term Research Project in Athletic Drug Abuse, Indiana University Medical Center, Summer 1993, 1994.
- Evaluation of archived data and preparation of statistical database

Teaching Experience

- **Teaching Consultant**, General Chemistry Laboratory, The Pennsylvania State University, 2004-2005.
- **Supervising Teaching Assistant**, General Chemistry Laboratory, The Pennsylvania State University, 2003/2004 Academic Year.
- **Teaching Assistant**, General Chemistry Laboratory, The Pennsylvania State University, 2002/2003 Academic Year.

Publications

Geoffrey M. Bowers and Karl T. Mueller. *Electric field gradient distributions about strontium nuclei in cubic and octahedrally symmetric crystal systems.* Physics Review B, **71** (2005) 224112, 7 pages.

Geoffrey M. Bowers, Andrew S. Lipton, and Karl T. Mueller. *Strontium Quadrupolar Parameters in Strontianite and Celestine as Determined by QCPMG NMR at 21.14 T.* Solid State Nuclear Magnetic Resonance, **29** (2006) 95-103.

Geoffrey M. Bowers, Ramesh Ravella, Sridhar Komarneni, and Karl T. Mueller. *NMR Study of Strontium Binding by a Micaceous Mineral.* Journal of Physical Chemistry B, **110** (2006) 7159-7164.

Miscellaneous

- 10 professional research presentations; 4 by research advisor.
- Primary author of seven funded, peer-reviewed research proposals for instrument time at Pacific Northwest National Laboratory; valued at > $915,000.
- Recipient of 11 awards and honors. Includes awards based on research, teaching, and presentation skills, a symposium chairmanship, and designation as a National Merit Finalist.